

Two-dimensional radiation inversion

The multichannel, multicamera bolometer system is used to perform tomographic inversions to obtain two-dimensional radiation profiles in the triangular shaped plane of W7-X. In contrast to looking at chord brightness profiles of each camera individually, tomography yields a geometrically entangled resolution of the line-integrated measurements of both systems together simultaneously. As previously elaborated on in section 2.3.2, the underlying mathematical problem is ill-posed, i.e. the number of free parameters, represented by the total number of pixels or voxels is far greater than the number of constraints, i.e. the line of sight intersections. Tomographic reconstructions are used to solve multidimensional geometric problems of inversion to find solutions for a system with such a finite number of information. Due to the nature of the measurement system and environment, the approach to this challenge is given by an iterative solution to the initial, in equation (2.32) introduced *Tikhonov regularisation* with more, to this particularly difficult problem advantageous algorithms. Let us first revisit the original posed set of equations to solve the regularised tomographic inversion problem with:

$$\begin{aligned} \tilde{\mathbf{T}}\vec{x} &= \hat{\vec{b}}, \\ \chi^2 &:= (\tilde{\mathbf{T}}\vec{x} - \hat{\vec{b}})^T (\tilde{\mathbf{T}}\vec{x} - \hat{\vec{b}}), \\ \min_{\mu} \left[\frac{1}{2} \chi^2 + \mu K \right] &\stackrel{!}{=} \min \Phi. \end{aligned} \tag{5.1}$$

*repeat of intro
→ drop or move*

Remember that $\vec{x} \in \mathbb{R}^m$ is the discretized emissivity on an established pixel grid, where $m = N_r \cdot N_\vartheta$ and $N_{r/\vartheta}$ the number of radial and poloidal intersections of that toroidal cross-section, i.e. the two-dimensional radiation distribution in the triangular shaped bolometer plane. The geometry and transmission coefficients of the bolometer camera system are therefore given by the matrix $\tilde{\mathbf{T}} \in \mathbb{R}^{n \times m}$, with $n = N$ the number of absorbers or lines of sight. Finally, $\hat{\vec{b}} \in \mathbb{R}^n$ is the experimentally measured, or as shown in the previous chapter section 4.4.3 forward model integrated, chord brightness profile. In almost all cases, but particularly for this system, $\tilde{\mathbf{T}}$ is ill-conditioned and can not be simply inverted. Therefore, the minimization of the regularized problem in Φ for a given regularisation functional K and positive coupling regularisation factor μ between K and calculated solution \vec{x} is much more practical. We consider $T^{(i,j)} = \tilde{T}^{(i,j)} / \sigma^{(j)}$ and $\vec{b}^{(j)} = \hat{\vec{b}}^{(j)} / \sigma^{(j)}$ for measurement uncertainty weighting purposes of absorber j . As pointed out before, μ / K is used to impose *a priori* knowledge of the system or desired smoothness and features on solution \vec{x} . For $\mu \rightarrow 0$ the calculated radiation distribution is dominated by the characteristics of the measurement system, i.e. the LOS camera system geometry, while for $\mu \rightarrow \infty$ the opposite is the case and \vec{x} adheres to the given regularisation functional K .

A simple approach to a smoothing functional K is a second-order gradient minimizing regularisation using the finite-difference matrix expression for the *Laplace*¹ operator Δ .

$$\begin{aligned}
 K &= (\Delta \vec{x})^\top (\Delta \vec{x}) \\
 \mathbf{H} &= \Delta^\top \cdot \Delta \\
 \min \left[\frac{1}{2} \chi^2 + \vec{x}^\top \mathbf{H} \vec{x} \right]
 \end{aligned} \tag{5.2}$$

Minimizing this finds the (a) solution with the least curvature, i.e. the smoothest gradients, which in poloidal direction already is a good fit for the expected radiation distribution. This aspect will later play a more important role when extending the *Minimum Fisher regularisation* in section 5.1.1. One should note that equation (5.2) still has to be solved iteratively to find the best μ for a provided *best-fit* criteria for χ^2 . Such linear algorithms can and have been successfully extended and combined with many different methods, e.g. neural networks approaches[183–185].

¹Pierre-Simon (Marquis de) Laplace * Mar. 23, 1749 †Mar. 7, 1827

5.1. Minimum Fisher Regularisation

At Wendelstein 7-X, the multichannel bolometer diagnostic system performs tomography using the *Minimum Fisher regularisation* and variations thereof for constructing a regularisation functional. This method has first been tested and established by Anton et al.[186] and was used successfully with this system by Zhang et al.[106]. The *Fisher^I information* (sometimes just *information*) of a probability density distribution $g(\vec{r})$ regarding the condition of \vec{r} is given by:

$$I_F = \int \frac{1}{g(\vec{r})} \left(\frac{\partial(g(\vec{r}))}{\partial \vec{r}} \right)^2 d\vec{r} \quad (5.3)$$

The likelihood of measuring a particular value of physical quantity in \vec{r} would be described by $g(\vec{r})$. Therefore, I_F describes the amount of information such a probability distribution contains about its characteristic in \vec{r} . Assuming a distinctly peaked likelihood profile of $g(\vec{r})$, one can easily see that this method finds the quasi correct \vec{r} for this emissivity or yields the largest information at that specific \vec{r} [187]. One should note that the variance of the distribution $g(\vec{r})$, σ_g is bound by the inverse of the Fisher information or that its accuracy is limited by I_F , which is given by the *Cramér–Rao^{II} bound*:

$$\sigma_g \geq \frac{1}{I_F} .$$

In other words: the solution of the Minimum Fisher regularisation (*MFR*) with the smallest information has maximum variance and is the smoothest. Furthermore, MFR has shown a good stability and robustness towards noisy data and is more suited for similarly smooth distributions, i.e. not peaked as described above[188, 189].

The very familiar approach above, especially section 5.1 is exploited to construct a tailored method for finding a smooth but well characterised radiation distribution from the one-dimensional, line integrated bolometer measurements. The second order linear regularisation of equation (5.2) is

^ISir Ronald Aylmer Fisher, FRS * Feb. 17, 1890, †July 29, 1962

^{II}Calyampudi Radhakrishna Rao, FRS * Sep. 10, 1920; Harald Cramér * Sep. 25, 1893, †Oct. 5, 1985

modified to a weighted first order derivative functional by introducing a diagonal matrix \mathbf{W} with $W^{(i,i)} = W^{(i)}\delta_{i,j} > 0$. In the n th iterative step of the algorithm, with $\nabla_{x/y}$ the corresponding discrete vector differential operator in one dimension, $\mathbf{H}^{(n)}$ becomes:

$$\mathbf{H} \rightarrow \mathbf{H}^{(n)} = \nabla_x^\top \mathbf{W}^{(n)} \nabla_x + \nabla_y^\top \mathbf{W}^{(n)} \nabla_y . \quad (5.4)$$

Looking back at section 5.1, one can also assume that $dI_F = (g'(\vec{r}))^2/g(\vec{r}) = (\nabla g(\vec{r}))^2/g(\vec{r})$, corresponding to the originally posed first order linear regularisation with a factor of $1/g$. Therefore, the functional operator \mathbf{H} for finding g with the lowest Fisher information becomes:

$$\begin{aligned} n = 0: \quad \mathbf{W}^{(0)} &= \mathbf{1}, \rightarrow \mathbf{H}^{(0)} = \Delta^\top \cdot \Delta , \\ n \geq 1: \quad \mathbf{W}_{i,j}^{(n)} &= \begin{cases} (1/g_i^{(n-1)}) \delta_{i,j}, & g_i^{(n-1)} > 0 \\ W_{\max} \delta_{i,j}, & g_i^{(n-1)} \leq 0 \end{cases} . \end{aligned} \quad (5.5)$$

For $n = 0$, singularity is avoided by letting \mathbf{W} be the unit diagonal matrix $\mathbf{1}$ and hence \mathbf{H} become the second order linear regularisation functional. At and beyond $n \geq 1$, the inverse of in the previous step calculated distribution $g_i^{(n-1)}$ yields particular smoothness for regions of small values by adding statistical weight to their corresponding second order gradients, while for larger numbers singular local structures can be amplified. For negative $g_i^{(n-1)}$, the weights are limited by an upper limit W_{\max} that is chosen beforehand on experience with the underlying reconstruction problem. Iteration of n finds the solution to the initial problem in equation (5.1) for \vec{x} by substituting $K \rightarrow \mathbf{H}^{(n)}$ until a minimum desired χ^2 is found. Let us derive a discrete and iterative set of equations and identities that can be used for a data set \vec{b} , provided by the bolometer camera system to calculate the two-dimensional radiation distribution \vec{x} with the minimum Fisher information I_F :

$$\begin{aligned} x \rightarrow r, i \quad y \rightarrow \vartheta, j \\ \nabla_x \rightarrow \nabla_r &= \frac{1}{\Delta r} (\mathbf{D}_{\text{dia}}^{(n_\vartheta)} - \mathbf{D}_{\text{dia}}^{(0)}) \\ \nabla_y \rightarrow \widetilde{\nabla}_\vartheta &= \frac{1}{\Delta r \Delta \vartheta} (\mathbf{D}_{\text{dia}}^{(1)} - \mathbf{D}_{\text{dia}}^{(0)}) \\ \rightarrow \mathbf{H}^{(0)} &= \nabla_r^\top \mathbf{1}^{n_r \times n_\vartheta} \nabla_r + \widetilde{\nabla}_\vartheta^\top \mathbf{1}^{n_r \times n_\vartheta} \widetilde{\nabla}_\vartheta \end{aligned} \quad (5.6)$$

The above dimensions shall correspond to the commonly used notations for the cylindrical coordinate system, i.e. $\vec{r} \rightarrow (r, \vartheta)$ and their pixel and matrix indices (i, j) . The discrete vector differential in radial direction ∇_r is written as a combination of two diagonal matrices, where $\mathbf{D}_{\text{dia}}^{(k)} \in \mathbb{R}^{n_r \times n_\vartheta}$ corresponds to

$$(\mathbf{D}_{\text{dia}}^{(k)})_{q,p} = \begin{cases} \delta_{q,p-k}, & k \geq 0 \\ \delta_{q-k,p}, & k < 0 \end{cases},$$

which for $k = 0$ gives the unit matrix $\mathbf{1}^{n_r \times n_\vartheta}$. A corresponding poloidal differential operator ∇_ϑ is slightly modified by dividing with the radial bin $1/\Delta r$ to further mitigate noise along the flux surfaces in accordance to Fisher information in section 5.1. Using equation (5.6) and equation (5.1) yields an expression for the calculated radiation distribution in the $(n + 1)$ -th step:

$$\vec{x}^{(n+1)} = (\mathbf{T}^\top \mathbf{T} + \mu \mathbf{H}^{(n)})^{-1} \mathbf{T}^\top \vec{b}. \quad (5.7)$$

Computationally, the inversion $(\cdot)^{-1}$ is the most costly operation of this algorithm, though using mathematically optimized and performant applications such as *SuperLU^I*[190] makes this feasible. Iterations in n are performed until:

$$\begin{aligned} (\chi^2)^{(n)} &= (\mathbf{T}\vec{x} - \vec{b})^\top (\mathbf{T}\vec{x} - \vec{b}) \leq \chi_{\min}^2, \\ \|\vec{x}^{(n)} - \vec{x}^{(n-1)}\| &\leq \sigma_{\min}, \end{aligned} \quad (5.8)$$

where χ_{\min}^2 and σ_{\min} are threshold values for terminating the iteration process. The smaller both of these values are set to, the longer the calculation takes and theoretically the more accurate the solution in \vec{x} is according to the above, however the quality of the resulting profile is, from experience, more tied to the preparation of the input data, its noise and error level and the construction of the inversion domain. This circumstance will later be thoroughly explored when benchmarking the algorithm and setup with surrogate input radiation profiles and phantom image reconstructions in section 5.3. Finally, looking back at the initial proposition of minimizing

^Igeneral purpose library for the direct solution of large, sparse, nonsymmetric systems of linear equations (*LU factorization of matrix A in a lower triangular L and an upper triangular U, A=LU*)

the Fisher information of the solution \vec{x} with an adequate regularisation in equation (5.1), one easily finds that

$$dI_F \sim \frac{(g')^2}{g} \quad \leftrightarrow \quad \vec{x}^\top \mathbf{H} \vec{x} \propto \frac{1}{g} (\nabla g)^2$$

when identifying the probability distribution $g(\vec{r})$ with the sought after emissivity profile \vec{x} and remembering the weighting in \mathbf{H} through \mathbf{W} . The MFR can and was used successfully with the bolometer camera system at W7-X. However, different improvements perhaps have to be made to the regularisation functional weighting. Due to the nature of the diagnostic setup, the influence and behaviour of the measurement environment, i.e. the entirety of the plasma device and construction thereof, the input \mathbf{T} is rather prone to errors. Particularly the resulting tomogram in \vec{x} is very sensitive to deviations between the assumed and actual line of sight geometry, which in fact is not reflected by a larger χ^2 or σ_{\min} . Thorough evaluation of the sensitivity of both parameter coefficient matrix \mathbf{T} and resulting reconstruction to variations in the camera geometry will be performed in section 5.2. In addition to that, further exploiting *a priori* knowledge about plasma radiation distributions, especially incorporating such into equation (5.5) and deriving from that will be beneficial to the overall quality of the bolometer tomography.

5.1.1. Radially Dependent Anisotropy

Modifications to $\mathbf{H}^{(n)}$ on the basis of *radial radiation distribution anisotropy* will be made to improve the performance of the MFR in regard to extracting emissivity concentrations around X-points and magnetic islands from the bolometer measurements in the tomogram. The previous chapter in particular established their importance to the scientific challenges posed by the real time feedback experiments and the occurrence of (partial) radiation detachment. Let us write a discrete anisotropy factor $k_{\text{ani}}^{(i)}$ that applies varying weight to the poloidal differential operator $\widetilde{\nabla}_\theta$:

$$k_{\text{ani}}^{(i)} = \begin{cases} \left[\left(\tan^{-1} \left(\frac{10}{N_S} (1 - (i - N_T)) \right) + \frac{\pi}{2} \right) \times \right. \\ \left. \frac{2}{\pi} \left(k_{\text{core}} + k_{\text{edge}} \right) \right] - 1 & , k_{\text{core}} > k_{\text{edge}} \\ \left[\tan^{-1} \left(\frac{10}{N_S} (i - N_T) \right) + \frac{\pi}{2} \right] \times \\ \frac{1}{\pi} (k_{\text{edge}} - k_{\text{core}}) + k_{\text{core}} & , \text{else} \end{cases} . \quad (5.9)$$

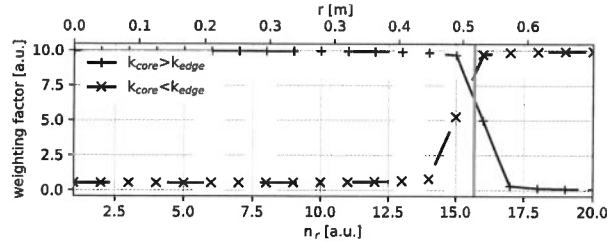


Figure 5.1.: Comparison between two radial anisotropy profiles k_{ani} for $k_{\text{core}} > k_{\text{edge}}$ and $k_{\text{core}} < k_{\text{edge}}$ each. The bottom abscissa notes the radial bin number, i.e. index and the top the corresponding radius in the $1.3V_P$ inflated cross-section. A grey line indicates the separatrix location r_a . Both lines are calculated using section 5.1.1 with $k_{\text{edge}} = 0.5$, $k_{\text{edge}} = 10$ and vice versa, $N_T = 15$ and $N_S = 2$ with a domain size of $n_r = 20$.

This representation applies for both favouring poloidal anisotropy inside and outside a threshold *target* radial bin $N_T \in [0, n_r]$. A parameter $N_S \in [1, n_r - 1]$ describes the width of the transition from smooth to anisotropic weighting and vice versa, while the values of $k_{\text{core}}, k_{\text{edge}} \geq 0$ represent the respective desired weight in those areas. Two examples for a radial representation of $k_{\text{ani}}^{(i)}$ can be found in figure 5.1, where each is derived for the same core and edge factors, as well as threshold and width parameters. The profiles are, if not within one or two bins of $N_T \pm N_S/2$, generally flat and can be assumed constant. Only around the threshold k_{ani} yields, depending on the width N_S , a more or less smooth transition between k_{core} and k_{edge} . For very small $N_S \leq 2$, a linear progression between core and edge anisotropy profile is expected.

The regularisation operator and functional can now be written as follows:

$$\begin{aligned} \mathbf{K}_{\text{ani}} &= \left(\frac{1}{k_{\text{ani}}^{(i)}} \delta_{i,j} \right)^{(i,j)} \hat{=} \frac{1}{k_{\text{ani}}} \mathbf{D}_{\text{dia}}^{(0)}, \\ \hat{\nabla}_\vartheta &= \mathbf{K}_{\text{ani}} \widetilde{\nabla}_\vartheta = \frac{1}{\Delta r \Delta \vartheta} \mathbf{K}_{\text{ani}} \left(\mathbf{D}_{\text{dia}}^{(1)} - \mathbf{D}_{\text{dia}}^{(0)} \right), \\ &\rightarrow \mathbf{H}_{\text{ani}}^{(n)} = \nabla_r^\top \mathbf{W}^{(n)} \nabla_r + \hat{\nabla}_\vartheta^\top \mathbf{W}^{(n)} \hat{\nabla}_\vartheta. \end{aligned} \quad (5.10)$$

The resulting $\mathbf{H}_{\text{ani}}^{(n)}$ differs only in an additional weight to the poloidal differential from the underlying MFR algorithm. Note that the radial operator

∇_r is not changed, since deliberately enforcing individual poloidal emissivity hotspots would inevitably reduce the robustness of the calculated results and question the credibility of the anisotropy method. It is assumed that, at least in the plasma core - read: not exclusively inside the separatrix - radiation is distributed smoothly along magnetic field lines. This way, the tomography algorithm is only allowed and not constrained to find localized structures in the radiation distribution for a given set of $(k_{\text{core}}, k_{\text{edge}}, N_T, N_S)$. This approach was also applied, particularly at W7-X by Zhang et al.[168], with the focus on a novel regularisation method that will be introduced below and used for comparison later. One should note that also Fuchs et al.[191] previously proposed a local anisotropy weighting, where there is a second set of weights introduced:

$$I_F = \int \frac{(k_{\text{ani}}^r \partial^r g(\vec{r}))^2 + (k_{\text{ani}}^\theta \partial^\theta g(\vec{r}))^2}{g(\vec{r})} d\vec{r},$$

of which the in equation (5.10) defined equations are an extension for $k_{\text{ani}}^r = 1$. One could argue that the radial variation of $k_{\text{ani}}^{(i)}$ in section 5.1.1 yields the same effect. However, this will not be further explored in this work.

5.1.2. Relative Gradient Smoothing

As noted above, Zhang et al.[106, 168] have proposed and applied another tailored reconstruction algorithm, also based on the already proven[186] Minimum Fisher regularisation, using a novel functional with relative gradient smoothing (RGS) of the iterated profile. It has been already successfully validated using simulation results by three-dimensional simulation model results for phantom radiation distributions from EMC3-EIRENE[168]. Note though that this was done for pure hydrogen plasma with dominating oxygen impurities. The idea is to modify the expression around the Fisher information I_F after which the regularizing expression \mathbf{K} is modelled.

$$\mathbf{K} \rightarrow \vec{x}^\top \mathbf{H}_{\text{RGS}} \vec{x} \propto \left(\frac{\nabla g}{g^2} \right)^2 \quad (5.11)$$

The regularizing weight in \mathbf{K} becomes the inverse square of the distribution $1/g^2$, which corresponds to the sought after emission profile. The RGS

5.2. Camera Geometry Sensitivity Towards Line of Sight Perturbations

functional matrix \mathbf{H}_{RGS} , with respect to equation (5.6) and following, now is:

$$\begin{aligned} n = 0: \quad & \mathbf{W}_{\text{RGS}}^{(0)} = , \\ n \geq 1: \quad & \mathbf{W}_{\text{RGS}}^{(n)} = \left(1/g_i^{(n)}\right)^2 , \\ & \mathbf{H}_{\text{RGS}}^{(n)} = \nabla_r^\top \mathbf{W}_{\text{RGS}}^{(n)} \nabla_r + \widetilde{\nabla}_\vartheta^\top \mathbf{W}_{\text{RGS}}^{(n)} \widetilde{\nabla}_\vartheta . \end{aligned} \quad (5.12)$$

This concludes the introduction of deliberately tailored tomographic reconstruction methods for the purpose of finding the two-dimensional emissivity distribution using the multicamera bolometer diagnostic at Wendelstein 7-X. Their respective application will be carried out later, after their sensitivity to the underlying geometry (perturbations) are thoroughly evaluated and potential errors or artefacts can be adequately assessed. Additional algorithms and comparisons thereof will not be highlighted here but have been in previous works[85, 186, 192].

5.2. Camera Geometry Sensitivity Towards Line of Sight Perturbations

One of, if not the most important aspect of a tomographic inversion with the number of absorbers $n_l \ll n_r n_\vartheta$ the number of pixels or voxels, is the accuracy and robustness of the underlying geometry coefficient input matrix $\mathbf{T} \in \mathbb{R}^{n_r \times n_\vartheta}$. Therefore, finding the local sensitivity of each LOS for a given inversion domain, i.e. size of the plasma V_P and number of radial and poloidal intersections $n_r \times n_\vartheta$, and their thorough validation through comparison, establishing limits and phantom image reconstruction shall be the first step towards sensible two-dimensional emission distributions from bolometric measurement data.

In section 2.3.2 the idea of finding the individual geometric contribution of the cameras absorbers to \mathbf{T} was schematically outlined and will now be revisited and pedantically exercised in order to build an adequate foundation for the following tomography. First one has to remind themselves that both the absorber-pinhole arrangement and the construction of the bolometer cameras are far from two-dimensional and each yield a significant toroidal extension and are only projected onto a singular plane at $\varphi_{\text{tor}} = 108^\circ$ for

sake of comprehensibility. It should be noted that the diagnostics geometry has already been presented in detail in section 2.2.3, where it was found that both VBCl/r and HBC are tilted in direction of the magnetic axis by $\sim 5^\circ$. In equation (2.1) and equation (2.27) the idea of infinitesimal absorber and aperture subdivisions as well as differential etendues was introduced. However, in practice this challenge can not be met with analytical means and has to be solved discretely. Therefore, both pinhole and detector are divided into n_A and n_M smaller fractions, respectively. Let us assume an area for tomographic inversion of V_P divided into $N_r \cdot N_\theta \cdot N_\varphi$ voxels, i.e. $1.3 V_{LCFS}$ into $30 \times 120 \times 10$ partial volumes. Let $T_M^{(i,j,k)}$ be the local sensitivity of absorber M to radiation in voxel $v^{(i,j,k)}$. With $L_{p,q}^{(i,j,k)}$ the LOS section length from differential absorber $dA_M^{(p)}$ through differential aperture $dA_A^{(q)}$ (see equation (2.26)) inside voxel $v^{(i,j,k)}$, the geometrical contribution to pixel $p^{(i,j)}$ can be written as:

$$\begin{aligned} T_M^{(i,j)} &= \sum_{k=1}^{N_\varphi} T_M^{(i,j,k)} = \sum_{k=1}^{N_\varphi} \left(\int_M L_M^{(i,j,k)} d\tilde{K}_M \right) \\ &= \sum_{k=1}^{N_\varphi} \sum_{p,q}^{n_M, n_A} L_{p,q}^{(i,j,k)} \left(\frac{\cos(\alpha) \cos(\beta)}{2\pi d^2} \right)^{(p,q)} dA_M^{(p)} dA_A^{(q)}. \end{aligned} \quad (5.13)$$

The superscript (p, q) on the fraction is used for simplicity and denotes that the incident angles α and β between LOS and face normals, as indicated in figure 2.7, as well as the distance d between the centers of $dA_M^{(p)}$ and $dA_A^{(q)}$ have to be calculated for each of the fractional absorber and aperture. The resulting *etendue* $\mathbf{T}_M^{(i,j)}$ for pixel $p^{(i,j)}$ is in units of [m^3] and corresponds to the partial volume of a LOS cone created by projection of absorber M through its respective pinhole.

5.2.1. Absorber and Aperture Segmentation

The first challenge is to find and verify the etendues for all bolometer detectors. Two common segmentation methods for dividing the absorbers and apertures into $N \in \{2, 4, 8\}$ parts are presented in figure 5.2. A comparison shows the varying location of the face (area) center and size of the individual subdivisions for an exemplary object, i.e. pinhole or detector in a stylised perspective. On the left, a rectangular interpolation is shown next

5.2. Camera Geometry Sensitivity Towards Line of Sight Perturbations

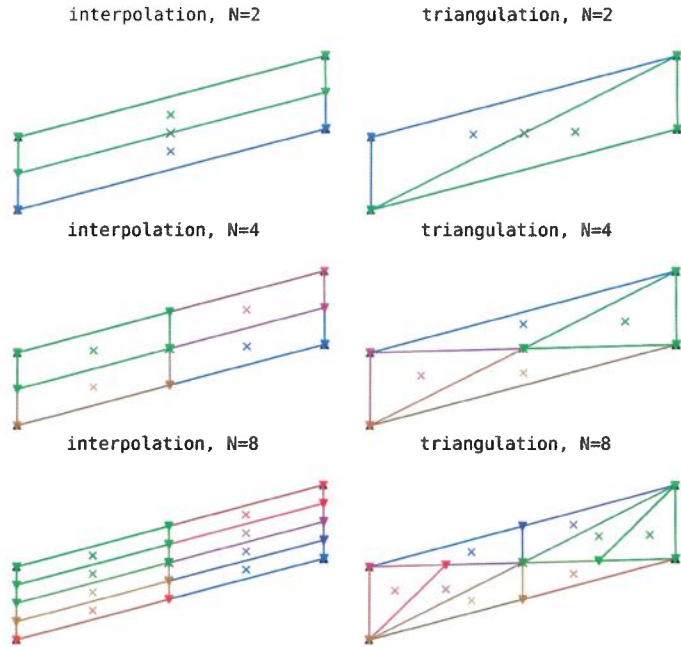


Figure 5.2.: Example for variations of subdividing the individual detectors and apertures with increasing number of compartments. Shown on the left is a method of rectangular splitting, on the right using a simple triangulation procedure for $N \in \{2, 4, 8\}$ the number of compartments. Each individual subcompartment is coloured differently.

to a common *Delaunay*^I triangulation on the right. Resulting subdivisions of the interpolation are constructed by dividing the longer and shorter - if applicable - sides of the respective face alternatingly m times in that order, which yields $N = 2^m$, $m \in \mathbb{N}$ parts. The triangulation is done using built-in functions for such Delaunay algorithms, e.g. Python's *SciPy*^{II} toolkit, limited to the same amount of segmentations as on the left for sake of comparability. Simply put, this method finds the set of triangles for a given set of discrete points \mathbf{P} inside its corresponding *convex hull*^{III} where no circumcircle of any triangle contains another point of \mathbf{P} , while a maximum of all individual

^IBoris Nikolajewitsch Delone * Mar. 15, 1890 †Jul. 17, 1980

^{II}a collection of mathematical algorithms and functions built on the NumPy extension

^{III}or convex envelope of a shape is the smallest convex set that contains it entirely

minimum angles of those triangles is achieved. The presented rectangular interpolation finds N parts of same size and shape for a given splitting of m times. However, the segmented face centres are spread rather unevenly with respect to the full absorber or pinhole, which similarly affects the set of (α, β, d) . For a triangulation of $N \geq 4$, which is a common setting, those are spread more uniformly, while $dA_X^{(i)}$ is not necessarily constant. A homogeneous distribution though is expected to yield a more accurate result due to the previously discussed locally varying transmission between aperture and pinhole in figure 2.8 and equation (2.1). equation (5.13) only computes the etendue for each fractional detector and pinhole combination once based on the individual differential area center, hence the accuracy of \mathbf{T} is assumed to benefit from a diversified segmentation, which in fact will be verified below. Based off of those splitting methods, comparisons in LOS geometry, etendues, volumes and finally sensitivity matrices will be performed.

In figure 5.3 a visual comparison between different segmentation resolutions and their three-dimensional coverage is shown for a typical $1.3V_P$ inflated equilibrium flux surface domain with toroidal expansion. The left image (a) shows the impact of dividing both pinhole and detector into two and eight parts respectively, while projecting the different lines constructed through the individual center and corner points onto the opposite side of the torus. They form a trapezoidal polyeder whose convex hull is illustrated as a cone using different colours. Both of the red boxes are achieved by finding the full extension of the LOS from the noted absorbers and corresponding aperture, i.e. tracing each corner of the detector face through any from the pinhole onto the enclosing plane and finding their convex hull, which takes also the lowest transmissible areas or geometry of the etendue into account - see figure 2.8. An infinitesimal splitting finds the full transmission for this construct, while one has to keep in mind that this theoretically takes $\geq 2N^2 \cdot n_\varphi n_r n_\vartheta$ iterations to find $L_{p,q}^{(i,j,k)}$ the intersection of LOS and voxel without prior knowledge about its geometry. For $N \rightarrow 10^3$ this alone requires 3.6×10^9 operations, which justifies the reduction of number of segments to eight each in this case. One immediately finds that splitting both absorber and aperture into eight segments each (green) yields a significantly improved coverage of the full LOS cone compared to $N = 2$ (blue). The latter has a spatial discrepancy to the enclosing projection at the opposite of the torus of $> d\varphi d\vartheta r_a$, while for $N = 8$ this is reduced to $< 1/2 d\varphi d\vartheta r_a$. Since the depicted channels are

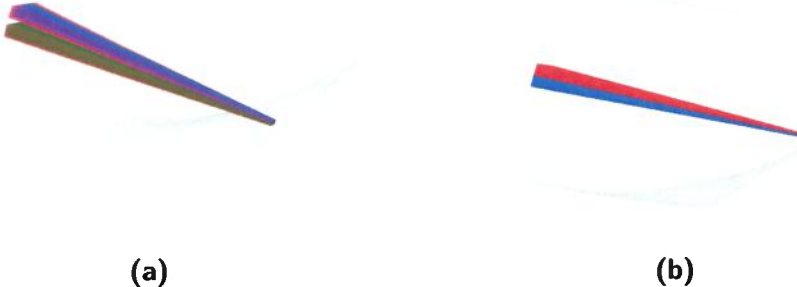


Figure 5.3.: (a) Comparison for example LOS cones for channel 14 and 16 of the HBC with rectangular splitting at (blue) $N = 2$ and (green) $N = 8$ for both the detector and pinhole. Shown in both cases is the *full* LOS cone in red, created by projecting detector corners through respective opposite side corners of the pinhole, and the sum of the individual N^2 cones from the center of the detector elements through the corners of the pinhole rectangles in a different colour. **(b)** Line of sight cones from $N = 8$ split detectors and pinholes of neighbouring channels 15 and 16 of the HBC in red and blue. In both images, all of it is enclosed by a grey mesh, representing the previously introduced $1.3V_P$ hull of the extrapolated magnetic flux surfaces, wherein the LOS cones are defined and their volume calculated.

14 and 16, which are positioned almost perfectly symmetrical around the center detector and camera axis, it is assumed that this visual approach and conclusion are adequately supported. The left figure 5.3:(b) shows neighbouring LOS cones of channel 15 and 16 for $N = 8$. No gap is found between them, while they also do not cover the same volume twice or overlap at any point. In fact, in figure 2.22 one can already see that the poloidal LOS coverage in the plane of the bolometer, for a set of $n_r = 30$ and $n_\theta = 150$ at $N = 8$, particularly from the HBC is very good and features no local voids or irregularities. Only the fan of the first five VBCI detectors, towards the outboard side over the magnetic axis, indicates a one pixel wide gap from $0.75r_a$ to the boundary of the mesh. However, this area is entirely viewed by the horizontal camera. One remembers that the systems spatial resolution at the magnetic axis is 5 cm, which is in agreement with this assessment of the LOS cones.

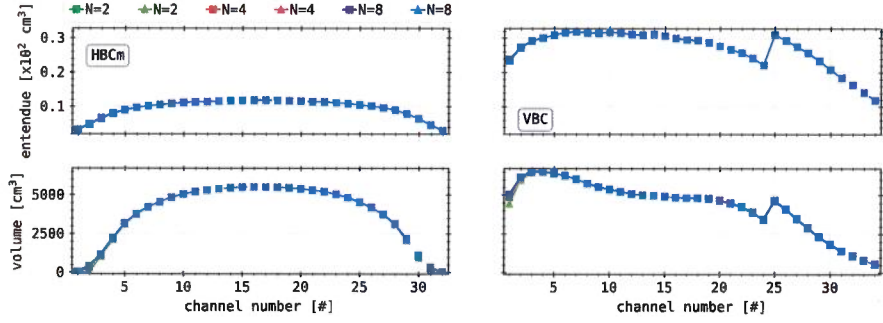


Figure 5.4.: Collection of etendues and LOS cone volumes of all bolometer camera channels for varying interpolation methods and amounts. The left images include the HBC, while the right shows channels from the VBC, which is made up out of the left and right sub-array with individual pinholes. Rectangular interpolation results are depicted with squares, triangulation results with triangles and different colours for $N = \{2, 4, 8\}$. The top images show the collective etendue per channel and the lower display the total LOS volume.

Figure 5.4 presents the impact of varying segmentation methods and N on the integrated LOS etendues and cone volumes. In figure 2.20, the commonly used V_M and K_M have been shown, which are produced for the same set of $N = 8$ and $n_r, n_\theta, n_\varphi = 30, 150, 10$, using a triangulating pinhole and absorber segmentation. The values of V_M are calculated, as described above for the full expansion cone, by tracing all of the individual sub-absorbers center through the corners of each pinhole fraction, constructing their convex hull and finding its volume. Equation 5.13 and following already generally describes how the individual channels sensitivity is computed, while K_M is just the sum over all pixels of $\mathbf{T}_M^{(i,j)}$. Overall, both segmentation methods and all degrees of refinement are qualitatively in very good agreement with each other. In this plot, differences are almost not noticeable, besides deviations in LOS volume of the outermost HBC and inboard VBCI channels for a triangulation of $N = \{2, 4\}$. Those discrepancies are small compared to their respective maximum, however at the lower V_M they become non-negligible, which therefore requires a triangulation of $N \geq 5$ for validity. The previously noted - see section 4.4.3 - minor asymmetry in the HBC detector arrays geometry can not be seen here, although a much more thorough evaluation

5.2. Camera Geometry Sensitivity Towards Line of Sight Perturbations

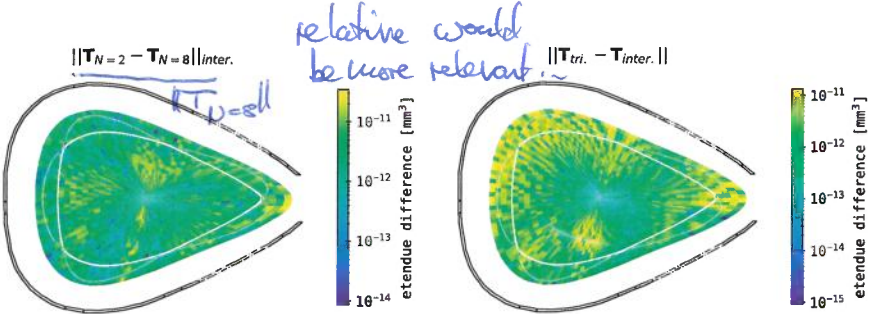


Figure 5.5.: Comparison between the total etendue or local sensitivity of the LOS system of the bolometer for different interpolation resolutions and methods. For both, the absolute logarithmic value of the difference between the sensitivities is plotted on the respective mesh grid that has been used to calculate the etendues. A Poincaré plot for the associated magnetic field is superimposed, showing the last closed flux surface and enclosing magnetic islands at that toroidal location. This is enclosed by a cut through the first machine wall. The left image shows the difference between $N = 2$ and $N = 8$ rectangular interpolations, while the right similarly displays the contrast between the prior and triangulations of the same resolution.

of the camera constructions impact on \mathbf{T} will be done further below. Finally, figure 5.5 shows the variation between individual pixel distributions of \mathbf{T} for different refinements and segmentation methods for the same grid mesh as introduced for figure 2.22 of all bolometer camera arrays combined. The left figure presents the absolute difference on a logarithmic scale between $N = 2$ and $N = 8$ for a rectangular subdivision across the inversion domain. Centred around the magnetic axis, structures of higher and lower absolute deviations alternate in poloidal direction and extend as far as the boundary. In certain areas, e.g. the top and outboard side, those rays are interrupted by areas of randomly distributed values which also feature $\Delta K_M \sim 0$. The most prominent parts in this plot are the areas of higher discrepancy in the center towards the inboard island and along the edge of the VBCI array, from the lower side across the magnetic axis towards the top of the triangular plane, as well as the intersecting darker lines. With respect to the integrated etendue and LOS volume per channel with an order of magnitude of $\sim 10^{-10}$ – 10^{-14} mm^3 , a variance of 0.5×10^{-10} – 10^{-14} mm^3 is of no

importance to the initial challenge of tomographic reconstruction of bolometer measurements. Looking back at the central MFR iterative expression for the radiation profile $x^{(n)}$ in equation (5.7), a variation of 10^{-11} mm^3 in \mathbf{T} becomes negligible when evaluating the inversion since the condition of this expression is no longer only dominated by the geometry matrix. Particularly, assuming the variation or perturbation to \mathbf{T} , $\Delta\mathbf{T}$ be structured and not infinitesimal, which is very much true for this example, Ghaoui et al.[193] find that the error in the inversion is limited by the product of condition and euclidean norm $\kappa(\Delta\mathbf{T}) \cdot (\|\Delta\mathbf{T}\| / \|\mathbf{T}\|)$. Since $\kappa(\Delta\mathbf{T})$ is in fact potentially large but its norm significantly smaller, this upper limit underlines that such a difference in local sensitivity, i.e. variations in N correspond to perturbations of appropriate dimension and do not catastrophically change the results in $x^{(n)}$. Looking at the right plot in figure 5.5, which shows the difference between triangulation and rectangular subdivision at $N = 8$, one finds a very similarly looking and scaled image. However, the previously noted structures along the VBCI are far more extended and wrap along the separatrix towards the inboard side and enclose the areas of lower variations. Variations in colour can be attributed to its changed range of $10^{-11} \text{ e} - 15$. The same arguments as above towards the impact of changing between those segmentation methods on the reconstruction apply here as well.

So far it has been established that the segmentation of aperture and absorber and therefore finding a discrete, pixel or voxel based representation of the geometry coefficient matrix \mathbf{T} containing the etendues of all individual bolometer camera channels is adequately achieved by either triangulation or rectangular splitting with a resulting number of subdivisions $N > 4$, given a common setting of reconstruction grid expansion and refinement (i.e. $1.3 \times 150 \times 20 \times 10$, see above). From here on, we will assume that any given etendue, LOS volume or results derived therefrom are computed using a detector and pinhole triangulation with $N = 8$.

5.2.2. Line-of-Sight Geometry Perturbations

In the following paragraphs, a variation of perturbations to the presented geometry in section 2.2.3 and its effect on the corresponding parameter coefficient matrix \mathbf{T} in figure 2.22 will be discussed. This is done to test the robustness of the outlined approach to deviations in the designed construc-

5.2. Camera Geometry Sensitivity Towards Line of Sight Perturbations

tion and investigate upon the minor asymmetry in the forward calculated chord brightness profile from the otherwise ideally symmetrical STRAHL radiation distribution.

Centered Aperture and Camera Array

In a complex and large machine that experiences strong thermal effects during preparation and experiments such as Wendelstein 7-X, changes in the actual geometry of the diagnostic in comparison to the initially proposed design are not uncommon and in fact expected. Furthermore, this potential displacement is not constant either and can vary over multiple experimental campaigns. Hence, an automated, robotic, high precision location measurement of all pinholes for HBC and VBCI/r was conducted before the very first plasma and after the last experimental campaign OP1.2b. The provided benchmark data revealed that the HBC camera aperture, i.e. its *barycentre*, is displaced off the center of the machines vertical axis, which ideally is aligned also with the magnetic axis, by a few millimetres at $\vec{r} = \{-1.99\text{ m}, 6.152\text{ m}, -1.735\text{ mm}\}$. The LOS geometry of the HBCm is assumed to be symmetrical and cover the plasma area evenly, thus potentially introducing a significant perturbation by this shift to the inversion. Hence, a first test of the robustness of T is conducted by finding a hypothetical, centred at $z = 0$ horizontal camera that otherwise has the same geometry as the original HBC. Corresponding parameters and forward model chord brightness profiles are compiled accordingly.

A comparison between the original and shifted geometry with respect to the viewed plasma volume, as well as its impact on the local sensitivity in the triangular plane is shown in figure 5.5. The left set of red LOS rays is produced by tracing from the center of the detector through the center of the respective aperture. In this case, the new pinhole is constructed by shifting its center to $z = 0$ and tilting it so that its face normal points towards $\{0, 0, 0\}$. A resulting rotation and transposition between this and the original aperture is similarly applied to each detector of the horizontal camera array. The minor differences between the black and red LOS are, as expected, constant across the fan. Variations in etendue between the shifted and as-designed HBC on the right are roughly of same order of magnitude as the previous comparisons for selected segmentation methods in figure 5.5. However, its distribution is aligned with the orientation and geometry of the

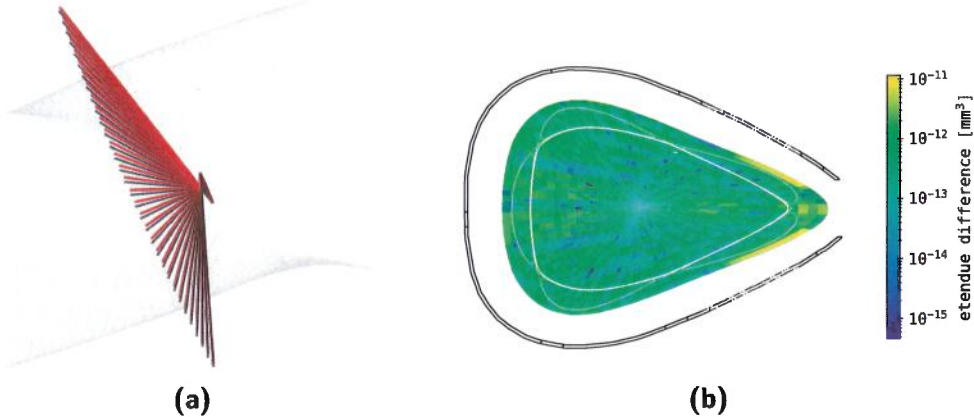


Figure 5.6.: (a) Comparison of center LOS of the (black) original HBC geometry and an adjusted (red) geometry, where the pinhole and respective camera array have been centred around $z = 0$, the vertical dimension of the W7-X coordinate system. (b) Impact of the geometry changes in (a) to the collective etendues of the horizontal bolometer camera, calculated and portrayed as in figure 5.5.

fan and features up-down symmetric, alternating structures in level of perturbation. They are approximately three LOS wide and each is intersected by single-pixel thick lines of lower ΔT in horizontal direction. In-between those bundles are individual LOS that have similarly reduced values, which again are bounded by single pixels of comparable variation. This is repeated in both directions towards the boundary of the evaluation domain, i.e. the edge of $1.3V_P$. Less prominent are underlying areas of slightly higher and lower variance, alternating in poloidal direction, with greater ΔT in front of the pinhole and on the opposite, inboard side. The largest discrepancy between the original and hypothetical camera geometry coefficients can be found on both sides, closest to the aperture, along the edge of the reconstruction area and inboard magnetic islands.

Based off of the results in figure 5.6 and the approach presented in equation (4.19) and following, one can easily now evaluate the impact of said displacement to the chord brightness profiles measured by the horizontal bolometer. Using the same STRAHL results that have been discussed in section 4.4, i.e. poloidally symmetrical radiation distributions and the new geometry coefficients T for a centred and upright HBC pinhole, this is

5.2. Camera Geometry Sensitivity Towards Line of Sight Perturbations

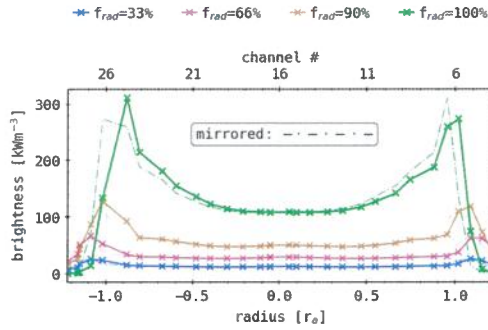


Figure 5.7.: Forward integrated chord brightness for the HBC at different f_{rad} for previously presented STRAHL results in figure 4.51 using the adjusted, hypothetical camera geometry from figure 5.6.

achieved in figure 5.7. As before, this image features a semi-transparent mirror image of the corresponding other half of the profile superimposed on each side for all radiation fraction levels. It has already been established that the original geometry yields asymmetric results, which is also very clearly true for this hypothetical camera arrangement. In fact, in direct comparison to the initial $\sim 2\text{--}5 \text{ kW/m}^3$ difference between the measured brightness along the separatrix before, the variation around $\pm r_a$ is significantly increased. For all f_{rad} , the profile is not only different at its peak around the LCFS but also at the center. At 100% radiation fraction, the brightness is shifted towards $r = 0$ and about 30 kW/m^3 higher on the lower side than on the top, i.e. $+1.0r_a$. This shift and increase can be found for all lower f_{rad} , however at a correspondingly smaller level. In contrast to figure 4.51, the two local maxima around the separatrix differ also qualitatively, where the lower side peak is very sharp, and the other is more akin to the previous shape. The portrayed changes to the camera geometry have shown to yield no more symmetric forward modelling results than the corresponding original LOS. This particular hypothetical generally yields a greater level of discrepancy between each channel and its respective counterpart than is the case for an unperturbed HBC. Therefore, the initial asymmetry in chord brightness can not be attributed to this deviation and not be corrected by its resulting transformation. However, this perturbation to the etendue coefficients in \mathbf{T} has produced large changes in the brightness profiles and thereby underlined

the importance of camera geometry towards the experimental measurements and the tomographic reconstruction's adequacy.

→ we can use this to connect with a view E profile (small plasmas)

Unilateral Camera Array Mirroring

A second variation to the horizontal camera is constructed by applying a rotation and transposition to one half of the array, i.e. channels 16 through 32 that adjusts their geometry to be in one plane with the remaining detectors and a mirror image of their counterpart. This hypothetical *mirror* (plane) would be one that is spanned by the normal of the LOS fan and the direction of channel no.15. The transformation is constructed so that the new location and orientation of absorber no.32 is equal to that of no.1, rotated by the opening angle of the camera 53° . Similarly, channel no.31 becomes the mirror opposite of no.2, rotated by $53^\circ - \angle(L\vec{O}S(1), L\vec{O}S(2))$ and so on. Resulting deviations to the original geometry are so small that a three-dimensional representation like in figure 5.6 yields no visible distinction between the two. Hence, figure 5.8 shows the etendue variation and the forward model integrated chord brightness profiles, again as in figure 4.51 for increasing levels of f_{rad} for this proposed adjustment to \mathbf{T} . The change in local sensitivity is, as instructed above, limited to the upper half of the camera array, while it is two orders of magnitude lower than before at $<10^{-13} \text{ mm}^{-3}$. No particular features akin to the structure of the LOS fan can be found here, while there is again a more prominent area of increased ΔT closer to the aperture and inboard magnetic island.

The chord brightness profiles for varying f_{rad} on the right of figure 5.8 are constructed the same way as before. With respect to the initial results, a decrease in variance between left and right half of the plot can be noted when inspecting the corresponding mirrored, semi-transparent lines. However, this minuscule deviation in the range of 0.5 – 1% is found in profiles produced from both intrinsically symmetrical camera geometry and radiation distributions. All possible sources of asymmetry besides the toroidal extension of the array have been eliminated in order to produce this plot. Therefore, one has to conclude that at least some level of asymmetry in previously and hereafter measured or forward integrated HBC profiles is due to the tilt of the LOS fan of 68.75° . Furthermore, the difference between this chord brightness profile and the initial results using the original geometry from figure 4.51 hence is dominated by the variation among the individual

5.2. Camera Geometry Sensitivity Towards Line of Sight Perturbations

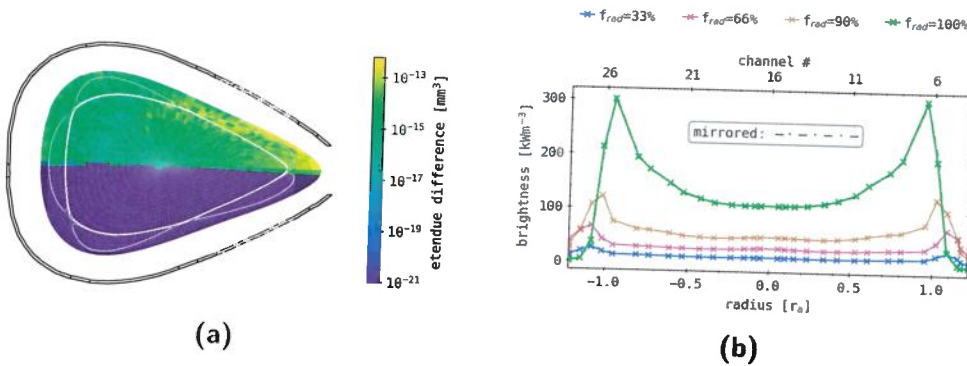


Figure 5.8.: (a) Impact of geometry changes on the collective etendues of the horizontal camera, where one half (*upper*) of the camera array has been rotated so that all channels lie in one plane and each is the exact mirror opposite - the *mirror* being a plane defined by the camera aperture normal, perpendicular to the LOS fan - of one from the other half. (b) Forward integrated chord brightness for the HBC at different f_{rad} for previously presented STRAHL results in figure 4.51 using the hypothetical camera geometry from (a).

horizontal camera LOS.

The evaluation of this perturbation in \mathbf{T} is concluded by underlining the fact that a change of this magnitude, i.e. 10^{-2} times smaller than the variability of different segmentation methods, yields almost no variation in forward calculation.

Upright and Virtual Horizontal Bolometer Camera

An obvious continuation of the previous geometric variation is to not only correct the intrinsic rotation within the as-designed HBCm camera array, but to extend the transposition of figure 5.6 to $z = 0$ with a rotation of the entire LOS fan into an upright orientation. The resulting artificial projections in red are shown in figure 5.9 in comparison next to the original horizontal camera in black. In addition to the shift of aperture and detector assembly to be centred around the horizontal axis of the machine, both are rotated individually into an equally perpendicular position to the latter. The new, centred fan, constructed by adjusting each absorber-pinhole trace into one plane - see the previous geometric perturbation above -, is rotated

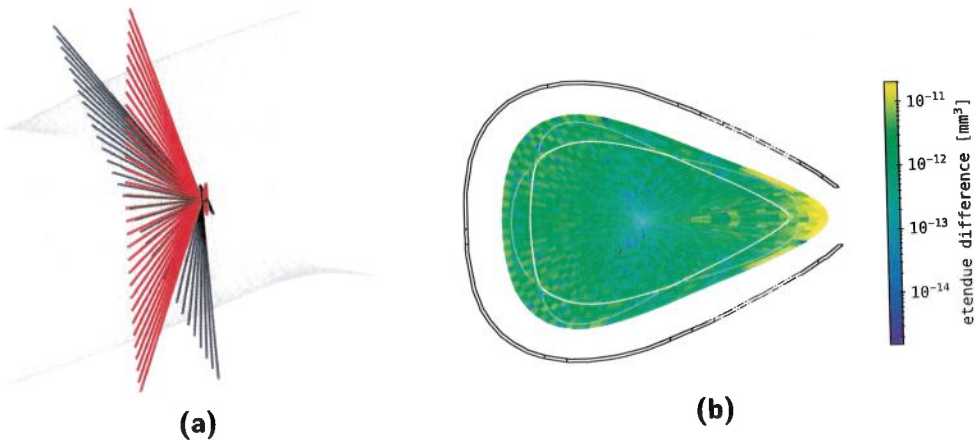


Figure 5.9.: (a) Comparison of the (black) original HBC LOS fan and (red) changed geometry, where the entire camera array has been rotated so that all channels lie in one plane that is vertically upright and centred around $z = 0$, the vertical dimension of the W7-X coordinate system. **(b)** Impact of the geometry changes in (a) to the collective etendues of the horizontal camera.

so that their two-dimensional projections in (x, y) are pointing towards $\{0, 0\}$. The aperture is also rotated into a position where its longer side, i.e. in direction of the detector array, is now also upright. Effectively, only a small transposition and rotation around the axis between pinhole center and device origin have been done and the size of the absorbers themselves, their nearest neighbour distance and respective position within the camera were not altered.

The right plot in figure 5.9 yields a level of perturbation similar to earlier at up to 10^{-11} mm^{-3} , with similar structures and distribution as in figure 5.5. Areas of lower error and variation around the magnetic axis between the upper and lower, center X-points are enveloped by largely homogenous deviation around $0.5 \times 10^{-12} \text{ mm}^{-3}$. Within both are individual pixels where the etendue difference is orders of magnitude smaller, distributed however with no recognizable pattern. The largest change in local sensitivity can be found, again, right in front of the aperture at the tip of the triangular plane and around the outboard magnetic islands.

Consistent with the earlier geometric evaluations, the forward model integ-

5.2. Camera Geometry Sensitivity Towards Line of Sight Perturbations

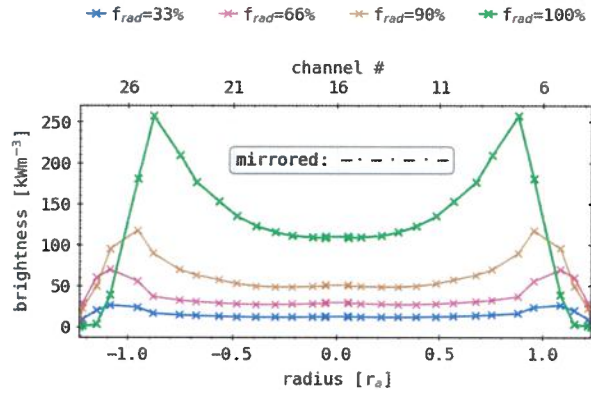


Figure 5.10.: Forward integrated chord brightness for the HBC at different f_{rad} for previously presented STRAHL results in figure 4.51, using the theoretical camera geometry of figure 5.9.

rated chord brightness for the STRAHL profiles from section 4.4 for varying levels of f_{rad} is calculated and presented in figure 5.11. This plot is perfectly symmetric across all radiation fractions around $r = 0$, underlined by no visible, semi-transparent mirror lines on either side. With respect to the initial results, the peak brightness for $f_{\text{rad}} = 1$ is increased to 260 kW/m^3 and significantly more localized. Furthermore, all lower levels of radiation and their maxima in particular are shifted towards the separatrix and further inside. Otherwise, the shown profiles are qualitatively very similar to the ones before.

An obvious continuation of the above geometric adjustment is to construct a pseudo artificial horizontal camera array that has absolutely no variations among its absorbers and their LOS. The attribute *pseudo* refers to this geometries' detector construction that is created by averaging size, shape and distance in-between the original HBCm absorbers that is therefore repeated 32 times to create this hypothetical device. This new, upright, centred, machine coordinate origin oriented camera with equidistant, equally sized detectors viewing the plasma through a parallel, centred aperture is also used to forward integrate the previous STRAHL results and find their respective chord brightness profiles. A plot for the varying radiation fraction levels $f_{\text{rad}} = 0.33, \dots, 1.0$ is accompanied by a two-dimensional deviation map in the triangular plane between this new geometries and the actual

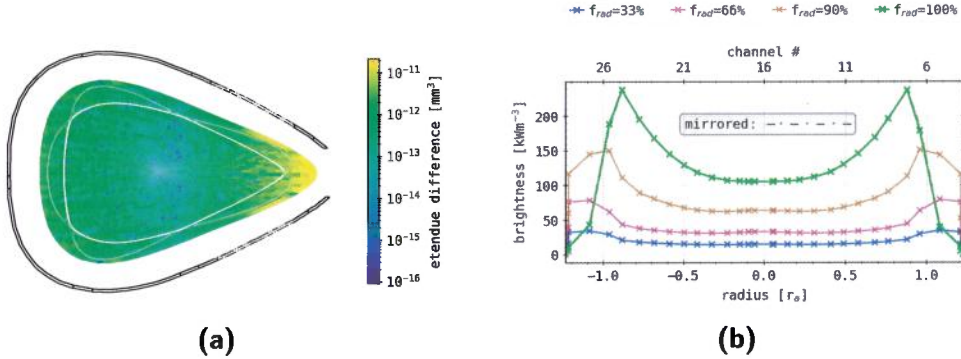


Figure 5.11.: (a) Impact on the collective etendues of the horizontal camera, where the entire array has been replaced by an artificial, symmetrical, vertically upright LOS fan with equidistant channels around $z = 0$, the vertical dimension of the W7-X coordinate system. The LOS geometry is similar to the one presented in figure 5.9. **(b)** Forward integrated chord brightness at different f_{rad} for previously presented STRAHL results in figure 4.51, using the camera geometry of (a).

local sensitivity in figure 5.11.

With respect to the previous analysis of perturbations in etendue in figure 5.9, this image presents similar magnitudes $\sim 10^{-11}\text{--}10^{-16} \text{ mm}^{-3}$ and comparable local maxima at the outboard side, closest to the pinhole of the artificial camera. Individual pixel artefacts can also be found here, though the poloidal structuring from before is far weaker and the characteristic of separate LOS can be noticed, originating at the aperture beyond the tip of the triangular domain. The also perfectly symmetric chord brightness profile on the right for $f_{\text{rad}} = 1$ is very akin to the one before, though with a slightly reduced maximum of 240 kW/m^3 . At lower radiation fractions, the intensity of the local extremes are significantly increased by up to 50% while also being further outside or even remaining beyond the separatrix. The overall shape however is still very similar.

A planar correction and rotation of the original HBCm geometry provided fully symmetrical forward model integrated measurements without significant qualitative discrepancies to those produced by the underlying camera. The change in local sensitivity between that and this particular hypothetical array is of same order of magnitude as the differences created by varying

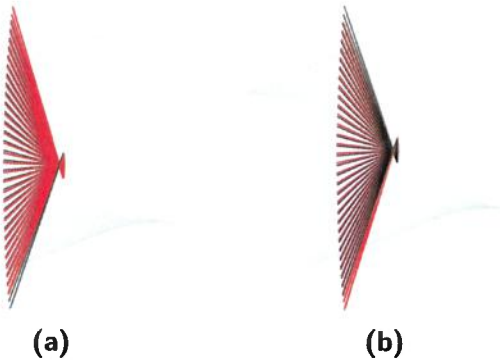


Figure 5.12.: (a), (b) Comparison of the (black) vertically upright and $z = 0$ centred (hypothetical) HBC LOS fan - see figure 5.9 - and (red) a (a) -2° (upward) and (b) $+2^\circ$ (downward) respectively tilted geometry, where the array has been rotated around the normal of the LOS plane.

detector and pinhole segmentation methods. A fully artificial horizontal camera that is achieved without any perturbation in orientation or detector construction also yields similarly symmetrical forward chord brightness profiles from STRAHL results for comparable etendue variations. On one hand, such small changes in \mathbf{T} have the potential to significantly change the measurements and hence any thereon based reconstructions, while on the other the as-designed local sensitivity of the horizontal bolometer camera is proven to be very close to a theoretical, ideal geometry.

Aperture Displacement

As it was already mentioned above, the entire machine and therefore also the integrated bolometer multicamera system is subject to large scale thermal drifts and mechanical stresses, i.e. cooling, vacuum pumping and the high temperature experiments themselves, which inevitably impact their geometry. Before the very first plasma and after the last experiment in operation phase OP1.2b, during which the measurement results presented in this work were produced, such an automated, high precision measurement of the position of all HBC and VBCl/r pinholes was conducted. There it was found that, with respect to the original design and first position measurement before the first discharge at W7-X, the system showed a displacement of 0.5–1.5 mm for the individual corners of the apertures. This particular shift yields a

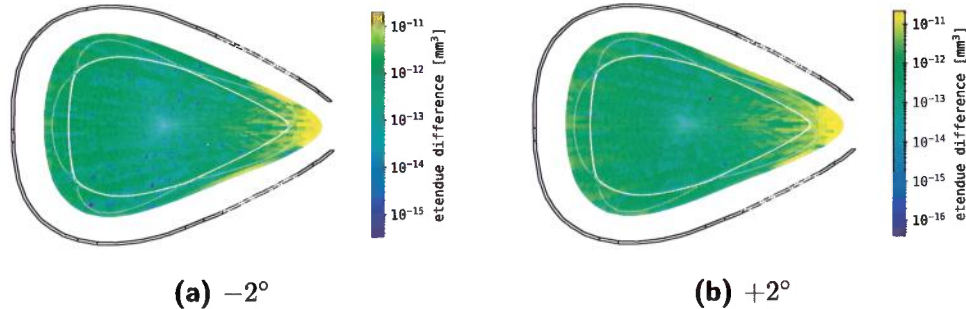


Figure 5.13.: (a), (b) Impact on the collective etendues of the horizontal bolometer camera for the theoretical geometries shown in figure 5.12, likewise respectively for (a) -2° and (b) $+2^\circ$ tilts.

downward - towards the lower side within the plane of the bolometer LOS fan - tilt of the camera of 2° . The absorber array is, due to the design of the bolometer, presumed to share the same displacement, though no equivalent estimation for their shift is available. Since there exist no additional information regarding the bolometer LOS perturbation, this deviation is assumed to neither be constant during an experimental campaign nor across the past operation and construction phases. A variation to the camera geometry of this order of magnitude was already performed when examining the local sensitivity of a vertically centred and aligned detector array. This most recent positional benchmark is of course taken into account for all prior and following calculations, however evaluating potential additional shifts during or in-between campaigns is crucial towards assessing the plausibility of experimental data reconstructions. Hence, a randomized transposition in the range of 0.5–1.5 mm is applied to the fully symmetrical, artificial LOS geometry that was achieved in the previous section. Two limiting cases, where this perturbation method yields $\pm 2^\circ$ tilt, i.e. in upward or downward direction of the fan, were chosen to gauge the impact of this error to the local sensitivity. For sake of comprehensibility, this will again only be examined in detail here for the HBCm, while the effect of disassociated forward integration and reconstruction camera geometries for phantom tomograms will be investigated upon later. The two upright and tilted LOS fans, based on the results in figure 5.9, are shown in figure 5.12 in a similar way as before. The respective variation in local sensitivity for the above set of hypothetical

5.2. Camera Geometry Sensitivity Towards Line of Sight Perturbations

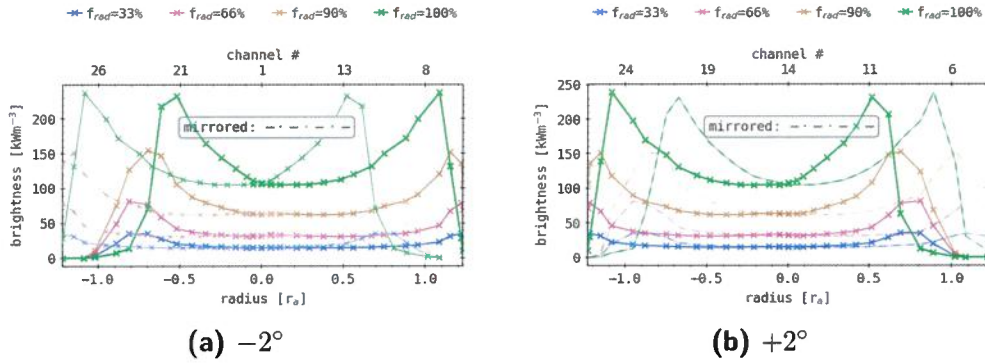


Figure 5.14.: (a), (b) Forward integrated chord brightness at different f_{rad} for previously presented STRAHL results in figure 4.51, using the theoretical geometries of figure 5.12, likewise for (a) -2° and (b) $+2^\circ$ tilts.

geometries can be found in figure 5.14. Compared to the previous differences in etendue in figure 5.11, similar structures of same order of magnitude are featured in this plot for both sets of lines-of-sight. At a misalignment angle of $+2^\circ$, the distribution appears slightly smoother, with smaller and less pronounced areas of decreased discrepancy, while the absolute range is insignificantly extended to $10^{-11}\text{--}10^{-16}\text{ mm}^{-3}$. Individual channels and their variation can be noted in the pixelated plot, though no particular features that underline the, from this perspective poloidal nature of the perturbation are noticeable. Again, the largest differences appear in front of the aperture and along the separatrix and domain boundary on the top and bottom. On the left, for a tilt of -2° , the same holds generally true, while the spectrum in etendue is slightly smaller at $10^{-11}\text{--}10^{-15}\text{ mm}^{-3}$ and a stronger, more contrasting local minimum is found around the magnetic axis and towards the middle upper and lower X-points. Singular and separate pixels of significantly decreased variance appear more frequently and with lower values here than on the right, while the maximum is again at the tip of the triangular plane. One should note that, despite the tilt in poloidal direction, there appears no gap in coverage of the reconstruction domain, i.e. the area of $1.3V_p$ by the newly constructed cameras.

Similar to the previous analysis, both of the presented LOS geometries and their corresponding parameter coefficients are used to forward model integ-

rate the chord brightness from STRAHL results in section 4.4. However, in order to assess the impact of this specific misalignment to a measurement that is performed under the assumption of a different geometry, one has to consider the results using the ideally upright, centred and symmetrical LOS fan of figure 5.9 in this case. The profiles in figure 5.14 are calculated with the new coefficients, while being presented using the information of the symmetric geometry - the abscissa of individual LOS radii is given by the prior geometries traces through the mesh, see equation (2.28). Both $\pm 2^\circ$ show significant lateral shifts towards (a) upper and (b) lower side of the separatrix, i.e. $\pm r_a$. While the relative position and height of the individual lines and local extremes for all levels of f_{rad} stay the same, the (a) left and (b) right part of the profiles are compressed, while the rest is shifted in the opposite direction. The relocated local maxima for $f_{\text{rad}} = 1$ have been moved from $\pm 0.9r_a$ to $\pm 0.5r_a$ - the other plots show a similar behaviour, underlined by the semi-transparent, mirrored lines in both images for all radiation fractions.

These results clearly show the importance of congruent measurement or forward calculation and reconstruction camera geometries. In this scenario - arguably the worst case -, an intrinsically and fully symmetrical emissivity distribution yields highly asymmetrical and radially transposed chord brightness profiles. An inversion performed under this premise, which will be explored in more detail in section 5.3, is badly pre-conditioned since the regularisation functional, see section 5.1, that does and can not account for this order of magnitude discrepancy. Later it will be found that tomography for misalignment geometries will not be able to find plausible radiation distributions, produce misleading results or even artefacts. It is of significance however to understand such effects and their impact for later experimental data reconstructions where no in-situ information on the actual LOS geometry or perturbation thereof is available.

5.2.3. Additional Artificial Camera Arrays

Upon investigation of possible LOS and camera geometry perturbations and their impact on the local sensitivity a forward model line-integrated measurements, the question of benefiting the tomographic inversions with additional, hypothetical and tailored detector arrays arose. This is largely motivated by the observed discrepancies during reconstructions of experi-

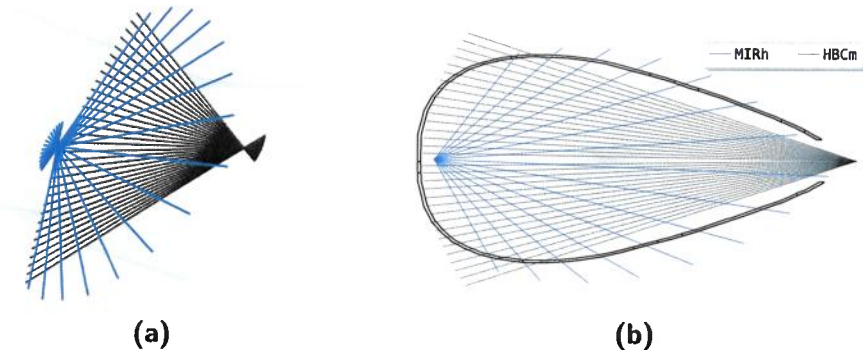


Figure 5.15.: (a) Comparison of the (black) horizontal bolometer camera LOS geometry and an artificial, *new* camera ("MIRh", blue) that is arranged opposite of the prior, spanning 15 new channels that cover the full torus cross-section homogeneously. **(b)** Same geometry comparison in projection of the toroidal plane of the bolometer camera assembly, i.e. $\varphi_{\text{tor}} = 108^\circ$.

mental data, which will be performed later in this chapter. While trying to find plausible radiation distributions that are in agreement with other diagnostics and intrinsically coherent, i.e. a temporal sequence of tomographic images shows comprehensible results, more cameras in particular locations were presumed to greatly improve upon their quality. Therefore, two sets of absorbers located opposite of the existing cameras were designed. One on the inboard side viewing the inside magnetic islands and X-points and one at the top of the triangular plane, viewing along the separatrix towards the outboard side and also the inboard island, both limited to fifteen LOS each.

Horizontally Mirrored Camera

The first new, artificial camera is presented in figure 5.15 alongside the original HBCm in both three- and two-dimensional perspective in a similar way as the previous LOS plots. This new geometry will be called *MIRh* - abbreviation/simplification of *MIRRored (horizontal)* (bolometer camera). The array is centred around $z = 0$ and designed to cover the poloidal cross-section evenly while also having individual pseudo detectors viewing regions of particular significance, i.e. magnetic islands and X-points. It is also tilted in toroidal direction - 68.75° , therefore with a toroidal reach of $\sim 5^\circ$ - and

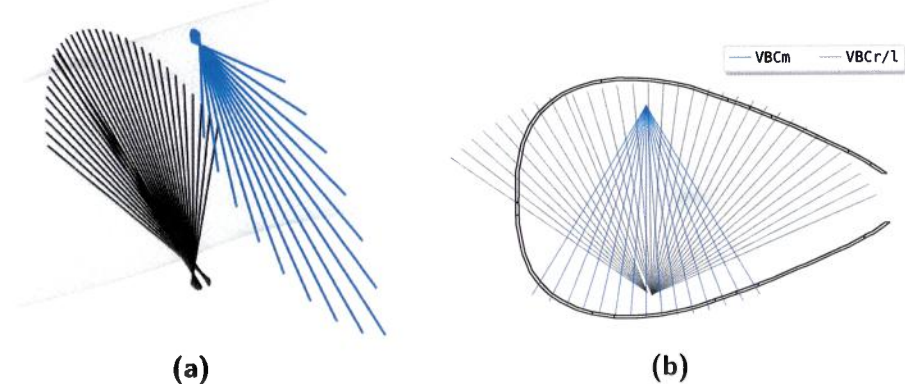


Figure 5.16.: (a) Both vertical camera arrays (black) next to a similarly *new*, artificial LOS fan of 15 channels ("VBCm", blue), which is created also opposite the VBCr aperture and covers. **(b)** Same geometry comparison in projection of the toroidal plane of the bolometer camera assembly, i.e. $\varphi_{\text{tor}} = 108^\circ$.

oriented antiparallel to its respective counterpart. Absorber size and shape within this camera are all the same and based on the respective HBCm average, while its aperture is equal to that of the latter. In contrast to the original horizontal camera, the MIRh pinhole is located much closer to the plasma and inside the enclosing first wall of the device, though the hypothetical construction puts the entire detector assembly outside said boundary, in some way being consistent with the space constraints at W7-X and the position of the VBCl/r.

Vertically Mirrored Camera

The second artificial camera is presented in a similar manner in figure 5.16 and, analogous with the prior, called *VBCm* - abbreviation for *Vertical Bolometer Camera (mirrored)*. In toroidal coordinates, this design is radially centred around the same position as the VBCr aperture center, which is reflected by its orientation in (b). The same detector dimensions with a constant spread, similar to that of the original vertical cameras, were chosen like in the previous design, though the LOS do not cover the entire, enlarged triangular plane. Their construction is solely focused on viewing the op-

5.2. Camera Geometry Sensitivity Towards Line of Sight Perturbations

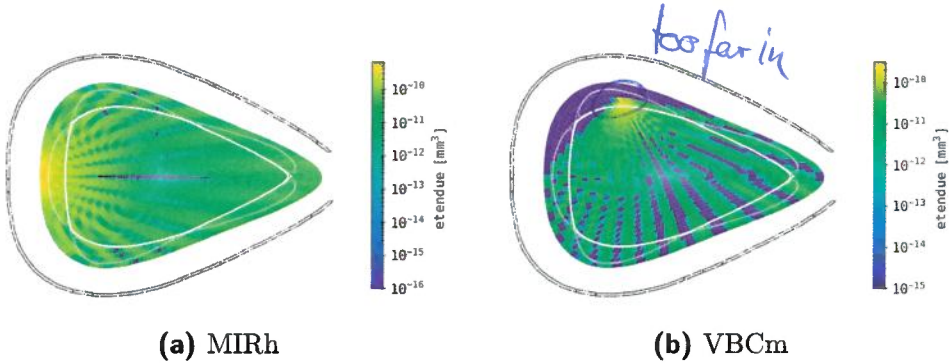


Figure 5.17.: (a), (b) Impact on the collective etendues of the entire bolometer camera system from the addition of the previously introduced *new*, artificial cameras from figure 5.16. On the (a) left, the local sensitivity of a hypothetical, horizontal camera (MIRh) is shown, while on the (b) right the same for a theoretical, vertical array can be found.

posite side X-points and magnetic islands, including those on the outboard and inboard side using multiple absorbers each. As mentioned before, its position relative to the separatrix and first wall of the device is analogous to that of the VBCl/r , i.e. the aperture is very close to the LCFS and the detector array beyond the limiting surfaces.

Figure 5.17 shows the resulting etendues of the new, artificial camera arrays on their own without any other LOS in the same way as before. In (a), the MIRh almost entirely covers the whole cross-section, except for a few singular pixels that have no etendue attributed to them in-between the individual LOS and a 1-2 pixel wide row inside the separatrix, around the magnetic axis of $\sim r_a$ length. Obviously, the maximum local sensitivity of $5 \times 10^{-10} / \text{cm}^3$ is found closest to the aperture on the inboard side, from which the etendue evenly decreases with increasing distance from the pinhole to 10^{-11} – $10^{-10} 1/\text{cm}^3$. Separation between the absorbers' coverage is larger closer to the edge of the LOS fan and to the edge of the inflated triangular domain. Profile and shape of the distinguishable LOS show that each characteristic feature of interest in this schematically indicated magnetic configuration is viewed by at least one detector each.

The right side image (**b**) similarly presents the etendues of the VBCm, clearly revealing the much stronger separation of the individual absorbers local sens-

itivity, even closer to the aperture. From its maximum of $2 \times 10^{-10}/\text{cm}^3$, an even reduction towards the pinhole opposite side of the domain along the LOS to 5×10^{-12} – $10^{-10} 1/\text{cm}^3$ is contrasted by gaps in coverage that are single - edge channels - to multiple pixels wide - center of the fan. Especially in-between the LOS that view around the magnetic axis, gaps are largest and extend the furthest towards the cameras' aperture. The much more spread construction of this artificial camera, combined with the smaller pinhole-detector distance compared to the HBCm, which is akin to that of the VBCl/r, yields a less wide LOS cone, as underlined by their presented separation. Furthermore, the close position of the array to the LCFS is highlighted by the void around and outside the separatrix and magnetic island on the upper inboard side where the maximum is located.

The designed two supplementary, artificial cameras *MIRh* and *VBCm* are constructed as similar as possible as the built, in-place counterparts. Hence, their etendues show no peculiarities, which was the goal for an improved global sensitivity and conclusive tomographic reconstruction. Application of said absorber arrays will be done further below during evaluation of various, complex phantom radiation distributions. The goal is to attain a perspective for a hypothetical extension of the multicamera bolometer system.

The evaluation of the bolometer LOS geometry in a context of tomographic inversion is thereby concluded for now. Comparison of different discrete segmentation methods and their impact on the three-dimensional, local sensitivity in a voxel grid based plasma tube has concluded that rectangular and triangulated approaches are equally valid and applicable for their respective task. Their corresponding fineness or resolution was also found to be sufficient above four individual parts of both detector and aperture, which yields a great reduction in computational tasks, though a general setting of $N = 8$ triangulated sub-detectors and -apertures has been established. Robustness of the crucial to a successful reconstruction, central geometric parameter matrix \mathbf{T} and perturbation thereof were examined thoroughly with the following hypothetical camera geometries. A variety of independent and combined changes to the original construction and their respective impact on the two-dimensional, local sensitivity distribution for tomography have been presented. This included chord brightness forward model integrations from fully symmetrical STRAHL radiation profiles using said results. Throughout this it was found that the orientation of the cameras

in the device introduces an intrinsic asymmetry to the LOS fans yield and hence their measurements. Beyond that, their individual deviation in local sensitivity generally is of order of magnitude found while comparing segmentation methods and is therefore assumed to be of lesser relevance. However, high precision measurements provided large discrepancies to the designed in-device aperture positions and the conclusive application to the previous models showed significant impact on the forward calculations. Therefore, one has to assume some level of additional, unknown, non-negligible error in \mathbf{T} , or more specifically to the regularisation functional \mathbf{K} when performing tomographic reconstructions. Finally, two entirely new cameras have been introduced, which now be used to improve the reconstruction of complex phantom radiation profiles and eventually gauge the efficacy of potential extensions to the existing multicamera system.

Very comprehensive, albeit
but well done
no conclusions required

5.3. Phantom Radiation Profiles

Tomographic reconstructions, particularly with badly conditioned - the number of LOS intersections is significantly smaller than the number of free parameters or pixels/voxels - detector systems are difficult to perform and potentially yield a high level of uncertainty in the final result, subject to assumptions about the underlying geometry and errors in the measurement. Furthermore, improvements to the algorithm of already proven methods like the *Minimum Fisher regularisation* similar to the previously introduced *radially dependent anisotropy* and *relative gradient smoothing weighting* generally need tailoring for individual, characteristic radiation distributions, i.e. varying relative weights for smooth or localised emissivities. Practical evaluating of these algorithms with a selection of common and/or expected two-dimensional *phantom radiation profiles* is crucial towards successful reconstruction of experimental data. Insights from previous investigations will be used for advantage upon improving the tomography of said phantom images.

First, a set of tools will have to be introduced for evaluating the results and their grade properly. One trivial task is to find both the two-dimensional and integrated deviation between phantom and tomogram. A *mean square deviation (MSD)* is introduced as:

$$\vec{m}_{\text{var}} = \frac{\sqrt{(\vec{x} - \vec{x}_{\text{phan}})(\vec{x} - \vec{x}_{\text{phan}})^T}}{\|x_{\text{phan}}\|} \cdot \vec{A}_p^T, \quad M_{\text{var}} = \|\vec{m}_{\text{var}}\|. \quad (5.14)$$

The above equation finds the relative, positive definite local deviation between the reconstruction and initial image $\vec{m}_{\text{var}} \in \mathbb{R}^m$, where $\vec{x}_{\text{phan}} \in \mathbb{R}^m$ is the radiation distribution of the phantom and $\vec{x} \in \mathbb{R}^m$ the resulting tomogram - remember that $m = N_\theta \cdot N_r$. The integrated *mean square deviation*, MSD is given by M_{var} , while \vec{A}_p is the area of the individual pixels $p^{(i,j)}$ associated with the radiation intensity in that location - for sake of simplicity let us write from here on

$$\vec{x}, \vec{A}_p \leftrightarrow x^{(i,j)} = x^{(i \cdot N_r + j)}, A_p^{(i,j)} = A_p^{(i \cdot N_r + j)}.$$

In order to find $A_p^{(i,j)}$ the *Heron^I formula* is used in equation (5.15) to separate the rectangular pixels into two triangles that fill the initial space and calculating their individual surface area. Let the pixel be:

$$p^{(i,j)} : \square (BCDE)^{(i,j)}.$$

The surface area $A_p^{(i,j)}$ of pixel $p^{(i,j)}$, constructed by the mesh intersection points $\{A, B, C, D\}$ is given by:

$$\begin{aligned} A_p^{(i,j)} &= A(\Delta(BCD)) + A(\Delta(CDE)), \\ a &= \overline{LM}, \quad b = \overline{MN}, \quad c = \overline{NL}, \quad p = \frac{1}{2}(a+b+c), \\ A(\Delta(LMN)) &= \sqrt{p(p-a)(p-b)(p-c)}. \end{aligned} \quad (5.15)$$

The values of $A_p^{(i,j)}$ are calculated once for a parameter set of magnetic field configuration, voxel grid resolution $N_\varphi \times N_\theta \times N_r$ and camera geometry - remember that the two-dimensional representation of the grid like in figure 2.22 is achieved by finding the intersection of the camera LOS fan plane with the voxel mesh. This also makes it very easy to find the total, integrated radiation power of the phantom and tomogram:

$$P_{\text{rad},2D}(\vec{x}) = \vec{x}^T \cdot \vec{A}_p = \pi R_{\text{maj}} \sum_{j=0}^{N_r} \sum_{i=0}^{N_\theta} x^{(i \cdot N_r + j)} A_p^{(i,j)}. \quad (5.16)$$

^IHero of Alexandria (Hérón hò Alexandreús) † 60 AD; Greek mathematician and engineer from Alexandria, Egypt during the Roman era

Remember that R_{maj} is the major plasma radius, i.e. the distance between center of the machine and the magnetic axis at the center of the plasma. Finally, the regularisation *fitness* or *robustness factor* χ^2 - see equation (5.1) -, which measures how well input and output forward integrated profiles are in agreement, is re-introduced as:

$$\chi^2 = \frac{1}{N_{\text{ch}}} \|(\vec{b}_{\text{phan}} - \vec{b}_{\text{tom}}) \vec{\sigma}^{-1}\| . \quad (5.17)$$

Remember that σ is the measurement uncertainty or deviation of each individual channel and N_{ch} the total number of channels. In practice, this is dictated by an error in acquisition, while for a forward phantom integration, an experimentally motivated and randomly distributed percentage between 1–2.5 % of the global maximum is applied. In this case, and for all following phantom reconstructions if not stated otherwise, the error is set to

$$\sigma^{(n)} = 0.025 \cdot \max(\vec{b}) \tilde{p}(n, \mathcal{N}(0, 0.5)) .$$

Here, $\tilde{p}(x, P)$ is a random sample for value x of a probability distribution P and $\mathcal{N}(\mu, \varepsilon)$ the *Gaussian normal distribution* of width ε and mean μ . With $\max(\vec{b})$ the global chord brightness peak, the error of channel n is at most 2.5 % of said value.

Equations 5.14 through 5.17 yield the necessary toolset to initially assess the quality of the phantom image reconstruction using the *Minimum Fisher regularisation tomography*. In the following pages, a comprehensive and diverse as possible set of hypothetical radiation distributions will be presented, alongside their individual tomographic reconstructions and corresponding errors, including both radial and chord brightness profiles from those, respectively. This exercise will be centred around experimentally motivated and more simplified and symmetric phantom images, from where more complex and challenging variations thereof are derived and reconstructed, while also trying to find an ideal - or suitable - set of anisotropy coefficients $\{k_{\text{core}}, k_{\text{edge}}\}$. This method will ultimately provide one with the practical limits of this approach for performing tomography on experimental data, which will be done so conclusively. If not stated otherwise, the employed voxel grid domain is $\{N_\varphi, N_\vartheta, N_r\} = \{30, 20, 150\}$ and in standard magnetic configuration.

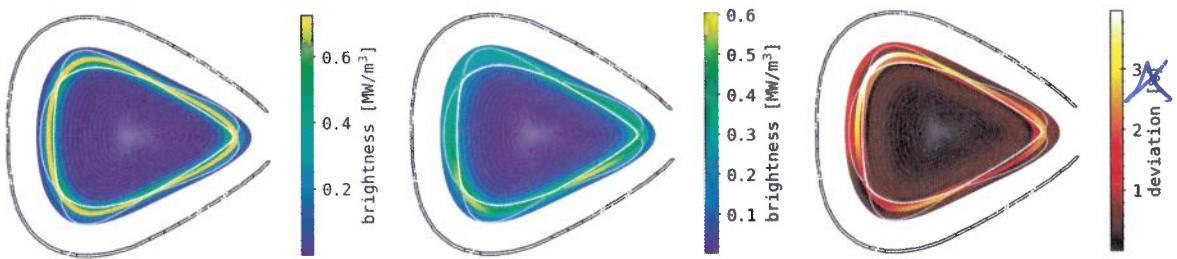


Figure 5.18.: Example of a (left) *phantom radiation distribution* and (center) its reconstruction using the Minimum Fisher tomography and standard bolometer camera geometry, including the (right) relative local deviation between the two prior. The phantom image is constructed as a uniform *ring* along a fixed flux surface with radius r_a and a normal distributed intensity in radial direction with a maximum of 1 MW/m^3 and $\sigma = 0.25 \text{ m}$. The inversion domain is the magnetic standard configuration, as previously described in section 2.3.1. The RDA parameters were chosen as $k_{\text{core}} = 2$ and $k_{\text{edge}} = 0.5$ with no smoothing in-between.

5.3.1. Symmetrical Ring in Scrape-Off Layer

The first phantom radiation profile that is used for forward integration and reconstructed with the MFR algorithm is shown, alongside its tomogram and their respective mean deviation from equation (5.14) in figure 5.18. A bright ring with a radially normal distributed emissivity is constructed around a radius of $r_0 = r_a$ with a maximum of $P_{\text{phan},0} = 1 \text{ MW/m}^3$ and FWHM of $\sigma_r = 0.25r_a$. The latter two values are experimentally motivated and chosen to yield sensible P_{rad} from the chord brightness profiles and two-dimensional integrated powers.

$$P_{\text{phan}} = \frac{P_{\text{phan},0}}{2\pi\sigma^2} e^{-\left(\frac{1}{2}\left(\frac{r-r_0}{\sigma}\right)^2\right)}$$

Individual values are and can only be attributed to discrete pixels on the grid. This is also due to the forward integration by $\mathbf{T}\vec{x}_{\text{phan}} = \vec{b}_{\text{ch}}$, where \vec{b}_{ch} is the chord brightness profile - also the measurement data in an experimental environment. The radius of a pixel is given by the radius of its rectangles $p^{(i,j)}$ *barycentre*. Hence, the actual maximum of the phantom emissivity is approximately 0.75 MW/m^3 since the pixel layer's center does not necessarily align with a particular radius, as given above. All plots also indicate, like

before, a half-transparent schematic of the separatrix and magnetic island structure. The middle plot shows the Minimum Fisher regularisation reconstruction for $k_{\text{core}} = 2$ and $k_{\text{edge}} = 0.5$. In this case, the anisotropy profile is a simple plateau, i.e. a *Heaviside^I step function* Θ_{N_T} for $N_T = 14$.

$$\Theta_g(x) = \begin{cases} 1 & , x > g \\ 0 & , \text{else} \end{cases}$$

This particular set of coefficients was deliberately chosen to mimic a typical configuration that would be used for experimental data tomography, i.e. in order to favor smooth radiation profiles in the core and enable anisotropy beyond the LCFS. Radial location and absolute value of the emissivity in the tomogram are very similar to its counterpart, however the distribution thereof is very asymmetric and focused strongly around the lower middle and inboard side X-point. The reconstructed emissivity is also much smoother and radially spread more than in the phantom along the entire separatrix. Gradients in poloidal direction are increased while they are significantly reduced perpendicular to the LCFS. At the inboard upper magnetic island and around the neighbouring X-points, the tomogram's radiation density is nearly constant between separatrix and domain boundary, while in the phantom no emissions can be found in the very last pixel shell towards the edge. These observations are also very much reflected in the right side *MSD* plot in figure 5.18 - see equation (5.14). The larger the brightness or value of deviation here, the greater the discrepancy in that particular location of the mesh between phantom and tomogram emissivity distribution. Variations of 1–3 % are largely centred around the pixels closest to the LCFS and magnetic structures. They match best, as described above, at the lower inboard and center, as well as worst around the opposite side X-points of the triangular plane. The average deviation along the separatrix is 2–2.5 %.

In figure 5.19, the individual radial and forward integration profiles are shown. The left image presents both radial emissivity distributions, which are derived using

$$p_r = p_{r^{(j)}} = \int_{2\pi} P_{\text{rad}}(r, \vartheta) d\vartheta \doteq \frac{1}{2\pi} \sum_{i=0}^{N_\vartheta} x^{(i,j)}, \quad (5.18)$$

^IOliver Heaviside, FRS * May 18, 1850 † Feb. 3 1925; English self-taught mathematician and physicist, developed technique for solving differential equations, vector calculus independently and rewrote Maxwell's

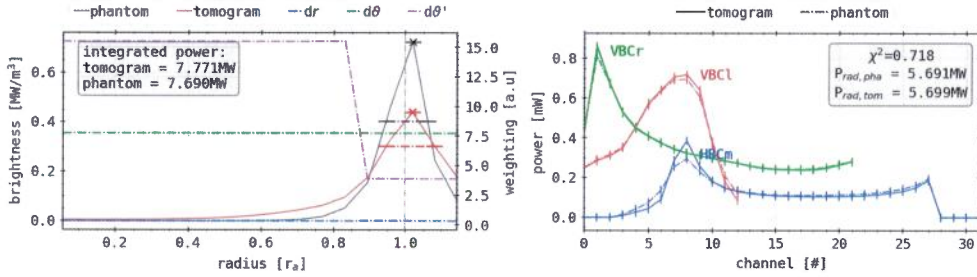


Figure 5.19.: Corresponding analysis for the results shown in figure 5.18. **(left)** Radial profile comparison between phantom and two-dimensional reconstruction, including the relative radial and poloidal weighting factor profiles dr and $d\theta$. Noted here are also the total integrated radiation powers for both. **(right)** Forward integrated chord brightness profiles of the individual arrays, using the standard camera geometry and the distributions from figure 5.18. The corresponding values for P_{rad} , as well as the fitness factor χ^2 are included.

where one remembers that $x^{(i,j)} = (\vec{x})^{(i,j)}$ is the phantom or tomogram radiation profile - later referred to as $p_r^{(\text{phan})}$ and $p_r^{(\text{tom})}$. equation (5.18) essentially yields the average of concentric pixel shells between the magnetic axis and domain boundary. For the individual lines, local maxima positions and values are indicated with by a \times -marker and their corresponding peak FWHM by a dash-dotted line at that particular height and location. Included next to p_r in the same plot are also the corresponding radial and poloidal weighting factors of the regularisation functional, i.e. the first order local gradients with $d\theta' = k_{\text{ani}} d\theta$ the impact of the anisotropy factor. Two-dimensional integrated powers, calculated using equation (5.16) are noted for both distributions individually. The plot on the right side features both forward integration profiles for all three bolometer cameras in a simplified presentation - results are shown over their discrete channel numbers rather than their LOS projected radii. This simply results from producing $\vec{b} = \mathbf{T}\vec{x}$, hence this plots abscissa is in units of power, i.e. the absolute, total power to the absorber instead of brightness or radiation density. Corresponding errors per detector are indicated as vertical lines as well for the forward integrated profile. Included here as well are both radiation power losses $P_{\text{rad},X}$ as measured by the bolometer cameras and introduced in equation (2.25)

and the corresponding fitness factor χ^2 .

Looking at the left image, a significant discrepancy between sharpness and absolute height of the radial profile peaks at r_a is immediately noticeable. The position of the maximum in both the phantom and tomogram line is slightly outside the separatrix, which is indicated by a grey dotted line. Height and width of the prior profiles peak are 0.73 MW/m^3 and 0.15 m respectively, while they are 0.45 MW/m^3 and 0.17 m for the latters. Conclusively, the $p_r^{(tom)}$ profile maximum extends far more in radial direction, though no emission can be found for either line for $<0.3 \text{ m}$ - the phantoms radial brightness vanishes inside 0.7 m . Integration of the two-dimensional emissivities using equation (5.16) yields 7.771 MW and 7.690 MW for the tomogram and phantom, which is equal to a 1.14% deviation. With a separate abscissa on the right, the regularisation weights are measured in the same plot. The radial gradient dr of 0.4 a. u. and standard poloidal factor $d\vartheta$ of 7.7 a. u. are both constant across the domain, since the underlying grid mesh was designed with constant step sizes. Modified by k_{ani} the anisotropy factor, $d\vartheta'$ becomes a step from 15.4 a. u. at 0.85 m to 3.9 a. u. at 0.9 m . Despite the unfavourable weighting and discrepancy in absolute height and position, the radial profiles of tomogram and phantom generally and qualitatively match well, which is underlined by the negligibly small error in integrated power. Similar circumstances are true for the forward integration comparison on the right in figure 5.19. Both sets of camera profiles yield a P_{rad} within 0.4% of each other, while the fitness factor χ^2 is also close to its target value unity. However, besides the nearly identical and certainly congruent within the error bars $VBCl/r$ lines, the $HBCm$ shows noticeable disagreement between the tomogram and phantom. Particularly, if not exclusively, the lower side range of this array, i.e. channel three through ten deviate significantly, where the phantoms profile is again less sharp and lower in absolute height. Furthermore, for both profiles, the lower and upper part are distinctly different in shape and height, which has been extensively explored in the previous section about the underlying camera geometry, though this is still being amplified for the tomogram. The vertical cameras accumulate, with a few exceptions, globally the most radiation with 0.9 mW and 0.7 mW at peak for the left and right array respectively. Only at the peak of the $HBCm$ tomogram forward integral of 0.39 mW , the $VBCr$ plot is surpassed around channel eight, as well as the $VBCl$ towards its minimum at channel twelve. Overall, the characteristic of both two-dimensional radiation distributions

is resembled by the structure of the individual and combined profiles, i.e. increased brightness at the separatrix, none outside and secondary emissivities at the core due to the cross-domain geometry of the LOS.

This simple phantom and reconstruction for a common set of anisotropy factors show the intricacies and particularities that come with the Minimum Fisher regularisation of such experimentally motivated emissivity profiles. Experience from this exercise is used to familiarize one with the previously introduced set of algorithms and tools, while building a foundation for the following artificial radiation distributions and their tomograms. Especially evaluating and tuning the k_{ani} coefficients towards characteristics of the individual phantoms will be explored further in the following sections.

5.3.2. Anisotropic Scrape-Off Layer Ring Combinations

Based on the profile in figure 5.19, various anisotropic two-dimensional emissivities are constructed in order to examine superimposed or convoluted poloidally symmetric and asymmetric distributions and their reconstructions. Particularly the impact of different k_{ani} parameter sets on the tomograms quality will be of focus here, while this is still being considered from the perspective of experimental data tomographies.

SOL Ring and 0° Core Anisotropy

The first combination phantom is constructed from a bright ring at the SOL like before, i.e. a maximum of 1 MW/m^3 with a normal distributed decay in radial direction of $\sigma_r = 0.25r_a$ width, and an additional, inside the separatrix core structure of 150% intensity of the prior at $0.7r_a$ and poloidal asymmetry towards the inboard lower X-point - for reference, this will be called 0°-orientation in the following exploitations. This superimposed emissivity is derived by convoluting two normal distributions in radial and poloidal direction of different widths, i.e.

$$P_{\text{phan}}(r, \vartheta) = \frac{P_{\text{phan},0}}{2\pi\sigma_r^2} \left(e^{-\frac{1}{2}\left(\frac{r-r_a}{\sigma_r}\right)^2} + \frac{3}{4\pi\sigma_\vartheta^2} e^{-\frac{1}{2}\left(\frac{r-0.7r_a}{\sigma_r} + \frac{\vartheta-\vartheta_0}{\sigma_\vartheta}\right)^2} \right). \quad (5.19)$$

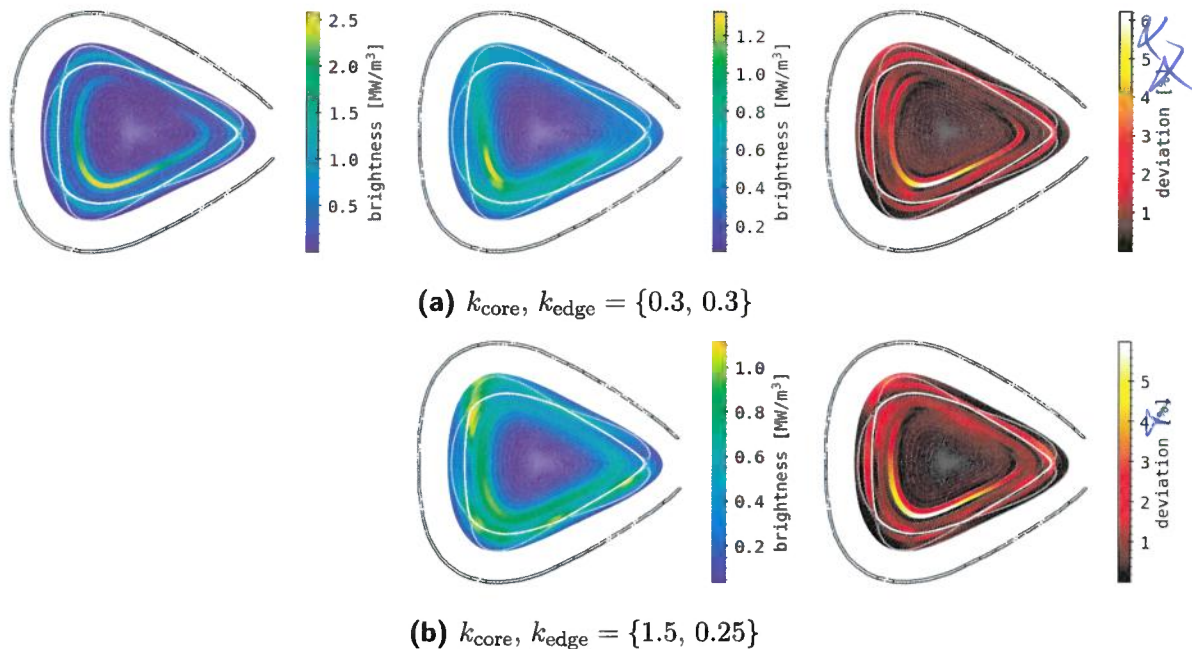


Figure 5.20.: Comparison of different RDA coefficient combinations for the same phantom radiation distribution (left), their reconstruction (center) and relative difference (right) using the Minimum Fisher tomography with standard bolometer camera geometry. The phantom image is constructed using a similarly bright ring around r_a as in figure 5.18, with a maximum intensity of 1 MW/m^3 , as well as an inside structure at $0.7r_a$ with a poloidally asymmetric maximum towards the lower side, close to the aperture of the VBC of 150% intensity of the prior. (a) A parameter combination preferring poloidal asymmetry equally in the core and edge. (b) RDA coefficients amplifying distinguishable structures in the edge and smooth radiation profiles in the core region. All distributions are plotted over the standard magnetic geometry mesh at 108° toroidally, as provided by section 2.3.1.

Here, the width in poloidal direction is $\sigma_\vartheta = 0.785 \text{ rad}$ or $\sim 15^\circ/\pi/4$ and $\vartheta_0 = 0^\circ$, the angle of the anisotropy - this particular orientation is chosen deliberately as a starting point from experience with previous experimental data reconstructions. The resulting phantom radiation distribution can be found in the top left of figure 5.20, accompanied by the reconstruc-

tions and two-dimensional error profiles for two sets of k_{ani} coefficients. In sum, the maximum emissivity becomes 2.55 MW/m^3 with visually clear separation between the two bright rings. The first set of anisotropy factors, again extrapolated using a Heaviside $\Theta_{14}(n)$ in the radial dimension, reads $k_{\text{core}}, k_{\text{edge}} = \{0.3, 0.3\}$ and the second $\{1., 5, 0.25\}$.

For the set of images in **(a)**, a parameter combination of $k_{\text{core}} = k_{\text{edge}} = 0.3$ equally supports and enables reconstruction of anisotropic structures in the core and outside the separatrix. The corresponding first reconstruction on the top features significantly lower emissions, about 45% of the input profile at 1.45 MW/m^3 . Structure and focus of the anisotropy are noticeably washed out and spread in both poloidal and radial direction. The maximum intensity inside the separatrix is also shifted clockwise and slightly outward towards the inboard magnetic island. That said, the most prominent difference between the phantom and tomogram is the interference or bleeding of the higher core emissivity with or into the homogenous, outside ring, which produces a global anisotropy in the reconstruction in contrast to the input distribution. Reflected in the MSD profile on the top right particularly is the poloidal shift of the inside asymmetry, since the largest error of 6.1 % is found at that location in poloidally counter-clockwise direction. Along the LCFS, with the exception of the lower inboard X-point, a nearly constant deviation of $\sim 2\%$ is indicated. In-between the core and SOL structures, the radial bleeding of emissivities yields significant error values in the lower and inboard area of 2–3 %. Despite the anisotropy coefficients setting, no additional asymmetries are produced in the tomogram due to the regularisation weights.

The second set of $k_{\text{ani}} = \{1.5, 0.25\}$ for plot combination **(b)** favours smooth and symmetrical emissions in the core and anisotropic profiles towards the edge. In fact, the corresponding reconstruction features significant poloidal asymmetries close to and outside the LCFS, particularly at and around the X-points. Most prominently, the global maximum of 1.21 MW/m^3 is found within a poloidally and radially extended anisotropy, reaching from inside the separatrix and upper inboard X-points to the edge of the respective magnetic island and domain boundary. Additional similar characteristics can be found at the original position from the phantom, as well as the respective lower X-points and along the outboard lower magnetic island. All show a significantly higher emissivity of $0.85\text{--}1 \text{ MW/m}^3$ compared to the in-between smoothed and spread out intensity of around 0.7 MW/m^3 . Con-

5.3. Phantom Radiation Profiles

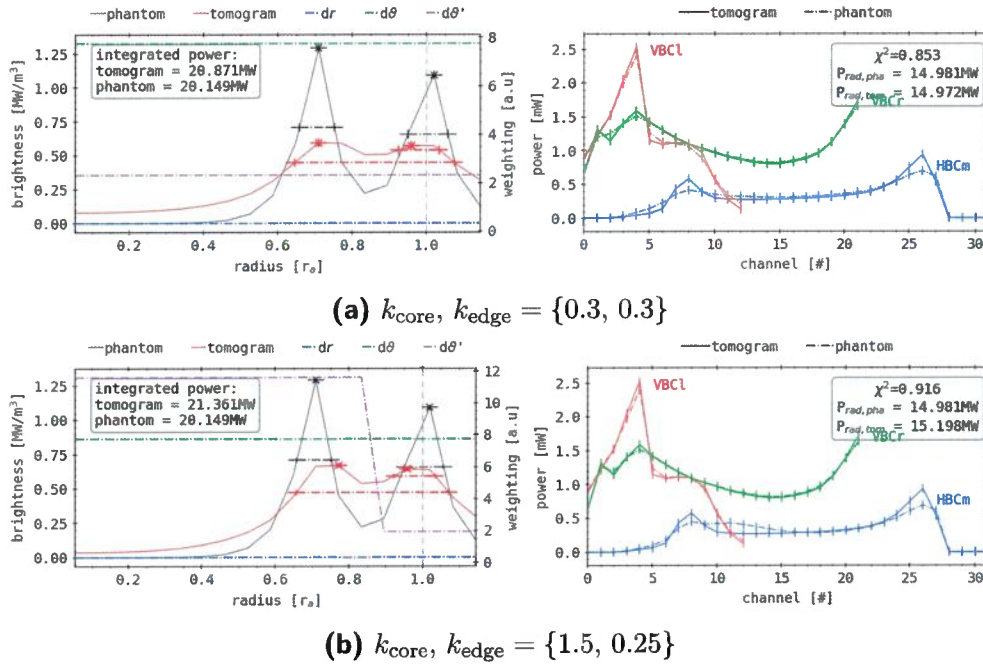


Figure 5.21.: Corresponding analysis for the results shown in figure 5.20.

The results are presented in the same way as in figure 5.19. (a) Parameter combination preferring poloidal asymmetry in the core and edge. (b) Coefficients amplifying distinguishable structures in the edge and smooth profiles in the core region.

sistent with the previous tomogram, the anisotropic structure at the core is also present at that radius, however with no noticeable poloidal shift of its peak at 0.95 MW/m^3 like before and a smoother profile. Coincidentally, the MSD on the bottom right represents those additional asymmetries around the core and LCFS well, though their are partially indicated by local minima due to the superimposed bright ring in the phantom. The maximum error is found in the same location as before, in the core with 5.9 %. Beyond that, the deviation profile is largely similar if not equal to the one above, including the relative error along the separatrix and in-between the inside characteristic.

The corresponding radial, regularisation weight and forward integrated profiles for the two-dimensional distributions in figure 5.20 can be found in

figure 5.21. Two sets of images show the results for the respective two k_{ani} parameter combinations from the previous plots in (a) and (b). For anisotropy factors $\{0.3, 0.3\}$, the poloidally average radial tomogram characteristic on the top left is again far smoother and features less pronounced local extremes than its phantom counterpart. Even at the innermost radii, the tomogram still yields non-negligible emissivities of at least 0.075 MW/m^3 and increases up until its first peak, which coincides with the location in the phantom, at $0.7r_a$. With 0.65 MW/m^3 , this maximum is less than half of the corresponding structure in the artificial distribution at 1.325 MW/m^3 , while no FWHM is produced for this shallow peak. The indicated width of the underlying emissivity *heap* between $0.6\text{--}1.15 \text{ m}$ is mismatched and of no concern for this comparison. The phantoms core anisotropy features a width of 0.15 m and is followed by a sharp decline to 0.2 MW/m^3 towards the separatrix, after which a second maximum close to 1 MW/m^3 around 1.05 m of the same width follows. In the reconstructed distribution, the intensity along the separatrix produces a second peak at 0.95 m of 0.65 MW/m^3 with a FWHM of around 0.15 m . Beyond, both phantom and tomogram radial profile decline to 0.12 MW/m^3 and 0.3 MW/m^3 , respectively at the boundary. Integration using equation (5.16) yields 20.871 MW and 20.149 MW for the reconstructed and artificial radiation distribution, which results in a deviation $\sim 3.5\%$. Due to the design of this first k_{ani} profile, poloidal and radial regularisation weights $d\vartheta'$ and dr are both flat across the domain at 2.4 a. u. and 0.35 a. u. - $d\vartheta$ is, as before, constant with 7.25 a. u. , which is of no particular concern here or in any of the following weighted MFR tomographies. Looking at the bottom left image, which presents the same set of results for the corresponding second combination of anisotropy coefficients, similar characteristics can be found in the tomograms radial profile. Except for the modified poloidal regularisation weight and $p_r^{(\text{tom})}$, this plot is congruent to the one above. Emissions in the core are still present in the tomogram towards $r = 0$, though as low as 40 kW/m^3 . Two significantly smaller and less pronounced peaks, though of slightly larger absolute value than the previous, are again found close to their artificial counterparts. Inside the separatrix, the maximum yields 0.65 MW/m^3 at 0.78 m with the same width of 0.15 m . Following a shallow local minimum, the second structure is produced around 0.95 m with the same height and width as the one on the left. Its decay towards the domain boundary is similar and concludes also at 0.3 MW/m^3 . This profiles' integrated power of 21.361 MW corresponds to an

5.3. Phantom Radiation Profiles

error of 5.6 %. A step in $d\vartheta'$ is result of the different anisotropy parameters, which happens down from 11.6–1.95 a. u. around 0.875 m between the radial characteristics.

On the right in figure 5.21, the forward integrated brightness profiles for each individual camera and both k_{ani} combinations are shown again in comparison between phantom and tomogram. The top image presents qualitatively, and for the VBC arrays also qualitatively well-matching artificial and reconstructed lines. Latter cameras plots are within their respective confidence interval and similarly larger in absolute terms like before. The VBCr forward integrals feature a smooth parabolic profile around the core, with the maximum of 1.7 mW in detector no. 21 that is the left-most in this array, looking along the inside edge of the core, close to this particular anisotropy. On the other side, i.e. within the right-most channels towards the outboard side of the triangular plane, detectors zero through five show smaller local peaks around 1.3 mW towards the edge of the camera. From the perspective of the VBCl, the most radiation is acquired in both distributions by its first right-most five detectors up to 2.6 mW, i.e. those watching the core anisotropy across the separatrix. The bright ring along the LCFS produces a small second local maximum around channel eight following the very sharp drop from the preceding peak. Only the last, outermost absorbers looking outside the magnetic structures yield smaller integrated powers than the HBCm. That said, the horizontal camera also yields two very similar profiles, where in both plots the right half of the array, the LOS watching the lower side and poloidal anisotropy in this phantom reconstruction, respond to higher emissivities with up to 0.9 mW. Forward line integrals through the asymmetry and enclosing ring in combination produce that particularly broader peak. The slightly hollowed out core between channel no. 10-20 is limited by a second lesser local maximum of 0.6 mW around detector eight on the other side, corresponding to the upper part of the brightness along the separatrix. Beyond absorber no. three and 28 towards the edge of the camera array, no radiation is *measured*. As noted before in the radial and two-dimensional profiles (figure 5.20), the tomogram plots generally present slightly less pronounced local extremes and smoother transitions in-between, e.g. for the VBCl between channel no. 5-12. This set of forward integrals achieves a good quality of $\chi^2 = 0.853$, while the difference between the two respective P_{rad} of 14.981 MW/m³ and 14.972 MW/m³ for the phantom and tomogram is less than 0.01%. For the same artificial distribution profiles, the

Very Worley

bottom right image in figure 5.21 shows largely the same results. However, the congruence between the vertical camera plots is significantly improved, which is also reflected by $\chi^2 = 0.916$. In the tomograms HBCm profile, the channels that cover the upper separatrix - no. four through ten - show a minutely sharper peak compared to above, though with a continuously higher power towards the core around 0.4 mW, outside the confidence interval. Furthermore, the error between the extrapolated total radiation powers increases to 1.4% with $P_{\text{rad,tom}} = 15.198 \text{ MW/m}^3$.

Looking directly for differences between the two tomographic reconstructions in both two-dimensional and individual profiles, the second anisotropy coefficient set yields a distribution that features significantly more localised structures around and outside the separatrix and a less pronounced asymmetry or smoother emissivity in the core. In addition, or rather because of it, its absolute brightness is also lower, though the corresponding MSD profile shows a lesser total discrepancy between the tomogram and phantom. In the radially averaged profiles, contrary to the previous assessments, the latter finds both stronger local maxima at those respective radii and a higher total brightness outside $0.6r_a$. The bolometer camera forward integrals show only minor if not negligible differences, except for a protruding HBCm profile with higher power from the left maximum towards the center. Cross-correlating the fitness factor, the integral of the two-dimensional brightness distribution and radiation power from the forward calculated detector yield only supports the subjective impression of a qualitatively lesser reconstruction. However, the difference in χ^2 conflicts with that examination, i.e. a larger error between $P_{\text{rad,2D}}$ and P_{rad} seemingly does not contribute to a worse fit of input and output of the MFR.

The comparison in figure 5.20 and 5.21, though individually presenting plausible, if not good reconstruction results, highlights a major problem with regularisation tomographies and particularly the anisotropically weighted MFR. The first set of $k_{\text{ani}} = \{0.3, 0.3\}$ is explicitly not well suited or intended to reconstruct this phantom radiation distribution adequately, however its corresponding tomogram subjectively resembles the input image very well. Most certainly, this does not say that this set of anisotropy coefficients yields the qualitatively and quantitatively best reconstruction results. Finding said ideal k_{ani} profile is a very difficult task and involves, including but not limited to, multidimensional algorithmic optimizations and incorporation of *a priori* knowledge and respective constraints. Underlined by the

corresponding, close-to-unity fitness factor χ^2 and the congruence of the forward integrated camera profiles, the first set of results represents an accurate reconstruction. However, the second set of $\{1.5, 0.25\}$ produces a qualitative similarly matching tomogram, radial and individual camera profiles, while finding a subjectively far less adequate two-dimensional radiation distribution. One should note that, purely examining the impact of singular k_{core} and k_{edge} coefficients, the first tomogram does show improved localisation in the core compared to the second, which in fact yields a smoother characteristic there. Also, the significantly lesser edge factor actually amplifies anisotropies in that area. The second reconstructions χ^2 and MSD both indicate a better tomography result. In a scenario of experimental input data, the fitness coefficient is the only measure by which to examine the efficacy of the MFR. This again amplifies the importance of a well-rounded and thoroughly examined set of phantom image reconstructions with a focus on the relationship between quantitative and qualitative matching. Later series of MFR tomographies will focus on this particular aspect and evaluate the influence of and relationship between k_{ani} and χ^2 , $P_{\text{rad/2D}}$ etc.

SOL Ring and 90° Core Anisotropy

The second set of phantom radiation distributions in figure 5.22 is derived using the same equation 5.19 as before and the same set of coefficients $P_{\text{phan},0}$ and $\sigma_{r/\vartheta}$, except for the poloidal mean $\vartheta_0 = 90^\circ$, i.e. the previous anisotropy shifted by $\pi/2$ in clockwise direction. All other parameters, including the anisotropy profile k_{ani} are kept constant. In the first reconstruction in the center of (a), compared to the previous tomogram for this set of coefficients, the inside anisotropy is of much brighter contrast and virtually merged with the outside separatrix ring around the inboard topside X-point and upper magnetic island, extending beyond to the domain boundary. The radial width of the core feature is also noticeably increased, while being less peaked and more plateau-shaped in radial direction. Very prominent is also the much stronger radiation at the inner radius $0.7r_a$ from the latter location down towards the opposite side island, where the previous asymmetry was centred around. The absolute height of the emissivity profile at its maximum is comparable to before with 1.18 MW/m^3 , though this intensity is spread much wider in poloidal direction. Towards the inboard lower X-point, the separation in brightness between LCFS and inside radiation increases again,

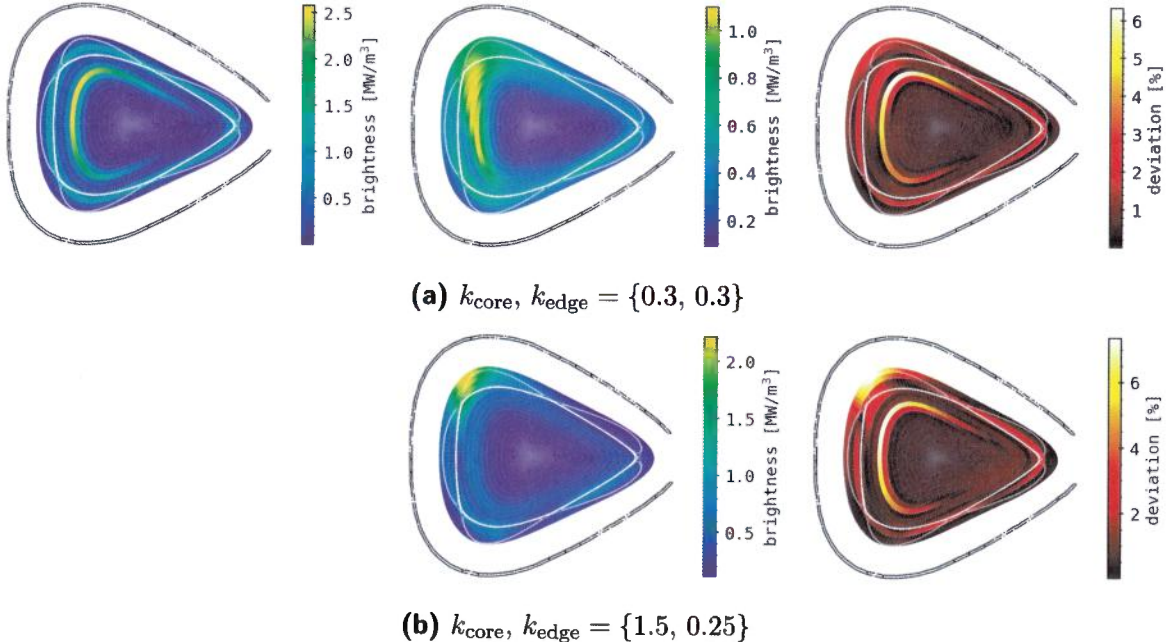


Figure 5.22.: (a), (b) Similarly constructed and reconstructed phantom radiation distribution as in figure 5.20, but the core structure has been rotated in clockwise direction by 90° . The tomographic inversion features the same RDA parameter combinations as before.

which along the prior yields $0.5\text{--}0.8 \text{ MW/m}^3$ at a significantly higher width of $\sim 0.5r_a$. Closer to the HBCm and top, no inside structure or increased emissivity is visible whatsoever. The corresponding MSD profile on the right therefore produces large errors of a maximum 6.2 % in $0.7r_a$ around the poloidal location of the input core anisotropy. Along this radius, larger deviations of $>4.5\%$ can be found in both directions for $\sim \pi/2$. A smoother and lower error profile of 2–3.5 % at and outside the separatrix correlates with the less sharp tomogram emissivity in that area.

The second set of anisotropy coefficients $\{1.5, 0.25\}$ in figure 5.22:(b) yields a fundamentally different reconstructed radiation profile, which essentially consists only of one bright spot outside the LCFS, at the edge of the inboard upper magnetic island neighbouring X-point towards the edge of the domain. Its brightness and therefore the global maximum emissivity of this

5.3. Phantom Radiation Profiles

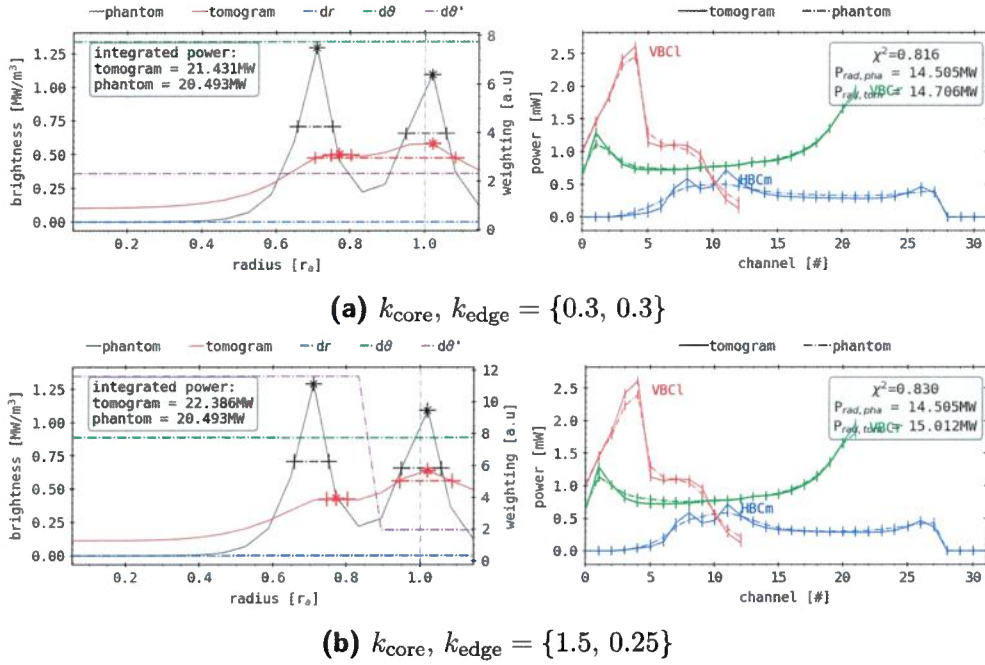


Figure 5.23.: (a), (b) Corresponding analysis for the results shown in figure 5.22, similar to figure 5.21, using the noted below anisotropy parameters for the tomographic inversion. The results are presented in the same way as in figure 5.19.

tomogram is 2.2 MW/m³. In the core around $0.7r_a$, only a negligible amount of radiation $\leq 0.5 \text{ MW/m}^3$ of very constant and smooth distribution can be found. Slightly elevated emissivities compared to that are shown close to and inside the magnetic island along the separatrix. Correspondingly, the MSD profile on the right presents the largest discrepancies of $\sim 7.4\%$ in the location of the input poloidal anisotropy and reconstructed bright spot close to the edge of the inversion area. Directly comparing this image to the profile above, besides the latter characteristic and absolute values, the only difference is the error gap close to the core asymmetry, which is due to the drastically different localised features.

In accordance to the previous reconstruction for the 0° anisotropy, figure 5.23 again features the individual radial (average) profiles, alongside the different regularisation weights with total integrated radiation powers and the

respective forward integrated detector signals and their conclusive P_{rad} . In **(a)**, following the corresponding results in the last set of images and figure 5.20, expectedly the same $p_{r,\text{phan}}$ is shown. The tomograms' counterpart presents less sharp local maxima that are also slightly shifted with respect to the initial plot. Leading from the center, the emissivity is similar to before at $<0.2 \text{ MW/m}^3$ until $0.5r_a$. The inside, almost unnoticeable peak at $0.76r_a$ is barely above 0.5 MW/m^3 and does not constitute the shape for properly measuring the FWHM, while the successive local minima is nearly at the same level. A conclusive second, largely flat or plateau-like peak around $1.02r_a$ at 0.6 MW/m^3 , with the same width as before, is still significantly below the input profiles maximum in that location. Obviously, the phantoms radial and all weighting parameter profiles are the same as in the first set of plots. The tomogram now yields 21.431 MW , corresponding to 4.4% deviation from the input. One should note here that $P_{\text{rad},2D}$ is ca. 0.3 MW higher than for an anisotropy at 0° , indicating that the underlying mesh of pixels is not fully up-down symmetric, since this factor is the only variable in this comparison.

On the right, the phantom forward integrated absorber powers are very similar to the initial results. The vertical cameras show qualitatively the same profiles, with an inboard maximum and peaks around the LCFS, since from their perspective the inside anisotropy isn't shifted much, which is reflected by the fact that the same channels find local and global maxima for both VBCI/r , i.e. in no. 1, 4, 8, 21. Values of said peaks are even equal within a tenth of a milliwatt. From the point of view of the horizontal camera however, the relative shape of the profile is flipped due to the asymmetry now aligning with the upper X-point. In contrast to before, a much broader and less sharp peak is found around channel no. 10 with 0.5 mW , corresponding to the line integration through outside ring and anisotropy, while there is no maximum in no. 26-28 and the power sharply falls to zero. Forward integration from the tomogram shows again slightly more pronounced characteristics, though being within the respective confidence interval throughout both vertical cameras. For the HBCm, core and lower side coverage, i.e. no. 15 and up, is also in similar agreement with the input. Channels viewing the upper part of the triangular plane present two individual peaks of $0.6\text{--}0.75 \text{ mW}$ around detector 9, which presents a small local minimum of 0.45 mW . Beyond, the measured power falls quicker than in the phantoms profile. From equation (2.25), $P_{\text{rad,phan}} = 14.505 \text{ MW}$ however

is 0.4 MW smaller than before and $P_{\text{rad,tom}} = 14.706 \text{ MW}$ therefore presents a 1.4% error. The subjectively worse match between the forward profiles compared to the initial set of results is supported by a slightly worse fitness factor of 0.816 a. u.

Looking at the image on the left in figure 5.23:(b), again the same $p_{r,\text{phan}}$, regularisation weight profiles and integrated phantom radiation distribution power are shown. Presented results are achieved using the same input artificial emissivity and a different $k_{\text{ani}} = \{1.5, 0.25\}$. The tomograms poloidal average, akin to the one above for the other set of anisotropy coefficients, an increased brightness throughout the core until past $0.5r_a$ starting from 0.12 MW/m^3 can be found. The inside characteristic, which was barely noticeable in the two-dimensional image previously, yields a similarly shallow plateau at $0.75r_a$ of 0.45 MW/m^3 and therefore also significantly smaller than in the first profile for this set of parameters. Like before, there is no local minimum in-between this and the virtually merged into conclusive second, global maximum in $1.05r_a$ of 0.68 MW/m^3 with a width of 0.15 m. Integration of the emissivity distribution produces $P_{\text{rad,2D}} = 22.386 \text{ MW}$ or an 8.5% larger total power than in the phantom.

The forward integrated detector signals on the right are largely very similar to the ones above. However, the vertical camera array results show increased discrepancies to the artificial brightness profiles, which are eventually beyond the confidence interval in locations of certain extrema, while the HBCm plot presents better overall agreement. In sum, a minimally improved fitness of $\chi^2 = 0.83 \text{ a. u.}$ compared to above contrasts a larger error in P_{rad} of 3.4% by 15.012 MW. With respect to the first set of forward integrals, this is a much worse reconstruction measured by χ^2 and the deviation in extrapolated radiation powers.

The superimposed artificial radiation distribution in figure 5.22 has proven to be, given the same approach and *a priori* knowledge about the characteristics, qualitatively and quantitatively more difficult or *worse* to be reconstructed. On one hand, the two tomograms show very strong differences between each other in terms of absolute value and localised features that are far more pronounced than in figure 5.20. On the other hand, both are subjectively and measurably, as indicated by the MSD profiles, worse inversions from forward integrating the very similar phantom emissivity. Irrespective of the set of k_{ani} , a core anisotropy in this location is shown to be more complicated to reconstruct with this set of cameras and LOS.

Due to the shape and location of the inside asymmetry, the much closer and therefore crucial vertical camera detector are not able to adequately resolve the structure, while the line integration from the point-of-view of the HBC yield larger interference. Contribution and impact of said anisotropy are lessened in this case by the increased distance and greater relative sensitivity to the symmetrical bright ring right in front of the pinhole. In fact, the same is true for the VBC1/r here, though with respect to the previous phantom distribution their LOS happen to be nearly perpendicular to the orientation of this core characteristic and hence only few, if not singular absorbers measure its emissivity. Thus, the detailed intensity profile and structure is largely lost, especially the explicit separation from the LCFS ring because of the unfavourable geometry. With respect to the applied anisotropy coefficients, the initial set enables the MFR to assume more of the particular inside brightness due to it providing a lower weight towards smooth, i.e. greater width profile characteristics. Though the spatial gap towards the separatrix is still lost because of the lack of local resolution, the second set essentially does the same while also only producing a ring of constant intensity inside the LCFS. This in turn then forces the algorithm to place $\sim 200\%$ of the above maximum emissivity in this location to in order to satisfy the original condition of $\min(1 - \chi^2)$.

The issues described above also serve as an example for one of the intrinsic limits of MFR tomographies with the multicamera bolometer system at W7-X. In addition to the fairly limited count of LOS for this kind of inversion problems - which is also motivation (see section 5.1) for the applied methodology -, location and number of points-of-view of those cameras impose even more challenges to the reconstruction of such arbitrarily complex radiation distributions. This furthermore underlines the importance of phantom image tomographies.

SOL Ring and 180° Core Anisotropy

The next logical continuation of the previous artificial radiation distributions is an additionally 90° shifted core anisotropy in combination with the ring of constant brightness around the separatrix. Again, this phantom in figure 5.24 is derived using equation 5.19 with $\vartheta_0 = 180^\circ$. All other parameters, including k_{ani} are also constant. In (a), the center image shows the tomographic reconstruction for a set of anisotropy coefficients $\{0.3, 0.3\}$. This

5.3. Phantom Radiation Profiles

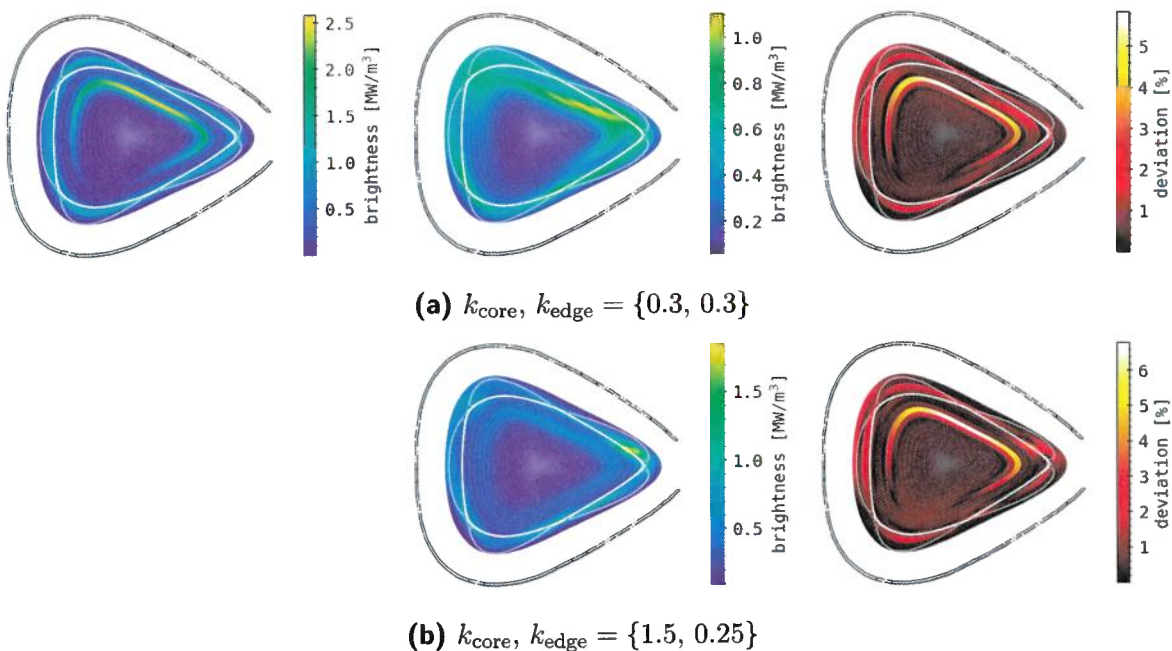


Figure 5.24.: (a), (b) Similarly constructed and reconstructed phantom radiation distribution as in figure 5.20, but the core structure has been rotated in clockwise direction by 180° . The tomographic inversion features the same RDA parameter combinations as before.

profile shows similar results to the corresponding tomogram in figure 5.20, where there is a distinctly brighter core structure at 1.1 MW/m^3 that is broadened towards the LCFS and a less intense ring around 0.7 MW/m^3 along the separatrix. The latter also features small local maxima of up to 0.9 MW/m^3 in X-points and areas where magnetic islands intersect. Particular about this plot is the continued increased brightness, almost following a straight line from that localised inside feature to the outboard upper magnetic island. Conversely, the respective SOL intensity is higher here than in the rest of the triangular plane at 1 MW/m^3 . In the opposite direction, along an imaginary extension of that line, the separatrix ring and core anisotropy merge on the inboard side, interfering with the emissivity distribution in the SOL. Inside the LCFS, no brightness can be found adjacent to the examined structure. At the very edge of the tomographic domain, there is still

significant radiation power towards the inboard upper area and boundary with $\sim 0.6 \text{ MW/m}^3$.

On the right, the MSD prominently shows this extension of the anisotropy towards the tip of the triangular plane, on the inside of the respective upper magnetic island, by an increased error value $\sim 3\%$ where there is close to no radiation in the phantom. Minor deviations $<2.5\%$ can be found in the corresponding inboard location and beyond the respective two upper magnetic islands. The inconsistency of the separatrix ring intensity in comparison to the artificial distribution is highlighted here as well by alternating increased and decreased discrepancies of 1.5–2.5% along the poloidal direction. The largest error of 5.8% is again located where the input anisotropy is placed and only decreases significantly after a $\pi/2$ sweep in both directions.

Reconstruction and error profile in figure 5.24:(b) for a set of $k_{\text{ani}} = \{1.50, 2.25\}$ present a very similar image with respect to the previous series of plots in figure 5.22:(b), where there is a hyper localised bright spot of greatly larger intensity than the rest of the distribution and respective tomogram for comparison. In this case, the upper inboard magnetic island and part of the separatrix feature a relatively small $0.2 \times 0.2 \text{ m}$ characteristic with a maximum 1.85 MW/m^3 that shows a very sharp decay radially, while extending noticeably in poloidal direction. With respect to this brightness, the rest of the tomogram presents no other significant contributions to the overall radiation power. However, with $<1 \text{ MW/m}^3$ some of the previously noted structures are found here as well, i.e. the variation in intensity along the LCFS, of which the very bright spot is a part, illuminated domain boundary at the inboard top and the core anisotropy.

The corresponding MSD profile yields a maximum deviation of 6.4% on the inside where the input feature is located in $0.7r_a$, similarly to the plot above. Compared to the latter, this error distribution overall shows noticeable variance 1–2% in the core and in-between the individual features, as was the case for the previous two examples of this particular phantom image. The prominence of the upper outboard magnetic island characteristic in the tomogram is reflected here also, as there is an increased error of $>4\%$ at and around the separatrix in that location. Coincidentally, the MSD along the inside of the LCFS is reduced accordingly with respect to the prior profile. Figure 5.25 presents the one-dimensional profiles for the set of results shown in figure 5.24 like before. For both sets of images, the respective phantom radiation distribution profiles and plots are kept constant between them,

5.3. Phantom Radiation Profiles

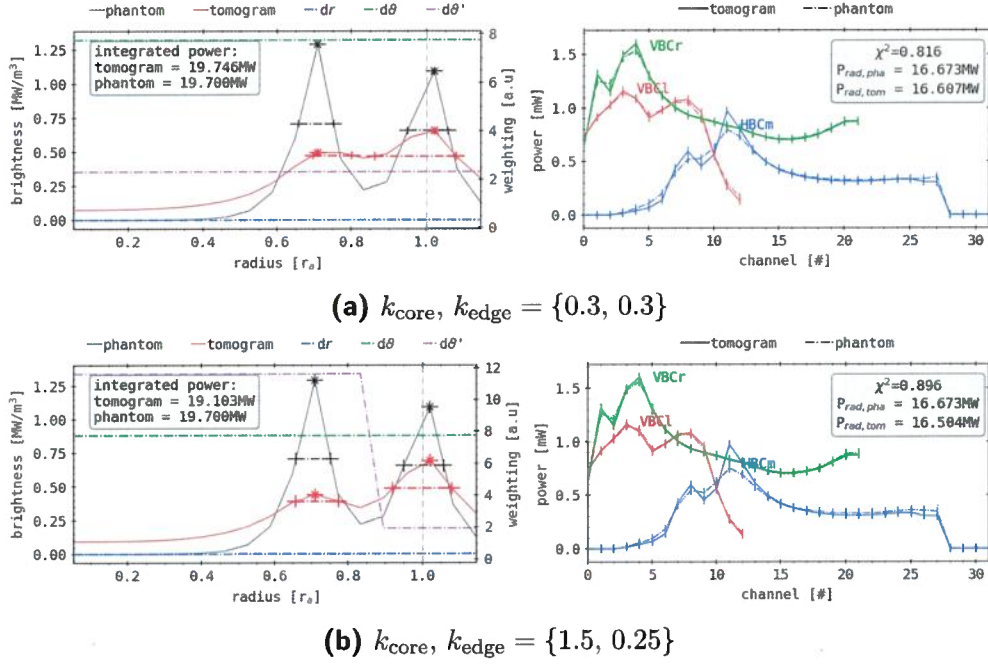


Figure 5.25.: (a), (b) Corresponding analysis for the results shown in figure 5.24, similar to figure 5.21, using the noted below anisotropy parameters for the tomographic inversion. The results are presented in the same way as in figure 5.19.

while the regularisation weights are the same as in the previous displays, i.e. figure 5.21. Also, the poloidally integrated radial profiles are congruent to those in the preceding plots. Two-dimensional integration of the emissivity finds a total power of 19.7 MW and the forward calculated brightness amounts to $P_{\text{rad,phan}} = 16.673$ MW. On one hand, $P_{\text{rad,2D}}$ is slightly smaller compared to the initial value by 2.3 %, while on the other the extrapolation from the detector powers is increased by 10.02 %. In (a), for $k_{\text{ani}} = \{0.3, 0.3\}$, the p_{rad} is akin to the one from the prior artificial radiation distribution, though with a slightly decreased intensity of 0.075 MW/m³ across the core and higher peak at 0.65 MW/m³ close to the separatrix in $1.05r_a$. The latter's width of 0.2 m is also larger with respect to the previous phantom, to which this profile's overall shape is still very similar. In total, the integration of the tomograms' emissivity produces $P_{\text{rad,2D}} = 19.764$ MW, less than 0.3 %

deviation from the input profiles absolute power.

On the right, the corresponding phantom and tomogram forward integrated absorber signals are shown, presenting a qualitatively and quantitatively different picture to the two other MFR reconstructions. Like before, in the input profile the HBC finds a large, stepped peak around channel no. ten starting from no. five and growing to 0.5 mW in no. eight and conclusively 0.75 mW in no. twelve, with a subsequent flat plateau across the core and sharp decline after detector no. 27. However, its relative intensity is far greater here due to the reduced power from the vertical camera channels. Those in particular show an entirely new picture, where the VBCr features also two successive local maxima in absorber no. two and four of 1.3–1.6 mW, viewing the outboard magnetic islands and tip of the triangular plane. Towards the center and other side of the cross-section, the profile declines with a closing minor increase to 0.85 mW where previously the maximum was found. This is continued by the VBCr core-side signals of channel null and following, also showing two distinct peaks around 1.1–1.15 mW in detector no. three and eight with a final pronounced drop in signal closest to the edge of the domain.

Forward integrated signals from the tomogram in (a) are overall well within the respective confidence interval for all cameras, except in detector no. eleven of the HBCm where there is a 0.2 mW greater achieved value here. In this location and for all other local extremes of any absorber array, the output results generally yield a more sharp and pronounced shape while transitions in the phantoms profiles are smoother and have smaller gradients. For the vertical cameras, both plots are congruent outside the latter locations. Summation and extrapolation of those results from the tomogram produces a total radiation power of $P_{\text{rad,tom}} = 16.607 \text{ MW}$, which less than 0.5 % of an error to the input distribution. Coincidentally, the fitness of $\chi^2 = 0.816 \text{ a. u.}$ is equal to that of the very first MFR tomography for the same set of anisotropy coefficients.

At the left in figure 5.25:(b), the reconstruction of the same phantom emissivity using $k_{\text{ani}} = \{1.5, 0.25\}$ finds a total power of $P_{\text{rad,2D}} = 19.103 \text{ MW}$, which is 3.3 % lower than in the input profile and latter reconstruction. The radial plot presents a slightly higher core brightness at 0.1 MW/m^3 compared to above, similar to that in figure 5.21:(b). While the inside peak of 0.45 MW/m^3 in the same location is smaller than before, it is noticeably more pronounced with a definite width of 0.1 m and a more distinct, follow-

ing minimum. With 0.7 MW/m^3 and 0.15 m FWHM , though in the same radial location, the concluding maximum is higher and sharper than above as well as in the initial tomogram.

Forward integrated signals corresponding to this set of results are in stronger agreement with the respective input data. Exceptions are the global maximum in the HBCm plot in channel no. eleven, where the discrepancy remains constant, and the lower side and core part of the array, which show a minutely larger error. Particularly the vertical cameras match up significantly better than for the k_{ani} profile counterpart. Therefore, the fitness is increased to $\chi^2 = 0.896 \text{ a. u.}$. However, the extrapolated power loss of $P_{\text{rad,tom}} = 16.504 \text{ MW}$ yields a discrepancy of 0.7% and is hence both further away from the actual, i.e. integrated two-dimensional power and value of the artificial emissivity.

The varying k_{ani} MFR tomographies for the phantom radiation distribution in figure 5.24 effectively show similar results and discrepancies with respect to the previous plots. Superimposed and localised, anisotropic emissivities of this kind are again shown to require further analysis in order to achieve comparable or adequate tomograms when compared to figure 5.20. The first reconstruction, like the respective profile in the last set of images, in fact also yields a core anisotropy that is clearly distinguishable from the smoother and less intense bright ring around the LCFS. This is however similarly smeared out and merges with said ring in the location where the second tomogram finds a strong maximum. Finally, again one finds significant amounts of radiation outside the separatrix and magnetic islands towards the upper inboard side of the triangular plane. The balanced weighting coefficients enable the MFR to achieve both an inside asymmetry and brightness outside, however with the aforementioned drawbacks due to $k_{\text{core}}, k_{\text{edge}} < 1$, which prefers localisation above smoothness. In direct contrast and compared to the corresponding plot in the prior set of results, for an anisotropy profile of $k_{\text{ani}} = \{1.5, 0.25\}$, the second reconstruction is found to provide a distinctly worse fitting emissivity and a much more localised power deposition. This can be attributed to the increased distance to the VBC camera and therefore decreased LOS resolution in that particular area. Furthermore, from the perspective of the HBCm, this anisotropy is viewed by only a few, i.e. one to three LOS and hence the sensitivity of the whole system towards such structures is constructed very unfavourably. In combination with the respective coefficient profile, this enables the MFR algorithm to concen-

trate large amounts of power in this region, while also omitting the desired smoothness due to the otherwise even distribution of radiation, however at a much smaller level, in the core and along the separatrix. Taking into account the position of the asymmetry and the structure and geometry of the bolometer camera system, this generally agrees with the findings from the prior phantom reconstructions. Integrated powers from both two-dimensional and detector signal profiles also deviate again by varying amounts within this set of tomographies and compared to the previous results. The congruence of the phantom radial plots among all artificial distributions though underlines the comparability of corresponding measures and deductions. Lastly, the relationship between $P_{\text{rad},2D}$ and P_{rad} between tomogram and phantom, as well as χ^2 is again inconsistent and thereby inconclusive, however this is in agreement with the last two phantom emissivity tomographies.

SOL Ring and 270° Core Anisotropy

The last phantom radiation distribution in this series of poloidally shifted core anisotropy reconstructions is, consequently, the same as before at an angle of $3/2\pi$, i.e. towards the outboard tip and lower side of the triangular plane. In figure 5.26, the artificial emissivity is produced using equation (5.19) with the same set of coefficients as for figure 5.26, except for $\vartheta_0 = 270^\circ$ or another $\pi/2$ shift of the poloidal location of the asymmetries peak in clockwise direction. As usual, all other parameter, including the two sets of k_{ani} are kept constant.

The localised maximum in the phantoms core in figure 5.26 is centred more towards the lower outboard magnetic island. In (a), the MFR finds the highest emissivity of 1.28 MW/m^3 in $0.7r_a$, closest to the lower edge of the latter island with a reduced poloidal expansion and sharper decay compared to the input data. This inside anisotropy is not distinctly separated from the emission that is placed along the separatrix and beyond. Significant radiation of $0.8\text{--}1.1 \text{ MW/m}^3$ can be found towards the opposite located magnetic island at the top and in the X-point on the lower inboard side, as well as the neighbouring X-points to the island closest to the anisotropy. With respect to the other tomograms of this k_{ani} profile, this one features a noticeable gap in the brightness distribution at the inboard top and center. Correspondingly, the MSD profile on the right reflects these characteristics with elevated error values of 2.5–3 %, particularly in and around the sep-

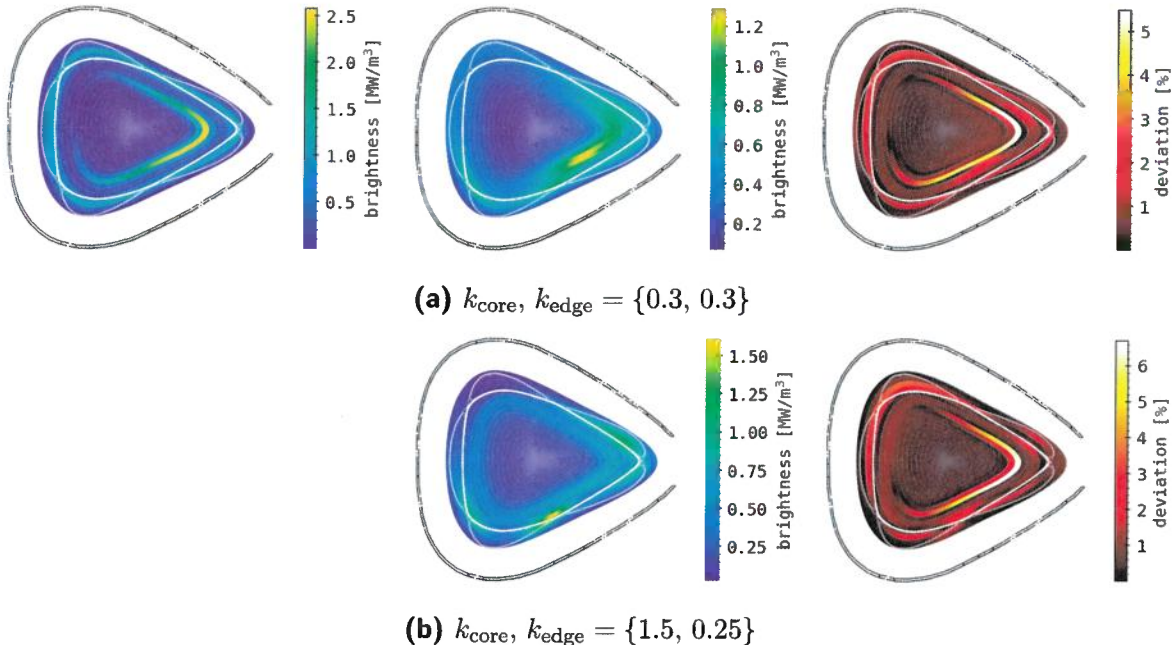


Figure 5.26.: (a), (b) Similarly constructed and reconstructed phantom radiation distribution as in figure 5.20, but the core structure has been rotated in clockwise direction by 270° . The tomographic inversion features the same RDA parameter combinations as before.

aratrix, except for the lower inboard X-point and outboard upper magnetic island. The global maximum is again located in the core where the input anisotropy is placed, i.e. around $\vartheta = 270^\circ$ with 5.5 % and large poloidal FWHM that spreads $\sim \pi/2$. In-between, smaller deviations around 2 % fill the area towards the tip of the triangular plane. Minor errors of 1.5 % are indicated in the radially outermost pixels on the inboard side from the discrepancy between the smeared out tomogram and sharp radial decay of the bright ring in the phantom.

In figure 5.26:(b), the second reconstruction for $k_{\text{ani}} = \{1.5, 0.25\}$ shows three distinctly localised bright spots of $>1 \text{ MW}/\text{m}^3$ in the inboard lower X-point, outboard upper magnetic island and lower central X-point with increasing intensity, wherein the latter is also the global maximum of $1.6 \text{ MW}/\text{m}^3$. The prior all have a similar shape of increased poloidal elongation and sharp

radial decay in both directions. Between the individual structures, outside the LCFS at the tip of the triangular bolometer plane and especially towards and around the location of the input emissivity, i.e. $0.7r_a$, a smooth and nearly constant brightness of $\sim 0.6 \text{ MW/m}^3$. The outboard side of the emissivity is slightly, almost unnoticeably brighter than the left by a few kW/m^3 . Remaining areas in the tomogram are without emission.

On the right, the corresponding MSD profile shows the impact of the local maxima through strongly varying error values along the separatrix and in magnetic islands in the range of 1.5–3.5%, particularly around the outboard side and aperture of the HBCm. The symmetrical bright ring around the core in the phantom, which is missing in the tomogram, is represented here by deviations $>3.5\%$ in $\sim 1.05r_a$. In the same location and with a similar shape and distribution as before, the global maximum is significantly larger at 6.35%. In-between the two features of the input profile, the discrepancy is noticeably smaller here at $\leq 2\%$.

The final set of line plots in this series of phantom radiation profiles, which corresponds to the previous combination of tomograms and MSD distributions in figure 5.26, can be found in figure 5.27. Regularisation weights, as well as phantom profiles are the same as before, while the latter are, obviously, also constant between the two rows (a) and (b). Integration of the artificial, two-dimensional distribution yields $P_{\text{rad},2D} = 19.357 \text{ MW}$ and extrapolation from the similarly congruent within this comparison forward measurement results finds $P_{\text{rad}} = 17.150 \text{ MW}$. Again, both are distinctly different to the previous values of radiation power, i.e. the latter is $>1 \text{ MW}$ or 14.5% larger and the prior $\sim 0.85 \text{ MW}$ or 4% smaller than for the initial phantom image. With respect to the last artificial distribution, this is also true, though to a lesser extent.

In (a), a slightly increased core brightness of 0.12 MW/m^3 is followed by an equally positioned and peaked inside local maximum of 0.52 MW/m^3 with a width of 0.1 m. A minor valley and, this time located on the inside of the separatrix, second maximum at $0.95r_a$ of 0.56 MW/m^3 and similar width conclude this radial tomogram profile at 0.3 MW/m^3 at the boundary. Integration of the corresponding two-dimensional image finds a radiation power of 19.517 MW or $<1\%$ more than in its phantom.

On the right, the phantoms forward integrated detector signals yield significantly higher powers at a maximum 2.5 mW in channel no. four of the VBCr, ca. 1 mW more than before. The relative intensity of the remaining

5.3. Phantom Radiation Profiles

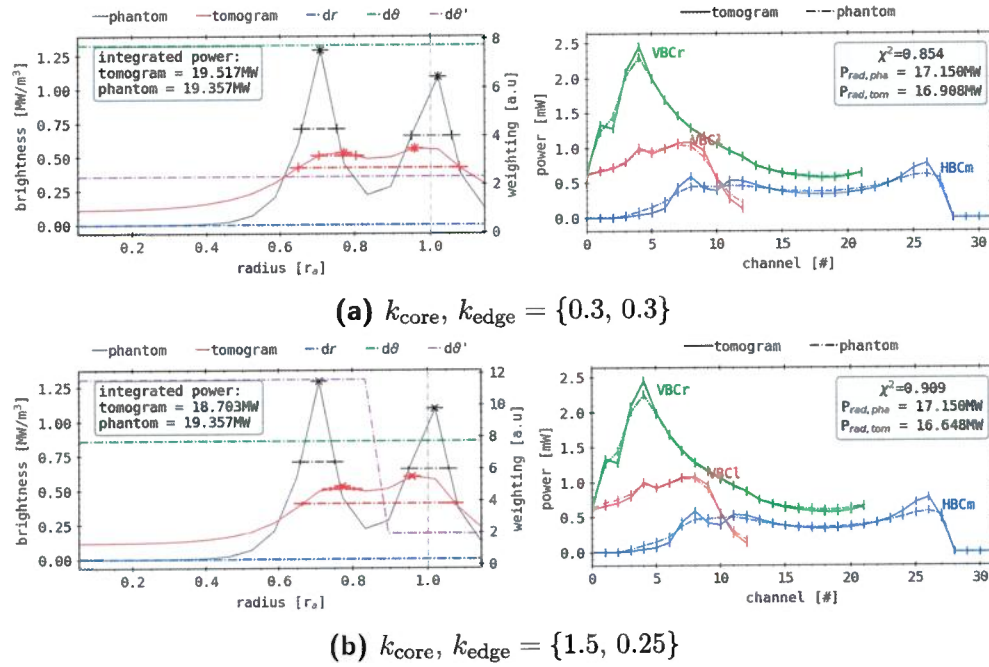


Figure 5.27.: (a), (b) Corresponding analysis for the results shown in figure 5.26, similar to figure 5.21, using the noted below anisotropy parameters for the tomographic inversion. The results are presented in the same way as in figure 5.19.

measurements is therefore decreased, though their total values do not differ as much. Left and right vertical camera arrays provide a respectively strong maximum towards the outboard side through VBCr detectors no. three to seven, a parabolic decay and comparatively weak core of <0.75 mW and a smoother second peak on the inboard side around 1 mW in absorber no. six to nine of the VBCl. The horizontal camera finds its maximum and the connected sharp decay on the lower side or between channel no. 24 and 28 at around 0.6 mW. Core and minor opposite side peak in this array are within 0.15 mW, while the upper part drop is smooth beyond detector no. 3. This weighting coefficient combinations tomogram profile is, again, generally within the respective error bars and therefore confidence interval, except for in locations of phantom plot extremes. In the VBCr plot, the outboard edge of the structure features an additional minor peak at 1.35 mW in channel

no. one. Coincidentally, the VBCI also shows a second, small bump in detector no. 4 within the profile of this arrays' measured local extremum. The horizontal cameras lower side maximum is larger here at 0.85 mW, whereas the other half of the array shows the already previously seen, connected two peaks and minima around 0.5 mW between absorber no. six and 13. In summary, this produces a fitness of $\chi^2 = 0.854$ a. u., which is the highest value among all $k_{\text{ani}} = \{0.3, 0.3\}$ reconstructions.

In (b), the radial profile is very similar to that on the top and akin to that in the first set of images corresponding to this weighting coefficient combination in figure 5.21. Core and inside peak portion of this plot show the same values and shapes with negligible variations in the absolute height of the local maximum. Localised towards the separatrix around $0.95r_a$ is the second peak at a slightly increased 0.63 MW/m^3 and of same width. Integration of the two-dimensional distribution yields $P_{\text{rad},2D} = 18.703 \text{ MW}$, significantly less than from the phantom at $>0.5 \text{ MW}$ or 3.4 %, particularly when compared to the above results.

Lastly, the forward integral detector signals on the right show comparable congruence to the phantoms results like before. Overall shape and absolute values are largely consistent to before and change only minutely. In parts, the local extremes are less pronounced, i.e. smaller or closer to the cameras phantom profile, as in the HBCm separatrix viewing absorbers no. six through twelve. However, some indicate larger discrepancies, like on the other side of the array between channel no. 23 and 27, or VBCr no. two and five. The range viewing the plasma core shows similar or better agreement between the input and output forward integrated data. Extrapolation of the respective signals finds $P_{\text{rad}} = 16.648 \text{ MW}$, now also smaller by 3 % than its correspondent from the artificial profiles. This ultimately produces a fitness of $\chi^2 = 0.909$ a. u., which is the overall and within the results of this particular set of k_{ani} second-highest matching quality, closely behind the first phantom reconstruction, where the core anisotropy was closest to the VBC detector arrays.

With respect to the two-dimensional results in figure 5.26, the shown tomograms are more akin in their reconstructive quality of the input radiation distributions to the initial set of images for $\vartheta_0 = 0^\circ$ than the two remaining MFR tomographies. Hence, not only is the perceived fitness of both tomograms greater than for the last reconstruction, but all measurements are in agreement with this evaluation. Still, though pointed out before already, the

development of χ^2 etc. and the subjectively worse match between phantom and tomogram for $k_{\text{ani}} = \{1.5, 0.25\}$ do not align here as well. Beyond that, both anisotropy coefficient profiles again yield, quantitatively, entirely different radiation distributions, while the first combination produces a more adequate result compared to the latter. Comparing with the other artificial radiation distribution tomographies, one can also find similar levels of diffusion of emissivity across the triangular plane on both images here. However, localisation and structural quality of maximum intensity regions are, at least in the case of figure 5.26:(a), significantly improved. Analogue trends to before of increased edge anisotropy and decreased, smoother emissivity in the core can also be found in this second reconstruction. Similar patterns, with respect to their relation within the benchmark of this type of phantom, can be noticed in the linear profiles and forward integrated detector signals in figure 5.27. Though the ratio of both total radiation power extrapolations within this set of tomographies is congruent, the evolution of χ^2 and MSD profile or maximum is not, which previously was also the case. Additionally, the presented MFR have provided yet another noticeably different sample of measurements, i.e. P_{rad} etc. for a (nearly) constant artificial input distribution. In conclusion, the sensitivity of the multicamera system towards this orientation of core asymmetries is akin to that of the first one. Local resolution and LOS coverage are improved in this area, near to the pinhole of the HBCm, as they also are closer to the VBC cameras aperture.

In summary, this exploration of superimposed, anisotropic phantom radiation images has provided significant insight into the efficacy and performance of the established *RDA MFR tomography* algorithm. Of particularly interest and relevance to later examinations of more complex artificial distributions is the gained experience about local sensitivity and its entanglement with the employed k_{ani} profiles. Especially important towards the tomography of experimental measurement data is the knowledge that explicitly opposite to the multiple camera apertures located structures or characteristics in the input distribution are more difficult to reconstruct and potentially yield quantitatively and qualitatively drastically different results for varying weighting coefficients. From the presented images and numbers it can be deduced that the congruence between input radiation profile and tomogram is primarily dependent on the distance of the emissivity and hence the local resolution and LOS coverage in that location. Fitness factor χ^2 ,

as well as a comparison between the integrated, two-dimensional radiation power and P_{rad} from the individual detector signals are not necessarily indicative of a good reconstruction, even across multiple k_{ani} combinations for the same set of input data. All the tomographies have in common that the pronunciation and absolute brightness, i.e. the sharpness of the particular localised features, of the artificial distribution is not entirely reproduced and the level of radiation is significantly reduced overall, though depending on the configuration relative trends are preserved to some extent. The selection of anisotropy parameters and their profile shape have also shown that, given the stark contrast in tomogram structures across the phantom variations, for $k_{\text{core}} > 1 > k_{\text{edge}}$ explicit anisotropic characteristics are lost and translated into the SOL. Here they are, for the given set of input profiles, mostly found in areas of increased LOS density - e.g. X-points and magnetic islands share areas of larger ε . This simultaneously also enforces smoother emissivity or less poloidal gradients in the core. Furthermore, at $1 > k_{\text{core}} = k_{\text{edge}}$, the inversion from LOS data of said properties is enabled in their original localisation, though with varying detail and width. Features of larger connection lengths or smooth and symmetrical emissions are not reproduced using such coefficients. Besides the two first tomographies in figure 5.20, i.e. for both k_{ani} profiles, the strong separation in the phantom between outside ring and core anisotropy is lost in the reconstruction. In case of (a), the radial width of both is increased and hence they partially merge in locations of higher intensity, while anywhere else it is decreased. With (b), except for the aforementioned localised peaks, core and SOL emissivity are largely the same and, if any, only show small minor gaps around the separatrix. This again supports the assumption of, on the one hand, unfavourable radiation distributions with respect to their structure corresponding to the bolometer camera system and, on the other, the need for specific, tailored regularisation weights for individual input data.

Employing the so far gained experience from the previous phantom emissivity tomographies, one will now continue to explore the weighting method and anisotropy coefficient space using established artificial input profiles, before extending the latter data space with more variations of complex, experimentally motivated structures.

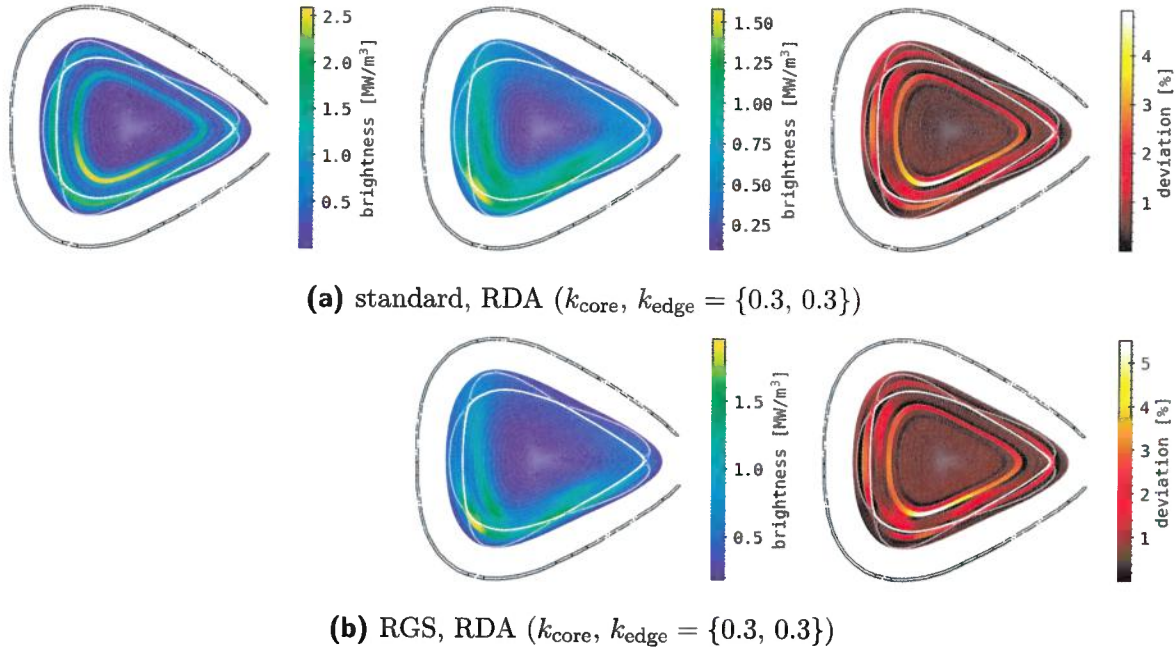


Figure 5.28.: Comparison between different reconstruction weighting methods, RDA and RGS, on the same phantom radiation distribution, using the same weighing coefficients and tomography parameters as well as camera geometries. The phantom image is constructed similarly to figure 5.20, while the outside ring at r_a is also adjusted to be poloidally asymmetric, with its maximum at the same position as the inner structure. **(a)** Standard Minimum Fisher information reconstruction with RDA. **(b)** Relative gradient smoothing, using the same RDA tomography parameters.

RDA vs. RGS

Before moving on, the first phantom radiation distribution will be revisited to examine the differences between *radially dependent anisotropy* and *relative gradient smoothing* regularisation methods when applied in a similar way. Both have been introduced in section 5.1.1 and section 5.1.2, while the prior has been employed extensively during the previous section. In order to adequately compare these results with one another, the same k_{ani} coefficients will be used with the RGS. One should keep in mind that this approach builds upon the RDA weighting of a given set of parameters.

In figure 5.28, the input phantom, resulting tomograms and MSD profiles for the two methods are shown. The artificial radiation distribution is based on the first superposition in figure 5.20, with a bright ring at r_a and a core anisotropy in $0.7r_a$, however with the change of similarly asymmetric intensity profiles in poloidal direction. The inside profile has a maximum of 2.5 MW/m^3 , while the one on the outside only 50% of that. Both of the structures feature the same orientation around $\vartheta_0 = 0^\circ$ - same definition as before -, a poloidal and radial width of $\sigma_r = 0.25r_a$ and $\sigma_\vartheta = \pi/4$, which gives

$$P_{\text{phan}}(r, \vartheta) = \frac{P_{\text{phan},0}}{(2\pi\sigma_r\sigma_\vartheta)^2} \left(\frac{1}{2} e^{-\frac{1}{2}\left(\frac{r-r_a}{\sigma_r}\right)^2} + e^{-\frac{1}{2}\left(\frac{r-0.7r_a}{\sigma_r}\right)^2} \right) e^{-\frac{1}{2}\left(\frac{\vartheta-\vartheta_0}{\sigma_\vartheta}\right)^2}.$$

The resulting phantom image is, as expected, largely an extension of the initially proposed core asymmetry at a higher intensity. For a constant k_{ani} profile of {0.3, 0.3}, the MFR tomography using just the RDA in (a) adequately reconstructs the two individual, radially separated emissivities, though with a significantly increased width in both polar directions. Immediately noticeable is the switched prominence of the two, where the outside is now the brighter structure with a maximum of 1.6 MW/m^3 and the inside is reduced to 1.25 MW/m^3 . An additional, much smaller secondary maximum can be found along the separatrix in the lower, central X-point of $\sim 1.35 \text{ MW/m}^3$. The greatly decreased separation between those extremes is lost towards the inboard top side and tip of the triangular plane, as well as opposite of the input anisotropy, where the relative intensity is also much more reduced compared to the phantom.

Its corresponding MSD profile therefore measures discrepancies $> 1.5\%$ along the separatrix all around the cross-section, in-between the position of the core and SOL structure. Also, the maximum error of 4.9 % is found at $0.7r_a$ towards 0° orientation due to the inversion of relative amplitude. All around at the LCFS and magnetic islands, the outside asymmetry produces variations of 1.8–3.2 %, with particularly larger values in the location of the secondary maximum and in the inboard lower and central island. Minor error values can be noted at the very edge of the domain and inside the core feature $< 1.5\%$.

At the bottom in figure 5.28(b), a RGS weighted MFR reconstruction for the same RDA k_{ani} coefficients finds a similar, however quantitatively distinctly different radiation distribution where local extremes are distributed

the same locally, though with significantly higher individual brightness. The global maximum at the lower inboard X-point is now at 1.95 MW/m^3 with a greatly reduced radial FWHM, while the inside anisotropy is mostly consistent with the above descriptions for a higher maximum intensity around 1.5 MW/m^3 . At the lower central X-point, the relative prominence of the previously found localisation is slightly reduced here at 1.6 MW/m^3 . The overall brightness in and around the remaining separatrix area and SOL is decreased due to the higher focus on the aforementioned extremes.

The respective MSD profile on the right hence shows smaller error values in the lower inboard location, though it finds higher discrepancies in the core of up to 5.5 % around $0.7r_a$ where the input inside asymmetry is located. Due to the otherwise strong qualitative congruence between the two tomograms, the second deviation plot is adequately described by the first one above.

Like before, figure 5.29 shows the corresponding one-dimensional radial and weighting, as well as forward integrated detector signal profiles of the above phantom and tomogram radiation images. All weighting coefficient profiles are at their usual level and are flat like before for $k_{\text{ani}} = \{0.3, 0.3\}$. Looking at the artificial distributions radial average plot, two similarly shaped peaks with a valley at 0.4 MW/m^3 can be found in $0.7r_a$ and $1.05r_a$, in descending order of 1.8 MW/m^3 and 1.45 MW/m^3 . Their FWHM differs minutely with $0.2r_a$ and $0.13r_a$ from inside to out. The inner core is dark up until $0.4r_a$, while at the edge of the domain one still measures 0.3 MW/m^3 . Integration of the two-dimensional emissivity distribution produces $P_{\text{rad},2D} = 26.921 \text{ MW}$ - significantly more than from any of the similar previous superpositions.

The detector signals on the right for the phantom radiation profile are also much higher compared to before. Both vertical cameras measure $>2 \text{ mW}$ and the global maximum in channel no. four of the VBCl finds 3.05 mW , corresponding on the lower inboard side with the brighter core anisotropy. A neighbouring peak around absorber no. eight is produced by the SOL asymmetry, followed by a decay to 0.2 mW in detector no. twelve at the edge of the array. The VBCr camera shows a smooth, parabolic core emissivity down to 1 mW and a conclusive, comparable to the inside peak in the left camera structure at 2.2 mW in channel no. four. Before decreasing to 1 mW at the edge in no. null, a small feature in absorber no. one interrupts this trend at 1.9 mW . The horizontal camera measures a maximum 0.9 mW in detector no. 26 on the lower side of the array and only 0.4 mW opposite in channel no. ten, with a shallow local minimum in the core at a similar intens-

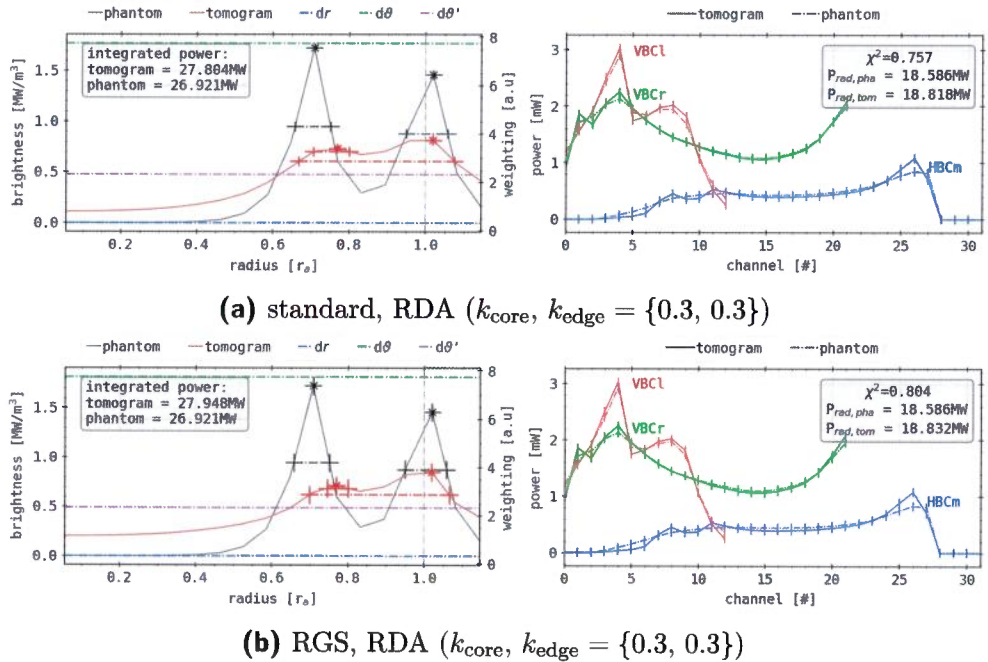


Figure 5.29.: (a), (b) Corresponding analysis for the results shown in figure 5.28, using the noted below anisotropy parameters for the corresponding tomographic reconstruction methods. The results are presented in the same way as in figure 5.19.

ity. While on the lower, right side of the camera the measured brightness drops sharply, on left towards the top a smooth decay until absorber no. two is found. Integration of the measurements yields a total camera observed radiation power of $P_{\text{rad,phan}} = 18.586 \text{ MW}$, which is also higher than for any of the previous phantom images, yet not in a corresponding level to the elevated $P_{\text{rad,2D}}$.

In figure 5.29:(a), the resulting tomograms poloidally averaged radial profile shows brightness inside the core of $>0.12 \text{ MW/m}^3$, increasing in a shallow parabola up until the first localisation in $0.72r_a$ of 0.8 MW/m^3 with a small FWHM of $0.15r_a$. After a minor valley, the second, global maximum of 0.8 MW/m^3 in $1.05r_a$ is more pronounced, though of similar width and shape, which is succeeded towards the edge by a steady decay to 0.4 MW/m^3 . Integrating the two-dimensional radiation distribution of the tomogram finds

5.3. Phantom Radiation Profiles

a total power of 27.804 MW, about 3.3 % larger than found in the phantom. Similarly, extrapolation of the forward calculated detector signals yields $P_{\text{rad}} = 18.818 \text{ MW}$, which is also 1.2 % larger than from the corresponding phantoms profiles. The prior are, overall, in positions of local extremes more pronounced and feature larger gradients. However, except for channel no. 26 of the HBCm, they remain within the individual error bars and therefore confidence interval. Around the latter, the horizontal camera produces a sharp peak for this distribution, while two smaller, separated structures are found around detector no. ten that are slightly above and their in-between minima below the phantoms lines. These generally only deviate $\pm 0.05\text{--}0.1 \text{ MW/m}^3$ from the respective phantom forward signals. Similar features appear in the tomograms profile of the VBCr between detector no. one and four. The respective fitness factor is calculated as $\chi^2 = 0.757 \text{ a. u.}$.

The results of the relative gradient smoothing method in figure 5.26:(b) show a comparable image in their radial profile p_r , showing a brightness of $>0.2 \text{ MW/m}^3$ in the core which increases similarly towards the first peak in $0.75r_a$ of 0.75 MW/m^3 . This localisation is particularly narrow at a FWHM of $0.075r_a$. A following local minimum is barely noticeable and blends seamlessly into the outside global maximum in $1.02r_a$ of 0.9 MW/m^3 with a $0.2r_a$ width. Summation of the respective two-dimensional distribution produces $P_{\text{rad},2D} = 27.948 \text{ MW/m}^3$, which is 3.8 % higher than in the phantom or 0.5 % than for the previous reconstruction. Correspondingly, the forward integrated absorber signals also show sharper local extremes and additional, smaller peaks in the same, aforementioned locations. They also remain, besides channel no. 26 of the HBCm, within the confidence interval of the individual phantom profile results and only show deviations in the range of $\pm 0.05\text{--}0.1 \text{ MW/m}^3$. Those minute differences are also expressed in the changes in $P_{\text{rad}} = 18.832 \text{ MW/m}^3$, which is 1.3 % larger than for the artificial forward results. Although the fitness is noticeably increased to $\chi^2 = 0.804 \text{ a. u.}$, a 6.2 % improvement compared to the application of just an RDA weighting. Comparing the application of standalone RDA and combined RGS and RDA regularisation weighting optimisations with the MFR tomography for the same phantom radiation profile and set of $k_{\text{ani}} = \{0.3, 0.3\}$ has produced only minor or almost negligible differences in the one-dimensional evaluations of radial and forward calculated profiles, or even integrated values of P_{rad} and $P_{\text{rad},2D}$. Deviations among those characteristic between the two sets of results are, on the one hand within the respective confidence intervals

of said profiles, and on the other of an order of magnitude that was previously observed by altering k_{ani} coefficients for a constant artificial radiation image. Like before, the cumulative trend of the changes from (a):RDA to (b):RGS+RDA is inconclusive at best due to the contradicting evidence presented by the singular power values, as well as the radial and camera profile and corresponding fitness factors. While the priors matching regresses, the latters congruence and quality improves noticeably. Therefore, judging just from the circumstances presented in figure 5.29, a combined RGS regularisation and RDA weighting tomography approach does not yield a significant advantage over just a standard MFR with RDA that would justify unrestricted utilisation instead of the latter. However, the two-dimensional distributions in figure 5.28 show a different picture which, subjectively, does favour the RDS+RDA with respect to the development and composition of the characteristic features of the phantom. Although the corresponding MSD profile does yield higher error values for the latter, strong separation between the core and SOL structures, as well as short, poloidal decay lengths are far more prominent here. Furthermore, the conclusive total brightness and its maximum also match the input data better, though one should keep in mind that none of the reconstructions is able to adequately invert the more intense anisotropy in the core and instead shift its feature to the separatrix. A possible drawback from this favoured stronger localisation of emissivity in the tomogram is the loss of less intense structures in close radial or poloidal proximity to said extremes and smoother profiles of larger connection lengths, i.e. the remainder of the bright rings opposite of the asymmetry.

This concludes the comparison between standard RDA weighting and combined RGS+RDA MFR tomography. A more elaborate and detailed exploration of said topic with more examples will not be performed here, nor be of subject to this work. Zhang et al.[106, 168] have already done such an extensive analysis. The above examinations only serve to further verify the standalone radially dependent anisotropy regularisation, which has been done so.

5.3. Phantom Radiation Profiles

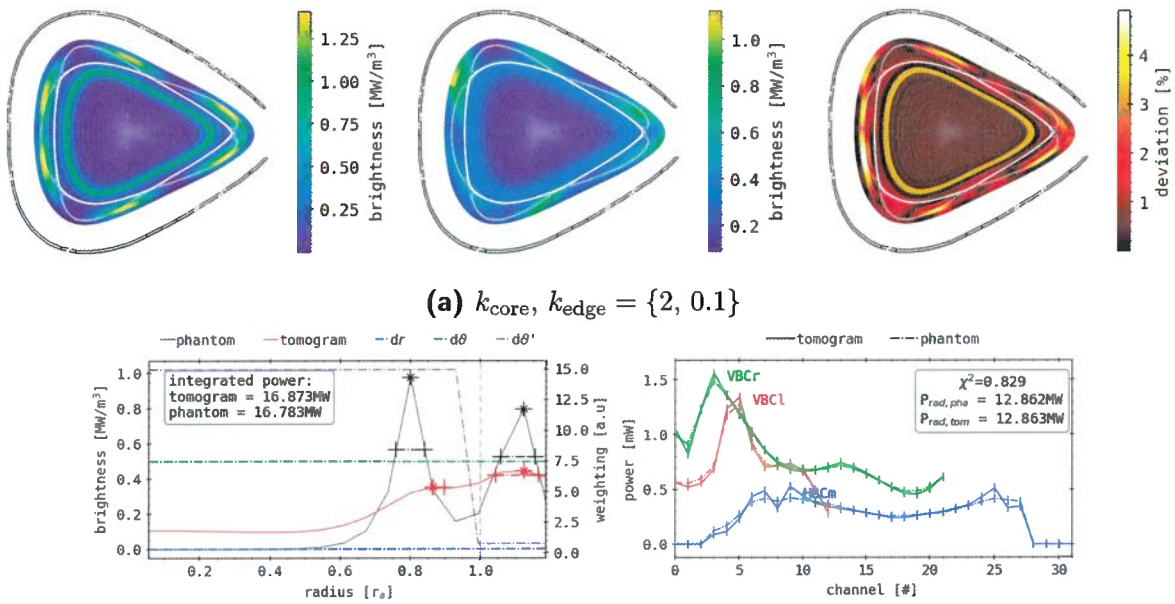


Figure 5.30.: Phantom radiation distribution reconstruction, mimicking a bright plasma core with six intensity maxima around the five islands of the magnetic standard configuration. The RDA coefficients that have been used support the accurate reconstruction of the designed profiles in the tomographic algorithm. **(a, top)** Phantom, tomogram and relative deviance, similar to figure 5.18. **(down)** Radial (left) and chordal (right) profile analysis, similar to figure 5.19.

5.3.3. Experimentally Motivated Anisotropic Phantoms

In the following paragraphs one will explore more complex, experimentally motivated and therefore particularly challenging to reconstruct phantom radiation profiles. The focus here will be specifically localised anisotropic distributions that also feature additional extremes in positions and number of the magnetic island and intersecting X-point structure. With the knowledge and experience gained from the previous analysis, this should prepare for and build the foundation necessary to adequately and confidently Reconstructive actual experimental data later on.

The first of this set of artificial emissivity profiles in figure 5.19 is a superposition of a symmetrical bright ring in the core at $0.7r_a$, like before, and a

distribution of six singular, localised structures around the triangular plane in the SOL, close to the magnetic islands in $1.1r_a$. This outside anisotropy is constructed *up-down* symmetrically, i.e. the discrete representation of the emissivity yields $P_{\text{rad}}^{(i,j)} = P_{\text{rad}}^{(i,n_\vartheta-j)}$, where n_ϑ is the number of poloidal bins and i and j the radial and poloidal indices for pixel $p^{(i,j)}$. One should note that this is trivial for n_ϑ even, however for an odd number of bins we construct the emissivity so that in pixel $p^{(i,m)}$ for $m = (n_\vartheta - 1)/2 + 1$ the absolute value is the average of the neighbouring cells, so essentially $P_{\text{rad}}^{(i,m)} = P_{\text{rad}}^{(i,m-1)}$. Using

$$m = \begin{cases} (n_\vartheta - 1)/2 + 1 & \text{for } n_\vartheta \text{ odd;} \\ n_\vartheta/2 & \text{for } n_\vartheta \text{ even} \end{cases},$$

$$\text{owidetilde}P_r^{(i,j)}(P, r_0, \sigma) = \frac{P}{2\pi\sigma^2} \exp\left(-\frac{1}{2}\left(\frac{r^{(i)} - r_0}{\sigma}\right)^2\right),$$

the up-down split phantom emissivity can therefore be written in two parts as

$$\begin{aligned} j \leq m : \quad P_{\text{phan}}^{(i,j)} &= \tilde{P}_r^{(i,j)}(\hat{P}, 0.7r_a, \sigma_r) + \frac{3}{2}\tilde{P}_r^{(i,j)}(\hat{P}, 1.1r_a, \sigma_r) \times \\ &\quad \frac{1}{2\pi\sigma_\vartheta^2} \exp\left(-\frac{1}{2}\left(\frac{1 + \sin(\vartheta^{(j)}\delta_\vartheta + \vartheta_0)}{2}\right)^2\right). \\ j > m : \quad P_{\text{phan}}^{(i,j)} &= P_{\text{phan}}^{(i,m-j)} \end{aligned} \tag{5.20}$$

Here, the radial width is designed as before, i.e. $\sigma_r = 0.25r_a$ while the poloidal dimension of the SOL anisotropies is set to $\sigma_\vartheta = 0.2617 \text{ rad}$ or $\pi/12$. The amplitude of the phantom is set to $\hat{P} = 1 \text{ MW/m}^3$, which directly corresponds to the brightness of the core structure. Hence, outside the separatrix, the individual island-like spots have a maximum of 150% of the prior intensity. Due to the already mentioned difficulties of mapping continuous emissivity distributions to such relatively large and coarse, discrete pixel grid, the actual global maximum brightness in the phantom yields 1.41 MW/m^3 . Two new parameter δ_ϑ and ϑ_0 are introduced, which will also be featured in the following artificial distributions, as the *poloidal frequency of the anisotropies*, i.e. the spatial periodicity of the structures (in the SOL) and an angular offset. Here, for $j \leq m$ or $\vartheta^{(j)} \leq \pi$ - the definition of the poloidal

bin number and dimension is changed from before to have its origin towards the center of the HBCm pinhole - one can find three distinguishable bright spots outside the LCFS. This is equal to $\sigma_\vartheta = 0.9549 \text{ rad}^{-1}$, while the first local maximum is rotated about one fourth of this period away from $\vartheta = 0$ and therefore $\vartheta_0 = 0$. On the opposite, inboard side at $j = m$ or $\vartheta^{(j)} = \pi$, a small minimum separates the two structures that are mirrored around a hypothetical, horizontal median through the HBCm aperture and magnetic axis. Both are aligned along the outside edge of the corresponding island and spread into the neighbouring X-points. The same is true for the two remaining sets of up-down symmetric bright spots with respect to their closest magnetic island.

A first reconstruction of the above artificial radiation distribution for $k_{\text{ani}} = \{2, 0.1\}$ can be found in the center of figure 5.30 as per usual. The anisotropic weighting profile is again given by Θ_{N_T} for $N_T = 17$, a simple step from k_{core} to k_{edge} (see section 5.3.1), and is designed to emphasize smooth structures of large angular width in the core for $r < r_a$ and anisotropic brightness profiles with smaller poloidal expansion. Immediately standing out is the now distinct asymmetry around the core between the individual mirrored, artificial peaks. Particularly the top inboard bright spot is far more intense with its global maximum of 1.15 MW/m^3 , while also being shifted closer to the corresponding X-point around $1.25r_a$, very close to the domain boundary. The respective lower structure is significantly weaker in its brightness with $\sim 0.6 \text{ MW/m}^3$ and is reconstructed even closer to the lower separatrix intersection than the upper. Neighboring to those, towards the pinhole of the HBCm, the up-down discrepancy is reversed so that the lower structure shows 0.9 MW/m^3 and the upper just around 0.6 MW/m^3 . However, their individual positions here are generally in very good agreement with their input counterparts, though with a lesser poloidal width and slightly increased radial expansion. In-between the previous two sets, no noticeable emissivity can be found in and outside the LCFS. On the outboard side, closest to the horizontal camera aperture, the upper bright spot is reconstructed similarly in agreement with the phantom at a reduced intensity of 0.9 MW/m^3 and larger radial expansion. Its mirrored feature on the lower side though is shifted towards the HBCm and domain boundary with a smaller brightness of 0.8 MW/m^3 and extends poloidally into the corresponding magnetic island. In the core, a very weak, smooth emissivity distribution can be noticed with just 0.45 MW/m^3 that extends from $0.65r_a - 0.95r_a$ and has a very small

gap along the separatrix to the enclosing bright features.

The MSD profile on the right shows complex structures around the LCFS and within the magnetic islands of $3\text{--}4.9\%$ that are distinctly pronounced and largely coincide with the individual localisations of the respective bright spots in the SOL. Furthermore, minor variability is found in-between said features with $<2.5\%$. Particularly the reconstructed, at the domain boundary localised emissivity yields additional variance of $3\text{--}3.5\%$ in that location. Towards the LCFS, the radially wide and blurred tomographic inversion of the core ring produces errors of $\leq 1.8\%$ at the separatrix and a constant 3.5% at $0.7r_a$, the location in the input profile.

The bottom two images in figure 5.30 present the radial and camera forward integrated chordal brightness profiles, including the regularisation weights across the radius as per usual. In the plot on the left, the phantom yields two pronounced, sharp maxima in $0.8r_a$ and $1.12r_a$ of 1.0 MW/m^3 and 0.8 MW/m^3 in the poloidally averaged radial profile, respectively. In-between the prior global maximum and outside peak with individual FWHM of $0.15r_a$ and $0.2r_a$, there is a distinct local minimum of 0.15 MW/m^3 in $0.92r_a$. No significant emissivity is found in the core until $0.55r_a$. The reconstructed radiation profile produces $\sim 0.1 \text{ MW/m}^3$ until $0.6r_a$, after which a small plateau with a shallow slope follows to 0.35 MW/m^3 up to $0.9r_a$. A conclusive peak in $1.15r_a$ at 0.45 MW/m^3 with a width of $0.1r_a$ extends until the domain boundary. The corresponding radial and poloidal regularisation weight profiles dr and $d\vartheta$ are as before, while the step in the modified anisotropic $d\vartheta'$ is now located in $0.975r_a$, right in-between the input profile extremes, from 15 a. u. down to 0.75 a. u. Integration of the two-dimensional phantom and tomogram images yield $P_{\text{rad},2D} = 16.783 \text{ MW}$ and 16.873 MW respectively, which corresponds to a 0.5% deviation.

On the right, the forward integrated camera profiles are shown. Extrapolation using said pseudo-measurements finds very strong agreement between the two with $P_{\text{rad}} = 12.862 \text{ MW}$ and 12.863 MW from the phantom and tomogram. However, the fitness factor $\chi^2 = 0.829$ a. u., when compared to the previous phantom image tomographies and their evaluation, is not particularly high yet within the range of adequate reconstructions. Forward integration of the artificial radiation profile shows a generally smooth line for the HBCm, where the core is slightly hollowed between channel no. 12 and 23 down to 0.25 mW . From absorber no. two to seven, i.e. from the upper side of the triangular plane, the perceived brightness increases steadily

5.3. Phantom Radiation Profiles

to 0.37 mW, while on the other side between detector no. 24 and 27 the power is nearly constant around 0.4 mW, after which a sharp decline to zero follows. The left vertical camera finds a very dominant peak in channel no. four and five of 1.2–1.25 mW that similarly drops quickly on both sides. Towards the core and detector no. zero, the profile increases minutely again, whereas towards the SOL and edge a small plateau between no. seven and ten around 0.8 mW is concluded by decay to 0.3 mW. Finally, the VBCr plot shows the global maximum in absorber no. four with 1.55 mW with linear declines on both sides. At the outboard side, from a small valley of 0.8 mW in detector no. one a step up to 1 mW concludes the right-hand sight of the camera fan. Towards the core and VBCl, the drop turns into a slight positive slope in absorber no. nine and minor peak of 0.7 mW in no. 13. A subsequent smaller decay to a secondary minimum of 0.45 mW in no. 19 is terminated by a small increment.

Overall, the tomograms forward calculated profiles are very similar in shape and character, while remaining within the indicated error bar confidence interval. However, in locations of extremes in the vertical camera plots it is more pronounced and exceeds or falls below the latter range by ≤ 0.1 mW. In the HBCm profile, additional features can be found on both sides of the core between channel no. five and ten, as well as no. 24 and 27. Towards the upper part of the SOL and separatrix, two small peaks in no. seven and nine of up to 0.5 mW, ca. 0.15 mW over the phantom baseline are separated by a lower minimum. On the other side, just one local maximum in no. 25 at 0.5 mW is followed by a sharper drop.

The performed and examined reconstruction in figure 5.30 using $k_{\text{ani}} = \{2, 0.1\}$ is able to find the specifically designed poloidal anisotropies with a sharp outline and close to their original position in the input phantom, while also reproducing a smooth, less bright structure in the core. However, this does not come without the introduction of a significant asymmetry in the island-like localisations around the separatrix, particularly where the LOS density and sensitivity is increased - this pattern has already been discussed before -, i.e. in front the HBCm and VBCl pinhole and the largest intersection of their LOS cones. Respective to the radial profile and its discrepancy with the artificial input, a strong radial broadening of the inside emissivity is highlighted here, though the SOL features yield only slightly higher radiation power on average. The outstanding congruence between the individual integrated and extrapolated power values $P_{\text{rad/2D}}$ underlines the

overall quality of the tomogram, which is supported by the good agreement of the forward calculated camera measurements and their corresponding fitness factor χ^2 . The latter describes an adequate reconstruction, however of no exceptional grade if estimated by solely with value. Again, like for all previous phantom MFR tomographies, a large variance in the singular power numbers when integrating from two- or one-dimensional profiles is found. The difference between the *actual* total power from the phantom and tomographic radiation profile and the absorber signals is greatly increased relatively and in absolute terms when compared to reconstructions of similar fitness, i.e. figure 5.27, though equally reduced or improved next to figure 5.29 and alike.

This MFR of a more complex, experimentally motivated phantom brightness profile using the same tools and gained knowledge from previous tomographies as a first attempt has proven successful. Given the *best-guess* anisotropic weighting profile and parameter combination, the achieved results adequately present both quantitative and qualitative features of the artificial input image. This is another important step towards the reconstruction of actual experimental data. Furthermore, in the following segment varying sets of k_{ani} for the same phantom and MFR method will be explored to solidify and expand the experience for this set of tools towards such data.

Anisotropic Weighting Parameter Variation

In figure 5.31, the same artificial emissivity distribution as in figure 5.30 is reconstructed using three drastically different, yet characteristically similar k_{ani} profiles. The goal is, in principle, to evaluate the impact of varying weighting factor ratios and orders of magnitude for such a given phantom that features anisotropic as well as smooth and uniform structures. A starting point is the already established benchmark for a set of $k_{\text{core}} = 2 \text{ a. u.}$ and $k_{\text{edge}} = 0.1 \text{ a. u.}$ from before. Hence, this parameter set is extended by (a) $k_{\text{ani}} = \{2, 0.3\}$, (b) $\{20, 0.3\}$ and (c) $\{2, 0.6\}$. For all of these, the regularisation weights configuration is the same as before, i.e. RDA method with a shape of Θ_{N_T} for $N_T = 17$. Furthermore, though in contrast, an extended examination is not performed here and the presentation of one-dimensional profiles as well as singular power values or fitness factors omitted. The focus is, after having already proven the generally applicability of this approach, to classify the new parametric weights with regards to their capability to

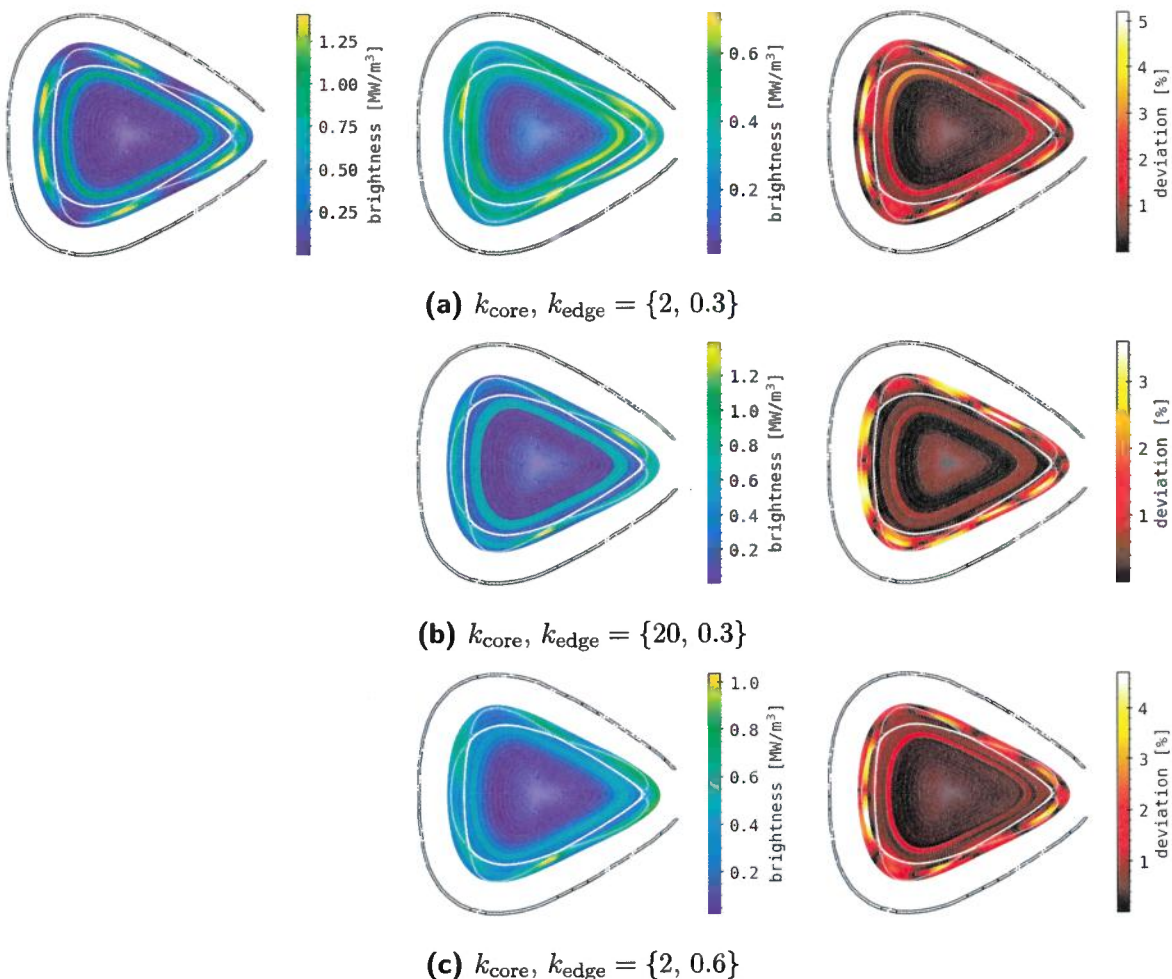


Figure 5.31.: MFR tomography like in figure 5.30 where the RDA coefficients have been varied and are noted below. **(a, top)** Phantom, tomogram and relative deviance, similar to figure 5.18. **(b, c)** Only the reconstruction and its respective error to the phantom image like above.

qualitatively reproduce the characteristic features in the artificial profile. In the top row of figure 5.31, the input emissivity distribution and corresponding reconstruction and MSD profile for the anisotropy coefficient set (a) are shown. This combination emphasizes comparatively three times larger

connection lengths in the SOL than the prior benchmark. One can easily establish that the maximum brightness is significantly decreased here with 0.75 MW/m^3 . This intensity however can be found in multiple places around the core: at the outer edge of the upper and lower outboard magnetic island, in the lower midplane X-point and inside the middle inboard island, towards the upper neighbouring separatrix intersection. In the SOL, the space in-between those localisation is relatively bright also at $>0.35 \text{ MW/m}^3$ and establishes a smooth and almost continuous ring that partially expands until the domain boundary. Particularly the first mentioned bright spot is accompanied by an elevated emissivity of $\sim 0.6 \text{ MW/m}^3$ inside the island structure. Inside the LCFS, a weakly detached from the outside, similarly wider and nearly symmetrical hollow ring can be found outwards from $0.7r_a$. It is also of about the same intensity as the SOL profile, while its local maximum closer to the HBCm pinhole is around 0.61 MW/m^3 . A corresponding MSD distribution on the right yields error values of up to 5.2 % in the locations of the input bright spots in the SOL. Along the island chain an average discrepancy of about 2.5 % is noted, though the input core ring at $0.7r_a$ leads to an also separated ring of increased variation of 2–3.4 %, where the profile is inverted to that in the tomogram.

The second row in figure 5.31 for parameter set **(b)** $k_{\text{ani}} = \{20, 0.3\}$ shows its respective MFR tomogram and MSD error distribution. This weighting combination again prefers longer connection length characteristics in the SOL and now amplifies emission from the core compared to the benchmark and prior reconstruction. Evolution of the ratio between k_{core} and k_{edge} from 20:1 to 6.67:1 to 66.67:1 underlines the change in focus of the regularisation coefficients towards concentration of radiation in the edge and then inside the LCFS. Hence, the tomogram finds its global maximum of 1.4 MW/m^3 in only two, more concentrated localisations at the inside of the upper outboard and edge of the inboard lower magnetic island towards the X-point. Minor variations can be found along the otherwise nearly continuous emissivity along the $1.1r_a$ radius with an intensity of $0.9\text{--}0.95 \text{ MW/m}^3$. At the tip of the triangular plane, the brightness expands outward until the domain boundary. A void gap separates the SOL from the sharply differentiated core profile at $0.7r_a$ with a smooth emissivity of 0.8 MW/m^3 . Correspondingly, the maximum error value is reduced to the overall higher radiation power in the tomogram at the respective radii. Coincidentally, outside the separatrix, the missing phantom characteristics are represented by 3.2–3.6 %

5.3. Phantom Radiation Profiles

deviation in and around their individual location. Like for the above image, the area in-between also shows elevated levels of discrepancy $\sim 1.6\%$. Inside the LCFS, only minor errors $\leq 1\%$ can be found around $0.7r_a$. At the very center for $< 0.3r_a$, negligible variance of $< 0.6\%$ encapsulate the magnetic axis.

Finally, the last line of plots in figure 5.31 presents the reconstruction and MSD for $k_{\text{ani}} = \{2, 0.6\}$, which now yields a core to SOL ratio of 3.33:1. The focus now is changed again to smoother, longer connection length characteristics in the SOL and less emphasis on a radiation majority in the core, which is underlined by the singular maximum outside the separatrix and secondary minor localisations. Sharply separated at the lower midplane X-point from the rest of the edge profile, an emissivity of 1.05 MW/m^3 contrasts the otherwise comparatively even and less intense, larger structures around the LCFS. Closer to the HBCm pinhole and opposite the global maximum, the brightness is slightly elevated around 0.85 MW/m^3 . Minor, almost negligible variations of 0.7 MW/m^3 also show on the inboard side near the respective X-points. They can be noticed at and close to the separatrix intersections around the triangular plane. The area in-between the prior features and ring at the core in $\sim 0.7r_a$ are at 0.55 MW/m^3 , while the latter is widened and fully symmetric. The final, corresponding MSD next to this tomogram yields increased error values of $3.5\text{--}4.6\%$ in locations of the phantoms input SOL characteristics and particularly the inboard lower magnetic island, where the global maximum of 4.7% is found. Due to the smoother and widened emissivity in the area surrounding those and beyond the separatrix, similar structures of $\sim 1.6\%$ deviation appear in the profile here. In $0.7r_a$, a distinct ring of increased discrepancy with a minor asymmetry closer to the inboard side of $1.8\text{--}2\%$.

Of the examined MFR tomographies in figure 5.31:(a)-(c), none exceeds the subjective quality that has been achieved in figure 5.30 by $k_{\text{ani}} = \{2, 0.1\}$. Irrespective of the quantitative agreement between artificial and reconstructed radiation distribution, the latter yields a significantly better distinction of SOL localisation, with furthermore largely reduced erroneous emissivity in-between and a continuous profile at the target location inside the LCFS at the same time. However, certain aspects of the input phantom are highlighted more in the other tomograms, i.e. a clearly separated and relatively brighter, symmetrical ring in the core for $k_{\text{core}} = 20 \text{ a. u.}$ or individual, more focused spots on the outside. Though the opposite effect presents when the

$k_{\text{core}} : k_{\text{edge}}$ ratio is shifted away from the previous sets trend, as is shown by the images in the top. Increasing the SOL regularisation weight further yields a lessened maximum intensity and stronger characteristic smoothness in that area, while the separation from the core and its relative brightness is hence more pronounced in the bottom. In conclusion, the tomographic inversion for such a - in the case of experimental data potentially - complex radiation distribution of varying symmetric and anisotropic profiles inside and outside the separatrix is benefited by a set of k_{ani} coefficients with a ratio of 10:1 and higher but no larger than 50:1 depending on the individual focus. Judging from the given tomograms and their RDA weights, an initial, educated guess for a set that adequately suits the reconstruction of smooth emissivities in the core and short connection length features in the SOL can therefore be constructed using $k_{\text{core}} = 2\text{--}10 \text{ a. u.}$ and $k_{\text{edge}} = 10^{-2}\text{--}0.5 \text{ a. u.}$ for similar profile shapes to section 5.1.1. Trivially, the opposite case is also true for equally inverted profiles.

Artificial Camera Supported MFR Tomography

Remaining still with the superimposed *island-like* phantom radiation distribution from figure 5.30, given the complexity of the image and the challenges its inversion poses, additional tomograms are produced using an extended set of cameras and therefore LOS that incorporate the previously introduced artificial *MIRh* from section 5.2.3. Exploration of said emissivity reconstruction using the vertical mirror array *VBCm* is omitted for the sake of simplicity - due to the position of the new camera and discrepancies in previous tomograms the latter is also expected to be less beneficial in those circumstances.

Results for a MFR tomography using the supplementary set of fifteen artificial detectors on the inboard side, covering the entire triangular plane are shown in figure 5.32. Regularisation weights and anisotropic coefficient profile $k_{\text{ani}} = \{2, 0.1\}$ are kept the same as in the first case. The new arrays forward calculated signals in (b) are indicated with ARTf (pseudonym for *ARTificial*). In (a), the tomogram shows a maximum brightness of 0.94 MW/m^3 around the SOL close to the upper inboard side X-point, at the outside edge of the upper outboard magnetic island and in the lower central X-point. Less bright localisations with $0.65\text{--}0.9 \text{ MW/m}^3$ in the remaining positions of the input characteristics can be found in the reconstruction. The

5.3. Phantom Radiation Profiles

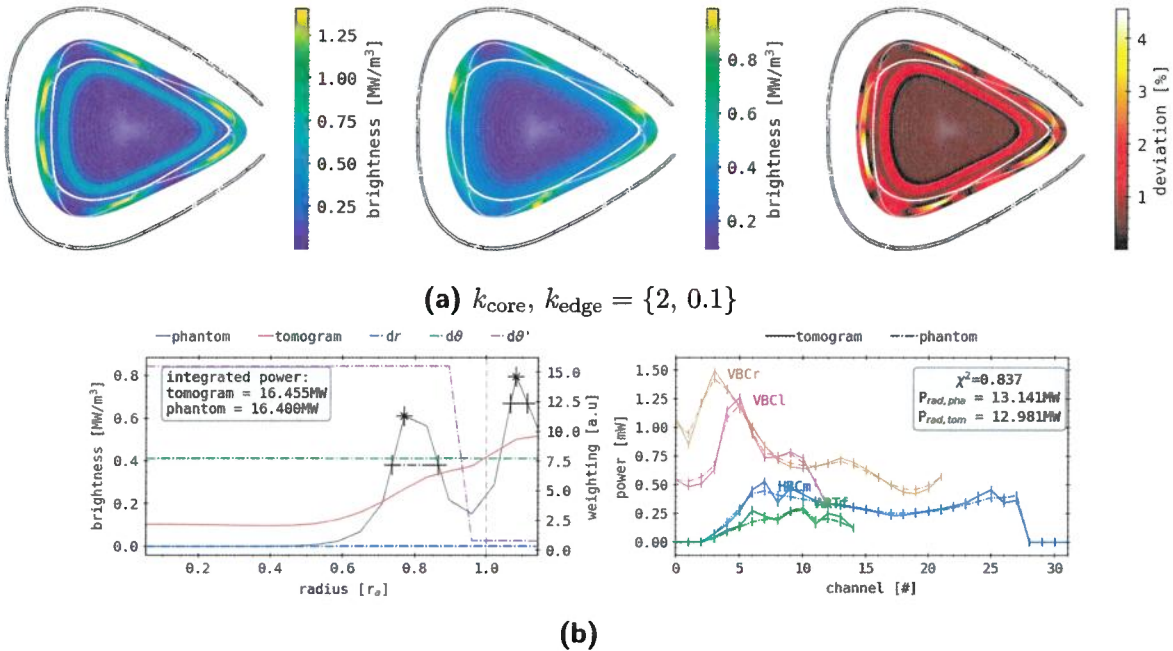


Figure 5.32.: Phantom radiation distribution reconstruction, mimicking a bright core and islands-like structures in the edge like in figure 5.30. In this case, the camera system is extended by an artificial, secondary horizontal camera on the opposite (poloidally) side of the HBCm - its geometry has been introduced in figure 5.15. The chosen RDA coefficients support the reconstruction of the given phantom distribution. (a) Phantom, tomogram and relative deviance, similar to figure 5.18. (b) Radial (left) and chordal (right) profile analysis, similar to figure 5.19. The new camera *MIRh* has been added in the chord brightness profile.

latter structures feature a slightly increased radial width compared to the phantom, while some also partially extend beyond the LCFS and towards the domain boundary, i.e. inboard and at the bottom middle X-point. They are accompanied by an also radially smoothed and symmetrical core ring of 0.5 MW/m^3 , coincidentally lacking the visible separation from the SOL emissivity into which it blends over.

On the right, the MSD yields a maximum error of 4.6 % outside the separatrix, precisely where the input phantoms bright spots are located, except

for the top outboard and inboard pseudo magnetic islands. In-between in smaller groupings, towards the LCFS and slightly beyond into the core, deviation values of 1.6–2 % are presented. A minor gap in radial direction is followed by a concentrated ring around $0.7r_a$ with a discrepancy of 2.2 % and a smooth core at <1 %.

In figure 5.32:(b), the usual composition of radial, anisotropic and forward calculated detector signal profiles are shown, accompanied by the singular two- and one-dimensional integrated power values. The shown regularisation weight and k_{ani} , as well as the phantoms poloidally averaged plots are the same as before. Though the general shape of the tomograms profile is similar, the minor peaks found previously for reconstructions of this artificial emissivity distribution are negligible here. In $0.8r_a$ and $1.1r_a$, small variations in the increasing slope in brightness from $0.5r_a$ and 0.1 – 0.52 MW/m^3 at the boundary are shown. Inside the core, up until the latters base point, the brightness is relatively constant around 0.95 MW/m^3 . An integrated power of $P_{\text{rad},2D} = 16.455 \text{ MW/m}^3$ corresponds to a 0.3 % deviation from the phantom. On the right, the individual camera forward calculated signals are extended by the results for ARTf. Qualitatively, the reconstructed results are similar to those from before, i.e. in figure 5.30:(b), though the per-absorber deviation is minutely increased, partially beyond the given confidence intervals for the vertical cameras. With respect to the extremum features presented in the phantoms profiles of all cameras, the tomograms lines are less articulated here compared to the previous results. The new artificial array yields signals of up to a maximum of 0.3 mW for both images, while the phantom shows a steady and smooth increase from channel no. two through ten after which a minor drop to 0.15 mW in no. eleven and conclusively 0.1 mW in no. 14 follows. Around detector no six and twelve, the phantoms plot presents noticeably pronounced local maxima beyond the error bars up to 0.3 mW . Extrapolation using the absorber data from the artificial profile finds $P_{\text{rad}} = 13.141 \text{ MW}$ and the reconstructed image 12.981 MW , yielding a 1.2 % deviation and an overall fitness of the tomogram of $\chi^2 = 0.837 \text{ a. u.}$. With respect to the first set of results in figure 5.30 and constant k_{ani} , the MFR employing an additional set of LOS from the artificial MIRh presents a subjectively improved radiation profile with significantly more distinct and accurately localised spots in the SOL. No improvement can be noticed in the separation or intensity of the emissivity inside the separatrix. However, judging from the poloidally averaged and forward calculated, one-

dimensional plots, including the integrated powers and fitness coefficient, a quantitative upgrade can hardly be argued for, especially given the previously examined variability in those parameters for different regularisation weights. This furthermore does not equate to a degradation in MFR results, though it can be concluded that the complementary detectors and their area of observations yield a positive effect on the tomographies quality for complex, superimposed radiation profiles of this kind. Conceptually, assuming that the point-of-view and orientation of the new camera significantly differs from the others, adding more LOS and therefore measurement points undeniably enhances the regularisation capabilities. Most critically, at least $(N_{\text{HBC}} + N_{\text{VBCr}})$ and at most $N \times (N_{\text{HBC}} + N_{\text{VBCr}})$ new intersections contribute to the algorithmic inversion and the N new absorber to $\mathbf{T} \in \mathbb{R}^{n \times m}$ - remember that n is the total number of absorbers and \mathbf{T} the transmission matrix. As discussed earlier, this also makes the geometric expression of local sensitivity more robust towards perturbations, as one can trivially verify using the same argument regarding the norm of the extended \mathbf{T}' and its condition $\kappa(\mathbf{T}')$, see Ghaoui et al.[193].

Inverted Anisotropic Phantom

For sake of completion, an inverted phantom to the original in figure 5.30 and 5.31 is reconstructed using an also reversed regularisation weight profile with $k_{\text{ani}} = \{0.3, 0.2\}$, and shape given by section 5.1.1. The artificial radiation distribution and MFR results are shown in figure 5.33 in the usual form.

On the left, the inside-out turned phantom shows a maximum brightness of 1.2 MW/m^3 , now in the core at $0.7r_a$ in eight up-down symmetrically distributed localised spots. Analytically, this profile can also be described by equation (5.20) when parametrically reconfigured with $r_{0,1} = 1.1r_a$ and $r_{0,2} = 0.7r_a$, i.e. the reversed order from before. Hence, a smooth ring of 1 MW/m^3 is found outside the separatrix in the SOL. Challenging with this particular phantom tomography is the potential obfuscation due to possibly increased interference from the symmetrical structure, given the position and orientation of the vertical and horizontal bolometer cameras. In the center of (a), the tomogram shows a continuous emissivity at the domain boundary and towards $1.1r_a$ of 0.55 MW/m^3 . This is followed by a comparatively sharp drop inwards to 0.35 MW/m^3 beyond the separatrix until $0.7r_a$ with

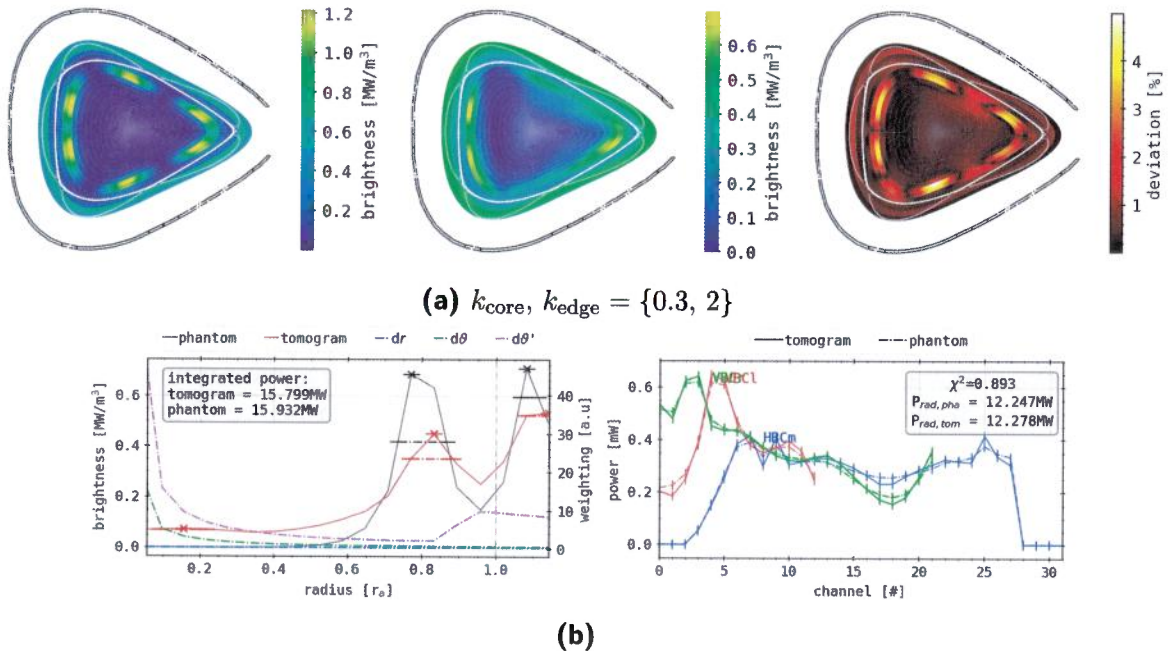


Figure 5.33.: Phantom radiation distribution reconstruction, mimicking a bright outside ring and islands-like structures on the inside of that ring, similar to figure 5.30 but inverted. The RDA coefficients have been changed accordingly to accompany the different orientation of poloidally symmetric and anisotropic radiation distributions. (a, top) Phantom, tomogram and relative deviance, similar to figure 5.18. (b) Radial (left) and chordal (right) profile analysis, similar to figure 5.19.

minor, unstructured variability in-between. At that radius, three prominent features can be found around the triangular plane: two, nearly symmetrical elongated bright spots towards the inboard magnetic island, separated by a small local minimum, where the lower is slightly increased in size and one larger at the outboard tip, extending into the lower half. All the prior have a strongly localised maxima of 0.69 MW/m^3 . Secondary, significantly weaker characteristics present close to the central top and bottom X-points at that same radius with $< 0.5 \text{ MW/m}^3$, isolated by distinct voids in brightness. For $< 0.7r_a$, only minor emissivities of $< 0.45 \text{ MW/m}^3$ are shown towards to the upper magnetic islands.

On the right in figure 5.33:(a), the MSD almost exclusively consists of and is dominated by six individual, sharply pronounced areas in locations of the original input characteristics with maximum error values of 4.9 %. Otherwise, no significant deviation besides small variations in-between those localisations >1.6 % can be found.

Below on the left in (b), a combined poloidally averaged profile of phantom and tomogram are shown. The prior increases quickly from $0.5r_a$ outward until $0.75r_p$ to 0.7 MW/m^3 in a peak of $0.15r_a$ FWHM. After a distinct valley of 0.15 MW/m^3 in $0.95r_a$, a second and conclusive, sharper peak to 0.675 MW/m^3 with a width of $0.05r_a$ follows, which decays to 0.5 MW/m^3 at the boundary. The phantoms plot is constant at 0.6 MW/m^3 in the core until $0.4r_a$ and increases from there parabolically in its first peak of $0.1r_a$ width to 0.45 MW/m^3 in $0.83r_a$. A higher, in the same location as before positioned local minimum of 0.25 MW/m^3 is concluded by again a second maximum at the edge of the domain with 0.57 MW/m^3 . Using equation (5.16), the two-dimensional phantom and tomogram radiation image yield 15.932 MW and 15.799 MW respectively, corresponding to 0.08 % deviation.

On the right in figure 5.33:(b), forward calculated camera profiles of the artificial emissivity distribution show significantly smaller maxima when compared to the original phantom in figure 5.30. The VBCl shows 0.605 mW in channel no. four, coinciding with the inboard side magnetic island, tangent to the separatrix, decaying quickly towards no. zero at the edge and inward to no. eight. A small bump to 0.395 mW and plateau with a conclusive drop provides the transition to the right side array results of the core. Decreasing from 0.35 mW in absorber no. 21 to 0.198 mW in no. 18, the VBCr profile increases gradually from there with small variations until the detectors viewing the outboard side separatrix and SOL, i.e. no. five through one, between which also 0.605 mW is measured by channel no. two and three. The horizontal camera produces a relatively flat plot between $0.27\text{--}0.4 \text{ mW}$, where the shallow minimum is found in the core by absorber no. 18. Just inside the two-sided sharp increase from no. two and 28, the arrays maximum measurements of 0.4 mW and 0.36 mW are indicated by detectors no. seven and 25 respectively, aligning with the upper and lower part of the SOL and LCFS. Small, local extremes with $\leq 0.1 \text{ mW}$ relative amplitude are presented around the prior global maxima. The forward integrated absorber signals from the tomograms' emissivity distribution are generally within the provided individual confidence intervals, while being

slightly more pronounced in locations of the aforementioned extremes. In a few cases, i.e. the VBCl channel no. one, VBCr and HBCm no. 17 and 18 or no. 25, the particular characteristics are amplified by <0.05 mW beyond that range. Extrapolation of the provided profiles yields $P_{\text{rad}} = 12.247$ MW from the phantom and 12.278 MW from the tomogram, a 1.09 % deviation that correlates well with the noted fitness factor of $\chi^2 = 0.893$ a. u..

In terms of - subjectively measured - reconstruction quality, this type of artificial emissivity superposition shows greater discrepancies for the same approach and settings when compared to the prior, inverted case in figure 5.31 and following. Due to the switched radial orientation of the employed contrasting profiles, the increased sensitivity of the bolometer camera detectors in the SOL and along the separatrix leads to an *obfuscating* effect on the anisotropic core structure. More specifically, the focus of the tomogram is entirely changed, certainly also due to the reversed k_{ani} regularisation weighting, placing the majority of the brightness in that area, expanding until the edge of the domain. The maximum emissivity is found in the core still, in locations similar to those in the phantom, though with greatly decreased resolution and accuracy. Features vertically above the VBC arrays are entirely missing, coinciding with the LOS with the most unfavourable ratio between integration lengths through SOL and anisotropic core profiles. However, this is contrasted by the noticeably and significantly improved match between the poloidally averaged and forward integrated results, their corresponding power values $P_{\text{rad},2D}$ and P_{rad} , as well as the better fitness χ^2 . In summary, similar experimentally measured radiation distributions will potentially be even more difficult to reconstruct adequately in terms of quality of more focused or localised features, respective their shape and relative intensity.

5.3.4. Geometry Error Propagation for Reconstructions

A conclusive, necessary step before statistically exploring the MFR method in more detail and applying the gained experience in tandem with the tomography of experimental bolometer data is to gauge the impact of faulty assumptions or measurement errors in the camera geometry and by extension the transmission matrix \mathbf{T} . The goal here is the find out if and how big of an influence the propagation of alignment errors or discrepancies in the determination of the pinhole (i.e. camera) position has on the final quality of the tomogram. Premise for this approach is the *directed* deviation of all

5.3. Phantom Radiation Profiles

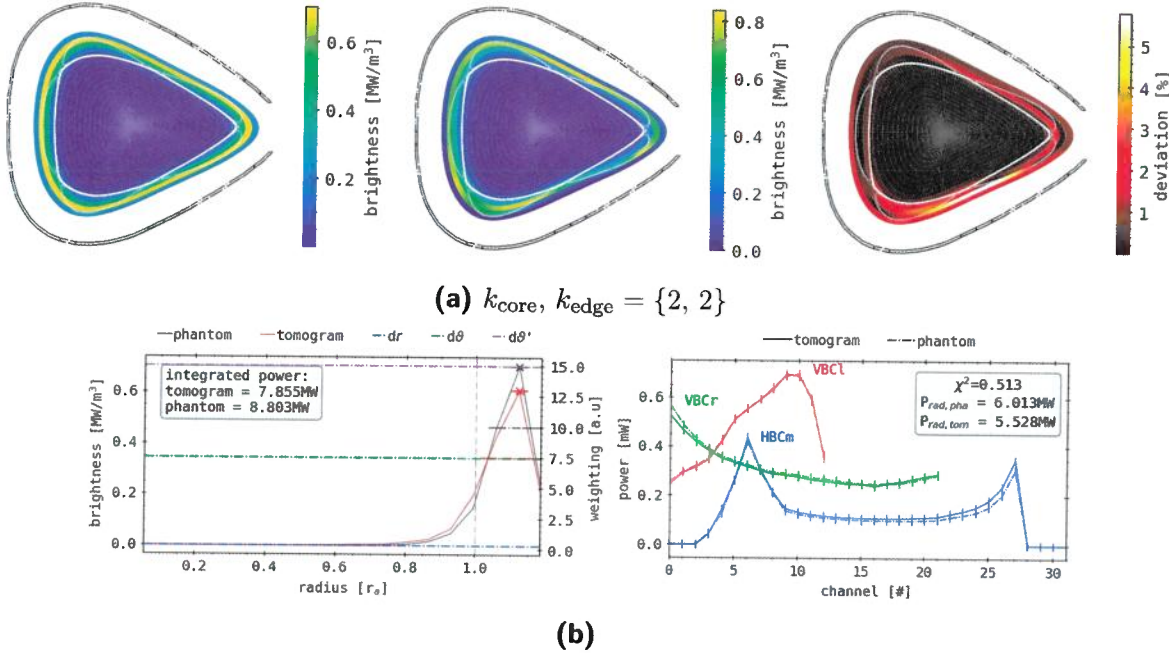


Figure 5.34.: Phantom radiation distribution and reconstruction of a bright ring around $1.1r_a$, similar to figure 5.18. The incorporated camera geometry for the tomographic inversion was altered and *rotated* (tilted) clockwise by 1° , as it was described and presented in figure 5.12. RDA coefficients equally support smooth, isotropic emissivity profiles in the core and edge. (a) Phantom, tomogram and relative deviance, similar to figure 5.18. (b) Radial (left) and chordal (right) profile analysis, similar to figure 5.19.

LOS, i.e. all pinholes and absorbers are shifted in the same way with respect to their assumed geometry, so that the perturbed LOS fan yields a distinct and significant rotation compared to its original orientation. Furthermore, this particular effect is to be unknown and only affects the calculation of the pseudo-measurements as input for the MFR, which is performed still with the benchmark geometry. For this very purpose, a fairly simple, symmetrical and most importantly already examined and reconstructed phantom radiation profile will be used, and a reconstruction performed using the also previously introduced LOS geometries with $\pm 1^\circ$ poloidal tilt from the *as-designed* con-

struction. Details respective their setup can be found in section 5.2.2. The baseline artificial brightness distribution and MFR as a benchmark will be that of figure 5.18 and section 5.3.1, a symmetrical, thin ring of radiation in $r_0 = 1.1r_a$ with no anisotropic variation, using a uniform $k_{\text{ani}} = \{2, 2\}$. In both cases, the entirety of the multicamera bolometer system has been rotated collectively by the given angle around their corresponding aperture center locations in clockwise (*positive*) or counter-clockwise (*negative*) direction.

The first set of results can be found in figure 5.34 and features the original phantom and reconstructed tomogram based off of the *as-designed* LOS system, as well as the forward integrated signals from the phantom, achieved with the misaligned geometry and used for the reconstruction and their reverse counterpart as before. At the center of (a), the tomogram places stronger asymmetries at and around the bottom inboard, on the edge of the lower outboard and in-between the upper two magnetic islands. Their individual maximum brightness is higher than the intensity of the input ring at $>0.7 \text{ MW/m}^3$, with 0.85 MW/m^3 the global peak in the latter location. Along $1.1r_a$, the emissivity is at least 0.6 MW/m^3 , except for a large gap towards the lower outboard field structure where it drops to 0.35 MW/m^3 . Coincidentally, the MSD profile yields the largest error values in that area with a large, expanded feature of 5.7 % between the two neighbouring islands. The remaining deviations are far below at $\leq 2.5 \%$ around the triangular plane, while minor variations can be found towards the edge where the emissivity in the tomogram was broadened.

In (b) on the left, both poloidally averaged profiles find the global maximum at $1.12r_a$, while the tomograms result is slightly lowered from 0.7 MW/m^3 to 0.6 MW/m^3 . Both peaks have a very similar rise and decay, and the same FWHM of $0.15r_a$. However, despite the strong agreement in the radial profile, integration of the two-dimensional distributions in phantom and tomogram provide $P_{\text{rad},2D} = 8.803 \text{ MW}$ and 7.855 MW respectively, which equals a 12 % difference. Obviously, the parameterised regularisation weight profile is flat at $k_{\text{ani}} = k_{\text{core}} = k_{\text{core}} = 15 \text{ a.u.}$

On the right, the forward integrated signals of phantom and tomogram are shown. Like described above, results from the artificial distribution are produced using the geometry with the $+1^\circ$ tilt in clockwise direction, while the back-calculated profiles from the tomogram are achieved by integration with the *as-designed* LOS alignment. Overall shape and characteristics of

5.3. Phantom Radiation Profiles

the plots are the same as in the initial MFR of this particular image, i.e. in figure 5.19. As in the latter, the horizontal cameras detectors indicate a noticeable asymmetry in both profiles, though the structure is the same towards and around each portion of the array that tangentially views a part of the separatrix. With respect to the established benchmark of this artificial distribution, the discrepancy between detectors viewing the upper and lower portion of the SOL is markedly reduced here from being half to just 0.06 mW difference in peak value. In the phantom, absorbers with LOS through the lower half of the triangular plane find lower emissivity values compared to the already reduced results from the tomogram. Although the integral power per channel is still within the corresponding error confidence interval, a relatively consistent deviation of $\sim 7.5\%$ can be found from no. ten onwards. The VBCr shows the reverse behaviour, where absorbers towards the outboard side, watching the SOL and LCFS yield higher brightness measurements of the same rate from channel no. five through zero. On the other side, the left vertical bolometer camera presents no significant variance between the two plots, besides a negligible decrease in the reconstructed results closer to the core, i.e. detectors no. three and below. In contrast to the visually well-matching profiles, extrapolation of the shown absorber signals indicates a large discrepancy with $P_{\text{rad}} = 6.013 \text{ MW}$ and 5.528 MW , a 5.9 % error between phantom and tomogram respectively. Comparing this to the first MFR of this artificial distribution, this is a 5.7 % deviation. The low fitness factor of $\chi^2 = 0.513 \text{ a. u.}$ underlines the latter observation.

A second set of results for the corresponding rotation of the LOS fans of all three cameras by -1° is shown in figure 5.35 and presented in the same way for also the same set of k_{ani} . In the center of (a), the phantom features an asymmetry and global maximum of 0.87 MW/m^3 around the inside edge of the upper inboard magnetic islands that extends along the $1.1r_a$ radius also towards the inboard side. A minor, secondary maximum of 0.7 MW/m^3 is located similarly to before between the lower two field structures in the SOL, while the rest of the ring is greatly reduced in brightness down to 0.45 MW/m^3 . Radially, its width is slightly increased to $\sim 0.2r_a$ compared to the phantom around the extremes and narrower elsewhere. Correspondingly, the MSD on the right shows large error values where the global maximum was found of up to 4.6 % and smaller ones of 3.2 % in the lower outboard magnetic island. The remaining SOL yields deviations $\leq 2.4\%$.

The tomograms poloidally averaged profile in figure 5.35:(b) is noticeably

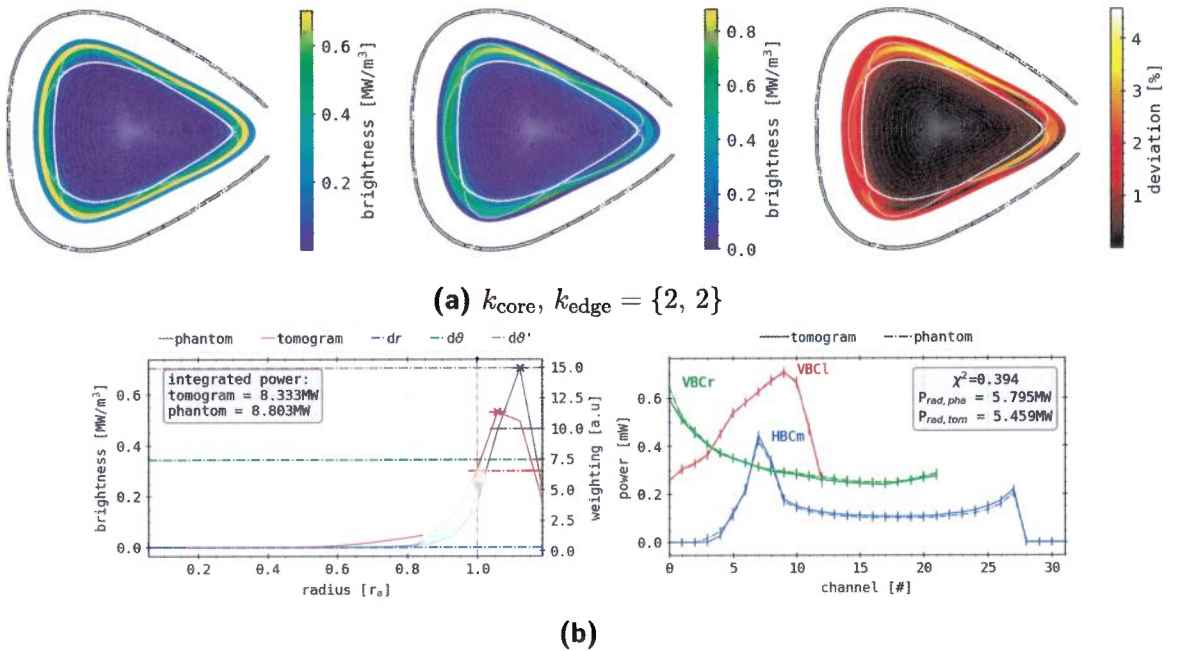


Figure 5.35.: Same phantom radiation distribution and reconstruction problem as in figure 5.35, but for a camera geometry rotation of -1° .
(a) Phantom, tomogram and relative deviance, similar to figure 5.18. **(b)** Radial (left) and chordal (right) profile analysis, similar to figure 5.19.

shifted towards the separatrix and core. All the profile inside and outside the LCFS is moved by $0.06r_a$ closer to the magnetic axis, including the location of the minutely reduced peak of 0.5 MW/m^3 in $1.05r_a$, though its width is increased to $0.16r_a$. In this case, the integrated power is higher at $P_{\text{rad},2D} = 8.333 \text{ MW}$, which is 6.1 % larger than its previous counterpart and decreased by 6.3 % respective the phantom baseline.

The previously examined and discussed dissymmetry in the HBCm results is amplified here on the lower side viewing the SOL, i.e. channel no. three through twelve, where the forward integrated signals are now double that of the opposite side, no. 23 through 27 in both phantom and tomogram. Otherwise, core and overall profile are qualitatively similar compared to figure 5.34. The prior shows about 0.1 mW like before, same as the aforementioned asymmetry on the left of up to 0.44 mW , hence a reduction to

0.21 mW from the absorbers viewing the upper SOL. No significant changes with respect to the initial benchmark can be found for the vertical bolometer array detectors. Like the last set of forward calculations, deviations between tomogram and phantom plot for all cameras are limited to the provided error confidence interval, though in contrast not particularly elevated in or around extremes. Extrapolation of the erroneous artificial radiation image results yields a slightly reduced $P_{\text{rad}} = 5.795$ MW compared to before and of the corresponding tomogram 5.4595 MW, equalling a 4.6% and 6.2% decrease, which also is a 1.8% raise with respect to the first set of numbers in figure 5.19. Finally, again clashing with the observations above is a weak fitness of $\chi^2 = 0.394$ a. u..

The criticality and importance concerning the underlying issue of this examination towards the MFR and its performance is highlighted by the variance of P_{rad} across the different sets of results. In this case, substantial increments compared to the baseline geometry extrapolation are found from the faulty profiles. Furthermore, the reproduced two-dimensional emissivity distributions show noticeable and particular characteristics that align with the designed error in the LOS orientation. Similarly, particularly in the HBCm forward calculated measurements, a correlating effect of the rotation on the shape and intrinsic asymmetry of the profile is very prominent. A significantly worse fitness coefficient compared to the previous supports the above findings, though the detector signal integration trend towards the *actual* radiation powers yield the contrary picture. From the presented impact of a distinct error in the transmission matrix \mathbf{T} , unfortunately no other attribute than the increased or decreased characteristic in the individual camera results for symmetrical radiation distributions definitively points towards such underlying discrepancies. In a worst case scenario like this cumulative deviation in the location measurement of the bolometer or changes in its construction alignment, a divergence of $\geq 10\%$ in both singular absorber data and tomogram values are to be expected and in an experimental context nearly impossible to account for.

5.3.5. Reconstructive Limits

The conclusive, final next step before approaching actual experimental data with the MFR algorithm and RDA method is the quantitative, i.e. statistical evaluation of the above explored, simple phantom emissivity distributions.

This section will focus on systematic iteration of the anisotropic regularisation weights k_{core} and k_{edge} individually over across larger spectra than before and recording the findings of the reconstruction for simple artificial images, i.e. a *bright ring* like before in section 5.3.1. For this purpose, the previously introduced and examined characteristics, i.e. extremes location and FWHM, *mean squared deviation* (MSD) of equation (5.14), integrated two-dimensional power values from the phantom and tomogram and the fitness factor χ^2 . At this opportunity, an additional measure is introduced to gauge the agreement between input and output of the algorithm. The *Pearson^I correlation coefficient (PCC)* ρ_c or $\rho_{x,y}$ between quantities x and y measures their linear correlation. The number ρ_c is the ratio of covariances and product of their respective standard deviations, therefore its result is binned by $[-1, 1]$. Let $E(\vec{x})$ be the *expected value* of variable \vec{x} , i.e. the vectorized representation of the phantom or tomogram like in equation (5.6) and section 5.3.3. The Pearson coefficient hence can be written as:

$$\begin{aligned} E(\vec{x}) &= \frac{1}{n_r n_\vartheta} \sum_{i=0}^{n_r n_\vartheta} x^{(i)} \stackrel{!}{=} \bar{x}, \\ \rho_{x,y} = \rho_C(\vec{x}, \vec{y}) &= \frac{E((\vec{x} - E(\vec{x}) \cdot \vec{1})(\vec{y} - E(\vec{y}) \cdot \vec{1}))}{\sqrt{\vec{x} - E(\vec{x}) \cdot \vec{1}} \sqrt{\vec{y} - E(\vec{y}) \cdot \vec{1}}} , \\ &\stackrel{!}{=} \frac{1}{\sigma_{\vec{x}} \sigma_{\vec{y}}} \text{cov}(\vec{x}, \vec{y}) . \end{aligned} \quad (5.21)$$

Isotropic Ring Combinations

In figure 5.36, these particular sets of attributes are collected for a simple artificial radiation distribution consisting of a singular bright ring at $0.5r_a$ after the example in figure 5.18. The left and right plot series are split into the individual k_{core} and k_{edge} variations across ranges of $[0.65, 1]$ a.u. and $[1.25, 1.8]$ a.u. respectively. While one of those is altered, the other is kept at unity, i.e. $k_{\text{ani}} = 1$ a.u., yielding no change in regularisation. From top to bottom, the presented images show: the global maximum brightness radial location, its full width at half maximum height (FWHM), individual core, SOL and total MSD according to equation (5.14), the core and absolute

^IKarl Pearson, FRS, FRSE * Mar 27, 1857 †Apr. 17, 1936; English mathematician and biostatistician

5.3. Phantom Radiation Profiles

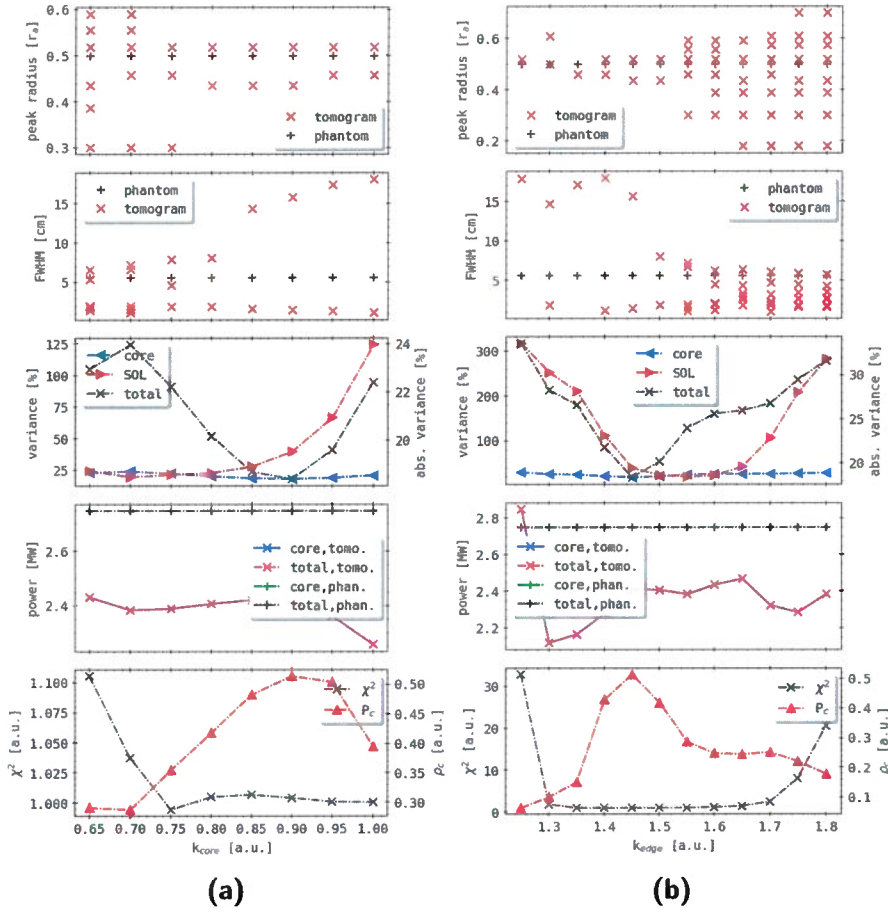


Figure 5.36.: MFR scan of phantom radiation distribution consisting of an isotropic ring at $0.5r_a$ with 0.1 m FWHM. (a) Core and (b) edge RDA coefficients are varied independently. In both, top to bottom: radial position of the maximum, FWHM, MSD for core, SOL and in total, total and core integrated 2D powers and fitness scales χ^2 and Pearson coefficient ρ_c .

integrated, two-dimensional power from equation (5.16) and finally the fitness factor χ^2 and Pearson coefficient ρ_c in the bottom figure. Each plot contains of course two sets of lines for phantom and tomogram separately, except the very last in which the quantities are derived from both together.

If applicable, multiple abscissa are indicated where the order of magnitude between the profiles is distinctly different.

At the top, the input radiation distributions maximum brightness radial location is obviously constant at $0.5r_a$ across both k_{ani} spectra. For $k_{\text{core}} \leq 0.75$ a. u. in column (a), the tomogram yields at least three individual peaks both inside and outside the respective target radius, though one data point can be found here very close at $0.52r_a$. Overall, features between $0.3 - 0.59r_a$ are presented, while beyond $k_{\text{core}} \geq 0.8$ a. u. only two extremes are shown in the tomogram relatively constantly in $0.55r_a$ and $0.45 - 0.5r_a$. When varying the SOL regularisation parameter in (b), for $k_{\text{edge}} = 1.25$ a. u. a singular maximum is located nearly precisely where the original ring is in the phantom, i.e. in $0.052r_a$. In $k_{\text{edge}} = 1.3$ a. u., this peak is at the aforementioned position and a secondary point is added in $0.6r_a$, after which in 1.35 a. u. again only one extremum in $0.47r_a$ follows. Beyond, count and spread of the tomogram features increases continuously, until for $k_{\text{edge}} = 1.8$ a. u. eight individual maxima are produced in the tomogram between $0.18 - 0.7r_a$, though still and throughout on is presented reliably in $0.52r_a$. Newly appearing peaks can be found consistently at that radius for larger k_{edge} than where they first are noted.

In the second line of plots, the corresponding FWHM of the phantom is 5.5 cm. The same respective number of data points is shown across the k_{core} and k_{edge} spectra as above, though this representation does not link the individual features explicitly across the images. In the core regularisation weight variation, for lower values $k_{\text{core}} \leq 0.8$ a. u. the grouping is significantly closer around the target width, even for the increased number of maxima shown, i.e. 1.5–8 cm. Beyond, the reduced amount of peaks is increasingly spread out more in their width to 1–18 cm for larger k_{core} . On the other side for varying k_{edge} , the opposite behaviour is presented, where for fewer features and smaller edge regularisation weights $k_{\text{edge}} \leq 1.45$ a. u., the distribution of data points is far wider at 1.5–18 cm. For higher k_{edge} , this is similarly reduced to 1–8 cm at simultaneously growing numbers of maxima.

In the next row of plots, the integrated relative variance calculated by equation (5.14) is shown, individually separated for the SOL, core and an absolute value across the entire, triangular plane reconstruction domain. On the left, until $k_{\text{core}} = 0.8$ a. u., the MSD in- and outside the separatrix are relatively constant around 25 % with minor deviation. For larger weighting parameters, the SOL discrepancy increases parabolic to 125 % in $k_{\text{core}} = 1$ a. u. while

5.3. Phantom Radiation Profiles

the core error remains low and even occasionally drops below 25 %. The total variance is the integrated sum of the prior two and yields 20–24 % up until 0.8 a. u. across which it steadily falls to 18.5 % in 0.9 a. u. and then becomes dominated by the SOL divergence, i.e. parabolically growing to 22.5 %. Across the spectrum of k_{edge} on the right, the core MSD is mostly constant around 30 %. Absolute and SOL deviation are similar in profile, though differ greatly in value until $k_{\text{edge}} = 14.5\text{--}15$ a. u.: starting at a maximum 320 % and 33.5 %, they continuously decrease until 30 % and 19 % respectively. The SOL error remains low as long as $k_{\text{edge}} = 1.65$ a. u., after which a near linear increase to 280 % is shown. Accordingly, the absolute deviance also rises immediately again and slightly plateaus around 1.6 a. u. and 25 % and then climbs to 31.5 % for $k_{\text{edge}} = 1.8$ a. u..

In the fourth line of images, the integrated power of the phantom from the core and conclusively also in total is 2.75 MW. Between $k_{\text{core}} = 0.65\text{--}1.0$ a. u., the tomograms $P_{\text{rad},2D}$ from in- and outside the LCFS does not change drastically and yields 2.25–2.44 MW, with most reconstructions producing close to 2.4 MW. On the right, for $k_{\text{edge}} = 1.25\text{--}1.3$ a. u. this value drops from 2.85–2.12 MW and then also increases to 2.4 MW in 1.45 a. u., around which it deviates across the rest of the spectrum by ± 0.1 MW. Core and total radiation power are equal here too.

The final set of plots presents the two aforementioned quality gauges fitness factor χ^2 and Pearson coefficient ρ_c , similarly with split abscissa for each number individually. Between $k_{\text{core}} = 0.65\text{--}0.75$ a. u., χ^2 decreases from 1.105–0.995 a. u. and after equalizes to 1 a. u. across the rest of the spectrum. The Pearson coefficient yields 0.29 a. u. for lower values and near linearly grows to its maximum 0.51 a. u. in 0.9 a. u. before dropping again to 0.39 a. u. for k_{core} unity. A comparable image is shown on the right, though the χ^2 decrease is absolutely larger from 33–2 a. u. and its plateau finalized by a parabolic rise to 21 a. u. towards $k_{\text{edge}} = 1.8$ a. u. The ρ_c maximum of 0.51 a. u. is now in 1.45 a. u. and is concluded by a small plateau between 1.55–1.75 a. u. around 0.25 a. u.

Focusing on one column of plots at a time, the vertical alignment for individual k_{ani} of features in the respective plots reveals an intuitive and characteristic behaviour across that spectrum. On the left, the fitness is closest to unity, while the Pearson coefficient is largest for $k_{\text{core}} = 0.9\text{--}0.95$ a. u.. At the same time, the cumulative core, SOL and absolute deviation in total are lowest and the error in integrated power is relatively constant at around

0.2 MW. However, though the peak localisations are comparatively improved for those values, the FWHM deviate greatly here with respect to the lower k_{core} . Similarly, on the right, the lowest individual and total two-dimensional variance is found for $k_{\text{edge}} = 1.45 \text{ a. u.}$. At the same time, ρ_c is largest and χ^2 is very close to unity, while the reconstructed structures are radially close to the location of the input profile. The corresponding widths are also in stark contrast here and $P_{\text{rad},2D}$ yields again an equivalent error, though a singular outlier for a smaller k_{edge} does not align with those observations. Conclusively, for this kind of simple and symmetric radiation distribution, there do exist ideal k_{core} and k_{edge} , individually given a fixed counterpart. In this case, the quality parameters shown are largely in strong agreement across the spectra and no significant characteristic is found that is in contradiction. However, a large drawback of this particular approach is the large parameter range that has not been explored by this relatively expensive method. For only one phantom image, a small spectrum of anisotropic weighting coefficients has been evaluated separately. For N the number of variations in this small window, one would have to perform at least $N \times N - 2N$ more reconstructions to find a definitive answer to what the actual optimum k_{ani} profile is. Another possible ansatz is the variation of the artificial brightness distribution for constant reconstruction settings, i.e. changing the radius of the ring in the previous data set instead of k_{core} and k_{edge} each.

This procedure has been applied in figure 5.37, where two similar types of previously presented, simple phantom radiation profiles have been varied and conclusively reconstructed using the Minimum Fisher algorithm for a set of constant $k_{\text{ani}} = \{2, 2\}$. The same set of quantities as in figure 5.36 have been measured for each of the results. In (a), the radial position of a magnetic axis concentric, isotropic singular thin, bright ring is altered between $0.35r_a - -1.3r_a$, while at the two very last iterations the actual maximum emissivity in the phantom is close to or outside the regularisation domain due to the aforementioned mapping to discrete cells. This inevitably leads to missing data points in the first plot of maximum brightness locations at the right edge of the spectrum, however the tomogram finds two individual peaks at a target radius of $1.3r_a$ in $0.28r_a$ and $0.55r_a$. Otherwise, the results are congruent except for in $0.8r_a$ where the reconstructed image yields a ring of slightly larger diameter. In contrast, the FWHM values differ significantly and nearly constantly, as the tomograms produce distributions with around 15–25 cm thickness and the phantom with 5–7 cm. The latter variability is

5.3. Phantom Radiation Profiles

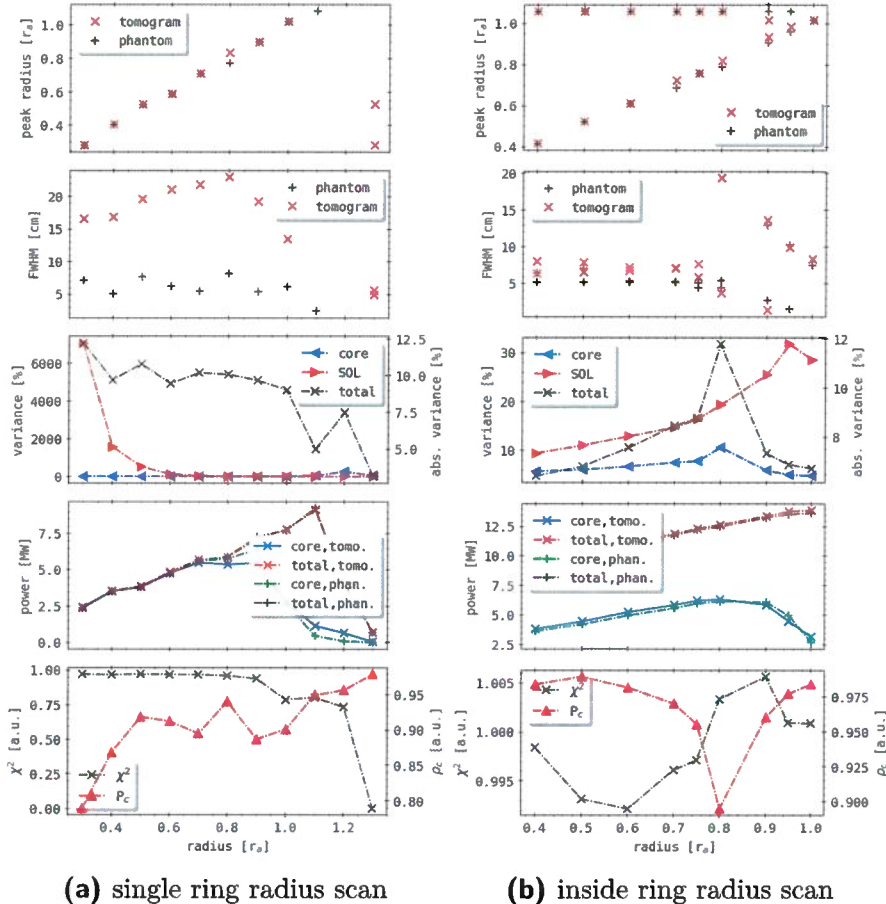


Figure 5.37.: MFR scan of phantom images consisting of (a) one or (b) two concentric, isotropic, equally bright rings. In (b) only the inside rings' and in (a) both rings' radii have been varied, while the same RDA coefficients $k_{\text{core}}, k_{\text{edge}} = \{2, 2\}$ are used throughout. The layout of the results is similar to figure 5.36.

again due to the discrepancy between continuous and discrete mappings. Towards the edge beyond r_a , this relation degrades as no peaks are found in the target profile and the tomogram shows similar and almost identical widths for both extremes around 5 cm. With increasing radius, the width in the tomogram grows slightly, though drops as quick closer to the LCFS.

Due to the shape of the artificial distribution, the SOL error is beyond 6000 % at the smallest diameter, where essentially no emissivity is placed in the phantom and small deviations in the reconstruction immediately lead to very large relative discrepancies. This then parabolically decays with increasing ring radius. Simultaneously in the core, comparatively much smaller values are presented, though the abscissa scale and difference in order of magnitude does not allow for a more detailed assessment. Only at $1.2r_a$ a noticeable and still very large error of ~ 500 % can be found inside the LCFS. On the other side, the absolute variance yields more comprehensible results, with values between 2.5–12.5 %. For the innermost ring, the total discrepancy is largest with 12.2 % and continuously decreases with larger radii, though a small plateau around 10 % and $0.7r_a$ – $1r_a$ precedes a sharper drop towards the edge of the spectrum, where the points show a strong variability. In $1.2r_a$, the absolute error increases again sporadically to 7.5 % before reaching the minimum at the edge of the domain.

Integrated power values of the two-dimensional distributions are generally in very good agreement throughout the radial variations, particularly the absolute $P_{\text{rad},2D}$ is basically congruent between the tomogram and phantom. The latter grows near linearly from 2.5 MW to 9.5 MW in $1.1r_a$ and quickly drops to 0.75 MW at $1.3r_a$ from there. Until $0.8r_a$ the total amount of emissivity is almost entirely focused in the core, though beyond this correlation obviously degrades and from $0.9r_a$ decays fast to null, where also the two profiles yields slightly different results with ± 0.5 MW deviation.

The very last plot on the left shows that the fitness factor χ^2 is nearly constant at ~ 1 a. u. until a ring radius of $0.9r_a$, while the Pearson coefficient ρ_c presents an at first steep and then staggered increase in that range from 0.79–0.89 a. u.. For larger diameter, the latter grows continuously to 0.98 a. u. and χ^2 decreases rapidly inversely parabolic to 0.75 a. u. in $1.2r_a$ and then null at the edge.

All the above indicates that the reconstruction of an isotropic, radially thin radiation distribution for a given set of regularisation parameters assuming such performs best for a concentrated emissivity in the range of 0.9 – $1.1r_a$, i.e. in and around the LCFS. Although fitness and Pearson coefficient both produce maxima at opposite ends of the spectrum and are not at unity at those radii, they yield sufficient values indicating good overall agreement between the forward and two-dimensional profiles. This is also true for the presented individual and absolute variance, as well as all the shown power

numbers. With respect to the first plots of extremes location and shape, the largest diameter have to be excluded or at least treated differently in terms of anisotropic weighting and statistic evaluation, further supporting the optimum up until that range.

Based off of that knowledge, the results plotted in the right column of images in figure 5.37:(b) can be interpreted much easier now. At the top, the outside and variable inside brightness ring are clearly distinguishable in $1.05r_a$ and with increasing radial position from $0.4 - 1.0r_a$, respectively. At the very outside for the last variation, the algorithm only yields one maximum at the aforementioned location, indicating a merging of the previous two. Across the spectrum, the reconstructed profiles produce overall congruent or at least very similar values up until $0.8r_a$. Beyond that, the points begin to converge and already for an inside ring radius of $0.95r_a$ only one maximum is found in the tomograms, though its position aligns with the phantom.

The FWHM below shows a nearly constant 4–7 cm in a varying number of points, i.e. one or two due to the similarly configured rings, up to $0.8r_a$ of the inside ring from the phantom. For larger radii of the latter and a decreased distance between the two, the individual points split and are now decreasing linearly from 13–8 cm and 3–1 cm, while at congruence of the rings the smaller width vanishes. Results from the tomograms are overall in agreement with a small tendency to overestimating the target FWHM by 1–2 cm, although occasionally one of the two points might match. At $0.8r_a$ and onward, the indicated profile shapes are split again, where the larger is now already at 19 cm and only two smaller diameters can be found before null. At those radii, similar or smaller deviations are shown.

In the core and SOL, the relative variance is much smaller than before, within 2.5–32.5 % overall, while the absolute error is within the same range of up to 11.9 %. Deviations in the core increase nearly linearly with the radius of the inner ring from 10–32 %, before decreasing at the last position to 28 %. At the same time, the core variance is almost constant around 5–6 % with a small, minor maximum at $0.8r_a$ of 10 %. As a combination of the latter two, the total error across the profile grows steadily from 6.5–9 % in $0.75r_a$, until peaking sharply in $0.8r_a$ and dropping just as quickly to 7.5 cm and finally 5.5 % at the last variation.

Across the radial spectrum, the tomograms and phantoms core and absolute integrated power values are, within a margin of <0.25 MW in congruence. The latter increases linearly from 10–14 MW, though the total emission from

inside the separatrix does so from 3.5 MW to a shallow and plateau-like maximum of 6.5 MW in $0.8r_a$ before decreasing again more quickly to 3 MW in the end.

Finally, the very last figure in the right column of figure 5.37, the fitness factor and Pearson coefficient for the variation and reconstruction of the double concentric brightness ring combination are presented. The prior is calculated in a narrow band of $\chi^2 = 0.992\text{--}1.006$ a. u., indicating strong agreement between phantom and tomogram, however the profile shown has a pronounced minimum below unity of 0.992 a. u. in $0.8r_a$. For inner ring radii below and above, values at or higher than 1.0 a. u. are produced and below $0.65r_a$ or above $0.9r_a$ even more than 1.003 a. u.. Similarly, ρ_c is close to unity and within a smaller range of 0.895–0.99 a. u.. From 0.94 a. u., a parabolic decay to a minimum of 0.895 a. u. in $0.6r_a$ is followed by continuous increase to the maximum of 0.99 a. u. in $0.9r_a$ and an insignificantly smaller, minor plateau at 0.955 a. u. beyond.

For the given configuration of $k_{\text{ani}} = \{2, 2\}$ and ring positions, i.e. a fixed larger concentric structure at $1.05r_a$ and a variable smaller inside, the applied algorithm yields generally acceptable results. In contrast to on the left, no significant deviations in reconstruction quality across the radial spectrum of the inner ring can be observed. Location and shape of the rings are consistently and accurately represented, while the overall power is congruent throughout. However, both absolute variance and fitness factor χ^2 indicate a worse match of the tomogram at an inner radius of $0.8r_a$, though beyond and hence for a smaller distance between the profiles the error decreases and χ^2 gets closer to unity again. On the other hand, ρ_c is smallest for the greater radial differences and closest to 1 a. u. in that range at and beyond $0.8r_a$. Coincidentally and trivially, the SOL deviation also peaks here and the individual peak detection eventually fails. Conclusively, the given radiation structures are reconstructed with the presented configuration nearly uniformly well, except a threshold value and negligible spacings. The prior appears to, judging from the shown results, not correlate with known characteristic of this system.

Anisotropic Island Combinations

Of much greater relevance towards the reconstruction of potentially more complex and anisotropic experimental data is the individual k_{core} and k_{edge}

5.3. Phantom Radiation Profiles

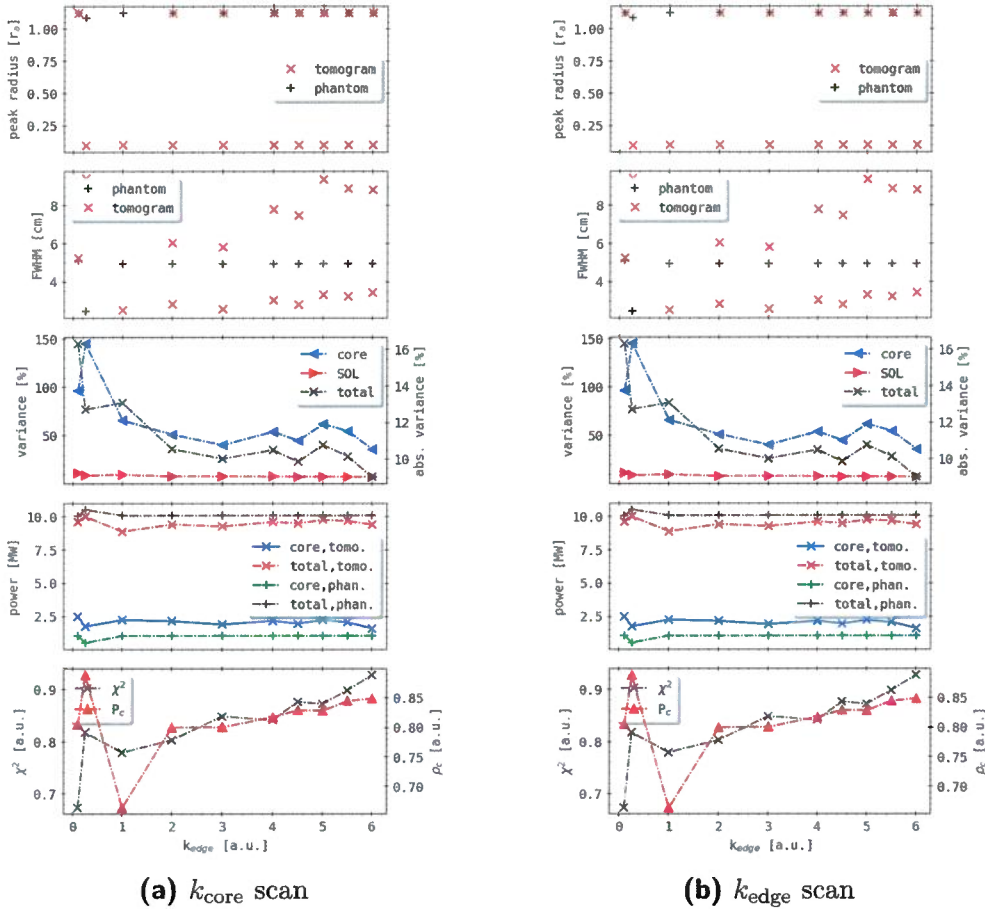


Figure 5.38.: MFR scan of a phantom image consisting of *up-down* symmetrical chain of island-like radiation spots at $1.1r_a$ of 0.1 m FWHM (exemplary artificial profile can be found in figure 5.30). **(a)** Core and **(b)** edge RDA coefficients have been varied independently. The layout of the results is similar to figure 5.36.

variation for an *island chain-like* artificial profile like in figure 5.38. Here, a ring of five island-like structures are placed, like before in figure 5.36 with one less feature, around the triangular at a radius of $1.1r_a$ and FWHM of 0.1 m.



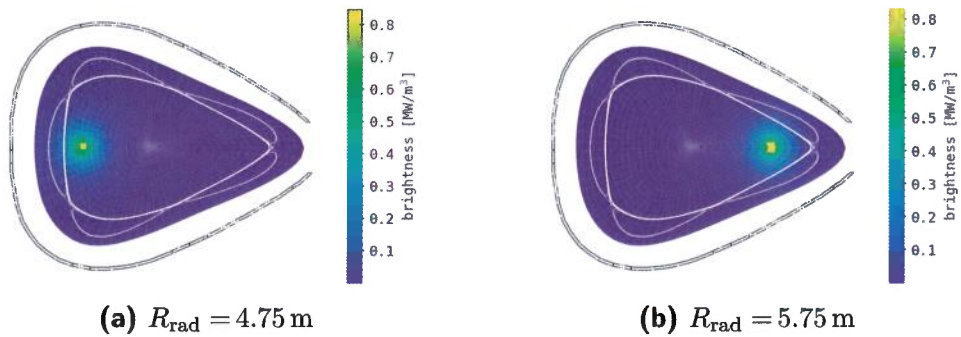


Figure 5.39.: Phantom images consisting of a singular bright spot of 0.2 m FWHM - (a) inboard and (b) outboard anisotropies.

Composite Phantom Images

At last, a less complex than before, though more intricate to reconstruct artificial radiation distribution is simultaneously introduced and MFR scanned by varying $k_{\text{core}} = \{0.4, 1\}$ in figure 5.40. In figure 5.39:(a), a singular, large bright sport with omnidirectional Gaussian profile and 0.2 m FWHM is placed in $z = 0$ and major radius $R_{\text{rad}} = 4.75 \text{ m}$. Its central, maximum brightness is 0.85 MW/m³.

In the tomograms, for $k_{\text{core}} \leq 0.75$ a. u. multiple, erroneous maxima are found in $0.62r_a$, $0.46r_a$ and one in $0.52r_a$, while the target value from the phantom is $0.41r_a$. However, across the spectrum, similarly close points are produced in $0.34r_a$ and then for $k_{\text{core}} \geq 0.7$ a. u. in $0.37r_a$. The corresponding FWHM of the artificial distribution is a constant 14 cm. At the lower $k_{\text{core}} \leq 0.75$ a. u., the majority of the faulty results from above yield <5 cm and as low as 1.5 cm. Across the spectrum, one of the peaks is accounted for by oscillating values between 6–9 cm, where the minimum is in $k_{\text{core}} = 0.85$ a. u. and the maximum in 0.95 a. u..

The relative variance in the core is nearly constant with 10–13 % until a small peak in $k_{\text{core}} = 1$ a. u. of 15 %. On the other hand, the SOL error is significantly larger and varies strongly, with a steady decay from 60 % to 35 % in $0.95r_a$, a minor plateau in-between and a conclusive maximum of 65 %. Obviously the shape of the absolute deviation is dominated by the outside error, hence the alike profile in the range of 13.5 % in 0.6 a. u. and 9 % in 0.95 a. u. It is terminated by a peak of 15 %.

5.3. Phantom Radiation Profiles

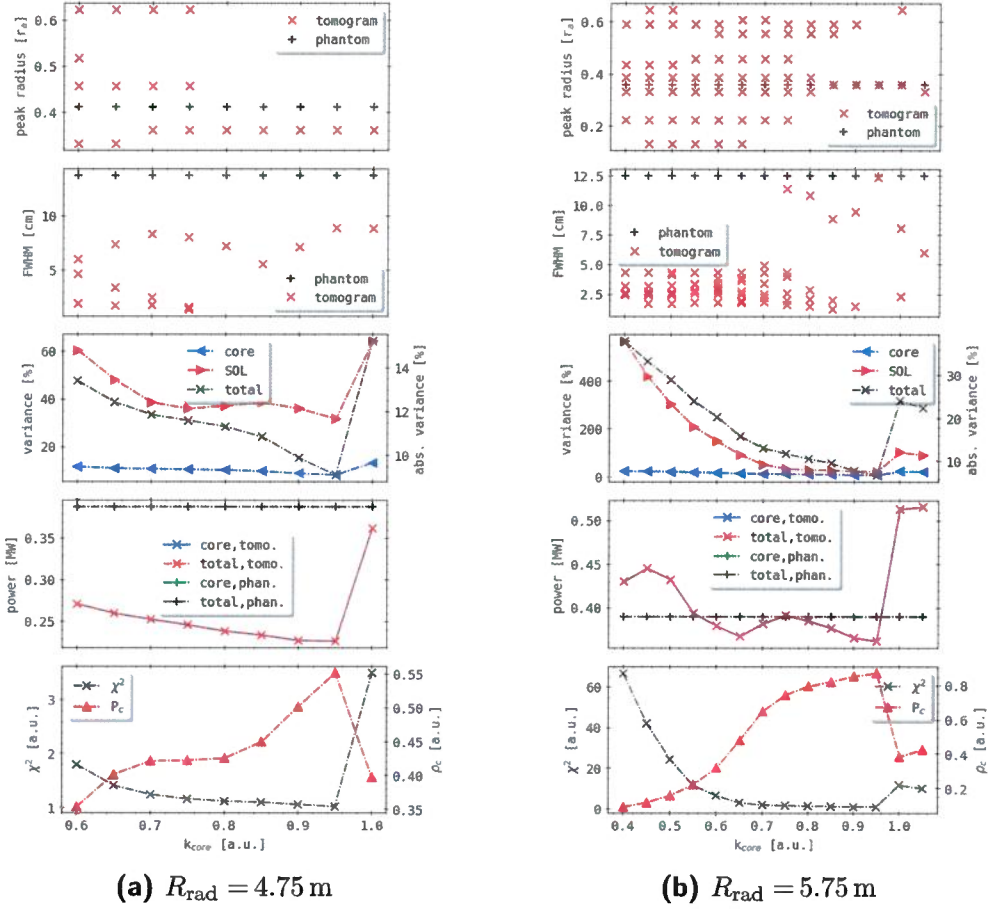


Figure 5.40.: Reconstruction scan for the corresponding phantom images in figure 5.39, a singular bright spot of 0.2 m FWHM - **(a)** inboard and **(b)** outboard anisotropies. In both, k_{core} has been varied in the same range. The layout of the results is similar to figure 5.36.

In the phantom, the total integrated power from the two-dimensional distribution is entirely represented by the core and constant at 0.39 MW. Results from the phantom also show congruence between the inside the separatrix and absolute calculated values throughout the k_{core} spectrum. Beginning in 0.27 MW, both linearly decay to 0.23 MW in 0.95 a. u. The final data point yields a drastic increase to 0.36 MW. Finally, the fitness χ^2 similarly

decreases with larger k_{core} from 1.9 a. u. to 1 a. u., followed by a sharp growth to 3.6 a. u. Curiously, the Pearson coefficient ρ_c indicates the opposite behaviour, i.e. increasing from 1 a. u. to a small plateau in 1.9 a. u. around $k_{\text{core}} = 0.75$ a. u. and then quickly to 3.5 a. u. before the conclusive drop to 1.5 a. u.

The k_{core} scan of the second tomogram in figure 5.39:(b) is shown in figure 5.40:(b). Here, the multiplicity and spread of the erroneous and individually reconstructed peaks is greatly increased compared to before. The input profile yields a value of $0.35r_a$. Until 0.8 a. u., six to seven maxima are found between $0.125r_a - 0.65r_a$, while throughout that spectrum the majority of features are consistently placed in $\{0.225, 0.33, 0.43, 0.59\} r_a$ and a few in $\{0.12, 0.42, 0.55, 0.625\} r_a$. Beyond, the number of points is decreased noticeably to three at most, even less for larger k_{core} and one is placed in location of the target structure. Concurrently, the representation in the plot of FWHM shows equally many points, with decreasing spread and amount with increasing inside anisotropy weighting. The bulk of the results is found for 2–5 cm and concentrated around 3 cm. From 0.75 a. u. on, singular points can be found >7.5 cm, descending with larger k_{core} from 11.5 cm. In 0.95 a. u., one result matches the target exactly.

Integrated error values from the SOL are very large and decrease parabolically from 460 % to <50 % in 0.95 a. u., then rise to 90–100 a. u.. Since the core variance is comparatively constant around 25 %, with a minor increment to 40 % in a similar range, the total discrepancy of 16–38 % throughout the k_{core} variation is dominated by the difference in SOL emissivity. The conclusive step in >0.95 a. u. is significantly more pronounced here in relation to the profile to 23 %.

From a constant, integrated power of 0.39 MW in the phantom distribution, the tomograms yield 0.36–0.44 MW up to $k_{\text{core}} = 0.95$ a. u. in an oscillating manner with a slight downward trend. Throughout, core and absolute values are identical, even in the large spike for ≥ 0.95 a. u. to 0.51 MW.

Fitness factor and Pearson coefficient both indicate an optimal reconstruction within the presented interval in $k_{\text{core}} = 0.95$ a. u., where χ^2 and ρ_c are closest to unity, i.e. ~ 1.5 a. u. and 0.87 a. u. respectively. The prior decays parabolically from 68 a. u., while the latter increases from null gradually, with a small steep portion around 0.65 a. u. and shallow end towards its aforementioned maximum. They decrease in quality afterwards, i.e. grow strongly again or drop sharply correspondingly.

The final k_{ani} variation results for the above, highly anisotropic phantom radiation distribution evidently pronounce a strong optimum within the limited range. For such clearly separated and singular emissivity features inside the separatrix, a factor of $k_{\text{core}} = 0.95 \text{ a. u.}$ yields adequate tomographic reconstructions in regard to the quantitative analysis. Given the generality of the approach and underlying artificial images, one expects similar behaviour with larger scale asymmetric features in superimposed profiles or experimental data. However, the variance of the quality of results in this small window somewhat mitigates the significance of said conclusions, since minor differences in either localisation, shape or k_{ani} may lead to severe changes in the tomogram. The asymmetry in reconstruction parameter profiles around the optimum is of particular concern for the exploration of non-artificial radiation data. Furthermore, the same is true for the noticeable discrepancies between the in- and outboard anisotropy and hence the images presented in the left and right column of figure 5.40, which can be trivially attributed to the geometry of multicamera bolometer system.

This concludes the efforts of benchmarking and evaluating the *Minimum Fisher regularisation* algorithm with *radially dependent anisotropy* weighting with a large set of deliberately designed and, albeit small scale, statistically varied set of phantom emissivity distributions as input. The propagation and their level of impact of errors in the underlying line-of-sight geometry has also been measured. Due to the nature of the multidimensional parameter dependency of the quality of MFR results, variations of such in an attempt to find optimal configurations or sets of coefficients like k_{ani} have proven difficult. However, for the select set of artificial radiation profiles and hence conceptually it was shown that there does exist an ideal combination of MFR parameters for a given emissivity distribution. As per design, there it was also found that regularisation weights $k > 1$ correspond to isotropic and coefficients $k < 1$ to anisotropic brightness profiles with improved quality factors for fitness, χ^2 and two-dimensional correlation, ρ_c .

which are?

Respective setups of symmetrical phantom images with reconstruction weights favouring smooth distributions have indicated geometric biases towards the individual camera apertures location, i.e. areas of increased lines-of-sight coverage along the lower part of the separatrix, inboard side and at the outboard tip of the triangular plane. Furthermore, from the perspective of the up-down symmetrically designed horizontal bolometer camera, this and the intrinsic

tilt of the detector fan leads to a systematic and intrinsic asymmetry in the produced forward and backward calculated radiation powers. Individual case testing with deliberately symmetric-asymmetric superimposed artificial profiles presented results of strongly divergent qualities, further underlining the previous assessment. Simultaneously, variation in k_{ani} highlighted significant discrepancies between the one- and two-dimensional pictures, hinting at independent qualitative developments in both.

Experimentally motivated phantom emissivity distributions, i.e. combined smooth, symmetric core and anisotropic SOL profiles mimicking hotspots in place of the magnetic islands prove to be a particular challenge for the MFR. With respect to the structure and localisation of the outside features, the regularisation weight optimisation is especially important. Addition of a hypothetical, inboard located horizontal camera has provided noticeable qualitative improvement for this type of phantom, suggesting and supporting the demand for an extension of the existing multicamera bolometer system. Finally, occlusion of the anisotropic profile on the inside by a homogenous, similarly bright ring yields promising results towards the inversion of experimental data compared to the initial case.

The previously introduced potential discrepancy between the assumed and actual *in-situ* geometry of the bolometer camera array was tested and evaluated in regard to its impact as an unknown, systematic error to the forward and backward calculated line integrated signals. Alteration of the aforementioned variance produces characteristic divergence of corresponding orientation in the MFR tomograms and profiles. However, that effect is indistinguishable from the various other variabilities in the reconstruction and of no such noticeable magnitude. This then provides an additional uncertainty to be taken into account when evaluating actual measurement data.

Iteration in k_{ani} and thorough quantitative analysis for principle emissivity shapes or combinations thereof was performed. Significant anti-/correlation between the individual variance, fitness and Pearson coefficients underlined the previously, only in isolated cases presented discrepancy to the subjectively perceived tomogram quality. The shown spectra also visually underline the proposed optima of MFR parameters through structural congruence or extremes in qualitative numbers.

(*) comprehensive, very worthy
to obtain significant conclusions (separation of features
near values
...)

5.4. Tomography of Experimental Data

At last, after finalizing the benchmarking of the core MFR algorithm with an extensive set of artificial radiation distributions, regularisation weight coefficients, variations and input geometries, one will proceed to perform tomography with experimentally measured data. However, due to the limited scope of this work, the set of experiments investigated in this section will also be focused on discernable and reasonable features in their respective tomographic reconstructions of adequate fitness and k_{ani} . The latter are established by finding a χ^2 closest to unity for a given optimum set of weighting parameters that is within a sufficiently, yet restrictively extended interval in line with the experiences and statistics of the previous segment. Introduction and approach to the below data is of exemplary character and will be done so with respect to the corresponding central plasma parameters. For sake of comprehensibility and manageability, presentation of the individual $P_{\text{rad}}(2D)$, χ^2 and forward and backward calculated detector signal profiles will be omitted. Their relevance towards the evaluation of this nature is limited, though they are recorded regardless and employed later on in an overarching comparison for all and per discharge experimental and phantom reconstructions.

XP20180725.44

The central plasma parameters for experiment *XP20180725.44* are shown in figure 5.41, including ECRH, HBC and VBC radiation power P_{rad} , diamagnetic energy W_{dia} , its temporal derivative, a selection of *Thomson scattering* LOS volumes and line integrated dispersion interferometry for electron density, as well as electron cyclotron emission temperature measurements. Thereof derived radiation fraction f_{rad} and integrated divertor heat load are plotted separately. This was partially already introduced and discussed in figure 2.27, only the electron quantities have been added in this case. Here, the magnetic configuration is that of a high mirror field (*KJM*), hence the slightly altered shape of the triangular plane, island structure, reconstruction domain and subsequent pixel grid.

After an initial smaller spike in n_e after plasma startup to up to $2.5/\text{m}^3$ in 0.2 s, with lesser pronounced maxima and absolute values the further radially outside the LOS volumes are located, the density decays again and then

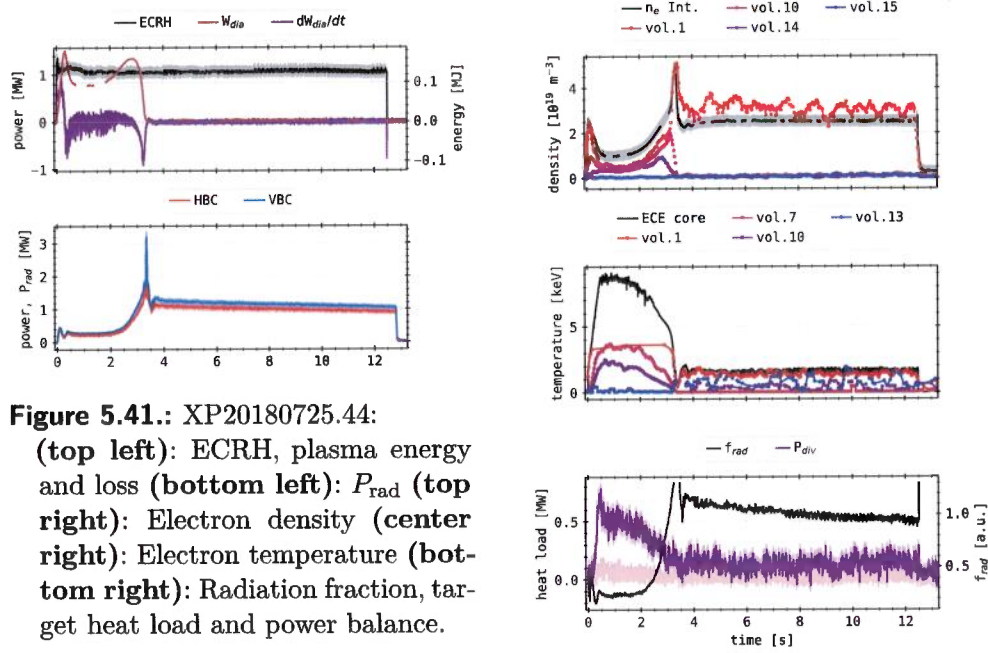


Figure 5.41.: XP20180725.44:

(**top left**): ECRH, plasma energy and loss (**bottom left**): P_{rad} (**top right**): Electron density (**center right**): Electron temperature (**bottom right**): Radiation fraction, target heat load and power balance.

parabolically increases to $5/\text{m}^3$ in 3 s. The latter shows a similar behaviour, though the outermost measurements rise earlier and may not even yield a peak at all. Afterwards, from 3–12.5 s only the innermost and interferometer data show significant n_e values around $2.5\text{--}3.75 \text{ } 1/\text{m}^3$ and all other volumes drop to null.

The electron temperature similarly has a strong increase within the first 0.5 s to up to 9 keV in the core and less the further outward the LOS volume is located, i.e. 2.5–3.8 keV. The outermost volume no. 13 does not increase before 3.2 s and is essentially null until then. Between 0.5–3.4, the temperature first gradually and then rapidly decreases to nearly zero - the innermost TS volume however yields no data points in that interval. Successively, T_e grows slightly and remains relatively constant around 1.9 keV until 12.5 s, while the outside volumes show lower temperatures and vary significantly within that range, though volume no. seven remains null and the profiles of no. ten and 13 might be within their respective uncertainty intervals, given the offset after discharge termination >12.5 s.

The radiation fraction is cut off at $f_{\text{rad}} > 1.4$ a. u. and generally follows the

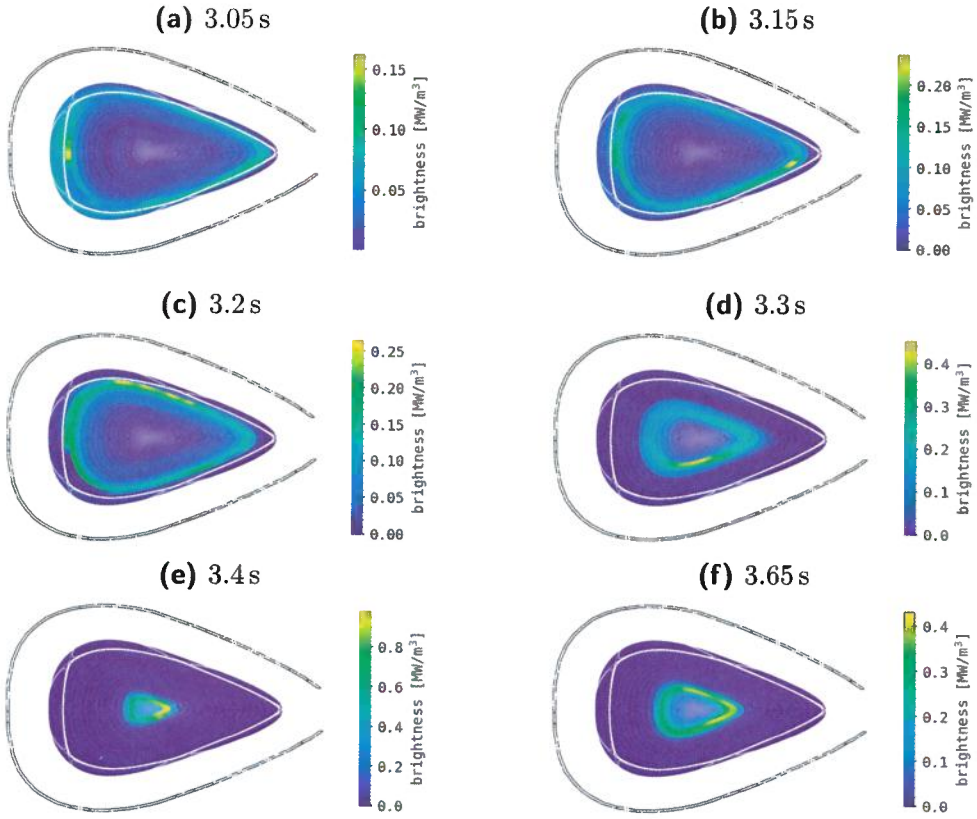


Figure 5.42.: XP20180725.44:

Tomograms for the above discharge on a $1.25 r_a$ inflated grid with $n_r \times n_\theta = 20 \times 150$ and KJM high mirror magnetic configuration. RDA parameters applied here are $k_{\text{core}}, k_{\text{edge}} = \{2, 0.25\}$ with $N_T = 15$ and $N_S = 2$. Central experiment parameters can be found in figure 5.41.

shape of both cameras P_{rad} profiles, since the ECRH can be considered constant throughout the experiment. Hence, the plot is broken up between 3.2–3.4 s, where the radiation power eclipses the heating by a factor of 3.2 and then also slowly decreases, which is concluded again by a spike beyond the spectrum due to the plasma and radiative decay after the shutdown of the microwave heating.

In figure 5.42, an excerpt of six points in time just before and across the

pronounced global maximum in 3.4 s from the multicamera, bolometric measurement is reconstructed using the same set of $k_{\text{ani}} = \{2, 0.25\}$ and secondary coefficients $N_T = 15$ and $N_S = 2$ (see section 5.1.1). This configuration strongly favours smooth and isotropic emissivity profiles inside the core up to two cells close to the separatrix and therefore more anisotropic structures beyond until the edge of the domain.

The first tomogram in (a) for $t = 3.05$ s shows a relatively even and smooth, shallow profile of $\sim 0.12 \text{ MW/m}^3$ along the LCFS of increased width. On the inboard side and towards the lower X-point, this is moved further inward and a distinct maximum can be found around $z = 0$ with 0.16 MW/m^3 , while the correspond island is also slightly brighter than the rest. The core is mostly dark with an emissivity $< 0.05 \text{ MW/m}^3$.

In (b) for $t = 3.15$ s, this somewhat smooth and thin ring has shifted radially inwards towards the magnetic axis. A decrease in radius by about two cells or $\sim 0.05r_a$ is accompanied by poloidal translation of the maximum emissivity of 0.23 MW/m^3 closer to the HBCm aperture, adjacent to the lower outboard magnetic island. The inboard side of the profile is still noticeably brighter with 0.17 MW/m^3 compared to the rest at 0.13 MW/m^3 . At $t = 3.2$ s in (c), the distribution has shrunk even further, however not homogeneously but rather by establishing a more pronounced edge towards the now entirely radiation-less SOL and separatrix area. Hence, the ring brightness grows slightly overall to $0.18\text{--}0.2 \text{ MW/m}^3$ and the peak power of 0.26 MW/m^3 can be found closest to the midplane, upper X-point with minor substructures and an increased poloidal width.

For $t = 3.3$ s, tomogram (d) shows a now significantly, radially smaller profile of very smooth emissivity, besides the maximum towards the lower inboard magnetic island. The latter, now smaller again yields 0.42 MW/m^3 and the, to $0.3r_a$ widened ring 0.3 MW/m^3 while its center and outside area remain without noticeable radiation.

Coincidental with the peak in P_{rad} , the core n_e measurements and dW_{dia}/dt , the second to last reconstruction for $t = 3.4$ s in (e) shows the smallest brightness profile at only a radius of $0.2r_{\text{ixa}}$, also featuring the highest overall and maximum emissivity of $0.7\text{--}0.97 \text{ MW/m}^3$. The highest radiation density is found towards the tip of the triangle-shaped plane, though due to the reduced size of the distribution this expands to nearly half the circumference of the latter. Still, this small ring appears slightly hollowed like before and otherwise smooth. Radial width or decay of said feature is comparable to

before, given the significantly different ratio between size and shape.

Finally, at the equilibrated plateau shortly after that peak in $t = 3.65$ s, tomogram (f) presents again a larger brightness profile with a radius of $\sim 0.3r_a$, with a similar structure but only less than half the intensity of the previous reconstruction, i.e. $0.3\text{--}4.3 \text{ MW/m}^3$. Width, poloidal smoothness and hollowness are also nearly congruent to the prior. Like in the preceding three tomograms, no radiation is placed outside the edge of the distinctly confined distribution.

This first exemplary discharge in figure 5.41 and its corresponding, selective MFR of experimental data in figure 5.42 yield plausible, albeit qualitative correlations. The behaviour of the two-dimensional radiation profiles corresponds well with the indicated plasma density and its temporal evolution, particularly the intrinsic discrepancy between the outer and inner LOS volumes. The same is true for the reduction and centralization of T_e during that time, coinciding with an increase and narrowing in the tomogram radiation powers for a constant input microwave heating and negligible plasma stored energy. Furthermore, with respect to the total P_{rad} of both cameras, the quantitative character of the brightness distribution across the selected points in time is also well-supported. Given the shape and structure of the reconstructed profiles, the applied anisotropic regularisation weight coefficients $k_{\text{ani}} = \{2, 0.25\}$, $N_T = 15$ and $N_S = 2$ produced adequate results that align with the established phantom image benchmarks.

*plotting radial profiles
for n_e, T_e and E would
allow to see it.*

XP20180809.13

The next exemplary discharge XP20180809.13 and its central plasma parameters are presented in figure 5.43. It is particularly characterised by a constant heating power P_{ECRH} , generally very low radiation fraction $f_{\text{rad}} \leq 0.25$ ~~a.u.~~¹⁰ and two distinct events that lead to noticeable, large spikes in radiative power loss P_{rad} . These are caused by the injection of tertiary impurities through the ablation of metal particles by a *Laser Blow-Off* (LBO) system - a concentrated, high power laser beam superheats, ablates ~~and ejects~~ from plasma-side coated glass tiles into the SOL. The injected amount is relatively small, though possible charge states increased, hence the negligible or small impact on W_{dia} and the electron density and temperature. The input P_{ECRH} is, after an initial step to 2 MW before 0.25 s and subsequent decay from 3.5 MW, set constant at 2.6 MW. Correspondingly, the plasma

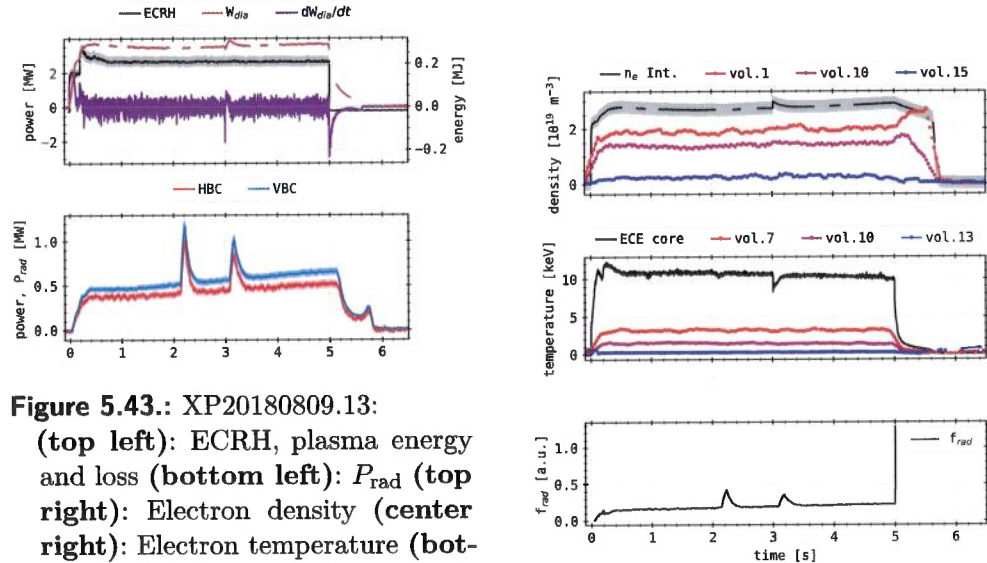


Figure 5.43.: XP20180809.13:

(top left): ECRH, plasma energy and loss (bottom left): P_{rad} (top right): Electron density (center right): Electron temperature (bottom right): Radiation fraction and target heat load.

stored energy increases sharply in the beginning to 0.29 MJ and also steadily remains here besides a small positive bump at the time of the second blow-off. Its derivative therefore consists largely of null-level noise except in the beginning and during that minor peak, i.e. up to 2 MW and $-2\text{--}1$ MW respectively. The bolometers P_{rad} increases initially to 0.4–0.5 MW and overall steadily grows to 0.5–0.7 MW between the two cameras before decaying, with a secondary peak to 0.3 MW in 5.7 s, 0.7 s after the input heating is turned off. As mentioned before, the two LBO events are highlighted here by large maxima of 1.4 MW in 2 s and 1.2 MW in 3 s. Both camera results are qualitatively in good agreement and are only separated, growing with discharge time by <0.1 MW. The indicated confidence intervals of those do not exceed ± 50 kW. From inside to out, the electron density decreases from 2.5–0.3 1/m³ in the interferometer measured to the most outward TS volumes, however remaining relatively constant throughout the discharge. Only in 3 s a small peak in the line integrated n_e indicates a secondary injection of impurities. The same is true for the corresponding temperatures of 11 keV down to null, hence the discrepancy between ECE provided values and TS volumes is significantly increased. Inner- to outermost, the

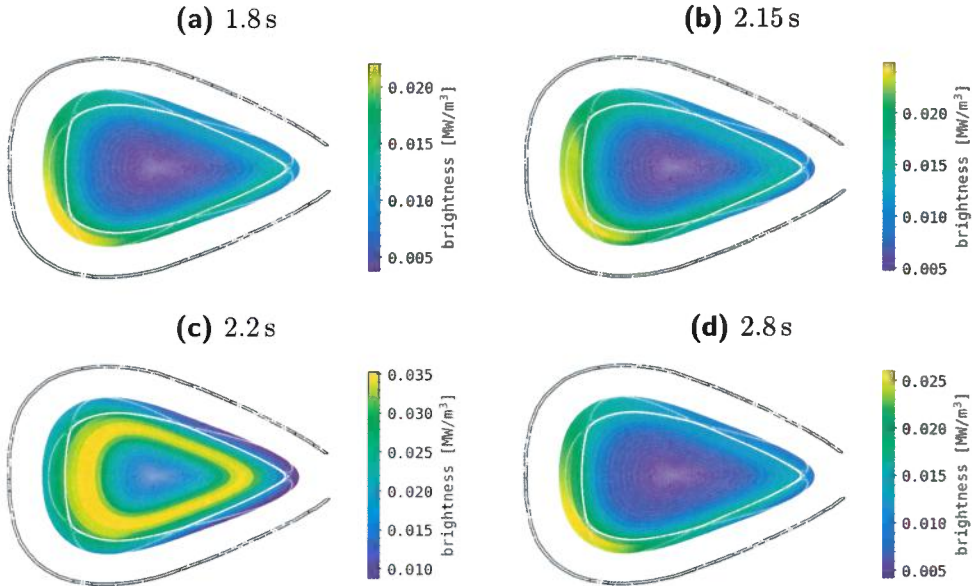


Figure 5.44.: XP20180809.13:

Tomographic reconstruction of experimental bolometer data on a $1.35 r_a$ inversion grid of standard magnetic configuration, otherwise similar to figure 5.42, between 1.8–2.8 s. RDA parameters are constant throughout at $k_{\text{core}}, k_{\text{edge}} = \{2, 0.5\}$ and $N_T = 14, N_S = 2$. Corresponding central experiment parameters can be found in figure 5.43.

latter though only yield 3.5–1.8 keV, while volume no. 13 constantly read zero. During the first only negligibly and after the second ablation, $T_{e,\text{ECE}}$ instantaneously drops from 11–8 keV, before quickly and steadily growing back to the previous level. Finally, as stated above, the f_{rad} remains low throughout the experiment at <0.3 a. u., only breaching that threshold in correspondence to the laser blow-offs to a maximum 0.4 a. u.

The selected points in time for the performed reconstructions in figure 5.44 coincide with just before $t = 1.8$ s, during 2.15–2.2 s the first and again equilibrated after the second event in 2.8 s. Again, they are all produced using the same set of $k_{\text{ani}} = \{2, 0.5\}$ and parameters $N_T = 14, N_S = 2$. Here, the underlying magnetic configuration for the experiment and constructed two-dimensional mesh is standard., whereas the domain size has been inflated

slightly more to $1.35r_a$. Plot (a) shows a maximum brightness outside the separatrix of particular, increased poloidal width, on the lower inboard side closest to the corresponding X-point of 22 kW/m^3 . Along the LCFS, the smooth intensity profile shows a relatively constant 15 kW/m^3 , though a very minor up-down asymmetry of $\pm 2 \text{ kW/m}^3$ is indicated.

In $t = 2.15 \text{ s}$, after the injection of secondary impurities but before a bolometer measured response in plasma radiation, minute changes in the absolute level of emission and its radial position hint at a contraction of the latter ring. The highest emissivity here is 25 kW/m^3 . One can also now notice a similarly bright inboard island of 23 kW/m^3 , expanding further on the lower peak from before. The rest of the profile is barely, if at all shifted inwards. During the maximum in P_{rad} at $t = 2.2 \text{ s}$, the total emissivity is, on one hand significantly increased to 35 kW/m^3 and on the other essentially constant in a fixed radius $\sim 0.7r_a$ and FWHM of $0.15r_a$ on the inside of the separatrix. On the outboard side, the tomogram is distinctly limited, i.e. no radiation is reconstructed beyond the radial decay of the ring. Toward the inboard boundary, the (half-)width of the profile is increased to $0.25r_a$ and hence a considerable brightness still can be noted beyond the corresponding island structure. Conclusively, for $t = 2.8 \text{ s}$ in figure (b) at which the plasma radiation again has equilibrated but before the second LBO, a qualitatively congruent emissivity distribution is presented. While the absolute power level is increased slightly to 26 kW/m^3 and the radial decay towards the outboard tip of the triangular plane is shortened, the remaining tomogram is otherwise the same as in $t = 1.8 \text{ s}$.

This set of MFR shows two major characteristics of interest with respect to the introduced data in figure 5.43: first the contraction of the radiation distribution and its evolution under injection of external impurities and second the subsequent equilibration thereof. Introduction of additional high-Z material into the discharge leads to a reduction in T_e under constant or minor increase of plasma stored energy and large power dissipation through radiation. The lack of precise temporal correlation between P_{rad} and the other plasma parameters during that event is not yet entirely understood. However, correlation tests, for example superimposing the outermost channels of the bolometers with the ECRH, have shown no significant deviation and therefore ruled out lagging of the prior in this context. No feedback was performed in this case, i.e. no parasitic computational load on the system like in section 3.2.1 is noted. The consequential centralisation of radiation is the

result of the strong ionisation of said material and hence its transport across the separatrix into the core. At this time, the plasmas' emissivity is entirely dominated by the *quasi* equilibrated impurity distribution, producing the smooth and constant profile aligned in the center and along the LCFS. The asymmetry or shift of the maximum brightness towards the inboard side is attributed to a combination of magnetic configuration, the location of the bolometer inside the W7-X vessel, the low f_{rad} and therefore condensation of radiation in the LOS in and close to X-points. Lastly, this process proves to be reversible, as the ablated impurity is then again kinetically transported to the SOL and ejected from the plasma after relaxation of the central parameters. Again, this set of experimental MFR are well in agreement with the previous extensive verification benchmarks and accompanying diagnostic data in figure 5.43.

XP20181010.32

The next experimental data tomography concerns the prime real-time bolometer feedback application in XP20181010.32. Background plasma parameters and scenario configurations have been thoroughly and extensively illustrated in section 3.2.3 and more specifically figure 3.20. A selected set of points in time and tomograms have been produced in order to highlight the effects of the supplementary injection of gas impurities through the *thermal helium beam*. The results can be seen in figure 5.45. Regarding the previous reconstructions, similar or identical settings have been used to find the corresponding tomograms, though the experimental scenarios are vastly different. As one can already tell from taking a glimpse at the plot collection below, the characteristic features here are distinctly pronounced and in stark contrast to the latter images at the same time.

In (a) for $t = 0.65$ s during a small plateau, i.e. before the injection via the thermal gas valves has begun and at low $P_{\text{rad}} = 1.5$ MW and $f_{\text{rad}} \sim 0.25$ a. u., the first tomogram yields a largely radiationless or dim profile of a maximum 0.3 MW/m³, which is found very concentrated, close to the lower inboard X-point and inside the lower outboard island. Secondary features of a lesser intensity ~ 0.2 MW/m³ are located next to the upper central X-point, as well as in and around the lower inboard island. In-between these structures, sporadic emissivity of < 0.15 MW/m³ is scattered around the separatrix, mostly in the SOL but not outside $1.3r_a$.

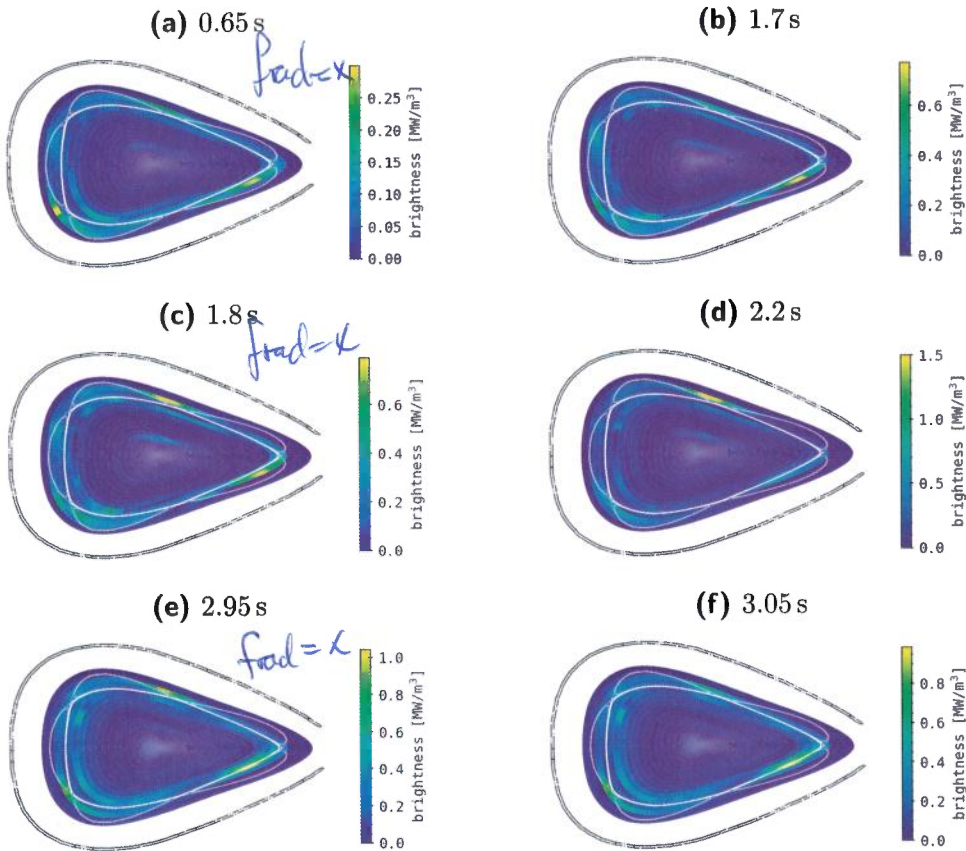


Figure 5.45.: XP20181010.32:

Tomographic reconstruction of experimental data on a $1.35 r_a$ inversion grid with $n_r \times n_\phi = 30 \times 150$, based off of standard magnetic configuration. Throughout 0.65–3.05 s, the RDA parameters are constant at $k_{\text{core}}, k_{\text{edge}} = \{2, 0.35\}$. Corresponding central experiment parameters have been previously introduced in figure 3.20.

Then, at 1.7 s, the overall quality of the profile does not change, though the only remaining maximum is than in the lower island at the tip of the triangular shaped plane. Its brightness is also greatly increased to 0.77 MW/m^3 , while the relative intensity of the other previous extremes around the X-points is reduced. At that time, the QSB has continuously injected helium

5.4. Tomography of Experimental Data

as an impurity into the SOL and the ECRH has reached its steady-state power level. In terms of plasma profiles, density, temperature and radiation are strongly increasing at this moment still.

With the earliest equilibration of n_e and T_e , $t = 1.8$ s shows an emissivity distribution of similar magnitude - slightly increased to 0.78 MW/m^3 -, however now with the primary, global maximum in the upper central X-point and the previous decreased minutely. Outside those, the profile remains largely unchanged. Shortly after in 2.2 s for figure (d), a strong injection sequence of the thermal gas inlet feedback valves is concluded and P_{rad} has a first preliminary maximum of 4.5 MW. Simultaneously, electron temperature and density show minor peaks across the spatial spectrum. At this time, f_{rad} reaches 75% and the radiation power distribution condenses almost entirely to 1.5 MW/m^3 in a singular, confined point close to the intersection of the two upper magnetic islands. Relatively, no significant other structures stand out, though in locations of previous extremes emissivities of up to 0.6 MW/m^3 can be noted.

Next, at 2.95 s in figure (e), the radiation fraction has decreased again to a temporary minimum of $\sim 80\%$ in reaction to another full flow feedback injection pulse of 0.3 s and its shut-off. At the same time, T_e shows a minor minimum, while n_e yields a small maximum across the included diagnostics and TS volumes. The total integrated radiation power loss has now essentially reached its *quasi steady-state* level, given the oscillations due to the gas valves opening and closing, of 5–5.5 MW. The overall maximum brightness in the corresponding tomogram is lowered however to 1.05 MW/m^3 , though the number of highlighted features of that intensity is increased. Besides the previous localisation in the upper central X-point, the concentrated emissivity of the lower outboard island is now the global maximum and moved inwards onto the LCFS. A secondary structure at the lower inboard X-points yields 0.85 MW/m^3 .

Finally, tomogram (f) at $t = 3.05$ s corresponds to an f_{rad} of $\sim 95\%$, also coinciding with a preliminary maximum in T_e and minimum in n_e . This takes place while the QSB valves are closed and no additional gas injection is performed for another 0.1 s. In the conclusive two-dimensional radiation distribution, the brightest feature of 0.97 MW/m^3 is located again on the separatrix close to the lower outboard island, while previously noted localisations are reduced in intensity to $\leq 0.7 \text{ MW/m}^3$. With respect to the remaining, more or less sporadic profile, its relative emissivity is more akin

to that in 2.95 s and 1.8 s, i.e. less condensed to the aforementioned extremes. This sequence of MFR profiles provides a fundamental insight into the behaviour and impact of high- f_{rad} radiation feedback controlled thermal gas injections. It also graphically highlights the before outlined difficulty of defining and finding an ideal or even adequate LOS combination for the real-time bolometer evaluation metric - see section 3.2 and section 4.3. Both can be reduced to the very pronounced focussing of emission in points of intersecting closed field lines in the SOL and magnetic islands. Throughout the temporal evolution of the emissivity distribution, this characteristic is presented by a noticeable and significant correlation with the, however indirectly, feedback controlled radiation fraction. Up to 80% of f_{rad} , the majority brightness condenses and shifts from the lower outboard in counter-clockwise direction towards the upper central X-point. Beyond this level, though at a significantly increased absolute power, this trend is reversed and, with the radiation fraction growing towards unity, the majority of emissivities move to the lower outboard island. This process in itself is again reversible and between 80–100 %, this reallocation goes back and forth with the opening and closing of the thermal helium beam valves. That said, only during opening of said valves and injection of gaseous impurities, brightness profiles like in (d) are measured and the plasmas' response leads to conditions as in (e)-(f). This is on one hand due to the location of the gas inlet and its connection along magnetic field lines to the bolometer measurement plane, and on the other the combination of f_{rad} level and plasma profiles. The latter means that emissions are *pushed out* towards the separatrix and SOL, as the temperature and density distributions peak and centralise, meaning a sharp drop-off at that radius - see the extensive STRAHL simulations based on data from this discharge in section 4.4. Hence, the tomograms find the majority of emissivities only in these particular locations for $r \geq r_a$. Regarding the configuration and selection of LOS for the real-time radiation estimate P_{pred} , this behaviour makes it particularly difficult to find an ideal or fitting set to adequately measure the power throughout the experiment. Hypothetically, a predictive collection only looking at the upper- and inboard-side SOL from both bolometer camera arrays inevitably overestimates, while in this case the opposite certainly underestimates the actual, total radiative power exhaust. A balanced set that watches all the above characteristics and also possibly integrates through intermittently lit areas is of great importance towards the success of such an application.

5.4. Tomography of Experimental Data

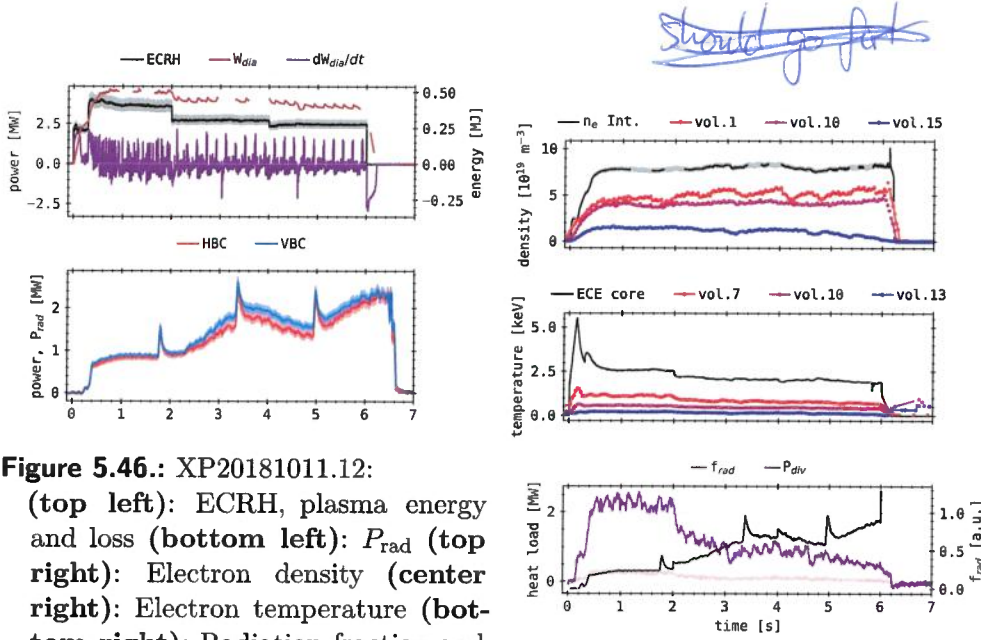


Figure 5.46.: XP20181011.12:

(top left): ECRH, plasma energy and loss (bottom left): P_{rad} (top right): Electron density (center right): Electron temperature (bottom right): Radiation fraction and target heat load.

In conclusion, the presented results and their interpretation are essential for following real-time, bolometer controlled radiation feedback experiments. However, the limited set of effectively one data point in XP20181010.32 makes predictions difficult.

XP20181011.12

The final example of experimental bolometer data *Minimum Fisher tomographic reconstruction* is given by XP20181011.12, of which the core plasma parameters are shown in figure 5.46 and the respective two-dimensional emissivity distributions in figure 5.47. This discharge is mostly characterised by two input power step-downs in the ECRH and intermittent impurity injections via the *laser blow-off* system, leading to, on one hand very pronounced events and on the other larger gradients in P_{rad} .

The heating power in the top left of figure 5.46 begins with a small step of 2 MW until 0.3 s and follows with the first plateau at 3.5 MW for 1.7 s. After, P_{ECRH} is reduced to 2.7 MW for the next 2 s, until it finally drops to 2.5 MW for the remaining 2 s of discharge duration. Accordingly, W_{dia}

gradually increases to 0.27 MJ and then 0.5 MJ for the first major step in input heating. On top of that and throughout the rest of the experiment, minor oscillations of ± 50 kJ can be noted in the diamagnetic energy. With the first step-down in power, W_{dia} drops 0.1 MJ and at the conclusive second another 50 kJ before quickly decaying after ECRH shut-off. Its derivative largely reflects the described variations with temporally correlating ± 2 MW. Both bolometer camera results are qualitatively in good agreement, while the VBC estimates P_{rad} to be ≤ 0.3 MW larger in some places. The radiation power increases with a noticeable delay of 0.3 s to 0.8 MW, of which the equilibration is interrupted by the first LBO event in 1.7 s, leading to a peak of 1.7 MW. After the heating power step-down in 2 s, the radiative power loss near linearly grows to 1.8 MW in 3.3 s, at which the second ablation into the SOL takes place and causes a maximum of 2.7 MW. Afterwards, P_{rad} decreases again to 1.6 MW, simultaneously to the corresponding ECRH reduction, before the last impurity injection produces a peak emissivity of 2.6 MW in 4.9 s. The final 1.6 s of plasma radiation are dominated by an additional, steady growth to 2.5 MW before its collapse.

In the top right of figure 5.46, the plasma electron density remains generally constant throughout the discharge, after an initial increase, around $8\text{--}1.5 \text{ 1/m}^3$ from the inner- to outermost measurements. Neither LBO events nor ECRH steps appear to perturb n_e in these diagnostics and volumes significantly, though volume no. 15 decreases slowly over time until it almost measures null at the termination of the experiment. A similar picture is presented by the respective temperature, however T_e as provided by the ECE core diagnostic finds a large peak of 6 keV with a subsequent parabolic decay to 2.5 keV. This value also responds with minor decrements of 0.1–0.2 keV to the heating power step-downs, concluding the discharge at 1.9 keV. To a much smaller extent, the innermost *Thomson scattering* volume also presents this behaviour, peaking at 1.5 keV and equilibrating after 2 s around 1 keV. Measurement performed further outward remain relatively constant at even lower temperatures.

The radiation fraction generally follows the shape of the P_{rad} profile since the ECRH is constant with respect to its plateaus. In 2 s and 4 s however, a small jump in f_{rad} is visible due to the step-down in input power. At the end of the experiment, where P_{rad} is near maximum and P_{ECRH} at its lowest level, the radiation fraction reaches 0.85 a. u., while its global maximum is 0.93 a. u. at the second LBO ablation. Integrated and individual target heat

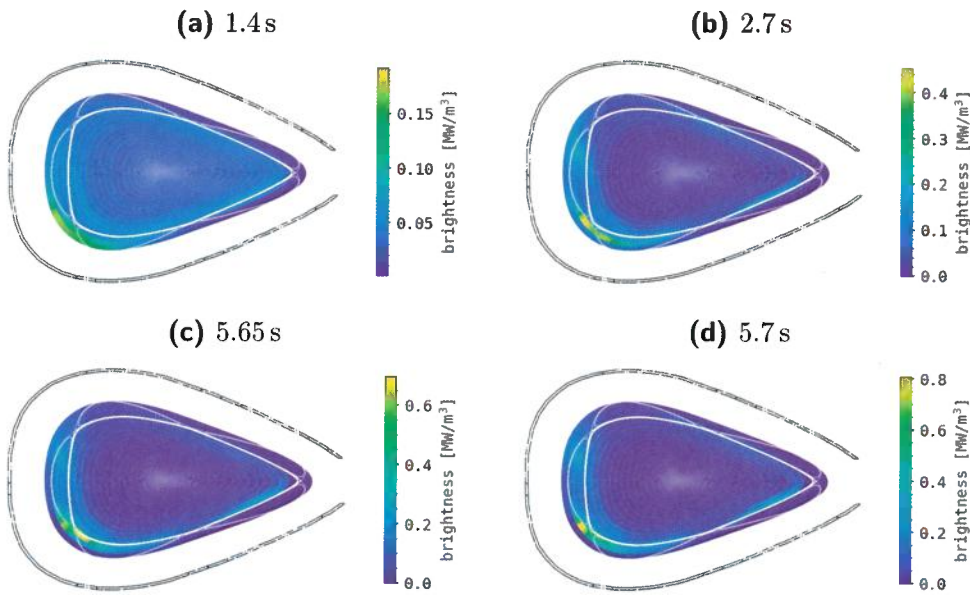


Figure 5.47.: XP20181011.12:

Tomographic reconstruction of experimental bolometer data on a $1.35 r_a$ inversion grid with $n_r \times n_\theta = 20 \times 150$ intersections, based off of the *KJM* high mirror magnetic configuration. RDA parameters are constant throughout at $k_{\text{core}}, k_{\text{edge}} = \{2, 0.35\}$ and $N_T = 14, N_S = 2$. Corresponding central experiment parameters can be found in figure 5.46.

loads show an inverse behaviour, the total P_{div} being largest around 2.3 MW during the first ECRH plateau and decreasing with the corresponding step-downs to first ~ 0.9 MW and then further gradually to 0.2 MW at the end of the discharge.

Figure 5.47 shows tomographic reconstructions of the respective bolometer measurement at four selected points in time. This experiment and hence the underlying MFR mesh are again based in a *high mirror field* magnetic configuration (*KJM*). Employed anisotropic regularisation weighting coefficients and parameters are kept constant at $k_{\text{ani}} = \{2, 0.35\}$ and $N_T = 14, N_S = 2$, similarly favouring smooth core and localised SOL emissivities. In (a) at $t = 1.4$ s, the radiation is near evenly distributed inside the separatrix at the outboard side, magnetic islands on the bottom, top and the

inboard side domain boundary with around 0.12 MW/m^3 . Only on the outside of the lower inboard X-point a strong and radially focused maximum of 0.19 MW/m^3 with a poloidal width of $\sim 0.125 \text{ rad}$ can be found. Minor variations $\leq \pm 0.01 \text{ MW/m}^3$ are presented along the lower inside the LCFS and in the core for $r < 0.7r_a$. At $t = 2.7 \text{ s}$ in figure (b), the inboard localisation slightly shifts radially towards the X-point and is now only one cell wide, while its emissivity increases to 0.45 MW/m^3 . Simultaneously, the overall brightness in the core and closer to the tip of the triangular plane remains constant, therefore decreasing significantly in relative terms. On the inside of the lower outboard island, towards the inboard structure as well as in its neighbouring islands, the intensity is raised to $0.25\text{--}0.3 \text{ MW/m}^3$. In (c) at $t = 5.65 \text{ s}$, the same behaviour as before is presented, now with a maximum emissivity of 0.7 MW/m^3 and secondary features at $0.3\text{--}0.4 \text{ MW/m}^3$. However, the localised characteristic has separated and expands now from the inboard magnetic island to the separatrix and X-point, where the peak lies. Finally, at 5.7 s in (d), the overall and maximum radiation density are increased again to $0.4\text{--}0.5 \text{ MW/m}^3$ and 0.8 MW/m^3 respectively. Now, the brightest feature is pushed outward again towards the edge of the inboard island and the inner structure is dimmed slightly.

The distribution of emissivity and its evolution throughout the course of this discharge is dominated by the characteristic condensation at the lower inboard X-point. Indications thereof can be seen in figure 5.42 at $t = 3.05 \text{ s}$, i.e. the tomogram with the highest f_{rad} in this sequence, however the configuration of the experiment and condition of the machine did allow for and achieve this particular profile of radiation. Experiment XP20181011.12 took place after the second boronisation of the W7-X vessel - a cleaning process and condition of the first wall using diborane gas and long duration glow discharges, after which the performance in terms of radiative power loss, impurity content, plasma density and temperature at a given input power is greatly improved. Hence, the qualitative structure of this set of tomograms is more akin to high radiation fraction experiments like XP20181010.32 etc., with the majority of emissions in the SOL and separatrix. However, in the first reconstruction at the lowest f_{rad} , the brightness beyond the LCFS is comparatively smooth, contrary to the corresponding $k_{\text{edge}} = 0.35 \text{ a.u.}$ which emphasizes anisotropic profiles. After a heating power step-down and external impurity injection, a similar contraction of emissivities like before applies to this distribution, condensing the now much larger total power to

a singular point. Further P_{ECRH} reduction, repeated ablation and therefore increase in radiation fraction conclusively leads to an inward shift of that feature. Finally, beyond that f_{rad} threshold and total intensity due to another decrease in input power and LBO event, this begins to move outward again, though in and along the respective magnetic island.

Regarding the performance of the MFR itself, the perhaps at this point generalizing k_{ani} weighting parameter configuration yields plausible results of adequate quality and is able to differentiate between minute changes between the selected profiles. The presented two-dimensional radiation distributions are also in line with the previously featured phantom image and experimental data reconstructions, i.e. transitions and proportions are in well in agreement with before. Particularly the capability to resolve single cell variations in location and brightness across a smaller range of intensity levels is proven here, especially given the increased uncertainty in actually measured data.

This concludes the, albeit limited application of the introduced and benchmarked MFR tomography algorithm on experimental bolometer data. Presented results have been achieved with confidence, particularly in light of the benchmarks performed in the previous section and underline the capabilities of said method. However, this is certainly only a, as was stated in the beginning, proof of concept. Implications should in no way be interpreted as generalized deductions, applicable to arbitrary input profiles, more so when taking into account the practically infinite experimental parameter space available.

5.4.1. Tomographic Reconstruction Statistics

The final step of this thesis is a *pseudo-statistical* analysis of the accumulated phantom image and experimental bolometer data Minimum Fisher reconstructions with respect to properties already introduced in the benchmarking process. The goal here is to, on one hand find possible underlying correlations in these numbers for artificial radiation distributions and on the other evaluate the fit of the previous tomograms with their corresponding core plasma parameters, i.e. power balance and P_{rad} .

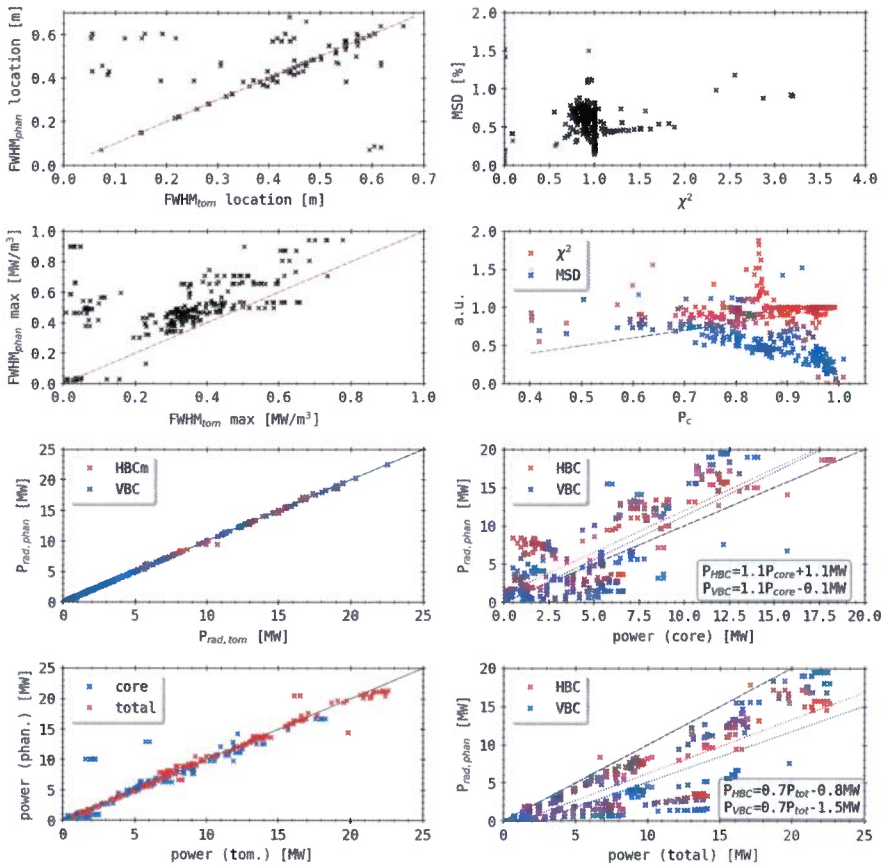


Figure 5.48.: Collected results of previously presented tomographic phantom radiation profile reconstructions in section 5.3. A red, dashed line indicates congruence between the two, i.e. 1:1 relation. **(left):** From top to bottom: FWHM position, FWHM maximum, P_{rad} from both cameras and two-dimensional, integrated emissivity. **(right):** From top to bottom: MSD over χ^2 , MSD and χ^2 over Pearson coefficient ρ_C , P_{rad} over integral of core emissivity and over total integrated radiation.

Phantom Reconstructions

Why not right after the phantom section?

First, combinations of the MFR phantom radiation image benchmark are collected and condensed into figure 5.48. Included are tomograms that yielded an absolute deviation from the phantom that is less than the integral of

the radiation distribution. In the left column of plots, the abscissa values are populated by data from the artificial input distributions, while the ordinate is defined by their respective tomogram match. The right column shows combinations of quality parameters MSD , Pearson coefficient ρ_c and fitness factor χ^2 , as well as the two-dimensional integrated powers and the individual P_{rad} extrapolations from the forward calculated detector signals. In all images, a 1:1 congruence line with 45° inclination is included to highlight ideal agreement in the data.

At the top on the left, the FWHM locations in the phantoms are compared to their reconstructed counterparts. However, as it was shown before, equality in number of radial extremes for both is not trivial, so value pairs ($FWHM_{\text{phan}}, FWHM_{\text{tom}}$) are produced here only where this is the case. Throughout the radial spectra, points are generally grouped close to or at the aforementioned line. Below, i.e. for tomogram maxima larger than their target, only a few outliers are measured, while for the opposite, $FWHM_{\text{phan}}(\text{loc.}) > FWHM_{\text{tom}}(\text{loc.})$ significantly more are found, particularly for greater discrepancies. Small groupings of points can be attributed to individual sets of one type of phantom image, e.g. a single bright ring or anisotropic island-like chains in the SOL. For the peak widths, the number of combinations is improved since every radial profile yields a result, as long as at least one extremum is produced. In the second plot, the corresponding maxima do not show a similar behaviour, presenting the input FWHM widths to be consistently larger. On average, $FWHM_{\text{phan}}(\text{max})$ is about 0.05 MW/m^3 larger than its reconstruction, whereas only a few points are below the line. Most results are grouped around $(0.35 \text{ MW/m}^3, 0.45 \text{ MW/m}^3)$, with smaller collections at the axis origin and $(0.075 \text{ MW/m}^3, 0.5 \text{ MW/m}^3)$. The next two plots compare P_{rad} from both forward calculated bolometer camera signals on the top and at the bottom the integrated two-dimensional radiation powers in the core and in total. The prior shows great congruence, with essentially only one outlier that yields an error $< 1 \text{ MW} \sim 10\%$. Otherwise, throughout the power spectrum $P_{\text{rad,phan}} = P_{\text{rad,tom}}$ within a confidence interval $\sigma_{\text{rad}} = 0.2 \text{ MW}$. No difference between HBCm and VBC~~X~~ can be noted. Below, a similar picture is presented, with the majority of the results collected closely around the 1:1 slope. However, the spread is noticeably increased, with a $\sigma_{\text{rad}} = 0.7 \text{ MW}$ and a non-negligible amount of outliers, some in larger groups with $> \pm 1 \text{ MW}$ deviation. The integrated core and total emission, as well as tomogram and phantom values show no particular

difference across the power spectrum.

In the first plot of the right column of figure 5.48, the integrated average MSD is compared to the fitness factor between forward and backward calculated detector signals. A distinct line at $\chi^2 = 1$ between 0.1–0.8 % underlines the discrepancy among the quality parameters that was highlighted before during the benchmark. So does the group of results just below 0.5 %, spreading across $\chi^2 = 1.1$ –1.8 a. u. A larger cloud of points from 0.7 to just below the fitness factor reaching unity, stretching from 0.4–0.9 % similarly shows that the two-dimensional correlation not necessarily and positively correspond to the MFR targets. However, the few and sparsely spread outliers do show that the general significance of these quality parameters holds still, especially taking the lack of data for $\chi^2 > 1$ and $>0.5\%$ into account.

In the next image, the previous two quantities are compared to the third estimate for congruence, the Pearson coefficient. Up to $\rho_c = 0.6$ a. u., almost no points are collected, with an initial smaller grouping of both parameters here around 0.8 a. u. Beyond, essentially separated by the indicated 1:1 line, χ^2 almost exclusively yields data above and the MSD below said feature. The prior shows points largely up to unity across the Pearson coefficients spectrum, with few outliers, a tight grouping of a large number of results closer to $\rho_c = 1$ a. u. and a particular column in 0.84 a. u. between $\chi^2 = 1.1$ –1.9 a. u. However, the MSD does the opposite, with the majority of its data below the line and a noticeable decay between 0.75–1 a. u. from 0.7 % to 0.2 %. Distinguishable clouds of points can be found along that near-linear trend.

The third plot of that column compares the individual cameras P_{rad} extrapolation from the forward calculated detector signals to the two-dimensional integrated power in the tomograms core. Additionally, separate linear fits for the HBC and VBC data are provided, including their parameters and colour-matched plot. Up to P_{core} and $P_{rad} = 7$ MW, data from both cameras is near equally distributed around the 1:1 line, with smaller, non-specific groupings, potentially corresponding to the same phantom image or MFR iterations thereof. For larger powers, only a small number of points can be found, particularly some outliers below the indicated line and the linear fit plots of both bolometer cameras. However, above said slopes, this amount is significantly increased and features distinct clusters around (7.5 MW, 12.5 MW) and (12 MW, 17 MW), including HBC and VBC data about equally. The corresponding linear fit function coefficients are calculated using a common

least squares regression algorithm, with P_{rad} and P_{core} as the in-/dependent variables respectively. The lines are represented by $P_{\text{HBC}} = 1.1P_{\text{core}} + 1.1 \text{ MW}$ and $P_{\text{VBC}} = 1.1P_{\text{core}} - 0.1 \text{ MW}$. Only the VBC plot intersects the 1:1 line for negligible powers, otherwise the fit functions exceed the core power consistently.

In the fourth and final image of the right column, the same plot is constructed with the total two-dimensional integrated power on the abscissa. Here, essentially all data points are under the 1:1 line, with the majority of those above both linear fits. Throughout the spectrum of tomogram emission levels, individual linear strings of results, their extrapolated trend originating in the coordinate origin can be found above and below, however not on the aforementioned regressions. The latter are given by $P_{\text{HBC}} = 0.7P_{\text{tot}} - 0.8 \text{ MW}$ and $P_{\text{VBC}} = 0.7P_{\text{tot}} - 1.5 \text{ MW}$. Most data is found in said line-like structures and smaller concentrations below $P_{\text{tot}} < 10 \text{ MW}$ and $P_{\text{rad}} < 10 \text{ MW}$. Above, those are spread out far more, however the general behaviour remains the same, with tighter groupings between the congruence and regression lines and noticeable point chains under the individual fits. At $P_{\text{tot}}, P_{\text{rad}} > 15 \text{ MW}$, particular horizontal feature of both camera results dominate the picture here.

Figure 5.48 visually highlights the deductions presented at the conclusion of the artificial radiation image benchmark of the introduced MFR algorithm. Results shown for FWHM location and value underline the radial matching capabilities, however at a lower fidelity in terms of the individual shape and given the discrepancy in multiplicity. The strong congruence in the comparison between bolometer camera radiative power loss extrapolations is evidence of, on one hand well preselected set of results and on the other equally effective tomography settings and success condition $\chi^2 = 1 \text{ a. u.}$ Similarly, the correspondence in absolute two-dimensional power values essentially adheres to the 1:1 line, however the degradation when compared to the above image is attributed to the intrinsic ill-posedness of the underlying inversion problem, i.e. large number of independent parameters. The same is true for the match between MSD and fitness factor, where for χ^2 approaching or at unity, the number of results increases and the tomograms' deviation is low, though still retains a noticeable spread and points are found far beyond that algorithmic cut-off. Overall characteristic and therefore conclusions here are reflected below in the comparison of fitness and Pearson coefficient, i.e. the concentrated results at $\chi^2 = 1 \text{ a. u.}$ towards

$\rho_c = 1$ and point clouds around there. The accompanying MSD data is in line with the interpretation of said two-dimensional quality measures, near linearly decreasing with increasing phantom-tomogram cross-correlation and vanishing at unity. Given this profile, the group of outliers in the previous plot and here above a fitness of 1 a. u. have to be certainly treated as such. They are connected to a particular set of artificial radiation distribution reconstructions of lesser adequacy - the corresponding MSD and ρ_c however indicate a good fit of tomogram and phantom. At last, the individual P_{rad} are not sufficiently represented by either the integrated core or total two-dimensional powers. The prior, at least for higher absolute radiation levels is potentially overestimated by the bolometer measurements, while their linear regression yields results supporting congruence at equal slopes for both cameras with minor absolute terms. Only the total radiation level presents somewhat linear coherence with P_{rad} of any camera, though at an arguably worse regression result, i.e. larger deviation of the corresponding plots from the 1:1 line and poorer parameters. Hence, the bolometers' extrapolation underestimates the - phantom contained - total emission, given the set of distributions and fits. The distinctive gap in results here suggests that for general groups of radiation profiles, more accurate predictive linear models could be calculated, though at possibly greater discrepancy to the ideal match of $P_{\text{rad}} : P_{\text{2D}}$ or even P_{tot} .

Experimental Data Reconstruction

Comparing MFR tomography results across different experiments statistically has proven difficult and so far has not produced substantial insight, however not beyond what was previously condensed from the established P_{rad} or chordal brightness data anyhow. This section will proceed and investigate the experimental inversions on a larger scale more closely, i.e. similarly to the evaluations above and for an applicable selection of parameters. The forward extrapolated and two-dimensional radiation powers in total and from the core are compared in figure 5.49. Collected data is selected only for $\chi^2 < 1000$, i.e. sensible results of the MFR and presented like before, including a line for exact identity of the quantities and plots for any respective linear regression fits.

The top image yields near ideal congruence of the forward and backward calculated P_{rad} from the experiment and tomogram. Except for lower total

5.4. Tomography of Experimental Data

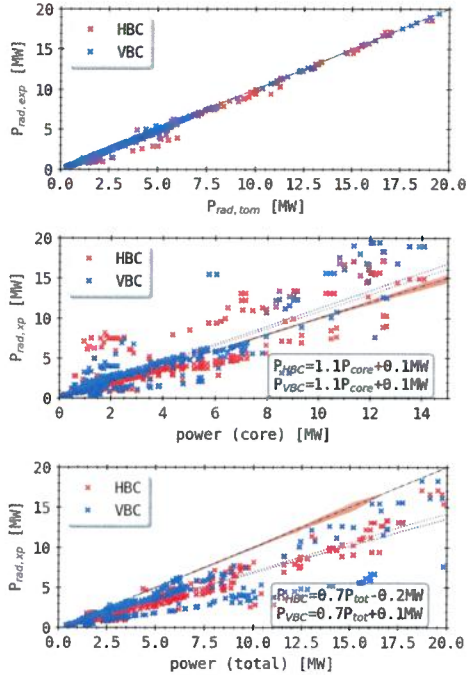


Figure 5.49.: Collected results of previously presented experimental data tomographic reconstructions in section 5.4. Included are reconstructions that yielded $\chi^2 < 1000$. A dashed 1:1 line indicates congruence between the axis and abscissa. If applicable, a regression linear fit for both cameras derived individually is noted in the bottom. A transparent error bar (orange) is indicated around the projected congruence. **(top):** P_{rad} of both bolometer cameras from experiment and tomogram. **(center):** P_{rad} of both cameras over integral of core emissivity. **(bottom):** P_{rad} of both cameras over total integral of emissivity.

powers $< 7 \text{ MW}$, where the deviation of some HBC extrapolations is noticeably increased, the points follow the 1:1 line almost precisely. At most, a discrepancy of $\pm 0.75 \text{ MW}$ applies here across the spectrum. In the following image, the input detector measurement P_{rad} is compared to the core integrated two-dimensional power from the tomogram. Here, the dispersion of results is significantly larger than before, with a tighter grouping up to 7 MW. Particularly the VBC adheres to the direct proportionality for lower powers, however constantly by about 0.25 MW larger, while the HBC yields equally smaller values that tend to drop off quicker at those levels. For $P_{\text{core}} > 7.5 \text{ MW}$, this is replaced by a wider spread in both cameras around the 1:1 line, with slightly more points – especially the VBC – above said border, though still following the general trend. Across the spectrum, denser clouds of data with intervals of $< 0.2 \text{ MW}$ correspond to reconstructions for different settings of the same samples of the same discharge. A growing standard deviation with larger overall powers coincides with the aforementioned distribution of results. The respective regression fits are identical at $P_{\text{rad}}^{\text{HBC/VBC}} = 1.1P_{\text{core}} + 0.1 \text{ MW}$. Finally, the last image shows the same bo-

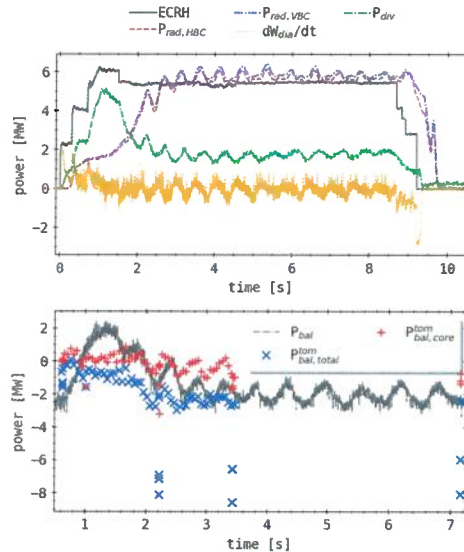
lometer measurements against the total integrated two-dimensional powers. Hence, overall similar behaviour is presented by the VBC and HBC up to 7 MW, though with a significantly lesser slope and therefore below the 1:1 line. Additionally, separate linearly increasing groups of points from the VBC in that range below the majority of data are shown. And again, beyond that threshold scattered values can be found around the fit lines, given by $P_{\text{HBC}} = 0.7P_{\text{tot}} - 0.2 \text{ MW}$ and $P_{\text{VBC}} = 0.7P_{\text{tot}} + 0.1 \text{ MW}$. A standard deviation interval around the proportionality line also grows with the abscissa values until 16.5 MW, after which it vanishes.

Keeping in mind that the presented results are collected from various experiments - data is included also for reconstructions that have not been explicitly discussed or shown in this thesis -, particularly of very characteristic emissivity distribution and transitions, the correlation between these and the images shown figure 5.48 is quite significant. Especially given the very generous threshold interval in χ^2 for preselection, the congruence between the forward and backward calculated P_{rad} is on par with the deliberately designed and adjusted phantom profile tomography results. The strong agreement is hence certainly a testament to the performance and algorithmic optimisation of the MFR. Looking back at the comparison between the extrapolated and two-dimensional integrated power from the core, the linear regression fits and their underlying data are noticeably improved with respect to the target proportionality line for the experimental reconstructions. Not only do both camera measurements yield the same prediction function within a certain rounding error, which is simultaneously very similar to the direct congruence line, the points are generally grouped closer around follow the latter more closely. However, this means that P_{rad} underestimates the total, in the tomogram contained emissivity by an amount that is about equal to the radiation power in the SOL, since the last image shows in a comparable manner that P_{tot} is consistently larger. The latter is also reflected in the accompanying fit results, which still deviate only slightly between the cameras here. In conclusion, the small set experimental data MFR has shown very promising results both qualitatively as seen previously, but also quantitatively, especially in respect to the phantom benchmark. Though the strong performance of the algorithm in combination with actual measurements is diminished or in question due to the reduced set of assessable parameters, i.e. additional P_{2D} or ρ_c .

5.4. Tomography of Experimental Data

Figure 5.50.: XP20181010.32:

Comparison between previously derived power balance for XP20181010.32 in figure 3.22 and the balance calculated from the integrated two-dimensional radiation distribution of the tomographic reconstructions presented in section 5.4. **(top):** Central experiment parameters towards the power balance. **(bottom):** Comparison of power balances derived from a common P_{rad} and the radiation distribution integrals.



Power Balance

The final application and evaluation of MFR data is done using a selection of the previously presented experimental results for different points in time during the discharges and using these to calculate their respective power balance. Firstly, central plasma parameters for XP20181010.32 as introduced and discussed in figure 3.20, alongside said P_{bal} and individual points for each MFR tomograms total and core P_{2D} are given in figure 5.50. The prior is included as direct reference as before. Below, a power balance is constructed using, on the one hand the continuous P_{rad} from bolometer measurements as a profile and on the other the separate integrated two-dimensional core and total radiation powers from reconstructions of that experiment. For a detailed, in-depth treatment of the full P_{bal} see figure 3.22, though one should note here that particularly in the very beginning of the discharge and throughout the continuing feedback injections and corresponding oscillations, it consistently fails to achieve equalisation, even under consideration of the intrinsically large standard deviation. The individual results from the tomography are largely concentrated in the first 3.5 s of the experiment, except for a single MFR performed towards the end in 7.2 s. Calculating P_{bal} using the integrated emissivity only from the core of the reconstructed brightness distributions shows an overall much improved

match, i.e. $P_{\text{bal}} \rightarrow 0$. Until the first minor adjusting gas feedback around 2 s and except for a singular outlier, a maximum deviation of -0.5 – 1 MW can be noted, though on average it is below 0.5 MW. At the same time, the total tomogram contained radiation power, consistently larger in absolute terms, hence contributes to a reduced balance of -1.75 – 0.25 MW. Up to 2 s, both feature a hollow plateau-like profile, after which both drop noticeably with the first minor feedback cycle to -1.5 MW and -3 MW respectively. The core calculated balance relaxes after, however about 0.25 s more quickly than the reference plot, to around equalisation. Its total counterpart $P_{\text{bal}}^{\text{tot}}$ has the minimum and increase after the injection even before that with an additional 0.1 s earlier, though only up to -1.5 MW again. This behaviour is, except for the decreasing amplitude in oscillation for both and reduction in base level after relaxation for the total power balance, i.e. to -2 MW, repeated until 3.4 s. Here and at 2.2 s, the latter yields outliers in P_{bal} that are beyond -6 MW and therefore can be disregarded as results of faulty MFR configurations. At last, the reconstruction in 7.2 s and the tomograms' emissivity are in line with the previous observations, including the outlier at <-6 MW.

The presented power balance calculated using the integrated two-dimensional radiation distributions show a significantly different profile than for the corresponding P_{rad} extrapolation. A reconstructed core brightness is in much better agreement with the premise of $P_{\text{bal}} \rightarrow 0$ like discussed in equation (2.37), as deviations from equalisation and variations due to the feedback are reduced compared to using P_{rad} or $P_{\text{2D}}^{\text{tot}}$. The latter shows similar behaviour, though naturally at a greater distance from the target equilibrium, while still also featuring fewer oscillations by the injection of thermal gas impurities. In this particular case at larger radiation fractions, $P_{\text{bal,tot}}^{\text{tom}}$ increases its deviation from null and the core calculated value, though the latter remains close to $P_{\text{bal}} = 0$. With respect to the previously shown phantom tomography benchmark and experimental reconstruction statistics, this is generally in line with the established picture there and the corresponding linear regression fit results.

Both, $P_{\text{bal,tot}}^{\text{tom}}$ and $P_{\text{bal,core}}^{\text{tom}}$, are seen as a parameter for calculating P_{bal} , an improvement in qualitative and quantitative terms compared to the standalone extrapolation of detector measurements. Given the initial example, in special applications or for an optimised algorithm of allocating MFR samples - the computational load for a continuous solution thereby is hardly

5.4. Tomography of Experimental Data

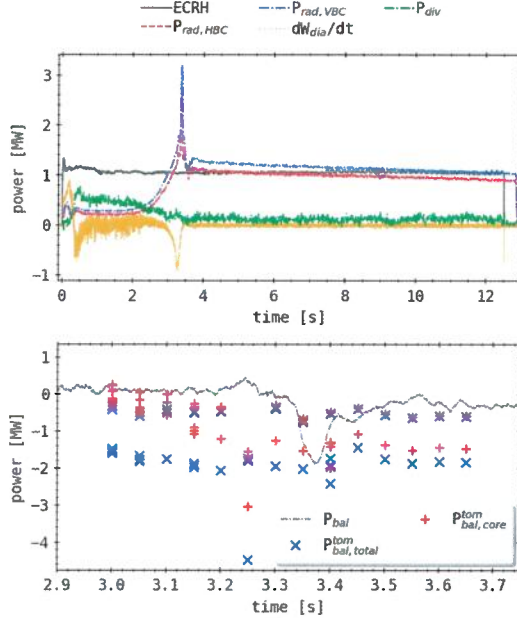


Figure 5.51.: XP20180725.44:
Comparison between power balances for XP20180725.44 as in figure 5.50. **(top):** Central experiment parameters towards the discharge power balance. **(bottom):** Comparison of power balances derived from a common P_{rad} and the radiation distribution integrals.

practical -, this approach may prove to be a better radiation power loss measure towards a global power balance. While a second set of P_{bal} using reconstructed solutions will be featured, extending this to a statistical level for a more thorough and generalized evaluation is out of scope for this work.

The second example is presented in a similar manner as before in figure 5.51 for XP20180725.44. Central plasma parameters in the top image, as well as the plasma global power balance profile calculated using P_{rad} from the extrapolated detector measurements at the bottom have previously been introduced and discussed in figure 2.27, as well as figure 5.41 and the following MFR reconstructions. In conclusion, this has underlined the quasi steady-state applicability of the equation in equation (2.37) and difficulties during scenarios of fast or drastic plasma transitions. The current example features both rapid dis-/continuous changes in radiation regimes or events and steady-state equilibria. Results of reconstructed two-dimensional powers shown here are centred temporally around the mentioned plasma collapse and condensation of emissivity to the core towards 3.35 s between 3–3.65 s. Immediately noticeable is the consistent and almost constant separation not

only between the total and core integral calculated P_{bal} but also among those, indicating a significant quantitative difference for various MFR configurations, i.e. k_{ani} parameters. The power balance derived from P_{2D}^{core} is close to or slightly below equality and its P_{rad} counterpart up to 3.1 s and therefore the radiative loss too large. Individual points are still within 0.3 MW of each other, while $P_{\text{bal,tot}}^{\text{tom}}$ is close and inside that interval, though one set of results is ≤ -1.4 MW here. All decrease further and hence increase their distance from the reference profile with time until the event in 3.35 s. The discrepancy among the individual sets of points also slightly grows, as in 3.25 s the core and total reconstructed balance suddenly drop to -1.5 – -4.6 MW with gaps of 1.4–2.6 MW in a singular group of outliers. However, towards and across the plasma collapse, the two values and their separate levels remain relatively constant, with minor variations of ± 0.5 MW compared to the -1.8 MW reference drop. Throughout the series of reconstructions, the integrated two-dimensional powers lead to a continuously but slowly decreasing balance with a trend from 0– -1.5 MW to -0.5 – -1.8 MW. This variation is about double that of the P_{bal} profile reduction after the event. Beginning in 3.3 s and continuing, one $P_{\text{bal,tot}}^{\text{tom}}$ coincides with the higher $P_{\text{bal,core}}^{\text{tom}}$ and the differentiation within has equilibrated at that level. For $t \geq 3.5$ s, the tomograms yield nearly constant results in both parameters for all configurations.

Similar results as before in figure 5.50 are presented here, as the contribution of the core integrated tomogram emissivity fits better to the target equalisation of $P_{\text{bal}} = 0$ and the P_{rad} calculated reference than its $P_{2D,\text{tot}}$ counterpart. Furthermore, both are less impacted by the previously discussed stronger and faster transitions noted in the standard derived plasma power balance. Despite the steady-state development, the values computed using tomography results deviate significantly from their target and more so than for the feedback controlled discharge. Though the discrepancy between the two set of points and for varying MFR parameter configurations is also of similar magnitude. The worse match of $P_{\text{bal,core}}^{\text{tom}}$ hence is likely due to the characteristic shape of the underlying reconstructed brightness profiles in figure 5.42 particularly after the collapse, since essentially no emissivity is placed here for $r > r_a$. Again, the ratio between the tomogram powers is well in line with the prior statistical analysis. Overall, this still remains a valid estimator of the radiative plasma power loss and input to its total

But using $P_{\text{rad,core}}$ only in the power balance makes no sense, right?!

equilibrium power balance.

5.5. Conclusions

This concludes the final physical chapter of this thesis and therefore the introduction, benchmarking and experimental evaluation of a tailored *Minimum Fisher regularisation* tomography algorithm for the multicamera bolometer diagnostic at W7-X. Tests applying geometric perturbations and using different methods of sensitivity discretisation have shown significant robustness of the MFR against such variations and simultaneously established a set of configurations that provide adequate transmissivity at favourable computational costs. The impact of essentially unknown discrepancies of the actual *in-situ* orientation compared to an *as-designed* assembly of the bolometer have been estimated using forward calculation and found to be non-negligible. However, it was measured to be of similar magnitude as other variabilities to the MFR and hence indistinguishable in the final tomogram. At the same time, supplementary artificial camera arrays of deliberately tailored geometry, specifically filling gaps in the previously examined setup, were introduced to the tomography and used to aid in the reconstruction of more complex phantom radiation distributions. STRAHL simulated radiation profiles have revealed a noticeable asymmetry in the symmetrical designed bolometer LOS configuration and corresponding transmissivity matrix \mathbf{T} , with a bias towards the upper separatrix area and SOL.

The benchmark has shown both the effectiveness and limits of said algorithm, underlining the existence of an ideal set of tomography parameters for a given input two-dimensional emissivity distribution. Anisotropy regularisation weight coefficients produced results of more localised ($k < 1$) or smooth ($k > 1$) radiation profiles as intended, hence corresponding also to improved quality measures ρ_c etc. The latter have shown to not be exclusively congruent and suggest that the quantitative or qualitative optimal tomogram is not necessarily achieved for $\chi^2 = 1$. Experimentally motivated artificial phantom images were proven to be particularly difficult to reconstruct, therefore provided valuable experience towards the reconstruction of actual experimental data. Iteration in k_{ani} across a much larger set of profiles than presented has further cemented the above evaluations. Statistical

analysis across all artificial emissivity distributions similarly agreed with those assessments, while also producing linear regression results correlating the two-dimensional radiation power and forward calculated P_{rad} . Thereby, both cameras find that core emissions exclusively are slightly overrepresented, and the absolute integrated power significantly overestimated by their corresponding extrapolations.

Practical application of the established knowledge about the RDA MFR algorithm, i.e. tomography of W7-X campaign bolometer measurements provided adequate and robust results, though does not yield insights beyond this initial impression due to its limited execution. However, evaluation of all experimental reconstructions combined presented nearly identical numbers compared to its artificial counterpart, evidently supporting the findings in this reduced set tomograms. Furthermore, at last, integrated powers were used to calculate global, *quasi steady-state* power balances for selected samples in time in comparison to the continuous P_{rad} profile. While no absolute improvement is measured for neither core nor total integral and the aforementioned discrepancy between P_{rad} and P_{2D} is reflected here significantly, both are characteristically more stable and a potential alternative for small interval inspections.

The Minimum Fisher regularisation tomography algorithm in combination with the radially dependent anisotropy weighting has hereby been formally and thoroughly benchmarked and tested for the particular application with the multicamera bolometer diagnostic at W7-X. Conclusions are robust and promise overall reliable results, though one has to keep in mind the difficulty of multidimensional parameter optimisation during such ill-posed reconstruction problems. Combination with previous synthetic data and geometric perturbations was successful in outlining the shortcomings of this setup and providing hypothetical upgrades thereto.

- comprehensive but not complete (generality unclear)
- Synthesis of results is missing:
- * What have to use?
 - * level of geometry uncertainty acceptable?
 - * "Structure separation" capability/limits?
→ quantitative broadening/peak red. factor
 - 364 * Power balance statement f) Practical errorbars ?!

Conclusion and Outlook

The importance of radiative power exhaust, majorly dependent on the experimental configuration, i.e. input heating and density, as well as impurity composition and concentration is well-understood. Towards the operation of existing and the development of future fusion reactors, be it for research purposes or as a DEMO power plant, exploration of deliberately impurity seeded and feedback controlled scenarios with focus on detachment physics for heat energy dissipation and machine safety is of great interest. Reliable and stable controlled radiative cooling in the confined region, in the SOL and divertor with radiation power fractions of $f_{\text{rad}} \geq 95\%$ is therefore necessary.

A real-time bolometer radiation feedback system, working together with thermal impurity gas valves in the SOL for injection has been designed and implemented during the operational phase OP1.2b at W7-X. It was applied successfully, achieving stable hydrogen plasma with controlled helium edge cooling at radiation fractions $\geq 85\%$ and peak values of up to 100%. Here, reduction of target heat loads of at least a factor of two was measured, while detachment of C²⁺ ionization radiation was visible already for $f_{\text{rad}} \sim 50\%$. A limited set of at least three lines of sight was validated as a proxy for fast radiation power loss extrapolations. Simultaneously, comparisons with dimensionless scaled, raw signals of singular detectors have suggested the programming with individual LOS for steady-state scenarios. However, computational and algorithmic limitations infer non-negligible latencies to the bolometer feedback and were difficult to optimise for during commissioning. Despite this, the intrinsic connection of P_{rad} and ultimately f_{rad} to the detachment process makes this approach essential for future applications.

Exploration and inference of the corresponding experimental parameter space was not able to determine a particular scaling or underlying correlation for the corresponding low-Z impurity seeded feedback experiments. It was established however that moderately scaled gas puffs, i.e. medium length and intensity, generally were very capable of reliably performing edge cooling without terminal plasma perturbation. Rudimentary models for this injection process, proposing two and three chamber systems have been found both to be equally capable of representing exemplary radiation measurements of feedback activations. However, respective input parameters provided no further significant insight. Given the systems limitations, evaluation of the line of sight sensitivity towards relevant radiation scenarios showed detectors viewing the separatrix and SOL region to be most viable for *a priori* real-time bolometer feedback configurations. No explicitly best set of three, five or seven detectors exists, though for feedback purposes, a robust selection of few vertical or/and horizontal bolometer camera channels can be provided that generally achieves $\geq 85\%$ prediction accuracy when compared to the full data set. Agreement for both analysis regarding only radiation data and also central plasma parameter between the two cameras underline these results. The one-dimensional transport simulation code STRAHL was used in combination with experimental data from feedback applications and input parameters modelled for comparison purposes. Results have shown carbon impurities to be the dominant contributor to SOL emissivity, while reduction of diffusivity, as well as electron temperature and density around the separatrix provided radiation profiles similar to experimental findings. Both see an inward shift from outside to inside the separatrix for $f_{\text{rad}} \rightarrow 1$. However, forward calculation of using STRAHL calculations produced no comparable level of asymmetry in the line of sight integrated chord brightness, suggesting larger discrepancies in the model ansatz.

Significant robustness and reliability for a tailored radially dependent anisotropy (RDA) weighting Minimum Fisher regularization (MFR) algorithm in combination with the W7-X multicamera bolometer system have been established through rigorous geometry perturbation testing and verification. A large scale benchmark thereof, involving numerous simple and complex phantom radiation profiles for reconstruction, has suggested the existence of an ideal set of anisotropy parameters for a given emissivity distribution,

366 *The feedback analysis is not really showing/understanding the limitations observed. The experiments seem to have been executed with wrong UX settings.*

though the dimensionality of this ill-posed optimization problem makes it essentially impossible to actually find such a set k_{ani}^* . By that, an intrinsic bias towards the upper SOL and separatrix area in the transmissivity matrix \mathbf{T} was found. Limited interval weighting factor variations have shown, as per design, $k \leq 1$ to correspond well to localised or smooth radiation structures in reconstruction, respectively. Evaluation of phantom image tomographies with additional, two-dimensional quality coefficients demonstrated potential misalignment between adequate fitness factors χ^2 and truly optimal reconstructions. For the set of artificial brightness profiles, P_{rad} consistently underestimates the actual, total power contained in the phantom. Lastly, application of this knowledge to experimental measurements presented results in line with the corresponding benchmark, and integration into power balance calculations provided a stable, albeit costly alternative to P_{rad} .

The central feature of this thesis, the core bolometer real time feedback system for radiative cooling and detachment purposes, is significantly hampered by its large intrinsic latency compared to other control candidates and corresponding computational limitations. Upgrades thereof will lead to a proportional improvement of the individual estimators and eventually also enable one to establish and implement a more complex and versatile P_{pred} model, taking operational configurability into account on a *per-experiment* basis. For that, a more delicate approach to an attempted scaling law would be beneficial and could add a predictive component to the provided radiation gauges. Similarly, a thorough analysis of the correlation between multichannel extrapolation P_{pred}^1 and single signal P_{pred}^2 , with focus on the derivative character and omitted volumetric scaling could provide necessary insights to the bolometer feedback.

Results for the multi-chamber model have a promising outlook and an educated parametric optimisation process with respect to experimental data and other SOL models might be necessary to yield a better picture about corresponding population and transport regimes therein.

Finally, a more detailed approach with a larger set of relevant phantom images to supplementary artificial bolometer cameras at the current location can provide solid candidates for the practical extension thereof. Nevertheless, it certainly aids the confidence when performing Minimum Fisher tomographies of measured data when extending the set of benchmark reconstructions

Chapter 6. Conclusion and Outlook

by more examples from the vast range of principle brightness profile shapes and their combinations that has not been touched upon in this work.

Bibliography

- [1] I. P. ON CLIMATE CHANGE (IPCC). *Climate Change 2021 – The Physical Science Basis: Working Group I Contribution to the Sixth Assessment Report of the Intergovernmental Panel on Climate Change*. Cambridge University Press, 2023 (page 1).
- [2] R. TOSCHI. »Nuclear fusion, an energy source«. In: *Fusion Engineering and Design*, Vol. 36.1 (1997), pages 1–8. DOI: [https://doi.org/10.1016/S0920-3796\(97\)00007-0](https://doi.org/10.1016/S0920-3796(97)00007-0) (page 1).
- [3] M. L. E. OLIPHANT, P. HARTECK and L. RUTHERFORD. »Transmutation Effects Observed with Heavy Hydrogen«. In: *Proceedings of the Royal Society of London Series A*, Vol. 144.853 (1934), pages 692–703. DOI: [10.1098/rspa.1934.0077](https://doi.org/10.1098/rspa.1934.0077) (page 1).
- [4] V. D. SHAFRANOV. »The initial period in the history of nuclear fusion research at the Kurchatov Institute«. In: *Physics-Uspekhi*, Vol. 44.8 (2001), page 835. DOI: [10.1070/PU2001v044n08ABEH001068](https://doi.org/10.1070/PU2001v044n08ABEH001068) (page 2).
- [5] H. .-. BOSCH and G. M. HALE. »Improved formulas for fusion cross-sections and thermal reactivities«. In: *Nuclear Fusion*, Vol. 32.4 (1992), pages 611–631. DOI: [10.1088/0029-5515/32/4/I07](https://doi.org/10.1088/0029-5515/32/4/I07) (page 2).
- [6] J. SPITZER LYMAN. »The Stellarator Concept«. In: *Physics of Fluids*, Vol. 1.4 (1958), pages 253–264. DOI: [10.1063/1.1705883](https://doi.org/10.1063/1.1705883) (page 4).
- [7] A. H. BOOZER. »What is a stellarator?« In: *Physics of Plasmas*, Vol. 5.5 (1998), pages 1647–1655. DOI: [10.1063/1.872833](https://doi.org/10.1063/1.872833). eprint: https://pubs.aip.org/aip/pop/article-pdf/5/5/1647/19230715/1647_1_online.pdf (page 4).

Bibliography

- [8] F. WAGNER. »Stellarators and Optimised Stellarators«. In: *Fusion Technology*, Vol. 33.2T (1998), pages 67–83. DOI: 10.13182/FST98-A11946996. eprint: <https://doi.org/10.13182/FST98-A11946996> (page 4).
- [9] C. BEIDLER et al. »Physics and Engineering Design for Wendelstein VII-X«. In: *Fusion Technology*, Vol. 17 (1990), pages 148–168. DOI: 10.13182/FST90-A29178 (pages 4, 5).
- [10] KLINGER, THOMAS. »A newcomer: the Wendelstein 7-X Stellarator«. In: *Europhysics News*, Vol. 47.5-6 (2016), pages 35–38. DOI: 10.1051/epn/2016506 (page 4).
- [11] J. GEIGER et al. »Physics in the magnetic configuration space of W7-X«. In: *Plasma Physics and Controlled Fusion*, Vol. 57 (2015), page 014004. DOI: 10.1088/0741-3335/57/1/014004 (page 5).
- [12] P. HELANDER. »Theory of plasma confinement in non-axisymmetric magnetic fields«. In: *Reports on Progress in Physics*, Vol. 77.8 (2014), page 087001. DOI: 10.1088/0034-4885/77/8/087001 (page 6).
- [13] A. H. BOOZER. »Non-axisymmetric magnetic fields and toroidal plasma confinement«. In: *Nuclear Fusion*, Vol. 55.2 (2015), page 025001. DOI: 10.1088/0029-5515/55/2/025001 (page 6).
- [14] M. SHUBOV. »Energy Balance Within Thermonuclear Reactors«. 2021. arXiv: 2104.06251 [physics.plasm-ph] (page 6).
- [15] R. SCHNEIDER et al. »Plasma Edge Physics with B2-Eirene«. In: *Contributions to Plasma Physics*, Vol. 46.1-2 (2006), pages 3–191. DOI: <https://doi.org/10.1002/ctpp.200610001>. eprint: <https://onlinelibrary.wiley.com/doi/pdf/10.1002/ctpp.200610001> (page 6).
- [16] H. DRAWIN. »Review paper A4. Plasma impurities and cooling«. In: *Physics Reports*, Vol. 37.2 (1978), pages 125–163. DOI: [https://doi.org/10.1016/0370-1573\(78\)90039-X](https://doi.org/10.1016/0370-1573(78)90039-X) (page 6).
- [17] F. REIMOLD. *Experimental studies and modeling of divertor plasma detachment in H-mode discharges in the ASDEX upgrade tokama*. PhD thesis. 2015. eprint: <https://mediatum.ub.tum.de/doc/1232875/1232875.pdf> (page 6).

- [18] T. EICH et al. »Scaling of the tokamak near the scrape-off layer H-mode power width and implications for ITER«. In: *Nuclear Fusion*, Vol. 53.9 (2013), page 093031. DOI: [10.1088/0029-5515/53/9/093031](https://doi.org/10.1088/0029-5515/53/9/093031) (page 7).
- [19] T. EICH et al. »Inter-ELM Power Decay Length for JET and ASDEX Upgrade: Measurement and Comparison with Heuristic Drift-Based Model«. In: *Phys. Rev. Lett.*, Vol. 107 (21 2011), page 215001. DOI: [10.1103/PhysRevLett.107.215001](https://doi.org/10.1103/PhysRevLett.107.215001) (page 7).
- [20] G. FUCHERT et al. »Energy confinement in W7-X, more than just a scaling law«. In: *Poster presented at 28th IAEA Fusion Energy Conference (FEC 2020)*, (2020) (page 7).
- [21] W. CONTRIBUTORS. »Fokker-Planck equation«. https://en.wikipedia.org/wiki/Fokker-Planck_equation#Plasma_physics. Accessed: 2024-03-01 (page 8).
- [22] W. CONTRIBUTORS. »Vlasov equation«. https://en.wikipedia.org/wiki/Vlasov_equation. Accessed: 2024-03-01 (page 8).
- [23] W. A. HOULBERG et al. »Bootstrap current and neoclassical transport in tokamaks of arbitrary collisionality and aspect ratio«. In: *Physics of Plasmas*, Vol. 4.9 (1997), pages 3230–3242. DOI: [10.1063/1.872465](https://doi.org/10.1063/1.872465). eprint: https://pubs.aip.org/aip/pop/article-pdf/4/9/3230/19108363/3230_1_online.pdf (page 9).
- [24] V. TRIBALDOS and J. GUASP. »Neoclassical global flux simulations in stellarators«. In: *Plasma Physics and Controlled Fusion*, Vol. 47.3 (2005), page 545. DOI: [10.1088/0741-3335/47/3/010](https://doi.org/10.1088/0741-3335/47/3/010) (page 9).
- [25] T. FÜLÖP and P. HELANDER. »Nonlinear neoclassical transport in toroidal edge plasmas«. In: *Physics of Plasmas*, Vol. 8.7 (2001), pages 3305–3313. DOI: [10.1063/1.1372179](https://doi.org/10.1063/1.1372179). eprint: https://pubs.aip.org/aip/pop/article-pdf/8/7/3305/19215506/3305_1_online.pdf (page 9).
- [26] R. DUX and A. PEETERS. »Neoclassical impurity transport in the core of an ignited tokamak plasma«. In: *Nuclear Fusion*, Vol. 40.10 (2000), page 1721. DOI: [10.1088/0029-5515/40/10/304](https://doi.org/10.1088/0029-5515/40/10/304) (page 9).

Bibliography

- [27] R. DUX. *Impurity Transport in Tokamak Plasmas*. Max-Planck Institute for Plasmaphysics, Garching, 2004 (page 9).
- [28] R. BALESCU. *Aspects of Anomalous Transport in Plasmas*. CRC Press., 2005. DOI: <https://doi.org/10.1201/9780367801601> (page 10).
- [29] B. P. VAN MILLIGEN, R. SÁNCHEZ and B. A. CARRERAS. »Probabilistic finite-size transport models for fusion: Anomalous transport and scaling laws«. In: *Physics of Plasmas*, Vol. 11.5 (2004), pages 2272–2285. DOI: 10.1063/1.1701893. eprint: https://pubs.aip.org/aip/pop/article-pdf/11/5/2272/19291661/2272_1\online.pdf (page 10).
- [30] L. GARCIA and B. A. CARRERAS. »Mesoscale transport properties induced by near critical resistive pressure-gradient-driven turbulence in toroidal geometry«. In: *Physics of Plasmas*, Vol. 13.2 (2006), page 022310. DOI: 10.1063/1.2172177. eprint: https://pubs.aip.org/aip/pop/article-pdf/doi/10.1063/1.2172177/14120654/022310_1\online.pdf (pages 10, 15).
- [31] A. LANGENBERG et al. »Impurity transport studies at Wendelstein 7-X by means of x-ray imaging spectrometer measurements*«. In: *Plasma Physics and Controlled Fusion*, Vol. 61.1 (2018), page 014030. DOI: 10.1088/1361-6587/aaeb74 (page 10).
- [32] D. MEADE. »Effect of high-Z impurities on the ignition and Lawson conditions for a thermonuclear reactor«. In: *Nuclear Fusion*, Vol. 14.2 (1974), page 289. DOI: 10.1088/0029-5515/14/2/017 (page 11).
- [33] W. CONTRIBUTORS. »Bremsstrahlung«. <https://en.wikipedia.org/wiki/Bremsstrahlung>. Accessed: 2024-03-02 (page 11).
- [34] W. CONTRIBUTORS. »Synchrotron radiation«. https://en.wikipedia.org/wiki/Synchrotron_radiation. Accessed: 2024-03-01 (page 11).
- [35] J. HOGAN and D. HILLIS. »Helium transport and exhaust in tokamaks«. In: *Nuclear Fusion - NUCL FUSION*, Vol. 40 (2000), pages 879–888. DOI: 10.1088/0029-5515/40/4/412 (page 12).

Bibliography

- [36] A. A. MAVRIN. »Effect of impurity radiation and helium particle confinement on tokamak–reactor plasma performance«. In: *Plasma Physics and Controlled Fusion*, Vol. 62.10 (2020), page 105023. DOI: [10.1088/1361-6587/abab5d](https://doi.org/10.1088/1361-6587/abab5d) (page 12).
- [37] H.-S. BOSCH. *Die Physik der Alpha-Teilchen in einem Fusionsreaktor mit Deuterium-Tritium-Plasmen*. Max-Planck Institute for Plasmaphysics, Garching, 2000 (page 12).
- [38] M. BALDEN et al. »Collection strategy, inner morphology, and size distribution of dust particles in ASDEX Upgrade«. In: *Nuclear Fusion*, Vol. 54.7 (2014), page 073010. DOI: [10.1088/0029-5515/54/7/073010](https://doi.org/10.1088/0029-5515/54/7/073010) (page 12).
- [39] V. ROHDE et al. »Dust investigations at ASDEX Upgrade«. In: *Physica Scripta*, Vol. 2009.T138 (2009), page 014024. DOI: [10.1088/0031-8949/2009/T138/014024](https://doi.org/10.1088/0031-8949/2009/T138/014024) (page 12).
- [40] S. SEREDA et al. »Impact of boronizations on impurity sources and performance in Wendelstein 7-X«. In: *Nuclear Fusion*, Vol. 60.8 (2020), page 086007. DOI: [10.1088/1741-4326/ab937b](https://doi.org/10.1088/1741-4326/ab937b) (pages 12, 193).
- [41] R. DUX et al. »Measurement and modelling of neon radiation profiles in radiating boundary discharges in ASDEX Upgrade«. In: *Plasma Physics and Controlled Fusion*, Vol. 38.7 (1996), page 989. DOI: [10.1088/0741-3335/38/7/004](https://doi.org/10.1088/0741-3335/38/7/004) (page 13).
- [42] A. KALLENBACH et al. »Divertor power load feedback with nitrogen seeding in ASDEX Upgrade«. In: Vol. 52. 2009. DOI: [10.1088/0741-3335/52/5/055002](https://doi.org/10.1088/0741-3335/52/5/055002) (page 13).
- [43] A. KALLENBACH et al. »Plasma surface interactions in impurity seeded plasmas«. In: *Journal of Nuclear Materials*, Vol. 415 (2011). DOI: [10.1016/j.jnucmat.2010.11.105](https://doi.org/10.1016/j.jnucmat.2010.11.105) (page 13).
- [44] A. KALLENBACH et al. »Optimized tokamak power exhaust with double radiative feedback in ASDEX Upgrade«. In: *Nuclear Fusion*, Vol. 52 (2012), page 122003. DOI: [10.1088/0029-5515/52/12/122003](https://doi.org/10.1088/0029-5515/52/12/122003) (page 13).

Bibliography

- [45] F. J. CASSON et al. »Theoretical description of heavy impurity transport and its application to the modelling of tungsten in JET and ASDEX upgrade«. In: *Plasma Physics and Controlled Fusion*, Vol. 57.1 (2014), page 014031. DOI: 10.1088/0741-3335/57/1/014031 (page 13).
- [46] U. WENZEL et al. »Observation of Marfes in the Wendelstein 7-X stellarator with inboard limiters«. In: *Nuclear Fusion*, Vol. 58.9 (2018), page 096025. DOI: 10.1088/1741-4326/aacb86 (page 13).
- [47] D. BAKER, R. SNIDER and M. NAGAMI. »Observation of cold, high-density plasma near the Doublet III limiter«. In: *Nuclear Fusion*, Vol. 22.6 (1982), page 807. DOI: 10.1088/0029-5515/22/6/008 (page 13).
- [48] M. GREENWALD. »Density limits in toroidal plasmas«. In: *Plasma Physics and Controlled Fusion*, Vol. 44.8 (2002), R27. DOI: 10.1088/0741-3335/44/8/201 (pages 13, 17).
- [49] B. LIPSCHULTZ et al. »Marfe: an edge plasma phenomenon«. In: *Nuclear Fusion*, Vol. 24.8 (1984), page 977. DOI: 10.1088/0029-5515/24/8/002 (page 13).
- [50] H. OHTSUKA. »A relation between light and metal impurities in tokamak plasmas«. In: *Nuclear Fusion*, Vol. 22.6 (1982), page 827. DOI: 10.1088/0029-5515/22/6/011 (page 14).
- [51] M. TOKAR. »Impurity Transport and Radiation«. In: *Fusion Science and Technology*, Vol. 57.2T (2010), pages 261–268. DOI: 10.13182/FST10-A9417. eprint: <https://doi.org/10.13182/FST10-A9417> (pages 15–17).
- [52] U. SAMM et al. »Radiative edges under control by impurity fluxes«. In: *Plasma Physics and Controlled Fusion*, Vol. 35.SB (1993), B167. DOI: 10.1088/0741-3335/35/SB/013 (page 15).
- [53] W. J. KARZAS and R. LATTER. »Electron Radiative Transitions in a Coulomb Field.« In: Vol. 6 (1961), page 167. DOI: 10.1086/190063 (page 15).

Bibliography

- [54] E. WANG et al. »Radiation characteristics of detached divertor plasmas in W7-X«. In: *Nuclear Materials and Energy*, Vol. 33 (2022), page 101283. DOI: <https://doi.org/10.1016/j.nme.2022.101283> (page 17).
- [55] S. P. LANGLEY. »The bolometer and radiant energy«. In: *Proceedings of the American Academy of Arts and Sciences*, Vol. 16. pp. 342-358 (1880) (page 21).
- [56] S. P. LANGLEY. *The "bolometer"*. Edited by P. GREGORY BROS. New York, The Society, 1881 (page 21).
- [57] S. ARRHENIUS. »On the influence of carbonic acid in the air upon the temperature of the ground«. In: *Dublin Philosophical Magazine and Journal of Science*, Vol. 41.251 (1896) (page 21).
- [58] J. M. GILDEMEISTER, A. T. LEE and P. L. RICHARDS. »A fully lithographed voltage-biased superconducting spiderweb bolometer«. In: *American Institute of Physics - Review of Scientific Instruments*, Vol. 74.868 (1999) (page 21).
- [59] H.-W. HUEBERS et al. »NbN hot-electron bolometer as THz mixer for SOFIA«. In: *Airborne Telescope Systems*, Vol. 4014 (2000) (page 22).
- [60] R. T. RAJENDRA KUMAR et al. »Room temperature deposited vanadium oxide thin films for uncooled infrared detectors«. In: *Materials Research Bulletin*, Vol. 38.7 (2003) (page 22).
- [61] L. GIANNONE, K. MAST and M. SCHUBERT. »Derivation of bolometer equations relevant to operation in fusion experiments«. In: *American Institute of Physics - Review of Scientific Instruments*, Vol. 73.3205 (2002) (pages 22, 38, 40).
- [62] H. HSUAN, K. BOL and R. A. ELLIS. »Measurement of the energy balance in ATC tokamak«. In: *Nuclear Fusion*, Vol. 15.657 (1975) (page 23).
- [63] M. DI MAIO, R. REICHLE and R. GIANNELLA. »Design of a ferroelectric bolometer«. In: *17th IEEE/NPSS Symposium Fusion Engineering*, Vol. 2.775 (1997) (page 23).

Bibliography

- [64] E. IBORRA, A. SANZ-HERVÁS and T. RODRÍGUEZ. »A new design of a semiconductor bolometer on rigid substrate for fusion plasma diagnostics«. In: *Review of Scientific Instruments*, Vol. 64.1714 (1993) (page 23).
- [65] D. D. ZHANG et al. »Design criteria of the bolometer diagnostic for steady-state operation of the W7-X stellarator«. In: *Review of Scientific Instrument*, Vol. 81.10E134 (2010) (pages 23, 25, 26, 58).
- [66] E. R. MÜLLER and F. MAST. »A new metal resistor bolometer for measuring vacuum ultraviolet and soft x radiation«. In: *Journal of Applied Physics*, Vol. 55.2635 (1984) (page 23).
- [67] I. FURNO et al. »Fast bolometric measurements on the TCV tokamak«. In: *Review of Scientific Instruments*, Vol. 70.4552 (1999) (page 23).
- [68] A. W. DEGELING et al. »AXUV bolometer and Lyman- α camera systems on the TCV tokamak«. In: *Review of Scientific Instruments*, Vol. 75.4139 (2004) (page 23).
- [69] M. BERNERT et al. »Application of AXUV diode detectors at ASDEX Upgrade«. In: *Review of Scientific Instruments*, Vol. 85.3 (2014) (page 24).
- [70] B. J. PETERSON. »Infrared imaging video bolometer«. In: *Review of Scientific Instrument*, Vol. 71.3696 (2000) (page 24).
- [71] B. J. PETERSON et al. »Preliminary Design of Imaging Bolometer Fields of View for Wendelstein7-X«. In: *Plasma and Fusion Research*, Vol. 11.2402101 (2016) (page 24).
- [72] B. J. PETERSON et al. »Calibration and sensitivity of the infrared imaging video bolometer«. In: *Review of Scientific Instruments*, Vol. 74.2040 (2003) (page 24).
- [73] S. N. PANDYA et al. »Calibration of a thin metal foil for infrared imaging video bolometer to estimate the spatial variation of thermal diffusivity using a photo-thermal technique«. In: *Review of Scientific Instruments*, Vol. 85.054902 (2014) (page 24).

- [74] B. J. PETERSON et al. »Bolometer diagnostics for one- and two-dimensional measurements of radiated power on the Large Helical Device«. In: *Plasma Physics and Controlled Fusion*, Vol. 45.1167 (2003) (page 24).
- [75] H. HANS MEISTER et al. »The ITER bolometer diagnostic: Status and plans«. In: *Review of Scientific Instruments*, Vol. 79.10 (2008) (page 24).
- [76] P. HOROWITZ and W. HILL. *The art of electronics*. Cambridge University Press, 1989 (pages 25, 37).
- [77] K. F. MAST et al. »A low noise highly integrated bolometer array for absolute measurement of VUV and soft x radiation«. In: *Review of Scientific Instruments*, Vol. 62.744 (1991) (pages 25, 38).
- [78] D. HATHIRAMANI et al. »Microwave stray radiation: Measures for steady state diagnostics at Wendelstein 7-X«. In: *Fusion Engineering and Design*, Vol. 88.6 (2013). Proceedings of the 27th Symposium On Fusion Technology (SOFT-27); Liège, Belgium, September 24-28, 2012, pages 1232–1235. DOI: <https://doi.org/10.1016/j.fusengdes.2013.01.003> (page 26).
- [79] R. KÖNIG et al. »Diagnostics design for steady-state operation of the Wendelstein 7-X stellarator«. In: *Review of Scientific Instruments*, Vol. 81.10E133 (2010) (page 26).
- [80] R. BURHENN et al. »Diagnostics Development for Steady State Operation of the Stellarator Wendelstein 7-X«. In: *Contributions to Plasma Physics (International Conference on Plasma Diagnostics, Pontà-Mousson, France, April 2010)*, Vol. 51.2-3 (2011) (page 26).
- [81] M. B. WEISSMAN. » $1/f$ noise and other slow, nonexponential kinetics in condensed matter«. In: *Rev. Mod. Phys.*, Vol. 60 (2 1988), pages 537–571. DOI: [10.1103/RevModPhys.60.537](https://doi.org/10.1103/RevModPhys.60.537) (page 37).
- [82] J. LOVELL. *Development of Smart, Compact Fusion Diagnostics using Field-Programmable Gate Arrays*. PhD thesis. Centre for Advanced Instrumentation Department of Physics, Durham University, 2017 (page 38).

Bibliography

- [83] D. ZHANG et al. »Concept to reduce the measurement error of the metal resistive bolometer through remedying the neutral gas pressure effect«. In: *2009 IEEE International Conference on Plasma Science - Abstracts*, Vol. 1-5 June, 2009 (2009). DOI: [10.1109/PLASMA.2009.5227389](https://doi.org/10.1109/PLASMA.2009.5227389) (page 43).
- [84] D. ZHANG et al. »Investigation of the Neutral Gas Pressure Effect on the Metal Resistive Bolometer«. In: *AIP Conference Proceedings*, Vol. 933.199 (2008) (page 43).
- [85] L. GIANNONE et al. »Tomography by the maximum entropy method for the W7-AS and W7-X multichannel bolometer systems«. In: *Review of Scientific Instruments*, Vol. 68.1 (1997), pages 762–765. DOI: [10.1063/1.1147912](https://doi.org/10.1063/1.1147912) (pages 43, 237).
- [86] D. ZHANG et al. »Thermal Drift Study on the Bolometer Diagnostic for Steady-State Fusion Plasmas«. In: *39th EPS Conference and 16th Int. Congress on Plasma Physics*, Vol. P5.040 (2012) (pages 44, 45).
- [87] F. PENZEL et al. »Calibration parameter drift compensation of metal resistive bolometers operating in a thermal varying environment«. In: *Fusion Engineering and Design*, Vol. 121 (2017), pages 100–104. DOI: <https://doi.org/10.1016/j.fusengdes.2017.05.094> (page 44).
- [88] Y. TAKAHASHI and H. AKIYAMA. »Heat capacity of gold from 80 to 1000 K«. In: *Thermochimica Acta*, Vol. 109.1 (1986) (page 45).
- [89] J. D. CUTNELL and K. W. JOHNSON. *Physics (4th Edition, Volume 1)*. Wiley, 1998 (page 45).
- [90] D. H. LLOYD. *Physics Laboratory Manual. 2nd Edition*. Saunders college Publishing, 1998 (page 45).
- [91] F. SEITZ. *The Modern Theory of Solids*. New York: Dover Publications, 1987 (page 45).
- [92] D. R. LIDE. *Handbook of Chemistry and Physics. 75th Edition*. New York: CRC Press, 1996 (page 45).
- [93] P. T. LANG and K. F. MAST. »Photoresponse of a miniaturized ultrabroad-band low-noise metal-film bolometer detector array«. In: *Journal of Optics*, Vol. 27.1 (1996), pages 25–29. DOI: [10.1088/0150-536x/27/1/004](https://doi.org/10.1088/0150-536x/27/1/004) (pages 49, 50).

Bibliography

- [94] H. MEISTER et al. »Broad-band efficiency calibration of ITER bolometer prototypes using Pt absorbers on SiN membranes«. In: *Review of Scientific Instruments*, Vol. 84.12 (2013), page 123501. DOI: [10.1063/1.4834755](https://doi.org/10.1063/1.4834755) (pages 49, 50).
- [95] B. HENKE, E. GULLIKSON and J. DAVIS. »X-Ray Interactions: Photoabsorption, Scattering, Transmission, and Reflection at $E = 50\text{--}30,000 \text{ eV}$, $Z = 1\text{--}92$ «. In: *Atomic Data and Nuclear Data Tables*, Vol. 54.2 (1993), pages 181–342. DOI: <https://doi.org/10.1006/adnd.1993.1013> (pages 49, 50).
- [96] E. D. PALI. *Handbook of Optical Constants of Solids*. Academic Press, 1997 (page 50).
- [97] M. HIRSCH et al. »The Impact of Microwave Stray Radiation to In-Vessel Diagnostic Components«. In: *AIP Conference Proceedings, International Conference on Fusion Reactor Diagnostics, Villa Monastero, Varenna, Italy*, Vol. 1612.39 (2013) (pages 51, 83).
- [98] M. FLORISTÁN et al. »Development and testing of 140 GHz absorber coatings for the water baffle of W7-X cryopumps«. In: *Fusion Engineering and Design*, Vol. 86.9-11 (2011) (page 51).
- [99] O. GRULKE. »Plasma Dynamics and Transport Studies in Wendelstein 7-X«. In: *International Atomic Energy Agency (IAEA)*, Vol. CN-258 (2018) (page 58).
- [100] D. ZHANG et al. »Feasibility Assessment of Bolometry as Impurity Transport Study Tool for the Stellarator W7-X«. In: *41st EPS Conference on Plasma Physics*, Vol. P1.068 () (page 58).
- [101] D. ZHANG et al. »Impact of impurity radiation locations on the plasma performance at W7-X stellarator«. In: *46th EPS Conference on Plasma Physics*, Vol. P2.1058 (2019) (page 58).
- [102] G. FUCHERT et al. »Global energy confinement in the initial limiter configuration of Wendelstein 7-X«. In: *Nuclear Fusion*, Vol. 58.10 (2018), page 106029. DOI: [10.1088/1741-4326/aad78b](https://doi.org/10.1088/1741-4326/aad78b) (pages 58, 148).

Bibliography

- [103] A. MURARI et al. »JET new diagnostic capability on the route to ITER«. In: *Fusion Engineering and Design*, Vol. 82.5 (2007). Proceedings of the 24th Symposium on Fusion Technology, pages 1161–1166. DOI: <https://doi.org/10.1016/j.fusengdes.2007.03.022> (page 58).
- [104] G. ARNOUX et al. »Heat load measurements on the JET first wall during disruptions«. In: *Journal of Nuclear Materials*, Vol. 415.1, Supplement (2011). Proceedings of the 19th International Conference on Plasma-Surface Interactions in Controlled Fusion, S817–S820. DOI: <https://doi.org/10.1016/j.jnucmat.2010.11.042> (page 58).
- [105] B. J. PETERSON et al. »Detailed design of imaging bolometer fields of view for Wendelstein7-X«. In: *43rd EPS Conference on Plasma Physics*, Vol. P4.018 (2016) (page 59).
- [106] D. ZHANG et al. »Optimization of Lines of Sight for Tomographic Reconstruction of the Bolometer Diagnostic at the W7-X Stellarator«. In: *40th EPS Conference on Plasma Physics*, Vol. P5.121 (2013) (pages 59, 231, 236, 298).
- [107] Y. FENG et al. »A 3D Monte Carlo code for plasma transport in island divertors«. In: *Journal of Nuclear Materials*, Vol. 241-243 (1997), pages 930–934. DOI: [https://doi.org/10.1016/S0022-3115\(97\)80168-7](https://doi.org/10.1016/S0022-3115(97)80168-7) (page 59).
- [108] D. REITER, M. BAELMANS and P. BÖRNER. »The EIRENE and B2-EIRENE Codes«. In: *Fusion Science and Technology*, Vol. 47.2 (2005), pages 172–186. DOI: [10.13182/FST47-172](https://doi.org/10.13182/FST47-172) (page 59).
- [109] E. CANDES and C. A. SING-LONG. *Applied Fourier Analysis and Elements of Modern Signal Processing*. Edited by E. BATES. Stanford, Statistics; SCOOL OF HUMANITIES & SCIENCES, 2021 (page 70).
- [110] S. KABANIKHIN. »Definitions and Examples of Inverse and Ill-Posed Problems«. In: *Journal of Inverse and Ill-Posed Problems*, Vol. 16 (2008), pages 317–357. DOI: [10.1515/JIIP.2008.019](https://doi.org/10.1515/JIIP.2008.019) (page 70).

- [111] J. MLYNAR et al. »Introducing minimum Fisher regularisation tomography to AXUV and soft x-ray diagnostic systems of the COMPASS tokamak«. In: *Review of Scientific Instruments*, Vol. 83.10 (2012), 10E531. DOI: 10.1063/1.4738648. eprint: <https://doi.org/10.1063/1.4738648> (page 71).
- [112] D. CALVETTI and L. REICHEL. »Tikhonov Regularization of Large Linear Problems«. In: *BIT*, Vol. 43 (2003), pages 263–283. DOI: 10.1023/A:1026083619097 (pages 71, 72).
- [113] J. FREIDBERG. *Plasma Physics and Fusion Energy*. Edited by M. I. OF TECHNOLOGY. Cambridge University Press, 2007 (pages 74, 75).
- [114] M. HIRSCH et al. »Major results from the stellarator Wendelstein 7-AS«. In: *Plasma Physics and Controlled Fusion*, Vol. 50.5 (2008), page 053001. DOI: 10.1088/0741-3335/50/5/053001 (pages 74, 193).
- [115] S. BOZHENKOV et al. »Power Balance Analysis of Wendelstein 7-X Plasmas Using Profile Diagnostics«. In: *43rd EPS Conference on Plasma Physics*, Vol. O2.106 (2016) (pages 75, 76).
- [116] S. BOZHENKOV et al. »The Thomson scattering diagnostic at Wendelstein 7-X and its performance in the first operation phase«. In: *Journal of Instrumentation*, Vol. 12.10 (2017), P10004–P10004. DOI: 10.1088/1748-0221/12/10/p10004 (page 76).
- [117] E. PASCH et al. »The Thomson scattering system at Wendelstein 7-X«. In: *Review of Scientific Instruments*, Vol. 87.11 (2016), 11E729. DOI: 10.1063/1.4962248. eprint: <https://aip.scitation.org/doi/pdf/10.1063/1.4962248> (page 76).
- [118] K. RAHBARNIA et al. »Diamagnetic energy measurement during the first operational phase at the Wendelstein 7-X stellarator«. In: *Nuclear Fusion*, Vol. 58.9 (2018), page 096010. DOI: 10.1088/1741-4326/aacab0 (page 76).
- [119] S. MARSEN et al. »Performance of ECR heating during the first operational phase of W7-X«. In: *43rd EPS Conference on Plasma Physics*, Vol. P4.002 (2016) (page 77).

Bibliography

- [120] Y. GAO et al. »Methods for quantitative study of divertor heat loads on W7-X«. In: *Nuclear Fusion*, Vol. 59.6 (2019), page 066007. DOI: [10.1088/1741-4326/ab0f49](https://doi.org/10.1088/1741-4326/ab0f49) (page 77).
- [121] Y. FENG et al. »On the W7-X divertor performance under detached conditions«. In: *Nuclear Fusion*, Vol. 56.12 (2016), page 126011. DOI: [10.1088/0029-5515/56/12/126011](https://doi.org/10.1088/0029-5515/56/12/126011) (pages 81–83, 116, 128).
- [122] Y. FENG et al. »Physics of the geometry-related detachment stability in W7-AS«. In: *Nuclear Fusion*, Vol. 45.2 (2005), pages 89–95. DOI: [10.1088/0029-5515/45/2/003](https://doi.org/10.1088/0029-5515/45/2/003) (pages 81, 82, 128).
- [123] A. KALLENBACH et al. »Impurity seeding for tokamak power exhaust: from present devices via ITER to DEMO«. In: *Plasma Physics and Controlled Fusion*, Vol. 55.12 (2013), page 124041. DOI: [10.1088/0741-3335/55/12/124041](https://doi.org/10.1088/0741-3335/55/12/124041) (pages 81–83).
- [124] G. PACHER et al. »Modelling of DEMO core plasma consistent with SOL/divertor simulations for long-pulse scenarios with impurity seeding«. In: *Nuclear Fusion*, Vol. 47.5 (2007), pages 469–478. DOI: [10.1088/0029-5515/47/5/012](https://doi.org/10.1088/0029-5515/47/5/012) (pages 81–83).
- [125] O. SCHMITZ et al. »Stable heat and particle flux detachment with efficient particle exhaust in the island divertor of Wendelstein 7-X«. In: *Nuclear Fusion*, (2020). DOI: [10.1088/1741-4326/abb51e](https://doi.org/10.1088/1741-4326/abb51e) (pages 81, 83).
- [126] F. H. TENNEY and G. LEWIN. »A fusion power plant«. In: (1974) (page 81).
- [127] E. MARMAR. »Recycling processes in tokamaks«. In: *Journal of Nuclear Materials*, Vol. 76–77 (1978), pages 59–67. DOI: [https://doi.org/10.1016/0022-3115\(78\)90119-8](https://doi.org/10.1016/0022-3115(78)90119-8) (page 81).
- [128] P. STANGEBY and G. MCCRACKEN. »Plasma boundary phenomena in tokamaks«. In: *Nuclear Fusion*, Vol. 30.7 (1990), pages 1225–1379. DOI: [10.1088/0029-5515/30/7/005](https://doi.org/10.1088/0029-5515/30/7/005) (page 81).
- [129] A. LOARTE et al. »Plasma detachment in JET Mark I divertor experiments«. In: *Nuclear Fusion*, Vol. 38.3 (1998), pages 331–371. DOI: [10.1088/0029-5515/38/3/303](https://doi.org/10.1088/0029-5515/38/3/303) (page 82).

- [130] P. HARBOUR et al. »The X-point scrape-off plasma in jet with L- and H-modes«. In: *Journal of Nuclear Materials*, Vol. 162-164 (1989), pages 236–244. DOI: [https://doi.org/10.1016/0022-3115\(89\)90276-6](https://doi.org/10.1016/0022-3115(89)90276-6) (page 82).
- [131] H. THOMSEN et al. »Radiative condensation and detachment in Wendelstein 7-AS stellarator«. In: *Nuclear Fusion*, Vol. 44.8 (2004), pages 820–826. DOI: [10.1088/0029-5515/44/8/002](https://doi.org/10.1088/0029-5515/44/8/002) (pages 82, 128).
- [132] T. S. PEDERSEN et al. »Plans for the first plasma operation of Wendelstein 7-X«. In: *Nuclear Fusion*, Vol. 55.12 (2015), page 126001. DOI: [10.1088/0029-5515/55/12/126001](https://doi.org/10.1088/0029-5515/55/12/126001) (page 83).
- [133] H. BOSCH et al. »Engineering Challenges in W7-X: Lessons Learned and Status for the Second Operation Phase«. In: *IEEE Transactions on Plasma Science*, Vol. 46.5 (2018), pages 1131–1140. DOI: [10.1109/TPS.2018.2818934](https://doi.org/10.1109/TPS.2018.2818934) (page 83).
- [134] M. KRYCHOWIAK et al. »Bayesian modelling of a thermal helium beam for measurement of electron density and temperature in the W7-X divertor plasma«. In: *Plasma Physics and Controlled Fusion*, Vol. 53.3 (2011), page 035019. DOI: [10.1088/0741-3335/53/3/035019](https://doi.org/10.1088/0741-3335/53/3/035019) (pages 83, 85, 86).
- [135] T. S. PEDERSEN et al. »First results from divertor operation in Wendelstein 7-X«. In: *Plasma Physics and Controlled Fusion*, Vol. 61.1 (2018), page 014035. DOI: [10.1088/1361-6587/aaec25](https://doi.org/10.1088/1361-6587/aaec25) (page 84).
- [136] J. WINTER et al. »Boronization in TEXTOR«. In: *Journal of Nuclear Materials*, Vol. 162 (1989), pages 713–723 (page 84).
- [137] J. WINTER et al. »Surface treatment of the first wall in fusion devices (carbonization, boronisation and related surface chemistry)«. In: *Vacuum*, Vol. 43.5 (1992), pages 413–417. DOI: [https://doi.org/10.1016/0042-207X\(92\)90046-Y](https://doi.org/10.1016/0042-207X(92)90046-Y) (pages 84, 164).
- [138] A. MESHCHERYAKOV et al. »Effect of vacuum chamber boronisation on the plasma parameters in the L-2M stellarator«. In: *Plasma physics reports*, Vol. 31.6 (2005), pages 452–461 (page 84).

Bibliography

- [139] F. BEDOYA et al. »Effect of boronisation on plasma-facing graphite surfaces and its correlation with the plasma behavior in NSTX-U«. In: *Nuclear Materials and Energy*, Vol. 17 (2018), pages 211–216 (page 84).
- [140] F. WAELBROECK et al. »Influence of boronisation on the plasma performance in TEXTOR«. In: *Plasma physics and controlled fusion*, Vol. 31.2 (1989), page 185 (page 84).
- [141] B. LIPSCHULTZ et al. »Influence of boronisation on operation with high-Z plasma facing components in Alcator C-Mod«. In: *Journal of nuclear materials*, Vol. 363 (2007), pages 1110–1118 (page 84).
- [142] B. BUTTENSCHÖN et al. »Reduction of intrinsic impurities by wall boronisation in Wendelstein 7-X as observed by VUV spectroscopy«. In: *The 46th EPS Conf. on Plasma Physics (Milan, Italy,) Vol. 2*. 2019, page 1048 (page 84).
- [143] F. REIMOLD et al. »From dilution to power exhaust & radiation collapse: Impurity transport and radiation physics in W7-X«. In: *Max Planck Society: Institute for Plasma Physics Colloquium, 26.02.2021; Greifswald, Germany*. 2021 (pages 84, 85).
- [144] F. EFFENBERG et al. »First demonstration of radiative power exhaust with impurity seeding in the island divertor at Wendelstein 7-X«. In: *Nuclear Fusion*, Vol. 59.10 (2019), page 106020. DOI: 10.1088/1741-4326/ab32c4 (pages 84, 85).
- [145] J. GEIGER et al. »Physics in the magnetic configuration space of W7-X«. In: *Plasma Physics and Controlled Fusion*, Vol. 57.1 (2014), page 014004. DOI: 10.1088/0741-3335/57/1/014004 (page 84).
- [146] M. MAYER et al. »Material erosion and deposition on the divertor of W7-X«. In: *Physica Scripta*, Vol. T171 (2020), page 014035. DOI: 10.1088/1402-4896/ab4b8c (page 84).
- [147] T. BARBUI et al. »Feasibility of line-ratio spectroscopy on helium and neon as edge diagnostic tool for Wendelstein 7-X«. In: *Review of Scientific Instruments*, Vol. 87.11 (2016), 11E554. DOI: 10.1063/1.4962989. eprint: <https://aip.scitation.org/doi/pdf/10.1063/1.4962989> (pages 85, 86).

- [148] R. DENKELMANN et al. »Measurement of rate coefficients for electron-atom collisions in a helium plasma by laser-induced fluorescence«. In: *Journal of Physics B: Atomic, Molecular and Optical Physics*, Vol. 32.19 (1999), pages 4635–4646. DOI: 10.1088/0953-4075/32/19/305 (page 85).
- [149] A. MLYNEK et al. »Design of a digital multiradian phase detector and its application in fusion plasma interferometry«. In: *Review of Scientific Instruments*, Vol. 81.3 (2010), page 033507. DOI: 10.1063/1.3340944. eprint: <https://doi.org/10.1063/1.3340944> (page 87).
- [150] A. BOBOC et al. »Upgrade of the JET far infrared interferometer diagnostic«. In: *Review of Scientific Instruments*, Vol. 83.10 (2012), 10E341. DOI: 10.1063/1.4737420. eprint: <https://doi.org/10.1063/1.4737420> (page 87).
- [151] J. KNAUER et al. »A new dispersion interferometer for the stellarator Wendelstein 7-X«. In: *Proc. 43rd EPS Conf. (Leuven, Belgium, 4–8 July 2016) P.* Vol. 4. 2016 (page 87).
- [152] A. SPRING et al. »Establishing the Wendelstein 7-X steady state plasma control and data acquisition system during the first operation phase«. In: *Fusion Engineering and Design*, Vol. 123 (2017). Proceedings of the 29th Symposium on Fusion Technology (SOFT-29) Prague, Czech Republic, September 5-9, 2016, pages 579–583. DOI: <https://doi.org/10.1016/j.fusengdes.2017.03.127> (pages 87, 92).
- [153] K. BRUNNER et al. »Real-time dispersion interferometry for density feedback in fusion devices«. In: *Journal of Instrumentation*, Vol. 13.09 (2018), P09002–P09002. DOI: 10.1088/1748-0221/13/09/p09002 (page 87).
- [154] L. STEPHEY et al. »Spectroscopic imaging of limiter heat and particle fluxes and the resulting impurity sources during Wendelstein 7-X startup plasmas«. In: *Review of Scientific Instruments*, Vol. 87.11 (2016), page 11D606. DOI: 10.1063/1.4959274. eprint: <https://aip.scitation.org/doi/pdf/10.1063/1.4959274> (pages 87, 88).

Bibliography

- [155] R. J. COLCHIN et al. »The Filterscope«. In: *Review of Scientific Instruments*, Vol. 74.3 (2003), pages 2068–2070. DOI: 10.1063/1.1537038. eprint: <https://doi.org/10.1063/1.1537038> (page 88).
- [156] N. H. BROOKS et al. »Filterscopes: Spectral line monitors for long-pulse plasma devices«. In: *Review of Scientific Instruments*, Vol. 79.10 (2008), 10F330. DOI: 10.1063/1.2957777. eprint: <https://doi.org/10.1063/1.2957777> (page 88).
- [157] G. A. WURDEN et al. »A high resolution IR/visible imaging system for the W7-X limiter«. In: *Review of Scientific Instruments*, Vol. 87.11 (2016), page 11D607. DOI: 10.1063/1.4960596. eprint: <https://aip.scitation.org/doi/pdf/10.1063/1.4960596> (page 88).
- [158] M. KRYCHOWIAK et al. »Detachment stabilization by feedback-controlled gas injection in stellarator Wendelstein 7-X«. In: *PSI-24 (virtual) conference, 25.01.2021 (Jeju, Korea)*. 2021 (pages 89, 131).
- [159] HIRSCH, MATTHIAS et al. »ECE Diagnostic for the initial Operation of Wendelstein 7-X«. In: *EPJ Web Conf.*, Vol. 203 (2019), page 03007. DOI: 10.1051/epjconf/201920303007 (page 89).
- [160] N. B. MARUSHCHENKO et al. »Optimization of ECE Diagnostics for the W7-X Stellarator«. In: *Fusion Science and Technology*, Vol. 50.3 (2006), pages 395–402. DOI: 10.13182/FST06-A1261. eprint: <https://doi.org/10.13182/FST06-A1261> (page 89).
- [161] A. URQUIZO. »PID controller«. <https://commons.wikimedia.org/wiki/File:PID.svg>. Accessed: 2021-03-24 (page 97).
- [162] E. WANG et al. »Impurity sources and fluxes in W7-X: from the plasma-facing components to the edge layer«. In: *Physica Scripta*, Vol. T171 (2020), page 014040. DOI: 10.1088/1402-4896/ab4c04 (pages 103, 193).
- [163] V. ERCKMANN et al. »Electron Cyclotron Heating for W7-X: Physics and Technology«. In: *Fusion Science and Technology*, Vol. 52.2 (2007), pages 291–312. DOI: 10.13182/FST07-A1508. eprint: <https://doi.org/10.13182/FST07-A1508> (page 138).
- [164] »Python SciPy signal find_peaks routine«. https://docs.scipy.org/doc/scipy-1.8.0/html-scipyorg/reference/generated/scipy.signal.find_peaks.html. Accessed: 2022-02-09 (page 143).

Bibliography

- [165] T. KLINGER et al. »Performance and properties of the first plasmas of Wendelstein 7-X«. In: *Plasma Physics and Controlled Fusion*, Vol. 59.1 (2016), page 014018. DOI: 10.1088/0741-3335/59/1/014018 (pages 148, 193).
- [166] D. ZHANG. »Plasma radiation behavior approaching high-radiation scenarios in W7-X«. In: *28th IAEA Fusion Energy Conference (FEC 2020)*, Vol. CID-984 (2020) (page 148).
- [167] W. CONTRIBUTORS. »Runge-Kutta methods«. https://en.wikipedia.org/wiki/Runge%20%93Kutta_methods. Accessed: 2022-04-23 (page 154).
- [168] D. ZHANG et al. »Bolometer tomography on Wendelstein 7-X for study of radiation asymmetry«. In: *Nuclear Fusion*, Vol. 61.11 (2021), page 116043. DOI: 10.1088/1741-4326/ac2778 (pages 164, 236, 298).
- [169] »Python NumPy FFT routine«. <https://numpy.org/doc/stable/reference/routines.fft.html>. Accessed: 2022-08-06 (page 178).
- [170] »Python NumPy FFT frequency bin routine«. <https://numpy.org/doc/stable/reference/generated/numpy.fft.freq.html>. Accessed: 2022-08-06 (page 179).
- [171] W. CONTRIBUTORS. »Coherence (signal processing)«. [https://en.wikipedia.org/wiki/Coherence_\(signal_processing\)](https://en.wikipedia.org/wiki/Coherence_(signal_processing)). Accessed: 2022-08-08 (page 179).
- [172] J. W. COOLEY and J. W. TUKEY. »An algorithm for the machine calculation of complex Fourier series«. In: *Mathematics of Computation*, Vol. 19 (1965), pages 297–301 (page 179).
- [173] A. G. PEETERS. »Reduced charge state equations that describe Pfirsch-Schlüter impurity transport in tokamak plasma«. In: *Physics of Plasmas*, Vol. 7.1 (2000), pages 268–275. DOI: 10.1063/1.873812. eprint: https://pubs.aip.org/aip/pop/article-pdf/7/1/268/19113408/268_1_online.pdf (page 191).
- [174] S. HIRSHMAN and D. SIGMAR. »Neoclassical transport of impurities in tokamak plasmas«. In: *Nuclear Fusion*, Vol. 21.9 (1981), page 1079. DOI: 10.1088/0029-5515/21/9/003 (page 191).

Bibliography

- [175] W. CONTRIBUTORS. »Crank–Nicolson method«. <https://de.wikipedia.org/wiki/Crank–Nicolson–Verfahren>. Accessed: 2024-03-01 (page 192).
- [176] R. DUX. »STRAHL User Manual«. In: (2006) (page 192).
- [177] P. R. GONCHAROV et al. »Stellarator Impurity STRAHL Code Development in NIFS«. In: *Plasma and Fusion Research*, Vol. 2 (2007), S1132–S1132. DOI: 10.1585/pfr.2.S1132 (page 192).
- [178] K. BEHRINGER. »Description of the impurity transport code STRAHL«. In: *Jet Report*, Vol. 87.JET-R 87 (08) (1987) (page 192).
- [179] NIST. »Atomic Spectra Database, NIST Standard Reference Database 78, v5.10«. <https://www.nist.gov/pml/atomic-spectra-database>. Accessed: 2021-03-24 (page 193).
- [180] EURATOM. »Open-ADAS, Atomic Data and Analysis Structure«. <https://open.adas.ac.uk/>. Accessed: 2021-03-24 (page 193).
- [181] T. KLINGER et al. »Overview of first Wendelstein 7-X high-performance operation«. In: *Nuclear Fusion*, Vol. 59.11 (2019), page 112004. DOI: 10.1088/1741-4326/ab03a7 (pages 199, 223).
- [182] D. ZHANG et al. »First observation of a stable highly-radiative divertor regime at stellarator W7-X«. In: *45th EPS Conference on Plasma Physics*, Vol. O3.103 (2018) (page 223).
- [183] R. L. PARKER. »Understanding Inverse Theory«. In: *Annual Review of Earth and Planetary Sciences*, Vol. 5.1 (1977), pages 35–64. DOI: 10.1146/annurev.ea.05.050177.000343. eprint: <https://doi.org/10.1146/annurev.ea.05.050177.000343> (page 230).
- [184] C. PENG, W. RODI and M. N. TOKSOZ. »Smoothest-model reconstruction from projections«. In: *Inverse Problems*, Vol. 9.2 (1993), page 339. DOI: 10.1088/0266-5611/9/2/012 (page 230).
- [185] R. J. STERITI and M. A. FIDDY. »Regularized image reconstruction using neural networks«. In: *Inverse Problems in Scattering and Imaging*. Edited by M. A. FIDDY. Vol. 1767. International Society for Optics and Photonics. SPIE, 1992, pages 112–119. DOI: 10.1117/12.139010 (page 230).

- [186] M. ANTON et al. »X-ray tomography on the TCV tokamak«. In: *Plasma Physics and Controlled Fusion*, Vol. 38.11 (1996), page 1849. DOI: [10.1088/0741-3335/38/11/001](https://doi.org/10.1088/0741-3335/38/11/001) (pages 231, 236, 237).
- [187] R. A. FISHER and E. J. RUSSELL. »On the mathematical foundations of theoretical statistics«. In: *Philosophical Transactions of the Royal Society of London. Series A, Containing Papers of a Mathematical or Physical Character*, Vol. 222.594-604 (1922), pages 309–368. DOI: [10.1098/rsta.1922.0009](https://doi.org/10.1098/rsta.1922.0009). eprint: <https://royalsocietypublishing.org/doi/pdf/10.1098/rsta.1922.0009> (page 231).
- [188] B. FRIEDEN. »Applications to Optics and Wave Mechanics of the Criterion of Maximum Cramer-Rao Bound«. In: *Journal of Modern Optics*, Vol. 35.8 (1988), pages 1297–1316. DOI: [10.1080/09500348814551451](https://doi.org/10.1080/09500348814551451). eprint: <https://doi.org/10.1080/09500348814551451> (page 231).
- [189] B. FRIEDEN. *Probability, Statistical Optics, and Data Testing: A Problem Solving Approach*. Springer Series in Information Sciences. Springer Berlin Heidelberg, 2012. URL: <https://books.google.de/books?id=gdf6CAAAQBAJ> (page 231).
- [190] X. S. LI. »An Overview of SuperLU: Algorithms, Implementation, and User Interface«. In: Vol. 31.3 (2005), pages 302–325 (page 233).
- [191] F. J. »Two-dimensional reconstruction of the radiation power density in ASDEX Upgrade«. In: *21st EPS Conference Controlled Fusion and Plasma Physics (27 June – 1 July, 1994, Montpellier, France)*. European Physical Society. 1994 (page 236).
- [192] D. LI et al. »Application of Bayesian tomography method to the visible spectroscopic diagnostic on HL-2A tokamak«. In: *Plasma Physics and Controlled Fusion*, Vol. 63.3 (2021), page 035002. DOI: [10.1088/1361-6587/abd0a3](https://doi.org/10.1088/1361-6587/abd0a3) (page 237).
- [193] L. EL GHAOUI. »Inversion error, condition number, and approximate inverses of uncertain matrices«. In: *Linear Algebra and its Applications*, Vol. 343-344 (2002). Special Issue on Structured and Infinite Systems of Linear equations, pages 171–193. DOI: [https://doi.org/10.1016/S0024-3795\(01\)00273-7](https://doi.org/10.1016/S0024-3795(01)00273-7) (pages 244, 311).

Measurement algorithm

Algorithm 1: Bolometer measurement routine and feedback.

Result: calibration, measurement, real-time feedback

input : Δt , ranges, S , c , N , M , V_M and K_M
output : at runtime: $P_{\text{pred}}^{(1)}$, $P_{\text{pred}}^{(2)}$; post: calibration, κ , τ , R , ΔU , $P_{\text{pred}}^{(n)}$

TRIGGER \rightarrow initialization [$T1 - 60\text{s}$];

K_M , $V_M \leftarrow$ input file (standard geometry);

S , $c \leftarrow$ file/visual input, selection and single channel;

$U_{AO,n} \leftarrow$ memory address, initialize 0 V;

NI® 6321 \leftarrow initialize two-channel analog output;

// output as long as main data acquisition

// does not return successfully

while measurement incomplete do

 for $n \in \{1, 2\}$ do

$U_{AO,n} \leftarrow$ read $P_{\text{pred}}^{(n)}$;
 device FIFO $\leftarrow U_{AO,n}$;
 flush FIFO to voltage output;

 end

end

:

}

parallel

Algorithm 1: Bolometer measurement routine and feedback.

```

:
mode register  $\leftarrow$  full range  $\pm 80$  mV;
filter register  $\leftarrow$  sample time 0.4 ms;
 $V_{\text{off}} \leftarrow 10$  s offset measurement mean;

mode register  $\leftarrow$  two-stage calibration;
for absorber  $\in$  (measurement, reference) do
    // 10000 samples over 4 s
    for  $i = 0, i < 10000, i \rightarrow 10000$  do
        if  $2000 < i < 6000$  then
             $R, \tau \leftarrow$  max current and decay;
             $\kappa \leftarrow$  linear resistance change by ohmic heating;
        end
    end
end
mode register  $\leftarrow$  individual range (10 mV, 20 mV);
filter register  $\leftarrow$  sample time  $\Delta t$ ;
(1)FIFO  $\leftarrow$  initialize  $|S| \times (M + 2)$  array;
(2)FIFO  $\leftarrow$  initialize  $(M + 1)$  array;
 $P_{\text{pred}}^{(n)}, \Delta U \leftarrow$  initialize  $N$  sample array;
:

```

Algorithm 1: Bolometer measurement routine and feedback.

```
:
// final measurement
for  $i = 0, i < N + 1000, i \rightarrow N + 1000$  do
    if  $i > 1000$  then
         $\Delta U^{(i)} \leftarrow \Delta t$  integrated absorber voltage;
        // store samples in FIFO
        for  $j \in S$  do
            |  $(1) \text{FIFO}_j^{(i \bmod M)} \leftarrow \Delta U_j^{(i)}$ ;
        end
         $(2) \text{FIFO}^{(i \bmod M)} \leftarrow \Delta U_c^{(i)}$ ;
        // mean over previous  $M$  samples
        for  $j \in S$  do
            |  $(1) \text{FIFO}_j^{(M+2)} \leftarrow (1) \text{FIFO}_j^{(M+1)}$ ;
            |  $(1) \text{FIFO}_j^{(M+1)} \leftarrow 1/M \sum_k^M (1) \text{FIFO}_j^{(k)}$ ;
            // derivative
            |  $d(\Delta \tilde{U}_j^{(i)})/dt \leftarrow ((1) \text{FIFO}_j^{(M+2)} + (1) \text{FIFO}_j^{(M+1)})/\Delta t$ ;
        end
         $(2) \text{FIFO}^{(M+1)} \leftarrow 1/M \sum_k^M (2) \text{FIFO}^{(k)}$ ;
        // memory address for feedback
         $P_{\text{pred}}^{(1)} \leftarrow \text{equation (3.1)} \leftarrow K_M, V_M, d(\Delta \tilde{U}_j^{(i)})/dt, (1) \text{FIFO}^{(k)}$ ;
         $P_{\text{pred}}^{(2)} \leftarrow \text{equation (3.2)} \leftarrow (2) \text{FIFO}^{(M+1)}$ ;
    end
end
// done, upload and saving
HDD  $\leftarrow P_{\text{pred}}^{(1)}, P_{\text{pred}}^{(2)}, \Delta U, \kappa, \tau, R$ , calibration currents;
W7-X archive  $\leftarrow P_{\text{pred}}^{(1)}, P_{\text{pred}}^{(2)}, \Delta U, \kappa, \tau, R$ , calibration currents;
```

Confirmed by Supervisor,
Greifswald, 05.03.2024

PROF. DR. THOMAS KLINGER

Confirmed by doctoral candidate,
Greifswald, 05.03.2024

PHILIPP SCHOLL, GEB. HACKER

List of Figures

1.1.	Stellarator Wendelstein 7-X: Cut-away rendering of the outer vessel, superconducting magnetic coils, cooling and supporting structure. The translucent red band is the plasma tube (last closed magnetic flux surfaces). ©IPP	3
1.2.	Flux tube of the last closed flux surface around the W7-X torus and cross-sections in the triangle- (left) and bean-shaped (right) plane. At 108° toroidally, the bolometer camera system is located.	5
2.1.	Detector schematic. Diagram of a single blackened detector foil with frame, substrate and meander. Layer dimensions are noted, however not pictured to scale	28
2.2.	(Left) Detector chip backside with four reference and measurement absorbers each connected in Wheatstone bridges as pairs. (Right) Bolometer group head assembly from plasma side (top) to cable connection pins (bottom).	29
2.3.	Overview of one (vertical bolometer) camera head. (Left) Two subdetector arrays mounted on two water cooled detector holders, separated with an optic baffle, behind a rotating shutter inside the ellipsoidal camera head at the front of the diagnostic port. (Right) Graphite tile cap in front of the stainless steel aperture plate as thermal protection with indicated line of sight cone, wire mesh microwave protection and backplate connectors.	30
2.4.	Lines of sight of (left) horizontal bolometer camera, consisting of 32 individual detectors, and (right) vertical bolometer possessing two subdetector arrays of 20 channels each, viewing the plasma through their own respective apertures.	31

List of Figures

2.5.	Mockup of how detectors are located in relation to their respective aperture A inside the camera housing C . D0 and D1 are located on the same subarray and hence in the same plane. D2 is on another part of the camera array that is angled differently towards the pinhole.	32
2.6.	Normalized arbitrary transmission functions of different size relations of aperture a to detector d . The W7-X core bolometry is built with $d < a$	33
2.7.	Angular relations of aperture, line of sight and detector. Angles of β and α denote the angles between normals and line of sight. The distance between detector and aperture is called d . A lighter shade of grey indicates the partially shadowed section.	34
2.8.	(a): (top) Detector A and B behind aperture with bolometer-like geometry. (bottom) Normalized transmission for both dimensions of the detectors. (b): Map of the normalized etendue for both absorbers on the left along a and b . Their sizes and distances are representative of the W7-X bolometer.	35
2.9.	(a): Schematic Wheatstone bridge with measurement (M) and reference (R) resistors R_M and R_R respectively. Both are thermally linked to an absorber, while the measurement part only is exposed to incident power. The bridge is connected with a voltmeter and AC excitation source. (b): Equivalent circuit for calibration of the Wheatstone bridge, with DC voltage U_{cal} , cable resistances R_C and an additional load R_L for current measurement I	37
2.10.	An example for a normalized single power stage of 0.5 s and resistive absorber response as described above. Shown on the left is the incident power. In the center are both the gain and time derivative of the voltage drop across the absorber. The final image on the right shows the sum of the latter, which again yields the input power.	39

- 2.11. Example of the first (left) and second (right, both - top) Ohmic heating stages as described for measurement and reference absorbers. One easily notices the difference in absorber response between reference and measurement part of the same bridge. The maximum current before the exponential decay during the first heating pulse corresponds to $\Delta I(0)$ 41
- 2.12. Example for a set of calculated normalized heat capacities, resistances and cooling times for both measurement and reference detectors as described below. Small groups of four consecutive detectors in each property hints at similarities in composition irregularity. Reference channel number 32 in the middle figure shows an especially low heat capacity, indicating an issue with the thermal contact of the meander bridge. 42
- 2.13. The left image shows the unaltered detector signal as measured by the data acquisition for the main HBC array in the W7-X experiment XP20180927.37. The middle is the subtracted, assuming linear, temperature drift for each of those channels. Note how either every channel has different drift functions or entirely different temperatures. The right picture shows the measurement results of two *Pt100* resistive thermometers from the back of the HBC array over the course of the experiment 44
- 2.14. Equivalent circuit for bridge imbalance measurements ΔU of Wheatstone bridge, with AC excitation voltage U_{ex} , cable resistances and capacity R_C and C_C 46
- 2.15. (a): Photoresponse signals for a thin gold foil bolometer absorber (solid) and gold diode (dotted) to synchrotron radiation[93]. (b): Efficiency of bolometer absorber over incident photon energy as derived and measured by Meister et. al[94]. 50

List of Figures

- 2.16. (a): Before and after the ceramic coating treatment and wire mesh installation in front of the detector arrays. Shown are the results of MISTRAL^I tests with and without microwave countermeasures. (Right) Transmission factor of wire mesh over channel number. Subsets of detectors are grouped into blocks inside the larger camera array, hence the steps in this curve. Their angle between the lines of sight and mesh normal is equal, yielding the same transmission coefficient. 52
- 2.17. Calibration parameters of the core bolometry system at W7-X during OP1.2b. (a) Resistance of the absorber as calculated by equation (2.7). (b) Normalized heat capacity of the detector from equation (2.10). (c) Cooling time from exponential decay fit to an ohmic heating stage as depicted in figure 2.11. (d) Absolute offset in acquisition before the discharge begins. 54
- 2.18. Operational performance numbers of the core bolometry system at W7-X during OP1.2b. (Top Left) Standard deviation from measurements without plasma background, i.e. 100 samples before ECRH starts. (Top Right) Thermal signal drift (positive). (Bottom Left) Median of signal during plasma discharges. (Bottom Right) Maximum signal for every experiment. 55
- 2.19. (a): Trapezoidal LOS cone through an exemplary volume element. The blue lines indicate the intersection of the line of sight and domain, i.e. test cube. Marked red is the length of the center LOS inside the volume. (b): A schematic assembly of the plasma vessel at 108° toroidally with outlines of the LCFS and attached 5/5-island chain from an exemplary Poincaré map. The estimation domain is marked with the dot-dashed line and red fill pattern. Approximately this equals 130% of the surface area/volume of the LCFS. 60
- 2.20. Line of sight volumes V_M (top) and Etendues K_M (bottom) of all camera arrays. Note how the bolometers have been designed in a way that all cameras roughly contribute the same LOS volume, while due to differences in the pinhole design etendues are twice as large for the vertical arrays. 63

- 2.21. XP20181010.36 (**top**) Absorbed power per channel P_M by equation (2.19) over time for HBC (left) and VBC (right). (**bottom**) Total radiative power loss as extrapolated from the above detector measurements using equation (2.25). Example discharge with thermal helium beam density control by interferometry in standard magnetic configuration and 5.72 MW input ECRH power, achieving $1.2 \times 10^{20}/\text{m}^3$ and 2.5 keV electron density and temperature, respectively. 64
- 2.22. (**left**): Standard magnetic configuration based grid with 20 radial and 150 poloidal divisions that covers $1.3 V_{\text{LCFS}}$. Marked are the center position of the individual apertures (black crosses) for all cameras. For reference one line of sight cone (noted in electrical channel number) per camera array has been included. (**right**): Total geometry contribution per pixel summed up from all three camera arrays. 66
- 2.23. Normalized effective plasma radius r_{eff} in units of the minor plasma radius $r_a=0.539 \text{ m}$ along the line of sight of each detector and camera array. Both methods from equation (2.28)(a) and (b) are shown as 'min' and ' ε ', respectively. 67
- 2.24. XP20180725.44 Example chord brightness profiles for equation (2.29) at (**top**) 3.0 s and (**bottom**) a temporal evolution between 3.1–3.35 s. Plot abscissa is given by the minor plasma radius normalization of equation (2.28)(b). The location of the last closed flux surface at 1.0 (-1.0 respectively) has been marked. This discharge was performed in a high magnetic mirror configuration at 1.3 MW ECRH power. 69
- 2.25. XP20180725.44 Example of local radiation distribution profiles at $t = 3.0 \text{ s}$. (**top-left**): Poloidally averaged radial radiation profile with absolute vertical and lateral error bars. (**top-right**): Two-dimensional radiation distribution, with Poincaré overplot of plasma islands and separatrix. (**bottom-left**): Radially averaged poloidal radiation profile with error bars. (**bottom-right**): Individual poloidal radiation distribution. 72

2.26. XP20180808.4 Example for power balance as in equation (2.37). (top-left) : Microwave power and divertor target heat loads, including individual elements (top-right) : Radiative power loss as measured by the bolometer cameras (bottom-left) : Plasma stored energy measured by diamagnetic loops and its time derivative (bottom-right) : Individual power balance for both bolometer cameras (blue, red) and a general result from the mean with error bar (grey).	78
2.27. XP20180725.44 Example discharge as previously exhibited. (top-left) : ECRH power and divertor target heat loads (top-right) : P_{rad} as measured by the bolometer cameras (bottom-left) : Plasma stored energy measured in W_{dia} and its time derivative (bottom-right) : Power balance for both bolometer cameras (blue, red) and their mean.	79
3.1. (left) : Standard magnetic configuration last closed flux surface (transparent, grey) inside ten divertor modules assembly (dark red). Five flux tubes that helically revolve around the core plasma and follow the island chains in front of the divertors included (red, yellow, purple, green, blue)[143]. (right) : Ten divertor elements (half-module HM 1-5, up (1) and down (0)) and helium beam gas boxes with positions of bolometry system (108° toroidally) and field lines that connect at the seeding points (red, blue)[144]	85
3.2. (a) : Gas injection box at the upper plasma edge with all 5 capillary nozzles as used for divertor operation. Included are spectroscopy lines of sight (orange) perpendicular to the beam and the last closed flux surface (red). Superimposed is the result of one EMC3-EIRENE for He line emission[147]. (b) : Relative toroidal position of all involved diagnostics. One filterscope system is located in the same divertor as one of the gas valve boxes, while interferometer and electron cyclotron measurements are done in different locations.	86

3.3. Schematic of a FIFO array. Time progresses from right to left, i.e. sample A is acquired before B, ..., Y and Z. Currently stored samples are B, ..., Y. When sample Z is acquired, sample A is removed from the FIFO array, the oldest data point at this moment.	94
3.4. Real-time feedback system benchmark result for 7 mW at 1 Hz laser diode power and frequency. The detector response was created using the algorithm for $P_{\text{pred}}^{(1)}$ with $M = 1$ the FIFO array length. A total, minimum latency of 13.6 ms was achieved during the test.	96
3.5. A block diagram of a PID controller in a feedback loop. Desired process value or setpoint SP $r(t)$ and measured process value PV $y(t)$. The control function $u(t)$ is used for feedback[161].	97
3.6. Example of how the control function $u(t)$ changes for the same setpoint SP (grey dashed) and system but different proportional, integrals and differential parts.	98
3.7. Laser test results without real-time radiation feedback. The expected number of samples and average sample time are shown in red. (left): Number of samples per laser half period over sample number (right): average sample time over laser half period, as derived from the leftover acquisition time.	99
3.8. Laser test results without real-time radiation feedback for 1.6 ms and 3.2 s. Both show the average sample times per laser half period over acquisition duration. The expected average sample times are shown in red.	100
3.9. Laser test results with real-time radiation feedback. The expected number of samples and average sample time are shown in red. (left): Number of samples per laser half period over sample number (right): Average sample time over laser half period, as derived from the leftover acquisition time.	101
3.10. Laser test results with real-time radiation feedback for 1.0 ms and 1.6 ms. Both show the average sample times per laser half period over acquisition duration. The expected average sample time is shown in red.	102

3.11. Laser test results without real-time radiation feedback and additional, synthetic PC load. The expected number of samples and average sample time are shown in red. (left): Number of samples per laser half period over sample number (right): Average sample time over laser half period over acquisition time.	103
3.12. Line of sight selection for experiment number XP20180920.29, only containing of HBC channels from the top and center part of the triangular cross-section, i.e. the bolometer measurement plane around $\varphi = 108^\circ$ toroidally.	104
3.13. XP20180929.29 Very first radiation feedback controlled plasma discharge. (top left): Microwave heating power, plasma stored energy and loss (center left top): Radiative power loss, both cameras and prediction values (center left bottom): PID control $u(t)$, reference $r(t)$ and valve actuation (center left bottom): Control components (top right): Electron density of selected Thomson scattering volumes and line integrated ECE measurement (center right): Individual bolometer channels, used for $P_{\text{pred}}^{(n)}$ (bottom right): Radiation fraction(s).	105
3.14. XP20180929.29 Chord brightness profiles (top) in two-dimensional contours and (bottom) at significant points in time for both cameras HBC and VBC.	108
3.15. XP20180929.31: (top left): ECRH power, plasma energy and loss (center left top): P_{rad} , prediction values (center left bottom): PID control $u(t)$, reference $y(t)$ and valve actuation (bottom left): Control component(s) (top right): Electron density of Thomson scattering and dispersion interferometer (center right top): Electron temperature of Thomson scattering and ECE (center right bottom): Bolometer channels for $P_{\text{pred}}^{(n)}$ (bottom right): Radiation fraction(s).	111
3.16. XP20180929.31 Chord brightness profiles. (top) Two-dimensional contours (bottom) snapshots for both cameras, HBC and VBC around feedback gas puff.	114

3.17. Adjusted, simulated PID controller response based on f_{rad} in XP20180920.31. The impact of the feedback on the radiation fraction was modelled linearly by a cost function around a target \hat{f}_{rad} . The setpoint SP is set to 0.9 or 90%. (left): The algorithm was allowed to control K_p and K_i . The ratio is noted above, while their values are shown normalized. (right): PID control derived K_i and K_d . The proportional K_p was taken from the experiment data, as seen in figure 3.13.118	118
3.18. Simulated PID response based on f_{rad} in XP20180920.31 including an ansatz with damping over $N\Delta t$ previous samples. Results are obtained for $\hat{f}_{\text{rad}} = 0.5$ and $N = 17$.	118
3.19. Line of sight selection for experiment number XP20181010.32, only containing VBC channels. The LOS cones cover all magnetic islands, as well as the core region and parts of the in-between X-points of separatrices.	120
3.20. XP20181010.32: (top left): ECRH power, plasma energy and loss (center left top): P_{rad} , prediction values (center left bottom): PID control $u(t)$, process value $y(t)$ and valve actuation (bottom left): Control components (top right): Electron density (center right top): Electron temperature (center right bottom): Bolometer channels for $P_{\text{pred}}^{(n)}$ (bottom right): Radiation fractions and target heat loads (individual, integrated).	121
3.21. XP20181010.32 Chord brightness profiles. (top) Two-dimensional contours (bottom) snapshots for both cameras, HBC and VBC around feedback gas puff.	126
3.22. XP20181010.32 Power balance for both P_{rad} of the individual camera arrays and a (grey) mean with error bar, derived from the intrinsic errors of the contributing physical quantities.	128
3.23. XP20181016.16: (top left): ECRH, plasma energy and loss (center left top): P_{rad} (center left bottom): Process value $y(t)$ and valve actuation (bottom left): Control components (top right): Electron density (center right): Electron temperature (bottom right): Radiation fractions and target heat load.	132

List of Figures

3.24. XP20181016.16 Power balance for both P_{rad} (red, blue) of individual camera arrays and a (grey) mean with error bar. 133

3.25. XP20181016.16: Chord brightness profile of HBC and VBC. 134

3.26. XP20180920.32: **(top left)**: ECRH, plasma energy and loss
(center left top): P_{rad} **(center left bottom)**: Process value $y(t)$ and valve actuation **(bottom left)**: Control components **(top right)**: Electron density **(center right)**: Electron temperature **(bottom right)**: Radiation fractions and target heat load. 136

3.27. Spatial-temporal evolution of C^{3+} radiation in front of the divertor in HM51. Plasma and target facing side (direction) are indicated. The measurements are performed by the same filterscopes, i.e. same lines of sight. 137

4.1. XP:20181010.32: Example of how peaks in experimental data are detected. Shown here is $P_{\text{rad},\text{HBCm}}$, as well as the feedback valve control in port AEH51. The peaks found in the lower plot are transparently overlaid onto the upper. Same colours indicate cause and effect relation between seeding and plasma parameter ($P_{\text{rad},\text{HBCm}}$) changes. Algorithmic peak detection width set to **(a)** 75 ms and **(b)** 150 ms. 143

4.2. Peak database of P_{rad} for both bolometer cameras individually from hydrogen seeding experiments. Changes in radiation power are shown for **(top left)** the change in seeding control, **(top right)** the approximate injected gas amount, **(bottom left)** the time between the maximum peak values and **(bottom right)** the time delay between peaks over the respective seeding control change. 145

4.3. Similar plot as figure figure 4.2, with the gas used for seeding being helium. Peak searching algorithm parameters are kept the same. 146

- 4.4. Selected experiment parameters for previously presented peaks in P_{rad} from seeding experiments. (**top left**) change in radiation power over change in seeding control with electron density colour map (**top right**) radiation fraction over heating power with n_e map (**bottom left**) radiation power delta over temporal peak delay with ECRH colour code (**bottom right**) electron density by heating power with radiation fraction map. 147
- 4.5. Peak database from main gas valve. Changes in radiation power P_{rad} of both cameras for (**top left**) the change in gas flow, (**top right**) the approximate injected gas amount, (**bottom left**) the time between the maximum peak values and (**bottom right**) the time delay between peaks over the respective gas flow. 149
- 4.6. Experiment parameters for main gas valve. (**top left**) change in radiation power over change in seeding control with electron density colour map (**top right**) radiation fraction over heating power with n_e map (**bottom left**) radiation power delta over temporal peak delay with ECRH colour code (**bottom right**) electron density by heating power with radiation fraction map. 151
- 4.7. XP20180920.49: Experimental data of P_{rad} for both bolometer cameras and PID components of gas seeding valve controller. This is an excerpt between 4.2 s and 8.2 s where two consecutive seeding stages were applied and the radiation power responded accordingly. 152
- 4.8. Two chamber model schematic, with N_p the plasma chamber population and N_w the wall chamber population, including their respective source and loss rates $\tau_{x,y}$ and Γ_s 153
- 4.9. Parameter variation for two chamber model in equation (4.3). Included are variations of seeding rate (**a**) Γ_s and limit parameter (**b**) $N_{w,\text{lim}}$, as well as wall-to-plasma loss rate (**c**) τ_p and initial population value (**d**) $N_{w,0}$, while the other model parameters have been kept constant. 155

4.10. Application of model equation (4.3) on experimental data from XP20180920.49 in-between 4.2 s and 8.2 s. The respective parameters of this solution are $\Gamma_s = 0.648 \text{ a. u./s}$, $\tau_{w,p} = 0.1 \text{ a. u./s}$, $N_{w,\lim} = 1.388 \text{ a. u.}$, $\tau_p = 0.436 \text{ a. u./s}$, $N_{p,0} = 0.011 \text{ a. u.}$ and $N_{w,0} = 0.075 \text{ a. u.}$	157
4.11. Three chamber model schematic, with the plasma chamber population N_p , N_w the wall chamber population and an additional chamber for a scrape-off layer population N_s . The seeding location has changed to the SOL, including the loss channel from there. There is also a second pair of respective source and loss rate terms between the individual model chambers.	158
4.12. Parameter variation for three chamber model in equation (4.3). Included are variations of limit parameters (a) $N_{w,\lim}$ and (b) $N_{p,\lim}$, plasma source and feedback injection rates (c) $\tau_{s,p}$ and Γ_s , as well as (e) $\tau_{w,s}$ source and (f) τ_s loss rates of the plasma scrape-off layer, while other model parameters have been kept constant.	161
4.13. Application of the model from equation (4.6) on the experimental data of XP20180920.49 in-between 4.2 s and 8.2 s. The final set of parameters from a least-square fit is $\tau_{s,p} = 0.1 \text{ a. u./s}$, $N_{p,\lim} = 17.9 \text{ a. u.}$, $\tau_{p,s} = 14.931 \text{ a. u./s}$, $\Gamma_s = 18.08 \text{ a. u./s}$, $N_{w,\lim} = 2.579 \text{ a. u.}$, $\tau_{w,s} = 2.561 \text{ a. u./s}$, $\tau_s = 2.772 \text{ a. u./s}$, $N_{p,0} = 0$, $N_{s,0} = 0$, $N_{w,0} = 1$. The weighting factor is $f = 10.957$	162
4.14. Example of how the quality of the prediction for the <i>weighted deviation</i> metric is calculated for the previously discussed XP20181010.32. (a) Comparison of traces $\varphi(t)$, calculated using equation (4.9), P_{rad} and $P_{\text{pred}}^{(1)}$ for a subset of three channels of the HBC. (b) Overview of 900 different combinations of three channel subsets for ϑ	168
4.15. Average prediction quality ϑ over a large number of experiments for combinations of three, five and seven channels using the <i>weighted deviation</i> metric. Prediction selections were limited to one of the individual camera arrays (a) HBCm and (b) VBC.	170

4.16. Example of how the quality of the prediction for the <i>correlation</i> metric is calculated for the previously discussed XP20181010.32. (a) Comparison of traces $\varphi(t)$, calculated using equation (4.10), P_{rad} and $P_{\text{pred}}^{(1)}$ for a subset of three channels of the HBC. (b) Overview of 900 different combinations of three channel subsets for ϑ	172
4.17. Average prediction quality ϑ over a large number of experiments for combinations of three, five and seven channels using the <i>correlation</i> metric. Prediction selections were limited to one of the individual camera arrays (a) HBCm and (b) VBC.	173
4.18. Example of how the quality of the prediction for the <i>mean deviation</i> metric is calculated for the previously discussed XP20181010.32. (a) Comparison of traces $\varphi(t)$, calculated using equation (4.11), P_{rad} and $P_{\text{pred}}^{(1)}$ for a subset of three channels of the HBC. (b) Overview of 900 different combinations of three channel subsets for ϑ	176
4.19. Average prediction quality ϑ over a large number of experiments for combinations of three, five and seven channels using the <i>mean deviation</i> metric. Prediction selections were limited to one of the individual camera arrays (a) HBCm and (b) VBC.	178
4.20. Example of how the quality of the prediction for the <i>FT correlation</i> metric is calculated for the previously discussed XP20181010.32. (a) Comparison of traces $\varphi(t)$, calculated using equation (4.11), P_{rad} and $P_{\text{pred}}^{(1)}$ for a subset of three channels of the HBC. (b) Overview of 900 different combinations of three channel subsets for ϑ	181
4.21. Average prediction quality ϑ over a large number of experiments for combinations of three, five and seven channels using the <i>FT correlation</i> metric. Prediction selections were limited to one of the individual camera arrays (a) HBCm and (b) VBC.	182

List of Figures

4.22. Experiment parameter analysis for the <i>weighted deviation</i> metric and the corresponding sensitivity results shown in figure 4.15. Included are maps of both cameras each for parameters (a), (b) microwave heating P_{ECRH} , (c), (d) radiation fraction f_{rad} and (e), (f) core electron temperature T_e	186
4.24. Comparison between <i>Thomson scattering</i> data and corresponding STRAHL simulation results for $f_{rad} = 33\%$ and 66% from experiment XP20181010.32. (a): Thomson scattering electron density and temperature data with individual second order spline interpolated lines (<i>interp.</i>), which were used as input for STRAHL simulations. (b): One-dimensional STRAHL simulation results of total carbon impurity radiation intensity.	194
4.26. Comparison between STRAHL simulation results for $f_{rad} = 33\%$ and 66% from experiment XP20181010.32. (a): one-dimensional STRAHL simulation results of carbon impurities for n_e and T_e on the left. The top shows the fractional abundances of the individual ionisation stages of carbon, while the bottom depicts the corresponding radiation intensities and total power density. (b): Individual and total radiation intensities for carbon, corresponding to the previously shown results in figure 4.24.	196
4.28. Comparison between input transport profiles and STRAHL simulation results corresponding to the calculations in figure 4.26. They are based off of the same experimental measurements (XP20181010.32) and compare $f_{rad} = 33\%$ and 66%. (a): radial fluid drift and diffusion profiles, which were used as input for the STRAHL calculations. (b): one-dimensional STRAHL simulation results of carbon impurity concentrations, relative to the total amount of atomic carbon in the simulation domain.	199

- 4.30. Comparison between *Thomson scattering* data and corresponding STRAHL simulation results for $f_{\text{rad}} = 90\%$ and 100% from experiment XP20181010.32. (a): Thomson scattering electron density and temperature data with individual second order spline interpolated lines (*interp.*). (b): STRAHL simulation results of carbon impurities. The top shows the fractional abundances and the bottom the radiation intensity fractions of the ionisation stages for carbon. 200
- 4.31. Individual and total radiation intensities for carbon, corresponding to the previously shown one-dimensional STRAHL simulation results in figure 4.30, for $f_{\text{rad}} = 90\%$ and 100%. 203
- 4.33. Comparison between two sets of radial transport coefficient profiles and corresponding STRAHL simulation results - the fractional abundance is shown here -, both for $f_{\text{rad}} = 100\%$ from experiment XP20181010.32. (a): normalized drift velocity profile and diffusion coefficient. (b): fractional abundances of carbon from STRAHL simulation results, corresponding to the different profiles on the left. 206
- 4.35. STRAHL simulation results of relative and total impurity radiation from carbon for the previously presented sets of radial drift and diffusion profiles in figure 4.33 for $f_{\text{rad}} = 100\%$ from experiment XP20181010.32. (a): relative radiation intensity for each individual ionisation stage of carbon. (b): Absolute radiation power and integrated loss for the same ion species. 207
- 4.37. Comparison between two sets of radial transport coefficient profiles and corresponding STRAHL simulation results - the fractional abundance is shown here -, both for $f_{\text{rad}} = 100\%$ from experiment XP20181010.32. (a): normalized drift velocity profile and diffusion coefficient. (b): fractional abundances of carbon from STRAHL simulation results, corresponding to the different profiles on the left. 208

4.39. STRAHL simulation results of relative and total impurity radiation from carbon for the previously presented sets of radial drift and diffusion profiles in figure 4.33 for $f_{\text{rad}} = 100\%$ from experiment XP20181010.32. (a): relative radiation intensity for each individual ionisation stage of carbon. (b): Absolute radiation power and integrated loss for the same ion species.	209
4.41. Comparison between two sets of input electron profiles and corresponding STRAHL simulation results around the separatrix - the fractional abundance is shown here -, both for $f_{\text{rad}} = 100\%$ from experiment XP20181010.32. The decay length of the extrapolated profiles, beyond the last closed flux surface was varied. (a): Electron density and temperature profiles from Thomson scattering measurements as before, where the decay length beyond the LCFS has been altered. (b): fractional abundances of carbon from STRAHL simulation results, corresponding to the different profiles on the left.	211
4.43. STRAHL simulation results of relative and total impurity radiation from carbon for the previously presented sets of electron density and temperature profiles around the separatrix in figure 4.41 for $f_{\text{rad}} = 100\%$ from experiment XP20181010.32. (a): relative radiation intensity for each individual ionisation stage of carbon. (b): Absolute radiation power and integrated loss for the same ion species.	212
4.45. STRAHL simulation results for different radial positions of the carbon impurity source around the separatrix in figure 4.41 for $f_{\text{rad}} = 100\%$ from experiment XP20181010.32. (a): fractional abundance of each individual ionisation stage of carbon. (b): Absolute radiation power and integrated loss for the same ion species.	214

- 4.47. Comparison between two sets of input electron profiles and corresponding STRAHL simulation results around the separatrix, both for $f_{\text{rad}} = 100\%$ from experiment XP20181010.32. The Thomson scattering measurement of electron density and temperature which is radially closest to the separatrix was rescaled. (a): Electron density and temperature profiles from Thomson scattering measurements. (b): fractional abundances of carbon from STRAHL simulation results, corresponding to the different profiles on the left. 215
- 4.49. STRAHL simulation results of relative and total impurity radiation from carbon for the previously presented sets of electron density and temperature profiles in figure 4.47 for $f_{\text{rad}} = 100\%$ from experiment XP20181010.32. (a): relative radiation intensity for each individual ionisation stage of carbon. (b): Absolute radiation power and integrated loss for the same ion species. 217
- 4.51. Forward integrated chord brightness profiles for the HBC at different f_{rad} for (a) from experiment XP20181010.32 and (b) STRAHL simulation results of total carbon impurity radiation distributions from previously presented electron density and temperature profiles in figure 4.26 and figure 4.30 of XP20181010.32. 219
- 4.53. Forward integrated chord brightness profiles for the HBC from STRAHL simulation results of total carbon radiation distributions for (a) different electron density and temperature profiles (b) varying transport coefficient profiles from figure 4.33 and figure 4.37, based on data from experiment XP20181010.32 at $f_{\text{rad}} \approx 100\%$ 221
- 4.55. Individual and total radiation power loss from carbon impurities, separated into core and SOL parts, for (a) different levels of f_{rad} , which are modelled from electron temperature and density profiles of experiment XP20181010.32, and (b) $f_{\text{rad}} \sim 100\%$ with similar underlying profiles but varying transport coefficients - they are the same as in figure 4.33 and figure 4.37. 222

List of Figures

- 5.1. Comparison between two radial anisotropy profiles k_{ani} for $k_{\text{core}} > k_{\text{edge}}$ and $k_{\text{core}} < k_{\text{edge}}$ each. The bottom abscissa notes the radial bin number, i.e. index and the top the corresponding radius in the $1.3V_P$ inflated cross-section. A grey line indicates the separatrix location r_a . Both lines are calculated using section 5.1.1 with $k_{\text{edge}} = 0.5$, $k_{\text{edge}} = 10$ and vice versa, $N_T = 15$ and $N_S = 2$ with a domain size of $n_r = 20.235$ 239
- 5.2. Example for variations of subdividing the individual detectors and apertures with increasing number of compartments. Shown on the left is a method of rectangular splitting, on the right using a simple triangulation procedure for $N \in \{2, 4, 8\}$ the number of compartments. Each individual subcompartment is coloured differently.
- 5.3. (a) Comparison for example LOS cones for channel 14 and 16 of the HBC with rectangular splitting at (blue) $N = 2$ and (green) $N = 8$ for both the detector and pinhole. Shown in both cases is the full LOS cone in red, created by projecting detector corners through respective opposite side corners of the pinhole, and the sum of the individual N^2 cones from the center of the detector elements through the corners of the pinhole rectangles in a different colour. (b) Line of sight cones from $N = 8$ split detectors and pinholes of neighbouring channels 15 and 16 of the HBC in red and blue. In both images, all of it is enclosed by a grey mesh, representing the previously introduced $1.3V_P$ hull of the extrapolated magnetic flux surfaces, wherein the LOS cones are defined and their volume calculated. 241
- 5.4. Collection of etendues and LOS cone volumes of all bolometer camera channels for varying interpolation methods and amounts. The left images include the HBC, while the right shows channels from the VBC, which is made up out of the left and right sub-array with individual pinholes. Rectangular interpolation results are depicted with squares, triangulation results with triangles and different colours for $N = \{2, 4, 8\}$. The top images show the collective etendue per channel and the lower display the total LOS volume. 242

- 5.5. Comparison between the total etendue or local sensitivity of the LOS system of the bolometer for different interpolation resolutions and methods. For both, the absolute logarithmic value of the difference between the sensitivities is plotted on the respective mesh grid that has been used to calculate the etendues. A Poincaré plot for the associated magnetic field is superimposed, showing the last closed flux surface and enclosing magnetic islands at that toroidal location. This is enclosed by a cut through the first machine wall. The left image shows the difference between $N = 2$ and $N = 8$ rectangular interpolations, while the right similarly displays the contrast between the prior and triangulations of the same resolution. 243
- 5.6. (a) Comparison of center LOS of the (black) original HBC geometry and an adjusted (red) geometry, where the pinhole and respective camera array have been centred around $z = 0$, the vertical dimension of the W7-X coordinate system. (b) Impact of the geometry changes in (a) to the collective etendues of the horizontal bolometer camera, calculated and portrayed as in figure 5.5. 246
- 5.7. Forward integrated chord brightness for the HBC at different f_{rad} for previously presented STRAHL results in figure 4.51 using the adjusted, hypothetical camera geometry from figure 5.6. 247
- 5.8. (a) Impact of geometry changes on the collective etendues of the horizontal camera, where one half (*upper*) of the camera array has been rotated so that all channels lie in one plane and each is the exact mirror opposite - the *mirror* being a plane defined by the camera aperture normal, perpendicular to the LOS fan - of one from the other half. (b) Forward integrated chord brightness for the HBC at different f_{rad} for previously presented STRAHL results in figure 4.51 using the hypothetical camera geometry from (a). 249

List of Figures

5.9. (a) Comparison of the (black) original HBC LOS fan and (red) changed geometry, where the entire camera array has been rotated so that all channels lie in one plane that is vertically upright and centred around $z = 0$, the vertical dimension of the W7-X coordinate system. (b) Impact of the geometry changes in (a) to the collective etendues of the horizontal camera.	250
5.10. Forward integrated chord brightness for the HBC at different f_{rad} for previously presented STRAHL results in figure 4.51, using the theoretical camera geometry of figure 5.9.	251
5.11. (a) Impact on the collective etendues of the horizontal camera, where the entire array has been replaced by an artificial, symmetrical, vertically upright LOS fan with equidistant channels around $z = 0$, the vertical dimension of the W7-X coordinate system. The LOS geometry is similar to the one presented in figure 5.9. (b) Forward integrated chord brightness at different f_{rad} for previously presented STRAHL results in figure 4.51, using the camera geometry of (a).	252
5.12. (a), (b) Comparison of the (black) vertically upright and $z = 0$ centred (hypothetical) HBC LOS fan - see figure 5.9 - and (red) a (a) -2° (upward) and (b) $+2^\circ$ (downward) respectively tilted geometry, where the array has been rotated around the normal of the LOS plane.	253
5.13. (a), (b) Impact on the collective etendues of the horizontal bolometer camera for the theoretical geometries shown in figure 5.12, likewise respectively for (a) -2° and (b) $+2^\circ$ tilts.	254
5.14. (a), (b) Forward integrated chord brightness at different f_{rad} for previously presented STRAHL results in figure 4.51, using the theoretical geometries of figure 5.12, likewise for (a) -2° and (b) $+2^\circ$ tilts.	255
5.15. (a) Comparison of the (black) horizontal bolometer camera LOS geometry and an artificial, new camera ("MIRh", blue) that is arranged opposite of the prior, spanning 15 new channels that cover the full torus cross-section homogeneously. (b) Same geometry comparison in projection of the toroidal plane of the bolometer camera assembly, i.e. $\varphi_{\text{tor}} = 108^\circ$	257

- 5.16. (a) Both vertical camera arrays (black) next to a similarly *new*, artificial LOS fan of 15 channels ("VBCm", blue), which is created also opposite the VBCr aperture and covers. (b) Same geometry comparison in projection of the toroidal plane of the bolometer camera assembly, i.e. $\varphi_{\text{tor}} = 108^\circ$ 258
- 5.17. (a), (b) Impact on the collective etendues of the entire bolometer camera system from the addition of the previously introduced *new*, artificial cameras from figure 5.16. On the (a) left, the local sensitivity of a hypothetical, horizontal camera (MIRh) is shown, while on the (b) right the same for a theoretical, vertical array can be found. 259
- 5.18. Example of a (**left**) *phantom radiation distribution* and (**center**) its reconstruction using the Minimum Fisher tomography and standard bolometer camera geometry, including the (**right**) relative local deviation between the two prior. The phantom image is constructed as a uniform *ring* along a fixed flux surface with radius r_a and a normal distributed intensity in radial direction with a maximum of 1 MW/m^3 and $\sigma = 0.25 \text{ m}$. The inversion domain is the magnetic standard configuration, as previously described in section 2.3.1. The RDA parameters were chosen as $k_{\text{core}} = 2$ and $k_{\text{edge}} = 0.5$ with no smoothing in-between. 264
- 5.19. Corresponding analysis for the results shown in figure 5.18. (**left**) Radial profile comparison between phantom and two-dimensional reconstruction, including the relative radial and poloidal weighting factor profiles dr and $d\vartheta$. Noted here are also the total integrated radiation powers for both. (**right**) Forward integrated chord brightness profiles of the individual arrays, using the standard camera geometry and the distributions from figure 5.18. The corresponding values for P_{rad} , as well as the fitness factor χ^2 are included. 266

List of Figures

- 5.20. Comparison of different RDA coefficient combinations for the same phantom radiation distribution (left), their reconstruction (center) and relative difference (right) using the Minimum Fisher tomography with standard bolometer camera geometry. The phantom image is constructed using a similarly bright ring around r_a as in figure 5.18, with a maximum intensity of 1 MW/m^3 , as well as an inside structure at $0.7r_a$ with a poloidally asymmetric maximum towards the lower side, close to the aperture of the VBC of 150% intensity of the prior. (a) A parameter combination preferring poloidal asymmetry equally in the core and edge. (b) RDA coefficients amplifying distinguishable structures in the edge and smooth radiation profiles in the core region. All distributions are plotted over the standard magnetic geometry mesh at 108° toroidally, as provided by section 2.3.1. 269
- 5.21. Corresponding analysis for the results shown in figure 5.20. The results are presented in the same way as in figure 5.19. (a) Parameter combination preferring poloidal asymmetry in the core and edge. (b) Coefficients amplifying distinguishable structures in the edge and smooth profiles in the core region. 271
- 5.22. (a), (b) Similarly constructed and reconstructed phantom radiation distribution as in figure 5.20, but the core structure has been rotated in clockwise direction by 90° . The tomographic inversion features the same RDA parameter combinations as before. 276
- 5.23. (a), (b) Corresponding analysis for the results shown in figure 5.22, similar to figure 5.21, using the noted below anisotropy parameters for the tomographic inversion. The results are presented in the same way as in figure 5.19. 277
- 5.24. (a), (b) Similarly constructed and reconstructed phantom radiation distribution as in figure 5.20, but the core structure has been rotated in clockwise direction by 180° . The tomographic inversion features the same RDA parameter combinations as before. 281

5.25. (a), (b) Corresponding analysis for the results shown in figure 5.24, similar to figure 5.21, using the noted below anisotropy parameters for the tomographic inversion. The results are presented in the same way as in figure 5.19.	283
5.26. (a), (b) Similarly constructed and reconstructed phantom radiation distribution as in figure 5.20, but the core structure has been rotated in clockwise direction by 270°. The tomographic inversion features the same RDA parameter combinations as before.	287
5.27. (a), (b) Corresponding analysis for the results shown in figure 5.26, similar to figure 5.21, using the noted below anisotropy parameters for the tomographic inversion. The results are presented in the same way as in figure 5.19.	289
5.28. Comparison between different reconstruction weighting methods, RDA and RGS, on the same phantom radiation distribution, using the same weighing coefficients and tomography parameters as well as camera geometries. The phantom image is constructed similarly to figure 5.20, while the outside ring at r_a is also adjusted to be poloidally asymmetric, with its maximum at the same position as the inner structure. (a) Standard Minimum Fisher information reconstruction with RDA. (b) Relative gradient smoothing, using the same RDA tomography parameters.	293
5.29. (a), (b) Corresponding analysis for the results shown in figure 5.28, using the noted below anisotropy parameters for the corresponding tomographic reconstruction methods. The results are presented in the same way as in figure 5.19.	296
5.30. Phantom radiation distribution reconstruction, mimicking a bright plasma core with six intensity maxima around the five islands of the magnetic standard configuration. The RDA coefficients that have been used support the accurate reconstruction of the designed profiles in the tomographic algorithm. (a, top) Phantom, tomogram and relative deviance, similar to figure 5.18. (down) Radial (left) and chordal (right) profile analysis, similar to figure 5.19.	299

List of Figures

5.35. Same phantom radiation distribution and reconstruction problem as in figure 5.35, but for a camera geometry rotation of -1° . (a) Phantom, tomogram and relative deviance, similar to figure 5.18. (b) Radial (left) and chordal (right) profile analysis, similar to figure 5.19.	318
5.36. MFR scan of phantom radiation distribution consisting of an isotropic ring at $0.5r_a$ with 0.1 m FWHM. (a) Core and (b) edge RDA coefficients are varied independently. In both, top to bottom: radial position of the maximum, FWHM, MSD for core, SOL and in total, total and core integrated 2D powers and fitness scales χ^2 and Pearson coefficient ρ_c	321
5.37. MFR scan of phantom images consisting of (a) one or (b) two concentric, isotropic, equally bright rings. In (b) only the inside rings' and in (a) both rings' radii have been varied, while the same RDA coefficients $k_{\text{core}}, k_{\text{edge}} = \{2, 2\}$ are used throughout. The layout of the results is similar to figure 5.36.	325
5.38. MFR scan of a phantom image consisting of <i>up-down</i> symmetrical chain of island-like radiation spots at $1.1r_a$ of 0.1 m FWHM (exemplary artificial profile can be found in figure 5.30). (a) Core and (b) edge RDA coefficients have been varied independently. The layout of the results is similar to figure 5.36.	329
5.39. Phantom images consisting of a singular bright spot of 0.2 m FWHM - (a) inboard and (b) outboard anisotropies.	330
5.40. Reconstruction scan for the corresponding phantom images in figure 5.39, a singular bright spot of 0.2 m FWHM - (a) inboard and (b) outboard anisotropies. In both, k_{core} has been varied in the same range. The layout of the results is similar to figure 5.36.	331
5.41. XP20180725.44: (top left): ECRH, plasma energy and loss (bottom left): P_{rad} (top right): Electron density (center right): Electron temperature (bottom right): Radiation fraction, target heat load and power balance.	336

List of Figures

- 5.42. XP20180725.44: Tomograms for the above discharge on a $1.25 r_a$ inflated grid with $n_r \times n_\theta = 20 \times 150$ and *KJM* high mirror magnetic configuration. RDA parameters applied here are $k_{\text{core}}, k_{\text{edge}} = \{2, 0.25\}$ with $N_T = 15$ and $N_S = 2$. Central experiment parameters can be found in figure 5.41. 337
- 5.43. XP20180809.13: (**top left**): ECRH, plasma energy and loss (**bottom left**): P_{rad} (**top right**): Electron density (**center right**): Electron temperature (**bottom right**): Radiation fraction and target heat load. 340
- 5.44. XP20180809.13: Tomographic reconstruction of experimental bolometer data on a $1.35 r_a$ inversion grid of standard magnetic configuration, otherwise similar to figure 5.42, between 1.8–2.8 s. RDA parameters are constant throughout at $k_{\text{core}}, k_{\text{edge}} = \{2, 0.5\}$ and $N_T = 14$, $N_S = 2$. Corresponding central experiment parameters can be found in figure 5.43. 341
- 5.45. XP20181010.32: Tomographic reconstruction of experimental data on a $1.35 r_a$ inversion grid with $n_r \times n_\theta = 30 \times 150$, based off of standard magnetic configuration. Throughout 0.65–3.05 s, the RDA parameters are constant at $k_{\text{core}}, k_{\text{edge}} = \{2, 0.35\}$. Corresponding central experiment parameters have been previously introduced in figure 3.20. 344
- 5.46. XP20181011.12: (**top left**): ECRH, plasma energy and loss (**bottom left**): P_{rad} (**top right**): Electron density (**center right**): Electron temperature (**bottom right**): Radiation fraction and target heat load. 347
- 5.47. XP20181011.12: Tomographic reconstruction of experimental bolometer data on a $1.35 r_a$ inversion grid with $n_r \times n_\theta = 20 \times 150$ intersections, based off of the *KJM* high mirror magnetic configuration. RDA parameters are constant throughout at $k_{\text{core}}, k_{\text{edge}} = \{2, 0.35\}$ and $N_T = 14$, $N_S = 2$. Corresponding central experiment parameters can be found in figure 5.46. 349

5.48. Collected results of previously presented tomographic phantom radiation profile reconstructions in section 5.3. A red, dashed line indicates congruence between the two, i.e. 1:1 relation. (left) : From top to bottom: FWHM position, FWHM maximum, P_{rad} from both cameras and two-dimensional, integrated emissivity. (right) : From top to bottom: MSD over χ^2 , MSD and χ^2 over Pearson coefficient ρ_C , P_{rad} over integral of core emissivity and over total integrated radiation.	352
5.49. Collected results of previously presented experimental data tomographic reconstructions in section 5.4. Included are reconstructions that yielded $\chi^2 < 1000$. A dashed 1:1 line indicates congruence between the axis and abscissa. If applicable, a regression linear fit for both cameras derived individually is noted in the bottom. A transparent error bar (orange) is indicated around the projected congruence. (top) : P_{rad} of both bolometer cameras from experiment and tomogram. (center) : P_{rad} of both cameras over integral of core emissivity. (bottom) : P_{rad} of both cameras over total integral of emissivity.	357
5.50. XP20181010.32: Comparison between previously derived power balance for XP20181010.32 in figure 3.22 and the balance calculated from the integrated two-dimensional radiation distribution of the tomographic reconstructions presented in section 5.4. (top) : Central experiment parameters towards the power balance. (bottom) : Comparison of power balances derived from a common P_{rad} and the radiation distribution integrals.	359
5.51. XP20180725.44: Comparison between power balances for XP20180725.44 as in figure 5.50. (top) : Central experiment parameters towards the discharge power balance. (bottom) : Comparison of power balances derived from a common P_{rad} and the radiation distribution integrals.	361

Statutory declaration

Eigenständigkeitserklärung

Hiermit erkläre ich, dass diese Arbeit bisher von mir weder an der Ma-the-ma-tisch-Naturwissenschaftlichen Fakultät der Universität Greifswald noch einer anderen wissenschaftlichen Einrichtung zum Zwecke der Promotion eingereicht wurde. Ferner erkläre ich, dass ich diese Arbeit selbstständig verfasst und keine anderen als die darin angegebenen Hilfsmittel und Hilfen benutzt und keine Textabschnitte eines Dritten ohne Kennzeichnung übernommen habe.

Greifswald, 05.03.2024

PHILIPP SCHOLL, GEB. HACKER

